



Full-scale experimental characterization of a non-isothermal realistic air jet for building ventilation : Local interaction effects, moisture transport and condensation prediction

Chi Kien Nguyen

► To cite this version:

Chi Kien Nguyen. Full-scale experimental characterization of a non-isothermal realistic air jet for building ventilation : Local interaction effects, moisture transport and condensation prediction. Thermics [physics.class-ph]. Université de Lyon, 2018. English. NNT : 2018LYSEI077 . tel-02061360

HAL Id: tel-02061360

<https://theses.hal.science/tel-02061360>

Submitted on 8 Mar 2019

HAL is a multi-disciplinary open access archive for the deposit and dissemination of scientific research documents, whether they are published or not. The documents may come from teaching and research institutions in France or abroad, or from public or private research centers.

L'archive ouverte pluridisciplinaire **HAL**, est destinée au dépôt et à la diffusion de documents scientifiques de niveau recherche, publiés ou non, émanant des établissements d'enseignement et de recherche français ou étrangers, des laboratoires publics ou privés.



N°d'ordre NNT : 2018LYSEI077

THESE de DOCTORAT DE L'UNIVERSITE DE LYON
opérée au sein de
L'INSA LYON

Ecole Doctorale N° 162
MEGA
(Mécanique, Énergétique, Génie Civil, Acoustique)

Spécialité/ discipline de doctorat :
Génie Civil

Soutenue publiquement le 25/10/2018, par :
Chi-Kien NGUYEN

**Full-scale experimental characterization
of a non-isothermal realistic air jet for
building ventilation: local interaction effects
and condensation prediction**

Devant le jury composé de :

Monika WOLOSZYN	Professeur des Universités, Université Savoie Mont Blanc	Rapporteuse
Amina MESLEM	Professeur des Universités, Université de Rennes	Rapporteuse
Pascal Henry BIWOLE	Professeur des Universités, Université Clermont Auvergne	Examineur
Catalin TEODOSIU	Maître de Conférences, UTCB Roumanie	Examineur
Frédéric KUZNIK	Professeur des Universités, INSA de Lyon	Directeur de thèse
Damien DAVID	Maître de Conférences, Université de Lyon 1	Co-directeur de thèse
Gilles RUSAOUËN	Maître de Conférences, Université de Lyon 1	Invité

Département FEDORA – INSA Lyon - Ecoles Doctorales – Quinquennal 2016-2020

SIGLE	ECOLE DOCTORALE	NOM ET COORDONNEES DU RESPONSABLE
CHIMIE	CHIMIE DE LYON http://www.edchimie-lyon.fr Sec. : Renée EL MELHEM Bât. Blaise PASCAL, 3e étage secretariat@edchimie-lyon.fr INSA : R. GOURDON	M. Stéphane DANIELE Institut de recherches sur la catalyse et l'environnement de Lyon IRCELYON-UMR 5256 Équipe CDFA 2 Avenue Albert EINSTEIN 69 626 Villeurbanne CEDEX directeur@edchimie-lyon.fr
E.E.A.	ÉLECTRONIQUE, ÉLECTROTECHNIQUE, AUTOMATIQUE http://edeea.ec-lyon.fr Sec. : M.C. HAVGOUDOUKIAN ecole-doctorale.eea@ec-lyon.fr	M. Gérard SCORLETTI École Centrale de Lyon 36 Avenue Guy DE COLLONGUE 69 134 Écully Tél : 04.72.18.60.97 Fax 04.78.43.37.17 gerard.scorletti@ec-lyon.fr
E2M2	ÉVOLUTION, ÉCOSYSTÈME, MICROBIOLOGIE, MODÉLISATION http://e2m2.universite-lyon.fr Sec. : Sylvie ROBERJOT Bât. Atrium, UCB Lyon 1 Tél : 04.72.44.83.62 INSA : H. CHARLES secretariat.e2m2@univ-lyon1.fr	M. Philippe NORMAND UMR 5557 Lab. d'Ecologie Microbienne Université Claude Bernard Lyon 1 Bâtiment Mendel 43, boulevard du 11 Novembre 1918 69 622 Villeurbanne CEDEX philippe.normand@univ-lyon1.fr
EDISS	INTERDISCIPLINAIRE SCIENCES-SANTÉ http://www.ediss-lyon.fr Sec. : Sylvie ROBERJOT Bât. Atrium, UCB Lyon 1 Tél : 04.72.44.83.62 INSA : M. LAGARDE secretariat.ediss@univ-lyon1.fr	Mme Emmanuelle CANET-SOULAS INSERM U1060, CarMeN lab, Univ. Lyon 1 Bâtiment IMBL 11 Avenue Jean CAPELLE INSA de Lyon 69 621 Villeurbanne Tél : 04.72.68.49.09 Fax : 04.72.68.49.16 emmanuelle.canet@univ-lyon1.fr
INFOMATHS	INFORMATIQUE ET MATHÉMATIQUES http://edinfomaths.universite-lyon.fr Sec. : Renée EL MELHEM Bât. Blaise PASCAL, 3e étage Tél : 04.72.43.80.46 Fax : 04.72.43.16.87 infomaths@univ-lyon1.fr	M. Luca ZAMBONI Bât. Braconnier 43 Boulevard du 11 novembre 1918 69 622 Villeurbanne CEDEX Tél : 04.26.23.45.52 zamboni@maths.univ-lyon1.fr
Matériaux	MATÉRIAUX DE LYON http://ed34.universite-lyon.fr Sec. : Marion COMBE Tél : 04.72.43.71.70 Fax : 04.72.43.87.12 Bât. Direction ed.materiaux@insa-lyon.fr	M. Jean-Yves BUFFIÈRE INSA de Lyon MATEIS - Bât. Saint-Exupéry 7 Avenue Jean CAPELLE 69 621 Villeurbanne CEDEX Tél : 04.72.43.71.70 Fax : 04.72.43.85.28 jean-yves.buffiere@insa-lyon.fr
MEGA	MÉCANIQUE, ÉNERGÉTIQUE, GÉNIE CIVIL, ACOUSTIQUE http://edmega.universite-lyon.fr Sec. : Marion COMBE Tél : 04.72.43.71.70 Fax : 04.72.43.87.12 Bât. Direction mega@insa-lyon.fr	M. Jocelyn BONJOUR INSA de Lyon Laboratoire CETHIL Bâtiment Sadi-Carnot 9, rue de la Physique 69 621 Villeurbanne CEDEX jocelyn.bonjour@insa-lyon.fr
ScSo	ScSo* http://ed483.univ-lyon2.fr Sec. : Viviane POLSINELLI Brigitte DUBOIS INSA : J.Y. TOUSSAINT Tél : 04.78.69.72.76 viviane.polsinelli@univ-lyon2.fr	M. Christian MONTES Université Lyon 2 86 Rue Pasteur 69 365 Lyon CEDEX 07 christian.montes@univ-lyon2.fr

Abstract

Understanding room air distribution with coupled heat-air-moisture transport is essential to the design of building ventilation systems. A proper design should ensure three major criteria: energy efficiency, occupants' thermal comfort and indoor air quality, whose requirements are steadily increasing. Indoor air distribution investigation involves two common methods: numerical simulation and full-scale measurements. Numerical simulation using CFD models (Computational Fluid Dynamics) is most efficient for predicting airflow distributions and for assessing ventilation performances in buildings. However, their accuracy and reliability remain a major concern, given the lack of proper and thorough validation studies, particularly from full-scale experimental studies.

Among indoor air distribution methods, mixing ventilation is one of the most commonly used, whose performance is determined by that of the injected air jet. In the past decades, although numerous research have been undertaken on air jet studies, there are still some issues deserving consideration. In fact, the majority of these studies focused on a symmetric arrangement of supply and exhaust air outlets with respect the room geometry. Besides, studies dealing with room coupled heat-air-moisture transport, which includes the condensation phenomenon on the room inner surface, are generally lacking in the literature. Hence, this work focuses on the following problematic: What is the behavior of a realistic air jet under interaction effects and how to characterize such air jets? In realistic indoor conditions promoting condensation on cold surface, how it is possible to quantify the condensation rate? To tackle these issues, a full-scale experimental investigation has been carried out in the environments controlled MINIBAT test cell (6.2 x 3.1 x 2.5 m).

The first part consists in characterizing a ceiling turbulent air jet in a realistic indoor airflow configuration. Our case study introduces architectural elements which make the air jet interacted with the room: a plenum box, a supply grille diffuser near a side vertical wall, an asymmetric arrangement of the air exhausts regarding the air supply. The indoor air metrology is based on a laboratory-designed mobile robot equipped with accurate sensors. Three cases are tested: an isothermal, a cold and a hot air jet. The experimental results show visible interaction effects of the room architectural elements on the air jet behavior: they have deviated the jet trajectory as well as deformed the jet cross-sectional shape. The jet main characteristics such as the jet dynamic/thermal spread rate, the maximum velocity and temperature decays are quantified. A graphical-based method is proposed to quantify the jet shape deformation using a so-called deformation indicator. The latter shows an acceptable performance in characterizing the deformation of jet cross-sectional profiles.

The second part of this work treats the phenomenon of moisture condensation on a glazing surface by reproducing the winter conditions within the test cell: an indoor hot

humid air jet and a cold outdoor climate. The condensation qualitative prediction, i.e. the moment of its appearance and its growth dynamic mechanism, is achievable using a macro-photography technique. A post-processing of these time-series images makes it possible to estimate the condensate mass flow rate. Comparisons between experimental and theoretical results show some agreement, which could validate the feasibility of the imaging techniques in full-scale condensation studies.

Detailed experimental data accompanied by well-known boundary conditions from this work could serve as a benchmark test for CFD models validation, in particular for airflow configurations with rupture of symmetry. Besides, with advances in computer sciences, the proposed image processing could be considerably improved by means of the artificial intelligence, for instance the artificial neural networks with deep learning-based image analysis.

KEYWORDS: Realistic air jet, interaction effects, mixing ventilation, dropwise condensation, image processing.

Résumé

La compréhension de la distribution de l'air intérieur accompagné du transfert couplé "chaleur-air-humidité" est essentielle à la conception des systèmes de ventilation des bâtiments. Une conception adéquate devrait garantir trois critères majeurs: l'efficacité énergétique, le confort thermique des occupants et la qualité de l'air intérieur, dont les exigences ne cessent d'augmenter. L'étude de la distribution de l'air intérieur implique deux méthodes courantes : la simulation numérique et les essais à l'échelle réelle. La simulation numérique utilisant des modèles CFD (Computational Fluid Dynamics) est la plus efficace pour prédire la distribution d'air et la performance des systèmes de ventilation dans les bâtiments. Néanmoins, leur précision et leur fiabilité demeurent une préoccupation majeure, compte tenu du manque d'études de validation approfondies, en particulier des études expérimentales à l'échelle réelle.

Parmi les méthodes de distribution d'air intérieur, la ventilation par mélange est l'une des plus couramment utilisées, dont la performance est déterminée par celle du jet d'air injecté. Au cours des dernières décennies, bien que de nombreuses recherches aient été menées sur les études des jets d'air, certaines questions méritent toutefois d'être examinées. En effet, la majorité de ces études se sont concentrées sur une disposition symétrique des bouches de soufflage et d'extraction par rapport à la géométrie du local. En outre, les études traitant du transfert couplé "chaleur-air-humidité", qui inclut le phénomène de condensation sur la surface interne du local, sont encore limités dans la littérature. Par conséquent, ce travail se concentre sur la problématique suivante : Quel est le comportement d'un jet d'air réaliste sous des effets d'interaction et comment caractériser de tels jets d'air ? Dans des conditions d'intérieur réalistes favorisant la condensation sur une surface froide, serait-il possible de quantifier le débit massique du condensat ? Pour apporter des réponses à ces questions, une étude expérimentale à l'échelle réelle est réalisée dans la cellule d'essais MINIBAT (6,2 x 3,1 x 2,5 m).

La première partie consiste à caractériser un jet d'air turbulent au plafond dans une configuration d'écoulement intérieur réaliste. Notre configuration introduit des éléments architecturaux qui font interagir le jet d'air avec la pièce : un plénum, une bouche de soufflage équipée de fixes ailettes et située près d'un mur latéral, une disposition asymétrique des bouches d'extraction par rapport au soufflage. La mesure des champs intérieurs est basée sur un robot mobile équipé de capteurs précis. Trois cas sont testés : un jet isotherme, un jet froid et un jet chaud. Les résultats expérimentaux montrent les effets d'interaction visibles des éléments architecturaux de la pièce sur le comportement du jet d'air : ils ont dévié la trajectoire du jet ainsi que déformé la forme du jet. Les principales caractéristiques du jet, telles que les taux d'expansion dynamique/thermique du jet, les décroissances de vitesse et de température maximales, sont quantifiées. Pour quantifier la déformation des profils transversaux du jet, une méthode graphique basée sur un indicateur de déformation est proposée et montre des résultats acceptables.

La deuxième partie de ce travail traite le phénomène de condensation sur une surface vitrée en reproduisant les conditions hivernales dans la cellule de test : un jet chaud et humide à l'intérieur et un climat extérieur froid. La prédiction qualitative de la condensation, c'est-à-dire le moment de son apparition et son mécanisme dynamique de croissance, est réalisable en utilisant une technique de macrophotographie. Un post-traitement de cette série chronologique d'images rend possible l'estimation du débit massique de condensat. Les comparaisons entre les résultats expérimentaux et théoriques montrent une certaine concordance, ce qui pourrait valider la faisabilité des techniques d'imagerie dans des études de condensation à l'échelle du bâtiment.

Des données expérimentales détaillées accompagnées de conditions aux limites bien connues issues de ce travail pourraient servir de test de benchmark pour la validation des modèles CFD, en particulier pour les configurations découlement avec rupture de symétrie. De plus, avec les progrès de l'informatique, le traitement d'image proposé pourrait être considérablement amélioré grâce à l'intelligence artificielle, par exemple les réseaux de neurones artificiels avec l'analyse d'images basée sur l'apprentissage profond.

MOTS-CLEFS: Jet d'air réaliste, effets d'interaction, ventilation par mélange, condensation en gouttelettes, traitement d'images.

Nomenclature

Symbols

A	Area	$[m^2]$
Ar	Archimedes number	$[-]$
b_v	Jet dynamic thickness	$[m]$
b_T	Jet thermal thickness	$[m]$
C_p	Thermal capacity	$[J/kg.K]$
DI	Deformation indicator	$[-]$
d	Diameter	$[m]$
e	Thickness	$[m]$
f	Frequency	$[Hz]$
g	Gravitational acceleration	$[m/s^2]$
h	Heat transfer coefficient	$[W/m^2.K]$
k	Turbulence kinetic energy	$[m^2/s^2]$
K_1	Jet maximum velocity decay coefficient	$[-]$
K_2	Jet dynamic spread rate coefficient	$[-]$
$K_{2,T}$	Jet thermal spread rate coefficient	$[-]$
K_n	Coefficient of non-isothermality	$[-]$
K_T	Jet maximum temperature decay coefficient	$[-]$
m	Mass	$[kg]$
\dot{m}	Condensation rate	$[kg/m^2.s]$
P	Perimeter	$[m]$
Pr	Prandtl number	$[-]$
q	Heat transfer rate	$[W]$
Q	Flow rate	$[m^3/h]$
R	Thermal resistance	$[m^2.K/W]$
RH	Relative humidity	$[\%]$
Re	Reynolds number	$[-]$
r	Radius	$[m]$
r	Specific humidity	$[g/kg_{as}]$
t	Time	$[s]$
T	Temperature	$[^{\circ}C]$
TI	Turbulence intensity	$[\%]$
u	Velocity	$[m/s]$
x	Axial distance from the diffuser face	$[m]$
Z	Vertical distance from the room floor	$[m]$

Greek Symbols

ΔT	temperature difference	[°C]
λ	thermal conductivity	[W/m.K]
ν	kinematic viscosity	[m ² /s]
ρ	density	[kg/m ³]
σ	standard deviation	[m/s]
τ	time constant	[s]
θ	droplet contact angle	[°]

Subscripts

0	initial/supply
95	95% of the amplitude
<i>amb</i>	ambient air
<i>AHU</i>	air handling unit
<i>c</i>	cut-off
<i>c</i>	isocontour
<i>C</i>	ceiling
<i>cc</i>	climatic chamber
<i>COOL</i>	cooling coil
<i>d</i>	single droplet
<i>Deq</i>	disk-equivalent
<i>EW</i>	East wall
<i>F</i>	floor
<i>GL</i>	glazing
<i>h</i>	hydraulic
<i>IN</i>	inlet
<i>l</i>	liquid
<i>ilv</i>	liquid-vapor interface
<i>m</i>	centerline/maximum
<i>MB</i>	MINIBAT
<i>NW</i>	North wall
<i>OUT</i>	outlet
<i>sat</i>	saturation
<i>sp</i>	set point
<i>S2S</i>	surface-to-surface
<i>SE</i>	outer surface
<i>SI</i>	inner surface
<i>tbz</i>	thermal buffer zone
<i>tot</i>	total
<i>w</i>	wall
<i>WW</i>	West wall

Contents

Abstract	v
Résumé	vii
Nomenclature	ix
Contents	xi
List of figures	xvii
List of tables	xxiii
1 Introduction	1
1.1 Building ventilation for comfort, health and energy: a look back in the history	1
1.1.1 Building ventilation design for human comfort	1
1.1.2 Building ventilation design regarding the energy efficiency	2
1.1.2.1 Energy crisis, climate change and energy efficient buildings	2
1.1.2.2 Building energy efficiency: huge potential for ventilation design	4
1.1.3 Building ventilation design regarding the indoor air quality	5
1.1.3.1 Sick Building Syndrome	5
1.1.3.2 Ventilation rate and IAQ	6
1.2 Indoor air distribution and ventilation performance prediction: a literature review	8
1.2.1 Tools for building ventilation performance prediction	8

1.2.1.1	Empirical models	9
1.2.1.2	CFD models	9
1.2.1.3	Full-scale experimental studies	10
1.2.2	Indoor air distribution methods	10
1.2.2.1	Displacement ventilation	11
1.2.2.2	Mixing ventilation	12
1.3	Problem statement and outline of the thesis	14
1.3.1	Problem statement	14
1.3.1.1	Turbulent free jet theory	15
1.3.1.2	From free jet theory to realistic jet in a complex geometry	16
1.3.1.3	Moisture transport and condensation	20
1.3.2	Outline of the thesis	21
1.3.2.1	Research objectives	21
1.3.2.2	Definition of the studied configuration	22
1.3.2.3	Expected outcomes	24
1.3.2.4	Manuscript organization	24
2	Experimental set-up	27
2.1	Introduction	27
2.2	MINIBAT experimental facility	27
2.2.1	General purpose of MINIBAT	27
2.2.2	History of MINIBAT	28
2.2.3	MINIBAT architecture	29
2.2.3.1	The test cell	29
2.2.3.2	The thermal zones	31
2.2.3.3	Existing metrology in MINIBAT	33
2.2.3.4	Performance test of MINIBAT	36
2.3	Test cell adapted configuration for the study	36
2.3.1	Airflow configuration for the test cell	37
2.3.1.1	Air supply and air exhaust mouths	37
2.3.1.2	Plenum box	38
2.3.1.3	Grille diffuser	38

2.3.2	Southern wall	38
2.3.3	Air handling unit for the test cell	40
2.3.3.1	Air handling unit description	40
2.3.3.2	Air handling unit metrology and regulation	40
2.3.3.3	Steam generator for the air handling unit	43
2.4	Summary: boundary conditions of the system	44
3	Indoor air metrology and experimental protocol	47
3.1	Introduction	47
3.2	Metrology for indoor air fields measurements	47
3.2.1	Indoor air velocity	47
3.2.1.1	Airflow parameters and characteristics	47
3.2.1.2	Flow measurement techniques	49
3.2.1.3	Choice of technique for the present study	51
3.2.1.4	Hot-sphere anemometer description	51
3.2.2	Indoor air temperature	54
3.2.2.1	Temperature measurement techniques	54
3.2.2.2	Thermocouples for the present study	55
3.2.3	Indoor air humidity	55
3.3	MINIBAT mobile robot description	56
3.3.1	Mobile robot system and sensors	56
3.3.2	Evaluation of measurement positions	59
3.3.3	Data acquisition system	60
3.4	Experimental protocol	61
3.4.1	Examining planes	61
3.4.2	Data acquisition parameters	62
3.5	Summary	63
4	Turbulent vertical axisymmetric free jet - Empirical model	65
4.1	Introduction	65
4.2	Jet zones decomposition	66
4.3	Isothermal axisymmetric free air jet characteristics	67

4.3.1	Centerline velocity decay	67
4.3.2	Jet dynamic thickness	69
4.3.3	Velocity profiles in the jet cross-section	70
4.3.4	Jet throw	70
4.4	Non-isothermal axisymmetrical free air jet characteristics	70
4.4.1	Criteria for vertical non-isothermal air jets	70
4.4.1.1	Local Archimedes number	72
4.4.1.2	Coefficient of non-isothermality	72
4.4.2	Velocity and temperature characteristics in a non-isothermal vertical air jet	73
4.4.2.1	Centerline velocity and temperature decay	74
4.4.2.2	Velocity and temperature profiles in the jet cross-section	75
4.4.2.3	Non-isothermal jet throw	75
4.5	Free air jet empirical model: Discussions	76
4.6	Turbulent characteristics of the indoor airflow	77
4.7	Summary: Criteria for characterizing an interacting air jet	78
5	Interacting air jet - Experimental results and analysis	81
5.1	Introduction	81
5.2	Test cases description	81
5.3	Indoor velocity and temperature fields	84
5.3.1	Data processing	84
5.3.2	Velocity fields	85
5.3.2.1	Description of the velocity fields over the horizontal planes	89
5.3.2.2	Description of the velocity fields over the vertical planes	89
5.3.3	Temperature fields	91
5.4	Interacting asymmetric jet characterization	95
5.4.1	Deviation of the interacting jet trajectory	95
5.4.1.1	Data processing	95
5.4.1.2	Amplitude and angle of deviation of the jet trajectory	96
5.4.2	Jet cross-sectional distributions	100
5.4.2.1	Data processing	101

5.4.2.2	Velocity and temperature distributions in the jet cross-section	102
5.4.3	Jet thickness and spread rate	104
5.4.3.1	Data processing	104
5.4.3.2	Jet dynamic and thermal spread	104
5.4.4	Maximum velocity and temperature decay	108
5.4.4.1	Data processing	108
5.4.4.2	Evaluation of the jet decays	109
5.4.4.3	Regression results	110
5.4.5	Quantification of jet profiles deformation	112
5.4.5.1	Deformation indicator definition	112
5.4.5.2	Jet profiles deformation evaluation	113
5.5	Characterization of the indoor flow turbulence	116
5.5.1	Energy spectral density analysis	116
5.5.1.1	Data processing	116
5.5.1.2	Energy spectra of the turbulent flow	117
5.5.2	Turbulence intensity and turbulent kinetic energy	119
5.5.2.1	Data processing	119
5.5.2.2	Results analysis	120
5.5.3	Turbulent kinetic energy spatial distribution	122
5.5.3.1	Data processing	122
5.5.3.2	Description of the turbulent kinetic energy fields over the horizontal planes	122
5.5.3.3	Description of the turbulent kinetic energy fields over the vertical planes	126
5.6	Summary	128
6	Quantification of the condensation rate on cold wall surface	131
6.1	Introduction	131
6.2	Condensation phenomenon: physical backgrounds	131
6.2.1	Homogeneous and heterogeneous condensation	132
6.2.2	Filmwise condensation (FWC)	133
6.2.3	Dropwise condensation (DWC)	134

6.2.4	Wettability and contact angle	135
6.2.4.1	Contact angle definition	136
6.2.4.2	Contact angle measurement	137
6.2.5	Thermal resistances in condensation process	138
6.2.5.1	Conductive resistance through a droplet	139
6.2.5.2	Resistance in the vapor	140
6.2.5.3	Interfacial resistance	140
6.2.5.4	Capillary depression resistance	141
6.2.5.5	Convective resistance	141
6.2.5.6	Constriction resistance	141
6.2.6	Overall heat transfer coefficient and condensation rate	142
6.2.6.1	Overall heat transfer rate	142
6.2.6.2	Drop size distribution	142
6.2.6.3	Overall heat transfer coefficient	143
6.2.6.4	Condensation rate	144
6.3	Experimental apparatus and protocol	144
6.3.1	Measurement devices	144
6.3.1.1	Digital camera	144
6.3.1.2	Infrared camera	145
6.3.1.3	Supervision camera	146
6.3.2	Experimental protocol	147
6.3.3	Data post-treatment using image processing methods	148
6.3.3.1	Condensation rate	148
6.3.3.2	Droplet volume as a function of the contact surface	148
6.3.3.3	Determination of the contact angle	149
6.3.3.4	Determination of the contact surface between the droplets and the solid surface: image processing	150
6.4	Experimental results and discussions	154
6.4.1	Experimental conditions	154
6.4.1.1	Description of the test case	154
6.4.1.2	Measurement of the boundary conditions	154

6.4.1.3	Air velocity, temperature and humidity evolution within the test cell	156
6.4.2	Pictures of the condensation process	159
6.4.3	Quantification of the condensation rate	159
6.4.3.1	Vapor dew point and glazing surface temperature	160
6.4.3.2	Condensation rate	161
6.4.4	Discussions on the image post-treatment	162
6.5	Summary	165
Conclusions and perspectives		166
Bibliography		168
Appendices		192
A	Uncertainty evaluation in sensors measurements	195
B	Calibration procedure for thermocouples	201
C	Thermocouple response time	205
D	Verification of the supply air flow rate	211
E	Cases studied boundary conditions	215
F	Scilab script for LiDAR mapping data conversion	227
G	Robot chassis specifications	233
H	Additional experimental results	239

List of Figures

1.1	Building ventilation design	7
1.2	Principle of mixing ventilation (a) and displacement ventilation (b)	12
1.3	The "Why, Which and How" of ventilation designs for buildings	14
1.4	Jet flow configuration definition and expected behavior of the jet	23
2.1	Simplified schematic of the test cell inner volume (millimeter unit)	29
2.2	Envelope composition of MINIBAT test cell	30
2.3	3D schematized model of MINIBAT	32
2.4	Pt100 probes repartition in the test cell envelope	34
2.5	Pt100 probes location inside the climatic chamber and the thermal buffer zone	35
2.6	MINIBAT temperature evolution over a period of 144 hours	35
2.7	Test cell schematic with airflow configuration (milimeter unit)	37
2.8	Plenum box scheme (milimeter units)	39
2.9	Grille diffuser scheme (milimeter units)	39
2.10	AHU system for the test cell	41
2.11	Probes location within the air handling unit and along the ductwork . . .	42
2.12	Precise steam generator unit for the air handling unit	43
2.13	The test cell wall boundary conditions with color code	46
2.14	Boundary conditions type associated to the ventilation ductwork within the test cell	46
3.1	Room air flow zones division following flow regimes (Loomans, 1998) . .	48
3.2	Omnidirectional hot-sphere anemometer Schiltknecht ThermoAir64	52

3.3	Anemometer absolute accuracy as function of mean velocity measured . .	54
3.4	K-type thermocouple $\varnothing 25 \mu m$	55
3.5	Sensirion SHT75 humidity/temperature probe	56
3.6	Accuracy limits of the SHT75 probe (Sensirion, 2018)	56
3.7	MINIBAT mobile robot scheme	57
3.8	Sensors position on the mobile robot	58
3.9	Lidar system for the mobile robot	60
3.10	Data acquisition systems schematic	61
3.11	Scanning planes within the test room	62
4.1	Jet zones decomposition	66
4.2	Isothermal axisymmetric free air jet simplified schematic with character- istics graphs	68
4.3	Scheme of vertical non-isothermal jets behavior (extract of (ASHRAE, 2009))	71
4.4	Non-isothermal axisymmetric free air jet simplified schematic with char- acteristics graphs	73
4.5	Criteria for characterizing an interacting asymmetric jet	80
5.1	Schematic of the various section-planes plotted	85
5.2	iso_120 - Jet mean velocity contours over the horizontal planes	86
5.3	cold_120 - Mean velocity contours map over the horizontal planes	87
5.4	hot_120 - Mean velocity contours map over the horizontal planes	88
5.5	Jet mean velocity contours over the vertical planes	90
5.6	cold_120 - Mean temperature contours map over the horizontal planes . .	92
5.7	hot_120 - Mean temperature contours map over the horizontal planes . .	93
5.8	Non-isothermal jets - Temperature contours map following X and Y direction	94
5.9	Data interpolation principle	95
5.10	iso_120 - Maximum velocity trajectory	97
5.11	iso_120 - Jet deviation: (a) in polar coordinates; (b) following Z	97
5.12	cold_120 - Extremum velocity and temperature trajectories	98
5.13	cold_120 - Jet deviation: (a) in polar coordinates; (b) following Z	98
5.14	hot_120 - Extremum velocity and temperature trajectories	99
5.15	hot_120 - Jet deviation: (a) in polar coordinates; (b) following Z	99

5.16 Comparison of the jet deviation in three test cases	100
5.17 Area and disk-equivalent radius of an isocontour	101
5.18 iso_120 - Dimensionless velocity profiles distribution	102
5.19 cold_120 - Dimensionless velocity and temperature profiles distribution .	103
5.20 hot_120 - Dimensionless velocity and temperature profiles distribution . .	103
5.21 Jet dynamic thickness and spread	105
5.22 Jet thermal thickness and spread	106
5.23 Jet maximum velocity decays	110
5.24 Jet maximum temperature decays	110
5.25 Linear regression of the maximum velocity decay	111
5.26 Linear regression of the maximum temperature decay	111
5.27 Hydraulic radius and disk-equivalent radius of an isocontour	113
5.28 iso_120 - Deformation indicator of velocity profiles	114
5.29 cold_120 - Deformation indicator of velocity and temperature profiles . .	114
5.30 hot_120 - Deformation indicator of velocity and temperature profiles . . .	114
5.31 Instantaneous air velocity signals and its energy spectra	116
5.32 Location of points analyzed	118
5.33 hot_120 - Energy spectral distribution	118
5.34 Standard deviation of the velocity, turbulent kinetic energy and turbulence intensity	121
5.35 iso_120 - Turbulent kinetic energy fields over the horizontal planes	123
5.36 cold_120 - Turbulent kinetic energy fields over the horizontal planes . . .	124
5.37 hot_120 - Turbulent kinetic energy fields over the horizontal planes	125
5.38 Turbulent kinetic energy fields over the vertical planes	127
5.39 Summary of the jet characterization	128
6.1 Two types of heterogeneous condensation	132
6.2 Contact angle and equilibrium of surface tensions of a single droplet . . .	136
6.3 Contact angle measurement using the half-angle method	137
6.4 Thermal resistances in a dropwise condensation process	139
6.5 Digital camera system for the condensation study	145
6.6 Location of the IR camera and a photo captured sample	146

6.7	Supervision camera system for the test cell	147
6.8	Contact angle and droplet radius	148
6.9	Determination of the contact angle	150
6.10	Example of captured image of droplets on cold glazing	151
6.11	Image processing steps for droplets contours finding	152
6.12	Image histogram before and after equalization	152
6.13	Boundary conditions evolution during the test period	156
6.14	Evolution of the indoor moist air velocity-temperature-humidity just before and during the test	157
6.15	Dropwise condensation dynamic mechanism	158
6.16	Temperature evolution of the moist air, the dew point and the glazing surface just before and during the test	160
6.17	Evolution of the condensate mass flow rate just before and during the test	161
6.18	Image samples of small and large droplets (5 x 5 mm) with their corresponding histograms	163
6.19	Image thresholding for the image sample of small droplets	164
6.20	Image thresholding for the image sample of large droplets	164
B.1	Calibration reflux thermostatic bath scheme	201
C.1	Thermocouple step change temperature as a function of time constant	206
C.2	The response time of two K-type thermocouples with different junction diameter $\varnothing 250 \mu m$ and $\varnothing 25 \mu m$	210
D.1	Decomposition of the outlet diffuser into small zones	212
D.2	Data table for the air flow rate of $100 m^3/h$	213
D.3	Data table for the air flow rate of $200 m^3/h$	214
E.1	iso_120 - Evolution of the measured boundary conditions	217
E.2	cold_120 - Evolution of the measured boundary conditions	220
E.3	hot_120 - Evolution of the measured boundary conditions	223
E.4	cond_150 - Evolution of the measured boundary conditions	225
G.1	Robot chassis parts and specifications	234
G.2	Robot chassis scheme	235

G.3	Robot chassis motors scheme	236
G.4	Robot chassis wheels scheme	236
G.5	Mecanum wheel operating principle	237
H.1	Dimensionless velocity contours map - Isothermal jet	240
H.2	Dimensionless velocity contours map - Cold jet	241
H.3	Dimensionless velocity contours map - Hot jet	242
H.4	Dimensionless temprature contours map - Cold jet	243
H.5	Dimensionless temperature contours map - Hot jet	244
H.6	iso_120 - Energy spectral distribution	245
H.7	cold_120 - Energy spectral distribution	246

List of Tables

1.1	Some room configurations studied in the literature	18
2.1	Test cell envelope composition (from outer to inner)	31
2.2	Thermophysical properties of MINIBAT envelope materials	31
2.3	MINIBAT boundary conditions using inner surface	45
2.4	MINIBAT boundary conditions using outer surface	45
5.1	Set points for the three test cases	82
5.2	Measured boundary conditions within the MINIBAT test cell	83
5.3	Air supply characteristics	83
5.4	Grid size and interpolation step	85
5.5	Jet spread coefficients and virtual origin	108
5.6	Values of U_0 and ΔT_0 in the three test cases	109
5.7	Empirical coefficients determination	112
5.8	Grid size and interpolation step	122
6.1	MINIBAT set points for the condensation test	155
6.2	Measured temperature boundary conditions for the condensation test . . .	155
6.3	Air supply characteristics for the condensation test	155
6.4	Droplets minimum equilibrium radius, fall-off radius and contact angle . .	162
C.1	Thermophysical properties of K-type thermocouple thermoelement materials and of ambient air at 20 °C	209
C.2	K-type thermocouple time constant following the junction diameter and the ambient air velocity	209

E.1	iso_120 - Measured temperature boundary conditions within the MINIBAT test cell	215
E.2	iso_120 - Measured air supply characteristics	216
E.3	cold_120 - Measured temperature boundary conditions within the MINIBAT test cell	218
E.4	cold_120 - Measured air supply characteristics	219
E.5	hot_120 - Measured temperature boundary conditions within the MINIBAT test cell	221
E.6	hot_120 - Measured air supply characteristics	222
E.7	cond_150 - Measured temperature boundary conditions within the MINIBAT test cell	224
E.8	cond_150 - Measured air supply characteristics	226

Introduction

1.1 Building ventilation for comfort, health and energy: a look back in the history

1.1.1 Building ventilation design for human comfort

For a long time, human protections and shelters from external climatic conditions had always been the very first objective of buildings. The building design was straightforward, it was focused on the **occupants comfort**. With respect to the local climate conditions, some ventilation techniques for the indoor environment were possible, mostly by natural ventilation¹ (e.g. through window and/or stack openings). The cooling and heating were only ensured by passive strategies. They were manually driven according to the occupants needs ([Courgey and Oliva, 2006](#)).

Since the final third of the 19th century, an enormous and rapid development of the mechanical, electrical and metallurgy industry has been observed in the human history. This period is also known as the Second Industrial Revolution or the Technological Revolution ([Morison, 2008](#)). These new technologies allowed the human to build higher buildings equipped with mechanical ventilation systems for more convenient occupant comfort. These systems, popular with the abbreviation HVAC&R², are capable to create an indoor climate environment relatively independent with regard to the outdoor climate conditions ([Swenson, 1995](#)). Therefore, now both mechanical and natural ventilation techniques are considered by designers and engineers in order to provide the occupant thermal comfort.

¹Natural ventilation is the process of supplying air to and removing air from an indoor space by means of pressure differences arising from natural forces.

²Heating, Ventilation, Air conditioning and Refrigeration

The first thermal comfort model was reported by [Fanger and al. \(1970\)](#), ([Fanger et al., 1988, 1989](#)). It has met a tremendous success. This model is defined in the international standard, the ISO 7730 (2005)³; as well as in American standard for HVAC&R designs, the ASHRAE⁴ standard 55 (2017).

Fanger's model defines a narrow range of indoor environmental parameters in which thermal comfort is met. However, this range may vary depending on various factors such as external environmental conditions or sociological perception of heat. More evolved comfort models were developed to take into account those differences of perception: they are called adaptive comfort models. Since then, research based on this approach has led to substantial improvements in comfort modeling. Detailed descriptions of the adaptive comfort models can be found in the following references: [Humphreys and Nicol \(1998\)](#); [De Dear et al. \(1998\)](#); [de Dear and Brager \(2002\)](#); [Nicol and Humphreys \(2002\)](#); [Nicol et al. \(2012\)](#). Besides, a succinct review on the evolution of methodological approaches regarding the determination of the thermal comfort can be found in [Antoniadou and Papadopoulos \(2017\)](#).

1.1.2 Building ventilation design regarding the energy efficiency

1.1.2.1 Energy crisis, climate change and energy efficient buildings

In the 1970s, during the oil crisis, a new concern had arisen: the **energy efficiency**, due to the "explosion" of the energy price. In fact, this crisis implied two major consequences in the human awareness of energy issues.

First, one realized that the fossil energy such as oil, coal, natural gas will run out one day. Thus, humans need to find alternative energy sources, such as nuclear power energy or renewable energy in order to be less dependent to the fossil fuels. Nevertheless, nowadays, nuclear energy still faces security and environmental issues, and renewable energy sources are still not fully developed. Thus, for the last three decades, fossil fuels still contributed up to 80% of the global energy demand (data as of 2017, ([IEA, 2018](#))⁵), despite the strong growth of alternative energy sources.

This marginal transition turned humans toward an other goal: the energy consumption reduction of all economic sectors⁶, and obviously the building sector included.

Here are statistical data that shows how the huge is the building energy consumption. The total final energy consumption (TFC) of the building sector accounts for:

³This standard was last reviewed and confirmed in 2015. Therefore this version remains current.

⁴American Society for Heating, Refrigeration, and Air Conditioning Engineers

⁵International Energy Agency

⁶one can define five major sectors, such as Industry, Transport, Residential, Commercial, Agriculture and others. The Building sector comprises the Residential and Commercial sub-sectors.

- 30% of the world TFC (2015 data, (IEA, 2017));
- 41% of the USA TFC (2011 data, (EIA, 2012)⁷);
- 38.1% of the Europe TFC (2014 data, (EEA, 2015)⁸);
- 45% of the French TFC (2014 data, (ADEME, 2015)⁹).

Besides, the world population has doubled between 1970 and 2017 and reached 7.6 billion people. According to a United Nations (UN) report, the world population is expected to reach 8.6 billion in 2030 and 9.8 billion in 2050 (UN, 2017). This significant growth could lead to more global energy demand, which might cause heavy environmental impacts such as green-house gas¹⁰ (GHG) emissions.

According to a report from Intergovernmental Panel on Climate Change (IPCC) in climate change (Lucon et al., 2014), the building sector contributes between 6% (electricity use excluded) and 25% (electricity use included) of the global GHG emissions worldwide (2010 data). In the USA, the building sector was responsible for nearly half (44.6%) of USA CO₂ emissions in 2010 (EIA, 2012). In France, the building sector represents 23.3% of the GHG emissions according to ADEME (2015).

The population growth, the increasing need for indoor living comfort and services, together with the majority of time that human spend inside buildings, make the energy saving and efficiency the priority objective for the building sector (Lucon et al., 2014). This is particularly true for HVAC&R systems, which consume energy for heating, cooling and ventilating the buildings.

Anyway, while encouragements and incitements for energy saving are not sufficient, the energy efficiency in buildings is a prime objective for energy policies at regional, national and international levels.

At the **European Union's (EU) level**, there is a legislative law aiming to promote the improvement of the energy performance of buildings within the Community, called Energy Performance of Buildings Directive (EPBD). It involves the EU Member States to adopt new regulations on building design, especially on thermal insulation and ventilation. The first version was published in 2002 (Directive 2002/91/EC, European-Commission). The latter was then replaced by the so-called "EPBD recast" Directive 2010/31/EU (2010). Along with the Energy Efficiency Directive 2012/27/EU (2012), the aim of the EU countries regarding the building energy consumption is clear: all new buildings are required to be nearly zero-energy buildings (NZEBs) by 31 December 2020. The EU ambitious ob-

⁷Energy Information Administration

⁸European Environment Agency

⁹Agence de l'environnement et de la maîtrise de l'énergie

¹⁰A green-house gas is a gas that absorbs and emits radiant energy within the infrared range. This process is the fundamental cause of the greenhouse effect. The primary greenhouse gases in Earth's atmosphere are water vapor, carbon dioxide, methane, nitrous oxide, and ozone.

jectives by 2020 is the "20-20-20 target" (European-Commission, 2014): 20% reduction of GHG emissions (in comparison with 1990), 20% increase of the EU renewable shares in the energy consumption and 20% improvement in the EU energy efficiency.

At the **national level**, the France has rapidly responded to the EU 2002 directive by a National Climate Plan "Factor 4" commitment (2003). According to this commitment, France aims to reduce by a factor 4 its GHG emissions by 2050 (with regard to 1990 level). As for the Building sector, given the largest part of the energy consumption as well as GHG emissions of this sector, regulations were established to improve the building energy performance and efficiency. They aimed to reduce the building total energy consumption by 30% by 2050. Replacing the 2005 Thermal Regulation (RT 2005), the 2012 Thermal Regulation (RT 2012) fixes, among other things, an average energy consumption threshold of $50 \text{ kWh/m}^2/\text{year}$ (in primary energy consumption) for new buildings.

1.1.2.2 Building energy efficiency: huge potential for ventilation design

As stated earlier, among building services regarding inhabitants living activities, HVAC&R systems accounts for a significant part of the building energy usage. In fact, in the USA, it represents 50% of the building consumption and 20% of the total final consumption (Pérez-Lombard et al., 2008). In France, according to ADEME, the part of HVAC&R systems accounts for 60% of the building energy consumption in the residential sector and 54% in the commercial sector (ADEME, 2015). Reasons are broad: it could be due to poorly designed buildings, or the lack of performance of HVAC&R systems, or even due to the different behaviors and habits of occupants.

Given these limitations, this is a real challenge for building designers, engineers and researchers to reduce the building energy consumption. In order to reach this objective, there is a need to rethink traditional ventilation designs, in order to assess and improve their performance.

As a practical support, standards and guidelines were developed to help ventilation designers: the ASHRAE Fundamental Handbook (2017) and standards (ASHRAE standard 90, 2016) for the USA.

In the EU, recently in August 2017, the European Committee for Standardization (CEN), and the International Standards Organisation (ISO), have published a set of standards¹¹ for a common methodology for calculating the integrated energy performance of buildings, in accordance with the Energy Performance of Buildings Directive. This set of EPB standards will be the basis for the Energy Performance Buildings assessment in Europe. The overall structure of the EPB standards has been envisaged to facilitate national implementation and to motivate Members States to adopt those standards in their national regulations. Among these EPB standards, there are standards that are specifically ded-

¹¹17 EN-ISO Energy Performance Buildings (EPB) standards and 29 EPB EN-standards

icated to the building ventilation design: EN 16798:2017 (CEN, 2017). France has also integrated these standards into their national standards, known as NF EN 16798 (AFNOR, 2017)¹². A succinct review about Europe achievements, perspectives and challenges within forty years of regulations on the building energy performance can be found in Papadopoulos (2016).

1.1.3 Building ventilation design regarding the indoor air quality

Consequences of improving building energy performances is that new buildings became air-tight (Passarelli, 2009). Natural ventilation systems were progressively replaced by central mechanical ventilation systems (e.g. the air handling unit) with a reduced air flow rate to minimize the infiltration of outside fresh air. These techniques led to a poor indoor air change rate and thus, a poor **indoor air quality (IAQ)**. Fresh air could not be supplied directly to the occupant breathing level. Ineffective air distribution led to stagnant-air zones

The problem was aggravated by the installation of modern building synthetic materials, furniture and cleaning products, such as dry wall, carpets, particle board, plastics, solvents, adhesives, etc. Along with other indoor air contaminants (CO₂, CO, dusts, moisture and molds, PM_{2.5}¹³), volatile organic compounds (VOCs) emitted by these materials are extremely harmful to the human health.

1.1.3.1 Sick Building Syndrome

The so-called "air-tight" building gave birth to a phenomenon named Sick Building Syndrome¹⁴ (SBS), which is believed to provoke sickness/illness and productivity losses in specific buildings. Its common symptoms on human health include: irritation, cough, shortness of breath, headache, fatigue, lack of concentration, etc. (Redlich et al., 1997). According to Murphy (2006), the sick building syndrome did not exist before 1970s. It was after the 1970s crisis that the term SBS became common concern because of the effects of this syndrome being experienced by more and more people.

Since then, intensive research investigations were carried out on the relation between the SBS and the redesigned "air-tight" building. Here is a non-exhaustive list of publications related to those investigations since 1990s: Baechler et al. (1991), Jaakkola and Miettinen (1995a,b), Wargocki et al. (2002, 1999), (Daisey J. M. et al., 2003), Seppänen and Fisk (2002, 2004), Joshi (2008). They concluded that the building ventilation

¹²Association Française de Normalisation

¹³Particulate Matter of $\varnothing 2.5 \mu m$

¹⁴an illness that people who work in certain buildings can get, caused by poor air quality inside the building (Cambridge Advanced Learner's Dictionary, 2017).

is strongly associated with occupant comfort and perceived air quality, as well as their productivity. They also pointed out that increasing air supply rate could improve the indoor air quality, and that an air supply rate below 25 L/s per person increase the risk of SBS symptoms. A comprehensive overview about the sick building syndrome is given by [Passarelli \(2009\)](#). His study shows that an inadequate ventilation and poor IAQ were the main cause and were responsible for nearly half 48% of the causes of SBS.

1.1.3.2 Ventilation rate and IAQ

Ideally, HVAC&R systems supply fresh outdoor air, mix the fresh air with recovered air and distribute the conditioned air to the building. To achieve good air quality the system must be able to supply sufficient fresh air to all occupied spaces in the building and to remove contaminated air, reducing the concentration of any air contaminants.

Many problems can result in an inadequate functioning of HVAC&R systems. For example, these systems rely on a clean fresh supply of outside air. If the air intakes are located next to a loading dock or other source of pollutants, contaminated air may be introduced into the building. Problems can also arise in the distribution of fresh air, and in the removal of contaminated air. Although the overall ventilation may appear adequate, ventilation in different parts of a building may be uneven, or fresh air from the supply may be shortcircuited to the return ducts, bypassing the occupants' breathing zone. In addition, the ventilation system itself can be the source of air contaminants. Unsealed fibreglass and other insulation material lining the ventilation ducts can release particules into the air. Such material can also become wet, creating an ideal and often concealed site for the growth of microorganisms.

Consequently, concerns about human health and indoor air quality raise another challenge for building ventilation designers. International policies have established, with the help of researchers, working groups and standardization organizations, design standards and guidelines regarding these concerns. One can take for example two standards in the USA ([ASHRAE and ANSI, 2016a,b](#)); one standard in the EU ([CEN, 2007](#)), which was replaced recently by the EN 16798 series ([2017](#)). In France, there is a national regulation ([Legifrance, 1982](#)) regarding the building ventilation for the indoor air quality but it was not updated since 1983.

According to a multidisciplinary review by [Sundell J. et al. \(2011\)](#), increasing the ventilation rate above currently adopted standards and guidelines should result in reduced prevalence of negative health outcomes. In fact, to obtain an acceptable IAQ with a minimum energy consumption, ASHRAE recommends a minimum ventilation rate in breathing zone of 2.5 L/s per person ([ASHRAE and ANSI, 2016a](#)), which is ten times less than the ventilation rate suggested by previous studies ([Seppänen and Fisk, 2004](#)). In France, the 1982's decree remains the reference concerning the ventilation rate in res-

idential buildings. It sets the minimum ventilation rate of $10 \text{ m}^3/\text{h}$ (about 2.8 L/s) at the air exhaust in service rooms. In addition, the air must be able to move freely from main rooms to service rooms.

Sundell J. et al. (2011) also pointed out that building operators and designers should avoid low ventilation rates unless alternative effective measures are employed to limit indoor pollutant levels. But again, the energy efficiency criteria seems difficult to achieve.

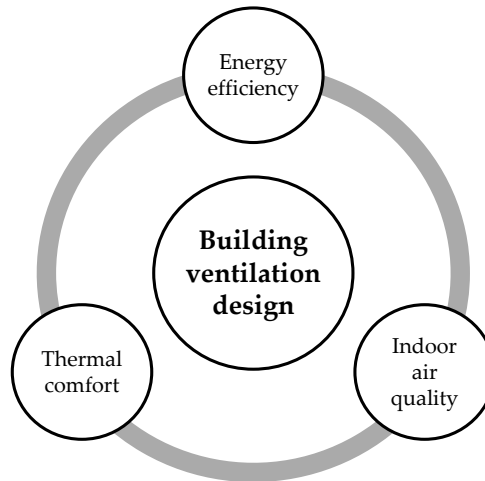


Figure 1.1 – Building ventilation design

In summary, let the three "thermal comfort", "energy efficiency" and "indoor air quality" criteria gravitate toward a centered circle on the "building ventilation design" (c.f. Figure 1.1). From what have been reviewed here above, these criteria seem to be strongly interdependent. Therefore, to give a meaning to the building ventilation design, great attention should be paid, ventilation performances need to be predicted, and compromises have to be made with respect to all these three aspects.

1.2 Indoor air distribution and ventilation performance prediction: a literature review

"No air conditioning is better than its air distribution."

- Willis Haviland Carrier,
HVAC systems founder.

In this quote, the "air conditioning" term represents the air conditioned from the ventilation system performance alone, whereas the "air distribution" term represents the air distribution within the indoor environment as a whole. The air change rate at the supply and exhaust levels do not provide enough information to predict the thermal comfort and air quality conditions for individual occupants. It is actually the indoor distributions of air velocity, turbulence intensity, temperature, humidity and contaminant concentration that impacts directly the occupants thermal comfort and the IAQ. Therefore, evaluations of the occupants comfort and the IAQ require the knowledge of the indoor air distribution.

Since then, tools for indoor air distribution prediction as well as ventilation performance determination have been developed. In addition, several indoor air distribution methods have been invented and applied for building ventilation design. These following sections will address these topics.

1.2.1 Tools for building ventilation performance prediction

Common tools for investigating and assessing indoor air distribution and ventilation performance include:

- analytical models;
- empirical models;
- small-scale experiments;
- full-scale experiments;
- multizone models;
- zonal models;
- CFD¹⁵ models.

This section does not intend to give an exhaustive description of each tool. A very comprehensive and detailed description of those methods can be found in this review (Chen, 2009). Only three methods are addressed below, which are empirical models, full-scale experimental models and CFD models.

¹⁵Computational Fluid Dynamics

1.2.1.1 Empirical models

Empirical models are developed from fundamental basis of the conservation equation of momentum, mass and energy. In order to establish their equations, most of the time, empirical models are based on observations and experiments (Abramovich, 1963; Rajaratnam, 1976; Chen and Rodi, 1980; Grimitlyn and Pozin, 1993), or sometimes based on CFD numerical simulations (Karimipannah and Awbi, 2002; Cho et al., 2008). Very often, empirical coefficients are required. Those parameters need to be adjusted case by case.

Often limited to cases with simplified geometry and simplified thermo-aeraulic boundary conditions, empirical models still prove their robustness and maturity. Indeed, empirical models have been developed for decades but still serve actually as references in building ventilation practical design guidelines (Awbi, 2003; Goodfellow, 2001) or fundamental handbooks (ASHRAE, 2013, 2017).

Due to their simplicity and cost-effectiveness, Chen (2009) concluded that empirical models *"have been a bread and butter tool for design engineers to estimate thermal comfort and indoor air quality in a ventilated space."*

1.2.1.2 CFD models

Computational fluid dynamics was first used in the 1970s for the building ventilation airflow prediction (Nielsen, 1975, 1976). Nowadays, the name CFD is tremendously well-known by ventilation communities (for both scientific and industry). It is a convenient and efficient simulation tool for assessing indoor airflow distribution in buildings and other enclosures, such as aircraft cabin, train, car, etc. (Chen, 2009).

Developments in numerical methods and in turbulence models have improved considerably the CFD models for both research and practical/industrial engineering applications (Blocken, 2014; Nielsen, 2015). Advanced progress on supercomputers also seems to significantly boost the CFD models capacity, which strongly relies on computer processing speed. Chen (2009) indicated that studies based on CFD models contributed nearly three-quarter (70%) of the building ventilation performance studies published from 2007 to 2009. He also pointed out that CFD simulation results were all validated by experimental data (in about two thirds of the CFD studies), which *"clearly indicates that the community has not yet trusted the CFD modeling without validation."*

The increasing trend of using CFD models for indoor air predictions and the building ventilation assessment is foreseeable. However, their accuracy and reliability remain a major concern and merit great attention, given the lack of proper and thorough validation studies, particularly from full-scale validation studies. Oberkampf et al. (2004), in his

extensive and comprehensive work¹⁶, has stated *"In validation, the relationship between computation and the real world, i.e. experimental data, is the issue."*

1.2.1.3 Full-scale experimental studies

As stated above, experiments (reduced-scale and full-scale) have been used for decades to generate data for empirical models establishment. Detailed data produced by extensive and reliable full-scale experiments, associated with well-known boundary conditions, could also be considered as reliable for CFD model validation purpose.

Full-scale experiments can be categorized into two types: laboratory experiments and in-situ experiments. In-situ experiments are not really suitable for validation purposes since boundary conditions are not controllable in most cases. Extensive in-situ experiments by [Hanzawa et al. \(1987\)](#), [Melikov et al. \(1988\)](#) and [Melikov and Langkilde \(1990\)](#) have provided some information about actual indoor air flow characteristics. However, they could not be used for CFD validations as boundary conditions are not known. On the other side, full-scale rooms built for laboratory experiments are often environmentally controllable, but still limited to a relative simple geometry (from a single room to a several small rooms) due to the investment cost. One can take for example a quite popular well-documented experimental study of a two-dimensional isothermal ceiling jet ([Nielsen, 1990](#); [Nielsen et al., 2010](#)). This study, as part of IEA Annex 20¹⁷, has been used intensively in the literature as a benchmark test¹⁸ to validate CFD models ([Luo et al. \(2004\)](#), [Foat et al. \(2018\)](#), etc.). However, this configuration is relatively simple and does not represent realistic and practical indoor air flow situations.

Hence, despite enormous investments in both equipment costs and efforts to carry out high quality measurements, full-scale experiments are valuable and even indispensable for CFD models validation. Nielsen, a CFD pioneer for building ventilation, said in his report (Fifty years of CFD for room air distribution, [2015](#)), that *"the CFD method has not replaced the experimental method. On the contrary, experiments made in recent years probably support CFD as important benchmark tests."*

1.2.2 Indoor air distribution methods

A building can be ventilated naturally thanks to wind and buoyancy driven forces; or ventilated mechanically with a mechanical ventilation system; or even hybridly, i.e. the combination of both methods ([Awbi, 2003](#)).

¹⁶Verification, validation, and predictive capability in computational engineering and physics, 2004

¹⁷International Energy Agency Annex 20 "Air Flow Pattern within Buildings" ([Lemaire, 1993](#))

¹⁸<http://www.cfd-benchmarks.com/>

The natural and hybrid ventilation strategies are beyond the scope of this study. Detailed studies on the natural ventilation applied in buildings can be found in these following references: [Allocca et al. \(2003\)](#); [Jiang and Chen \(2003\)](#); [Zhai et al. \(2015\)](#); [Etheridge \(2015\)](#); [Nomura and Hiyama \(2017\)](#).

According to a review study of [Cao et al. \(2014a\)](#), eight mechanical ventilation methods are recognized so far and have been employed in designs of building ventilation:

- mixing ventilation (MV);
- displacement ventilation (DV);
- personalized ventilation (PV);
- hybrid air distribution (HAD);
- stratum ventilation (SV);
- protected occupied zone ventilation (POV);
- local exhaust ventilation (LEV);
- piston ventilation (PiV).

Once again, one does not intend to analyze in detail pros and cons of every methods. Only two methods, considered as conventional method, will be described here: the mixing ventilation and the displacement ventilation. The other methods such as the personalized ventilation and the protected occupied zone ventilation were invented and tested recently. They could be promising methods for building ventilation designs regarding the occupants comfort, the IAQ and the energy efficiency. However, published studies showed that they still need to be coupled with conventional systems. More lecture about these methods can be found in the following references: [Melikov A. K. \(2004\)](#); [Kaczmarczyk et al. \(2004\)](#); [Yang et al. \(2010\)](#); [Cao et al. \(2014a,b\)](#); [Lipczynska et al. \(2015\)](#); [Melikov A. K. \(2015\)](#); [Xu et al. \(2018\)](#).

1.2.2.1 Displacement ventilation

Displacement ventilation (DV) is based on the supply of outdoor fresh air with relatively low velocity ($< 0.5 \text{ m/s}$) at the room floor level. As the air is displaced and warmed up by internal heat sources (occupants, electric devices), thermal plumes occur. The warmed and contaminated air is exhausted through mouths at the ceiling level. A schematic of the DV principle is given in the Figure 1.2(b).

In terms of room air distribution classifications, the DV is characterized as a fully stratified room air distribution system ([ASHRAE, 2017](#)). In fact, with this method, there is a vertical gradient of air velocity, air temperature and contaminant concentration within the indoor air volume.

A low air velocity means a low fan power, which means a low energy consumption.

DV systems are believed to have a high ventilation effectiveness¹⁹ regarding the occupant comfort and the IAQ in general (Skistad et al., 2004).

Nevertheless, the DV systems principle is based on convective flows and thermal stratification. Internal heat sources are imperative, thus DV systems are less suitable for heating applications: since the heated airflow can be bypassed by heat emitters, it might not penetrate in the room core (Cho et al., 2008). In addition, the combined effect of the cool air displacement at foot level and excessive temperature differences between head and foot levels can provoke a local discomfort for occupants (Melikov et al., 2005), (Magnier et al., 2012).

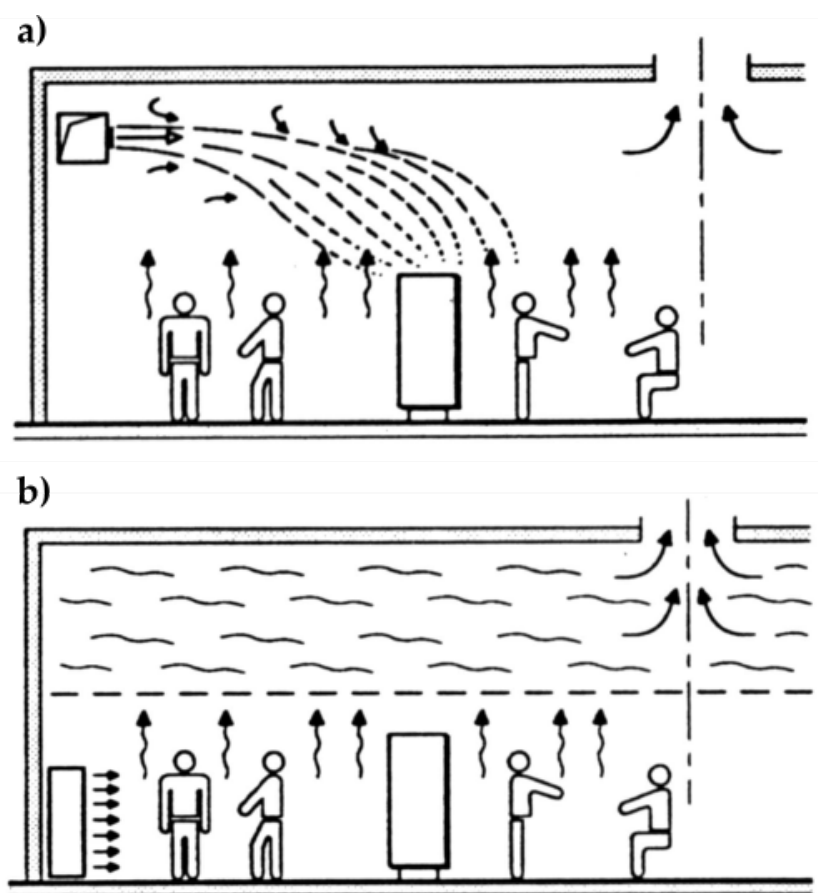


Figure 1.2 – Principle of mixing ventilation (a) and displacement ventilation (b)

1.2.2.2 Mixing ventilation

Mixing ventilation (MV) is based on the supply of outdoor fresh air, but this time with relatively high velocity (typically $> 1.0 \text{ m/s}$). The air inlets are located on the upper part of the room (ceiling or upper wall zone) (Awbi, 2003). The high velocity of the supply

¹⁹The ventilation effectiveness gives an indication on the effectiveness of the fresh supply air for indoor contaminant and heat removal (Mathisen et al., 2004)

air and its spreading within the room are supposed to guarantee an uniform mixing of the fresh supply air with the room air. The diluted contaminated air is subsequently exhausted through mouths, located at the floor level or at the ceiling level. A scheme of the MV principle is given in the Figure 1.2(a). For MV systems, an ideal mixing of the indoor air might be achieved thanks to a proper design of the supply/exhaust air terminal devices (ATD): air diffusers type, their dimensions and locations.

In contrast to displacement ventilation, the MV is classified as a fully mixed room air distribution system (ASHRAE, 2017). Indeed, the high mixing degree ensures that the air temperature and contaminant concentration is uniformly distributed within the indoor air volume.

Although MV systems are known to have lower ventilation effectiveness in comparison to other air distribution systems (Awbi, 2017), they are still the most common air distribution systems applied for building ventilation (Cao et al., 2014a). In fact, since MV function principle does not depend on the presence of internal heat sources, it can be employed for both heating and cooling applications.

At present, the application of the mixing ventilation is quite well guided for practical designers (Kandzia et al., 2013). In addition, several studies are conducted in order to improve the performance of the MV:

- some researchers carried out extensive studies on the effect of different parameters such as the ATD location, the supply air change rate, the floor or window temperature, on the MV ventilation effectiveness (Krajčák et al., 2012; Tomasi et al., 2013; Amai and Novoselac, 2016; Amai et al., 2017; Kosutova et al., 2018)
- other researchers studied the coupling of MV systems with other air distribution systems to improve the overall ventilation performance and effectiveness (Karimi-panah and Awbi, 2002; Cho et al., 2008; Assaad et al., 2017).

To summarize, the Figure 1.3 gives an succinct overview of what have been presented so far about issues related to the building ventilation design. We have detailed the three major criteria the building ventilation design should satisfy (the "Why?" question). We have detailed some principal models that allow predicting the ventilation performance (the "How?" question). Finally, we have seen the different air distribution methods, by which we have described the two most commonly applied for building ventilation (the "Which?" question).

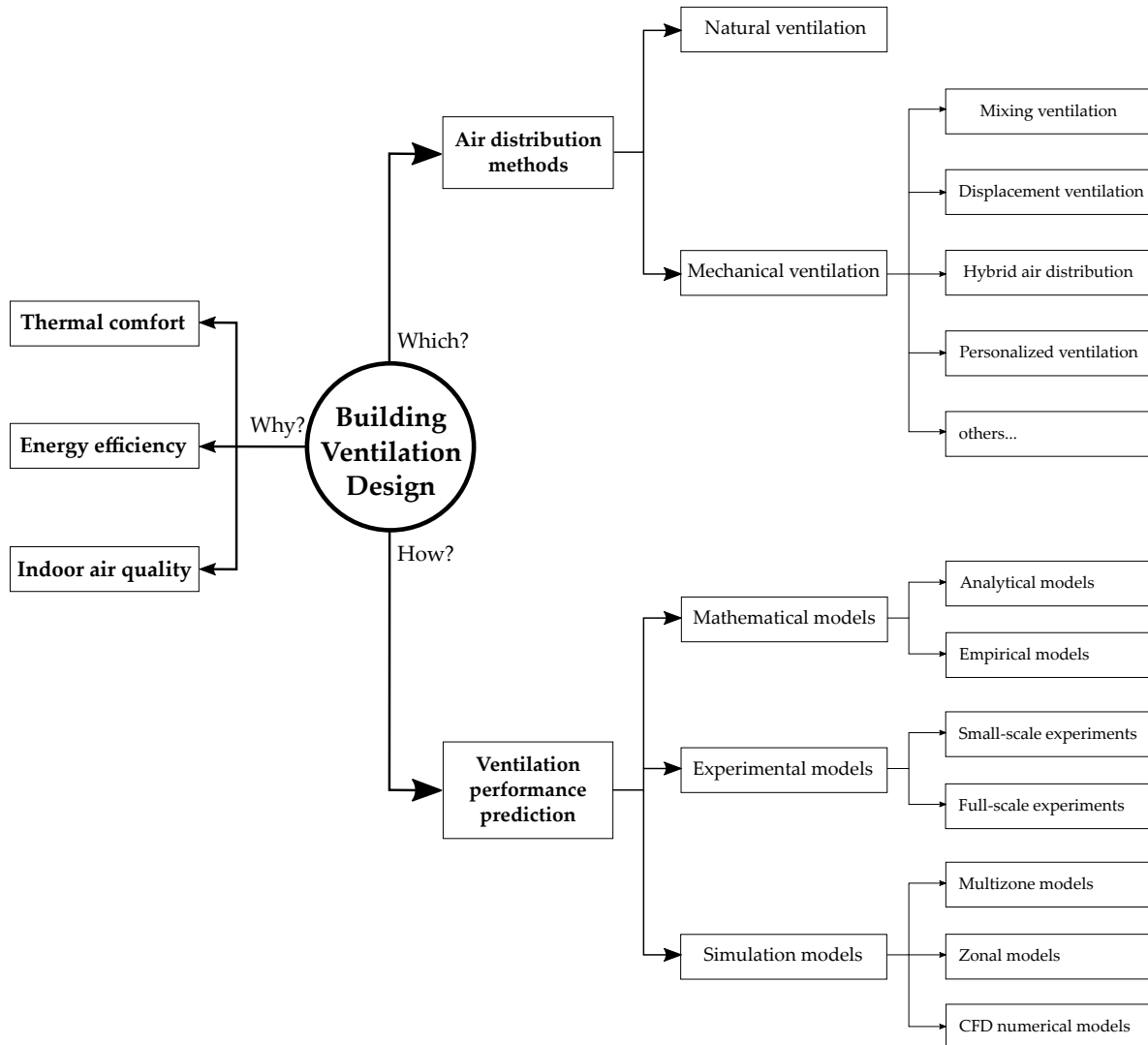


Figure 1.3 – The "Why, Which and How" of ventilation designs for buildings

1.3 Problem statement and outline of the thesis

1.3.1 Problem statement

With a mixing ventilation system, the air is supplied into the indoor environment through various types of diffusers and subsequently distributed by turbulent air jets, in most cases. For this ventilation method, the whole-field distributions of indoor air velocity, temperature, moisture and contaminants are mainly determined by the air jet characteristics and its mixing ability with the indoor air. These characteristics include typically:

- dynamic characteristics such as the jet momentum flow rate, its trajectory, its dynamic boundary layer, and its cross-sectional velocity distributions;
- thermal characteristics such as the thermal boundary layer, and the temperature distribution in the jet cross-section.

In other words, to predict the ventilation effectiveness of a mixing ventilation system, the performance of the air jet issued by this system is the primary and determining element.

1.3.1.1 Turbulent free jet theory

In fluid mechanics, a turbulent free jet is defined as a jet that develops in an infinitely large space without the presence of obstructions. The jet has high velocities, which makes it turbulent. This fluid dynamic phenomenon has been widely studied in the literature. The first theory for solving the jet problem was believed to be formulated by Kirchhoff in 1850's (as reported by [Mitrovic and Ricoeur \(1995\)](#)). Since then, numerous studies have been conducted in order to investigate the turbulent free jet. They were essentially based on experimental, empirical and analytical models ([Tollmien, 1926](#); [Corrsin, 1946](#)). The theory of turbulent jets was developed and detailed in well-known publications of [Abramovich \(1963\)](#) and [Rajaratnam \(1976\)](#).

Those early studies were focused on air jets with the following characteristics:

- turbulent high outlet velocity (high Reynolds number);
- axisymmetric free development;
- outlet with small dimensions;
- isothermal condition²⁰.

In HVAC design for building ventilation, the characteristics of air jets are relatively different. They are generally issued from an outlet with larger dimensions, they have a lower outlet velocity, and more importantly, the air jet is often non-isothermal²¹. This temperature difference provokes buoyancy forces, which are believed to affect the air jet trajectory, the location where the jet attaches or separates from the floor/ceiling.

Hence, early research in ventilation applications have already taken into account the non-isothermality of the air jet: [Koestel \(1954\)](#), [Shepelev \(1961\)](#), [Chen and Rodi \(1980\)](#), [Baker et al. \(1982\)](#), [Rodi \(1982\)](#).

Afterward, researchers started to investigate the fundamental basis of air jet temperature distribution alongside the air velocity distribution within mechanical ventilated spaces. One can take for example studies by [Tuve \(1953\)](#), [Nielsen \(1975\)](#), [Zhang et al. \(1990\)](#); [Zhang \(1991\)](#), [Zhivov \(1993\)](#), [Grimitlyn and Pozin \(1993\)](#). A succinct literature review is given by [Li et al. \(1993b\)](#).

In this review, the various empirical equations for characterizing an isothermal/non-isothermal free air jet are well-formulated and summarized. The main characteristics of a free air jet include: the jet centerline decay of velocity and temperature, the jet

²⁰supply air temperature equals surrounding air temperature

²¹supply air temperature does not equal surrounding room air temperature ([ASHRAE, 2017](#)).

cross-sectional velocity and temperature profiles and the jet throw²². The authors concluded that it is possible to predict the indoor air velocity and temperature based on the characteristics of diffuser air jets.

In addition, they insisted on the importance of quantifying the effects of the room geometry, the diffuser type and their location, in order to have a better understanding of the jet development as well as the indoor air distribution. Indeed, while a theoretical description of a symmetric free air jet development could be sufficient for a fundamental study, it does not represent a realistic configuration in which the air jet is not developed freely and symmetrically.

1.3.1.2 From free jet theory to realistic jet in a complex geometry

With the considerable progress in computer sciences as stated earlier in the section 1.2.1.2, studies on mixing ventilation and air jet were continued in both experimental field and CFD numerical simulation field.

On one hand, some researchers kept on conducting investigations on the air jet region. Here is a non-exhaustive list of related studies:

- Hussein et al. (1994) used recent velocity measurement techniques to obtain more in-depth information on a jet flow;
- Malmström et al. (1997); Malmström and Zou (2000) examined the influence of outlet conditions on axisymmetric free air jets: effects of the nozzle diameter and the supply air velocity;
- Zou (2000, 2001) studied the velocity decay of air jets in the far field from the outlet;
- Mi et al. (2013) examined the effect of Reynolds number on turbulence properties in the transition region of a circular jet.

On the other hand, intensive studies were carried out to investigate and predict the airflow distribution and characteristics within rooms ventilated mechanically by air jets. Here is a non-exhaustive list of related studies:

- Zhang et al. (1990); Zhang (1991); Zhang et al. (1992a,b) and Sun et al. (2004a) conducted CFD and full-scale studies on the two-dimensional indoor airflow under isothermal and non-isothermal conditions. Measurements were carried out only in the middle plane of the environmentally controlled full-scale room;
- Huo et al. (2000) conducted CFD simulation and full-scale experiments to describe three configurations of ATD for room air distribution analysis;

²²the distance from the centerline of an outlet perpendicular to a point in the mixed air-stream where the velocity has been reduced to a specified terminal velocity (ASHRAE, 2017).

- Hosni and Jones (2002) and Jia et al. (2002) conducted PIV²³ measurements to characterize the airflow field around a human body in a full-scale room. Measurements were done in several horizontal and vertical planes; the manikin, the air inlet and outlet were placed in the room axis;
- Kashirajima et al. (2002) carried out full-scale experiments of the indoor air distribution supplied by cold air jets. The air inlet is located at the ceiling, in the center of the room; various air diffusers were examined;
- Kuznik (2005), Kuznik et al. (2006, 2007) and Teodosiu (2013) carried out full-scale experiments (environmentally controlled room) and CFD simulations to characterize a non-isothermal horizontal air jet. Using automated mobile arm equipped with sensors, measurements were done in the median-plane only. In the last study (2013), the investigation of moisture transport has been taken into account;
- Meslem et al. (2010); Nastase and Meslem (2010); Nastase et al. (2011); Bragança et al. (2016, 2017); Bragança (2017); Meslem et al. (2018) conducted intensive studies on an innovative concept for optimized air distributions in buildings using a lobed diffuser (Vialle et al., 2015). Their experiments were carried out in a full-scale room with PIV measurements. The supply air diffuser is located at the ceiling, in the center of the room geometry;
- the following studies were performed in reduced-scale rooms: Posner et al. (2003) studied the influence of obstructions in the airflow distribution; van Hooff et al. (2012) analyzed the transitional flow of an isothermal horizontal plane jet; Serra and Semiao (2013) characterized a non-isothermal horizontal jet by 3D PIV measurements;
- Nielsen (1990); Nielsen et al. (2010) carried out experimental study of a two-dimensional isothermal ceiling jet. The geometry was standardized and has been used intensively in the literature as a benchmark test for CFD models validation;
- Hurnik et al. (2015) conducted a reduced-scale (1:5) experimental study to characterize the indoor air distribution in both the jet zone and the occupied zone. The various air jet configurations had been considered; important factors such as obstructions, internal heat sources had been taken into account. It was probably a complete experimental benchmark test for CFD validation;
- Li et al. (1993a), Cehlin and Moshfegh (2002), Magnier et al. (2012) studied the indoor air distribution supplied by low velocity air inlet (displacement ventilation) in full-scale rooms; measurements were done in the room median-plane.

In summary, numerous studies were conducted to investigate indoor air characteristics distributions by various types of assessment: reduced-scale/full-scale experiments

²³Particle Image Velocimetry

(Nielsen, 1990)

(Zhang et al., 1992b)

(Huo et al., 2000)

(Cehlin and Moshfegh, 2002)

(Hosni and Jones, 2002)

(Kashirajima et al., 2002)

(Posner et al., 2003)

(Kuznik et al., 2007)

(Serra and Semiao, 2013)

(Magnier et al., 2012)

(van Hooff et al., 2012)

(Bragança, 2017)

(Hurnik et al., 2015)

(Fatemi et al., 2013)

(Einberg et al., 2005)

Table 1.1 – Some room configurations studied in the literature

and CFD numerical prediction. The Table 1.1 presents some examples of the room geometries studied in the literature. Configurations of non-isothermal air jets have been well considered, impacts of obstructions or internal heat sources have been taken into account in some studies; nevertheless, in those configurations, the air supply and exhaust mouths are all located symmetrically with respect to the room geometry. This arrangement was probably made in purpose for which the air jet is believed to have a free development behavior and a symmetric distribution; and thus investigations were carried out merely in the axis of the room, i.e. the median-plane.

In realistic building ventilation systems, the position of the air supply and exhaust mouths in a room are rarely symmetric or aligned with the room geometry. For instance, the air supply mouth could be located near a vertical side wall and thus the air jet would not develop freely. Considering the interaction between the air jet and the room geometry, the airflow could potentially be distributed asymmetrically.

Up until now, to the best knowledge of the author, there are only a few experimental studies dealing with a non-isothermal realistic air jet configuration within a mechanically ventilated room. That is not to mention studies dealing with a humid air jet (presence of moisture) are quite limited. [Einberg et al. \(2005\)](#) carried out both CFD simulations and full-scale experiments for predicting indoor velocity and temperature distributions of an industrial air diffuser. Their test configuration is shown in the Table 1.1. They revealed that the flow around the diffuser is not completely symmetric as predicted by CFD simulations. The cause of the observed asymmetry was not identified. [Fatemi et al. \(2013\)](#) conducted a full-scale experimental study of a non-isothermal wall jet from a DV system, located in the corner of the room (c.f. Table 1.1). Given the lack of measurement points, the air velocity distribution was believed to be quasi-symmetric with respect to the jet axis. Lately, [Krajčůk et al. \(2012\)](#), [Tomasi et al. \(2013\)](#) and [Amai and Novoselac \(2016\)](#); [Amai et al. \(2017\)](#) carried out intensive experiments to assess the impact of the air terminal device types and location in full-scale rooms. However, studies were focused on the evaluation of the thermal comfort and the ventilation effectiveness; the indoor air distribution in the jet zone and the occupied zone was not addressed.

Besides, another factor could merit a fairly attention. It is the connection between the ductwork and the supply air inlet, as remarked by [Ren et al. \(2003\)](#). Due to the limited space above the suspended ceiling, a duct elbow or a plenum box must be installed before the air inlet. It potentially induces an abrupt change of the airflow direction, and might disturb the development of the jet, as observed by [Smoljan and Balen \(2010\)](#).

Therefore, the measurement of a realistic indoor air field distribution issued from a realistic asymmetric air jet appears to be necessary. Dealing with such air jets, an advanced analysis of the 3D airflow structures is strongly recommended. Detailed measurements from full-scale experiments accompanied by well-known boundary conditions could be reliable enough to serve as benchmark test for CFD models validation.

1.3.1.3 Moisture transport and condensation

The indoor airflow distribution implies the heat transfer (temperature) but also the mass transfer (moisture, contaminants). Moisture diffusion and transport in a space is a complex phenomenon, especially if the interaction with the airflow is taken into account. In fact, transfers of heat-air-moisture (HAM) within an enclosure are strongly interdependent and need to be taken into account in a global analysis (Woloszyn et al., 2003). The indoor air humidity is believed to have a significant impact regarding the occupant thermal comfort, the indoor air quality, the building energy consumption and the building envelope durability:

1. Low or high levels of relative humidity have straight effects on the perception of occupants' thermal comfort. For instance, high relative humidity reduces the effectiveness of sweating in cooling the body, while too low relative humidity causes chapped skin and lips, the long-term effect being a constant discomfort. That's why the indoor air humidity is needed to determine the thermal comfort, according to the Fanger model's (ISO 7730, 2005);
2. The humidity and mould were also qualified as common contaminants in indoor air that are believed to provoke the SBS (Passarelli, 2009; Redlich et al., 1997);
3. For the building envelope, excessive humidity promotes the growth of mould and condensation on walls, ceilings, furniture, which are very harmful to their durability.

As a result, numerous research programs have been carried out since the 1980s to study possible manifestations of moisture inside the buildings, for example: the AIVC²⁴ technical note 20 "Airborne Moisture Transfer" (1987), the IEA Annex 14 "Condensation and energy" (1992), the IEA Annex 24 "Heat, Air and Moisture Transport" (1996) and more recently the IEA Annex 41 "Whole building heat, air, moisture response" (2008). Since then, the topic of indoor moisture transport has gradually retained special attention. Several studies, based on both CFD models and experiments, were carried out to deal with the physical phenomena of the indoor heat-air-moisture coupled transfer in the whole-building scale: Karagiozis and Salonvaara (2001); Plathner and Woloszyn (2002); Teodosiu et al. (2003); Woloszyn et al. (2003); Mortensen et al. (2005); Woloszyn et al. (2009); Qin (2011); Tariku et al. (2010); Feng et al. (2012); Van Bellegheem et al. (2011, 2014).

Very recently, a whole new chapter dedicated to the "Moisture Management in Build-

²⁴Air Infiltration and Ventilation Centre

ings²⁵ was added to the ASHRAE Fundamental Handbooks²⁶ (ASHRAE, 2017). It shows clearly that great attention should be paid on the indoor moisture problem regarding the design of HVAC&R systems.

Some researchers give a special focus toward the indoor condensation problem (on surface and in the air volume), for instance: Jing et al. (2003); Liu et al. (2004); Hohota (2003); Teodosiu (2013); Gong et al. (2011); Ma et al. (2013); Palmowska and Lipska (2016); You et al. (2017).

Nevertheless, studies dealing with the condensation phenomenon are still limited given the transient, unsteady and even instantaneous characteristic of the phenomenon. A qualitative prediction of the surface condensation is possible. One can predict the location where the condensation takes place, the time of its production and its evolution in space/time (Liu et al., 2004; Gong et al., 2011; Teodosiu, 2013; You et al., 2017).

But the quantitative prediction techniques are lacking in the literature. These techniques intend to predict the condensation rate, i.e. the time evolution of the mass flow rate of condensed fluid per unit area. Studies on the condensation quantification were found at the micro-scale, e.g. on a metal plate surface of small size. Experimental studies were carried out on a controlled wind tunnel, the mass of the condensed fluid was achievable using a micrometric weight balance (Tiwari and Fontaine, 2009; Tiwari, 2011), or by means of high-definition image recording (Sakay, 2014; Sakay et al., 2016). Studies on the condensation quantification at the room reduced-scale are quite limited (Liu et al., 2004). No such studies were found at the room full-scale.

Therefore, there is a real need to investigate the indoor air distribution with the presence of moisture, including the surface condensation problem. With advanced techniques available nowadays, the condensation quantification might be achievable.

1.3.2 Outline of the thesis

1.3.2.1 Research objectives

Based on these previous statements concerning the need of knowledge about a realistic indoor air field distribution issued from an asymmetric air jet, as well as the need for indoor air field investigation with the presence of moisture and condensation situations, one could formulate the thesis problematic in the form of two following questions:

- *What is the behavior of a realistic asymmetric air jet under local interactions and how to characterize such an air jet?*

²⁵Chapter 36 presents data on indoor vapor release and measured indoor/outdoor vapor pressure/concentration differences, and discusses moisture sources and sinks that can reduce materials' durability, as well as the negative effects of insufficient or excessive indoor relative humidity.

²⁶there is no new chapter was added since the 2009 version.

-
- *Under indoor airflow conditions promoting condensation on cold surface, how it is possible to quantify the condensation rate?*

The present PhD study is a full-scale experimental study. The experiments were carried out in a controlled environmental chamber at our laboratory (CETHIL, France), known by the name "MINIBAT test cell". The author's main intention is to produce a new 3D benchmark test to validate CFD models for more realistic ventilation configurations. According to [Chen and Srebric \(2002\)](#), detailed data issued from benchmark test should contain complete and accurate information on simulated object geometry, initial conditions, boundary conditions and measurements with their uncertainties.

1.3.2.2 Definition of the studied configuration

The studied configuration needs to be carefully defined. The chosen one must include the following specifications:

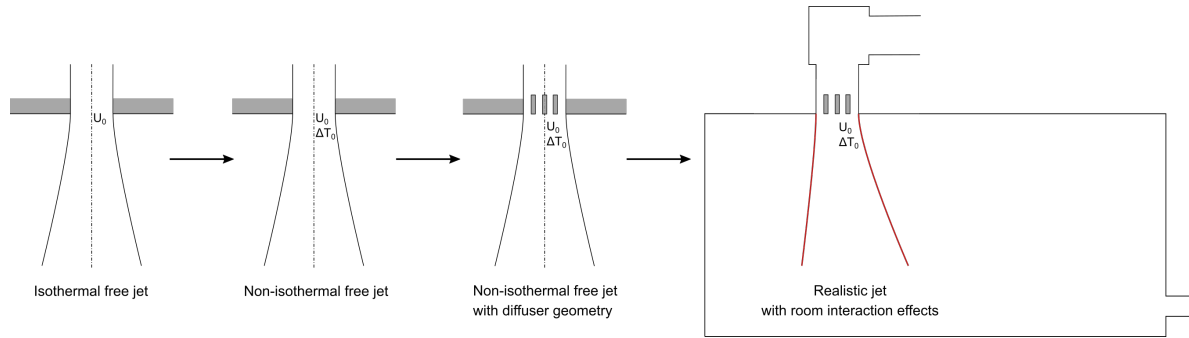
- an asymmetric air jet, i.e. the supply air inlet is not in the center nor the axis of the room;
- the exhaust air outlet is not aligned with the air inlet but should ensure the well-mixing of the indoor air;
- a plenum box in the supply circuit, before the air inlet;
- a diffuser mouth at the air inlet;
- a surface temperature gradient in the test cell to reproduce realistic conditions (e.g. summer or winter scenario);
- a vertical wall that allows promoting the condensation phenomenon.

A simplified schematic of the air jet configuration definition is given in the Figure [1.4\(a\)](#). Some transformation works were undertaken within the test cell enclosure for this study. Further details on the test cell along with those architectural elements above-mentioned will be given in the next Chapter [2](#).

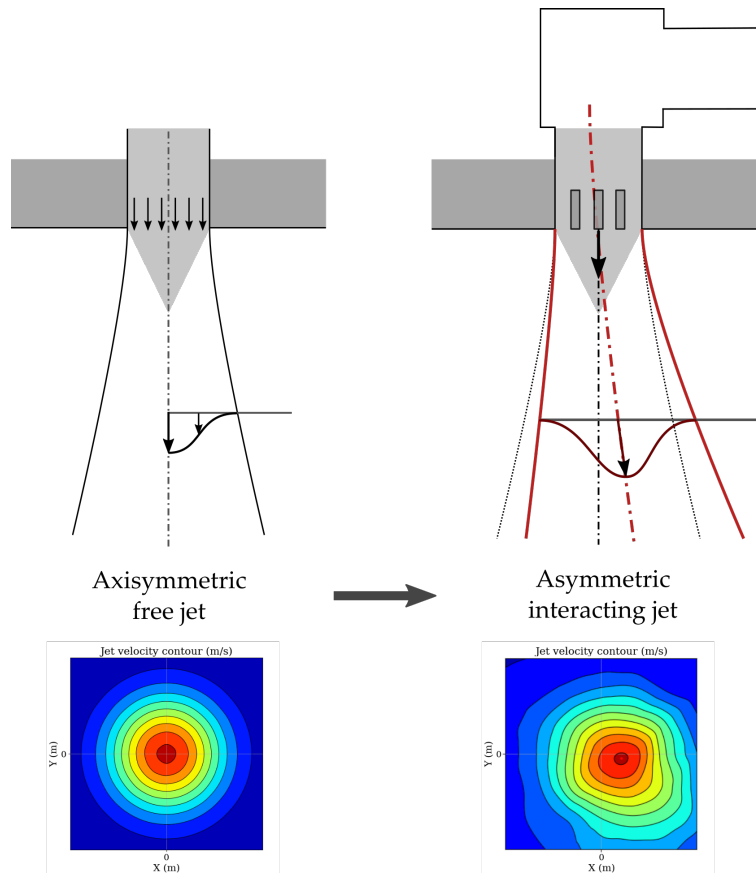
Given the presence of the plenum box, the air jet chosen is a vertical air jet issued from the ceiling. For a given cross-sectional plane, an axisymmetric free jet will have a symmetric and uniform spatial distribution: its velocity contours are supposed to have a circular form, as shown in the Figure [1.4\(b\)](#).

Then, the supply air inlet is moved away from the room axis but should not be too close to the side wall to avoid the Coanda effect²⁷. A grille diffuser is then fixed at the air inlet. The diffuser geometry should not be too complex in order to avoid approximations for CFD solving ([Chen and Srebric, 2002](#)). Lastly, air exhausts will be installed on the lower side of the other side of the room. This disposition should guarantee a homogeneous

²⁷Effect of a moving jet attaching to a parallel surface because of negative pressure developed between jet and surface ([ASHRAE, 2017](#)).



(a) Configuration study definition



(b) From free jet to interacting jet

Figure 1.4 – Jet flow configuration definition and expected behavior of the jet

mixing of the indoor air.

Hence, these various architectural elements presented will potentially disturb the air jet behavior, and thus a non-circular form of the velocity contours is expected, as can be seen in the Figure 1.4(b).

1.3.2.3 Expected outcomes

For the academic research, this study could contribute to a better characterization of a realistic asymmetric air jet having interaction with local architectural elements. A method of 3D analysis is proposed to investigate this kind of air jet. In addition, based on the achieved knowledge on the indoor air distribution, this study provides in-depth information about the condensation on cold surface. A measurement technique is proposed to deal with the qualification and quantification of this phenomenon.

The detailed experimental data issued from this study could be used as a 3D benchmark study for validating and improving CFD numerical models, especially for airflow configurations with rupture of symmetry. Besides, experimental results on surface condensation data could be extremely valuable for validation purpose since there was no similar studies in the literature.

This thesis is a part of an ANR²⁸ project named "Integrated Heat-Air-Moisture model within enclosures - Experimental validation", abbreviated under the name "HAM". The project was planned by a partnership between Technical University of Civil Engineering Bucharest (UTCB, Romania) and The Center for Thermal Sciences of Lyon (CETHIL, France) for three years (Jan/2014 - Dec/2016).

1.3.2.4 Manuscript organization

The remaining of the manuscript is divided into five chapters:

Chapter 2 describes the full-scale experimental set-up for this study. The actual configuration of the MINIBAT test cell and the existing metrology are detailed. Then, the various architectural elements installed within the actual airflow configuration are described. Finally, the description on the boundary conditions within the whole system is reported.

Chapter 3 explains in detail the metrology for the indoor air measurement. A mobile robot is specifically designed for the indoor air metrology since the indoor three-dimensional fields of air velocity, temperature and relative humidity are expected. Besides, the experimental protocol is also presented.

Chapter 4 provides a succinct description of an empirical model of an axisymmetric vertical free air jet. Its characteristics and its parametric coefficients are used to define reference criteria for characterizing the experimental jet.

Chapter 5 focuses on analyzing the behavior and the characteristics of the realistic interacting jet. The various test cases with the measured boundary conditions are pre-

²⁸Agence Nationale de Recherche

sented at first. The experimental results on the indoor air velocity and temperature fields are then reported. The characterization of the air jet includes: the trajectory deviation, the jet thickness and spread rate, the jet maximum velocity and temperature decay, and the jet cross-sectional profiles distribution and deformation. The turbulent characteristics of the indoor airflow are also analyzed.

Chapter 6 details the indoor condensation study on cold surface. The physical backgrounds of the phenomenon are presented at first. Then the measurement technique, the data processing method as well as some first experimental results and comparisons are detailed.

Finally, conclusions of the present work and the main recommendations for possible improvements in the future will be discussed.

Experimental set-up

2.1 Introduction

The study of the indoor distribution of air velocity, temperature and humidity fields within a mechanically ventilated room requires reliable and accurate experimental data. However, the quality of such measurements is only possible through an entirely controllable experimental test cell.

This chapter presents the full-scale experimental set-up of the current study. It is organized as follows:

- the section 2.2 provides a detailed description of the MINIBAT experimental facility;
- section 2.3 describes the adaptation that was conducted in MINIBAT to fit with the issues of the present study;
- section 2.4 summarizes the nature of the boundary conditions within our configuration study.

2.2 MINIBAT experimental facility

2.2.1 General purpose of MINIBAT

MINIBAT consists of a test cell whose thermal boundary conditions are fully controlled. The test cell has the dimensions of a realistic indoor rectangular room. The boundary conditions reproduce the effect of adjacent rooms along five faces of the test cell, and the effect of outdoor climatic conditions along the remaining face.

The test cell was designed to allow a very fine characterization of the indoor thermal environment under controlled and reproducible boundary conditions.

2.2.2 History of MINIBAT

MINIBAT experimental facility is located at the CETHIL laboratory (Villeurbanne, France). It was built during the 1980s and was used massively over the last thirty years as a tool for building physics tests. Here is a non-exhaustive lists of previous research carried out in MINIBAT from the oldest to the most recent:

- [Allard et al. \(1982\)](#), [Allard \(1987\)](#) studied indoor heat transfer by radiation and convection;
- [Inard et al. \(1996a,b, 1997\)](#) conducted experimental investigation within MINIBAT to validate a zonal model used for predicting the indoor air temperature distribution;
- the next research ([Castanet, 1998](#)) was dedicated to study the relation between the ventilation system, the occupant thermal comfort and the indoor air quality;
- in 2003, [Hohota](#) carried out experimental studies to validate an indoor CFD model which includes humidity transfer;
- [Kuznik \(2005\)](#), [Kuznik, Rusaouën, and Brau \(2007\)](#) used MINIBAT to investigate the behavior of a horizontal axisymmetric air jet developed near a ceiling. They validated their CFD turbulence models using the experimental data;
- lately, MINIBAT was dedicated to study physics of a double-skin facade system ([Gavan, 2009](#); [Kuznik et al., 2011](#); [Gavan et al., 2010](#));
- [Biwole \(2009\)](#); [Biwole et al. \(2009\)](#) studied 3D PTV (particle tracking velocimetry), a new method for the indoor airflow measurement;
- [Catalina, Virgone, and Kuznik \(2009\)](#) carried out a full-scale experimental study in MINIBAT with a cold ceiling. They evaluated indoor thermal comfort and validated their CFD model with the experimental data.

Hence, detailed and relevant experimental data has been obtained thanks to entirely controllable environment of the MINIBAT facility. Still, [Hohota \(2003\)](#); [Kuznik \(2005\)](#); [Gavan \(2009\)](#) noticed temperature fluctuations within the MINIBAT environment. This fluctuation had an amplitude of ± 1.5 °C. It could potentially influence the performances of MINIBAT.

MINIBAT was renovated and upgraded recently to make it more controllable. Thus, more accurate data can now be achieved. The description provided below concerns the new configuration of MINIBAT. Detailed information concerning the old configuration one can be found in [Kuznik \(2005\)](#).

2.2.3 MINIBAT architecture

2.2.3.1 The test cell

A simplified schematic of the test cell inner volume is given in the Figure 2.1. The test cell has an inner dimension of $L \times W \times H = 6.20 \times 3.10 \times 2.50 \text{ m}$. The four geographical directions North-South-East-West are also defined in the figure. They will be used later for walls name assignments.

We define a system of coordinate of the test cell (X; Y; Z). The origin of this system of coordinate is located at the lower corner between the East wall and the North wall. The X-direction follows the East-West direction, i.e. along the cell width dimension. The Y-direction follows the North-South direction, i.e. along the cell length dimension. The Z-direction goes from the floor to the ceiling.

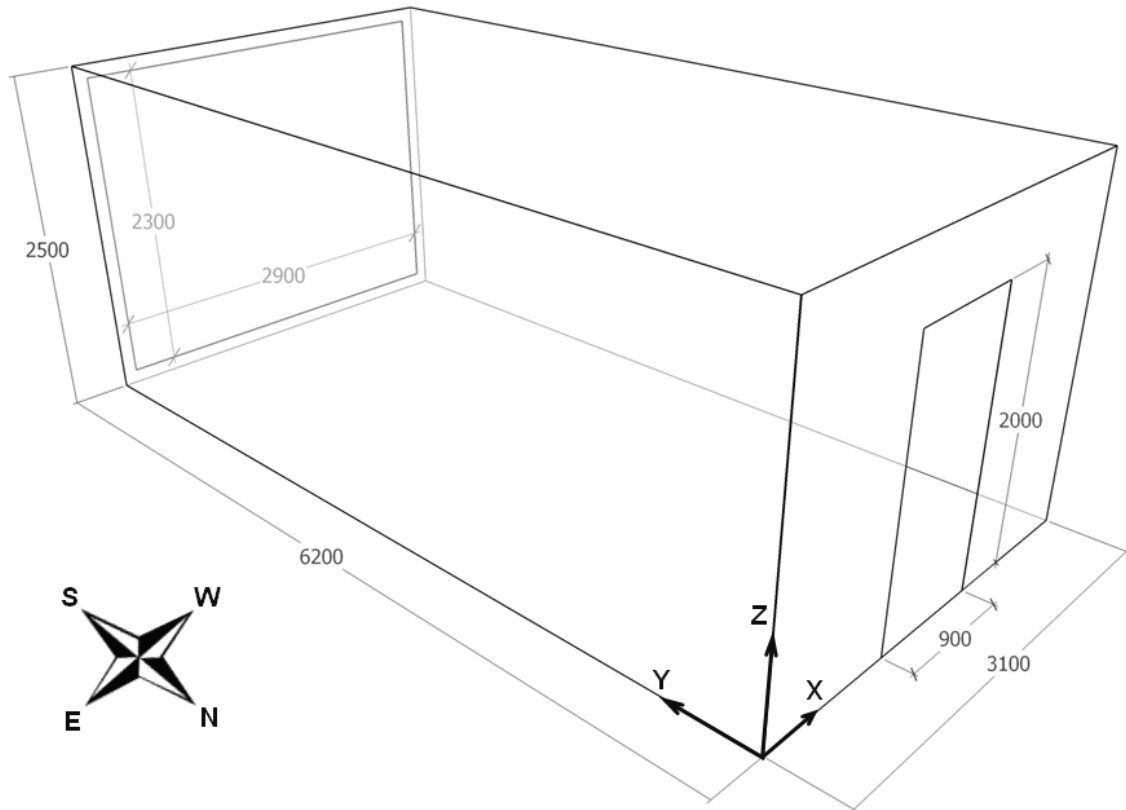


Figure 2.1 – Simplified schematic of the test cell inner volume (millimeter unit)

The test cell envelope comprises four vertical opaque walls, plus one ceiling and one floor. The southern facade of the test cell, whose dimension is $W \times H = 2.90 \times 2.30 \text{ m}$. It is interchangeable and adapted upon the demand of research studies.

The walls compositions are shown in the Figure 2.2. The illustration also provides the total thickness e_{s2s} and an estimation of the Surface-to-Surface thermal resistance

R_{S2S} of each wall:

- the opaque vertical walls are made of 5 cm thick agglomerated wood panels. They are covered on their internal faces by 1.3 cm thick plasterboard;
- the floor is made of 20 cm thick cellular concrete;
- the ceiling consists of 2.5 cm thick plywood plate, covered with 4.5 cm thick glass wool. A 1.3 cm thick plasterboard is fixed on the lower part of the ceiling.

All the inner opaque surfaces of the test cell are covered with gray painting and are varnished. By that way, the emissivity is homogeneous along all the test cell inner surfaces. The envelope materials and their thickness are summarized in the Table 2.1. The materials thermophysical properties which were used to compute the surface to surface thermal resistances are summarized in the Table 2.2.

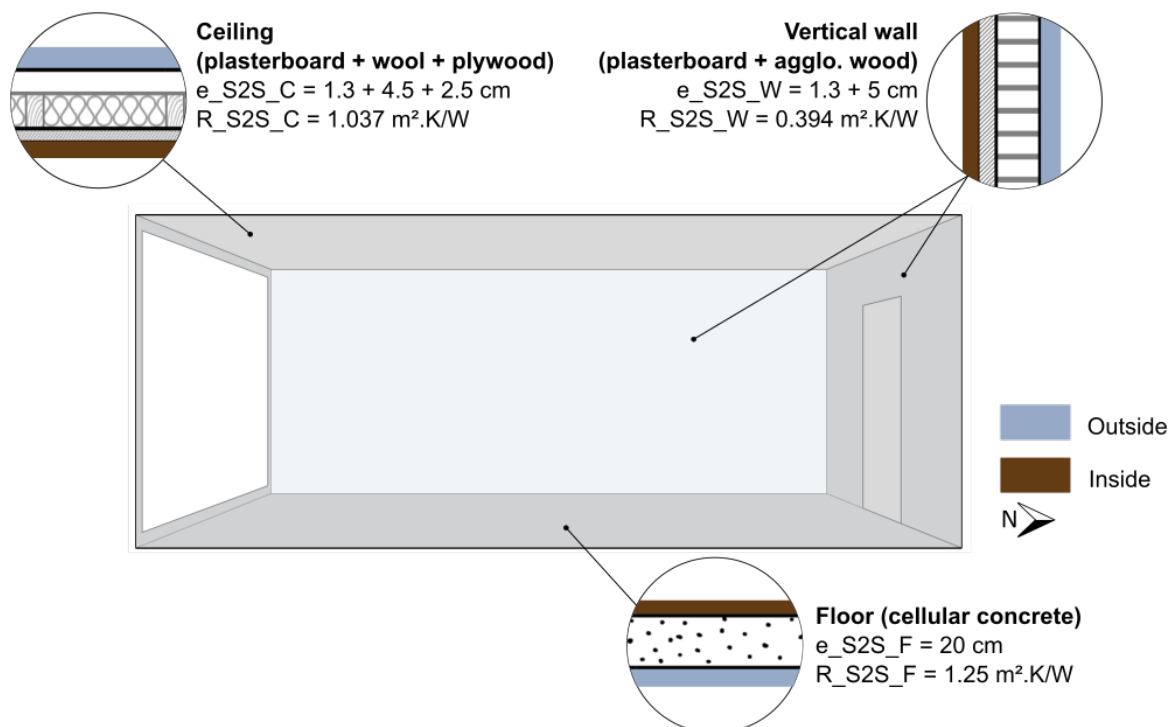


Figure 2.2 – Envelope composition of MINIBAT test cell

Wall name	Material	Thickness e [cm]	Resistance R_{S2S} [$m^2.K/W$]
Floor	Cellular concrete	20	1.250
Ceiling	Plywood plate	2.5	1.037
	Glass wool	4.5	
	Plasterboard	1.3	
Vertical wall	Agglomerated wood	5.0	0.394
	Plasterboard	1.3	

Table 2.1 – Test cell envelope composition (from outer to inner)

Material	Conductivity λ [$W/m.K$]	Density ρ [kg/m^3]	Capacity C_p [$J/kg.K$]
Cellular concrete	0.16	400	1000
Plywood plate	0.1	400	2045
Glass wool	0.06	72	1000
Plasterboard	0.35	817	1620
Agglomerated wood	0.14	544	1640

Table 2.2 – Thermophysical properties of MINIBAT envelope materials

2.2.3.2 The thermal zones

The test cell is surrounded by two thermal zones: a thermal buffer zone and a climatic chamber. A 3D schematized model of these zones is given in the Figure 2.3.

THERMAL BUFFER ZONE

The thermal buffer zone communicates with the test cell through five walls: North, East, West, the floor and the ceiling. It consists of two cavities: the first cavity is located below the test cell floor, the second cavity covers the upper part of the test cell. The external envelope of the thermal buffer zone is made of 20 cm thick layer of aerated cellular concrete and 10 cm thick layer of extruded polystyrene panels. This outer insulating layer, added on the East, West and ceiling walls, reduces the heat exchanges with the outdoor environment.

The thermal buffer zone is ventilated with a closed-loop air handling unit (AHU) entirely regulated in temperature. It is represented by the red boxes, located outside of the thermal buffer zone envelope (c.f. Fig. 2.3(e)). The air temperature is regulated at the air outlet of the AHU, before entering the thermal buffer zone. The accepted temperature range at the outlet of the AHU is [$10^\circ C$; $30^\circ C$]. By that way, we can reproduce thermal conditions similar to adjacent rooms along five walls of the test cell.

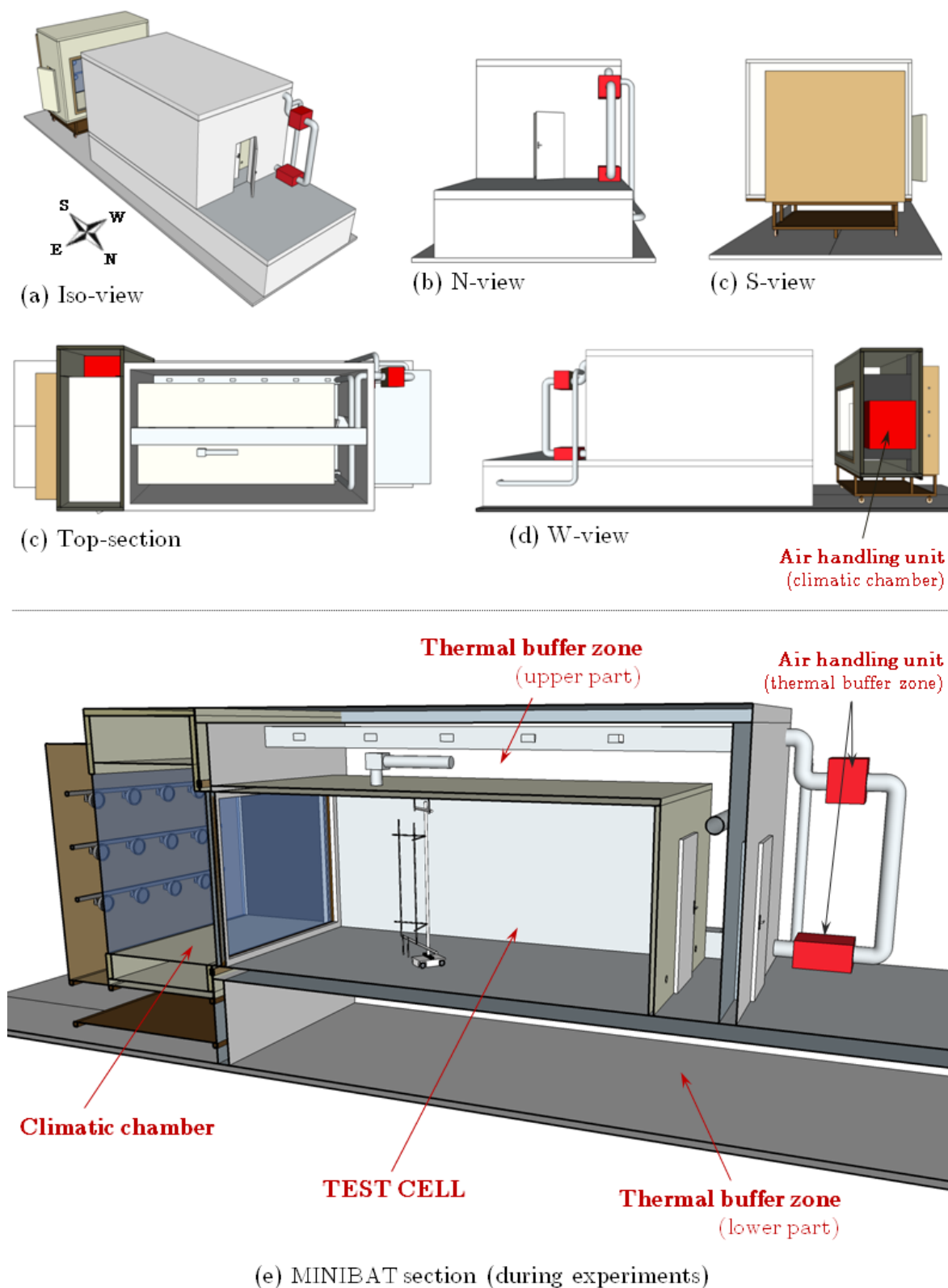


Figure 2.3 – 3D schematized model of MINIBAT

Where: Red boxes - Air handling units for the thermal buffer zone and the climatic chamber

The air distribution inside the thermal buffer zone is ensured by a ducts network, as shown in the Figure 2.3(c) and (e). The air is supplied into the thermal buffer zone through an array of lateral diffusers, which are installed in the upper part of the thermal buffer zone. The air is then extracted from the thermal buffer zone by two arrays of exhaust mouths located in the lower part throughout the East and West walls. This disposition promotes a regular and homogeneous air mixing within the thermal buffer zone volume.

CLIMATIC CHAMBER

The climatic chamber faces the south wall of the test cell. It consists of a movable air cavity which is regulated in temperature, plus an artificial lighting system which reproduces the sun radiation. The air handling unit used for the temperature regulation is located inside the volume of the climatic chamber (c.f. Fig. 2.3(c, d)). The temperature range in the climatic chamber is between -10°C and 40°C . Air mixing inside the climatic chamber is ensured by a centrifugal fan. Horizontal and vertical grille deflector are added at the AHU outlet to allow a homogeneous air distribution. By that way, we can reproduce various outdoor weather conditions in the climatic chamber, i.e. winter, mid-season and summer climatic conditions.

The artificial lighting system was not used for this study; it will not be described. Further information on the lighting system can be found in Gavan (2009) and Biwole (2009).

During experiments, the climatic chamber is moved toward the test cell so that they are in contact to each other (c.f. Fig. 2.3(e)). The MINIBAT experimental facility is not exposed to direct sunlight and outdoor environment. It is located inside a large building hall with 7 m of height.

2.2.3.3 Existing metrology in MINIBAT

WALL SURFACES TEMPERATURE

In order to precisely evaluate the surface temperature of the test cell walls, a network of 180 RTD¹ probes was implemented on both external and internal sides of the walls.

The probes are the 4-wire miniaturized (2 mm x 2.3 mm) Pt100². Each wall surface has 36 measurement points: 18 probes on the internal face and 18 probes on the external face. The North side (door) and the South side (glazing) each have 18 measurement points: 9 probes on the internal face and 9 probes on the external face. The exact positions of the probes are given in the Figure 2.4.

Their calibration has been conducted by Catalina et al. (2009). He reported that these

¹Resistance Temperature Detectors - temperature measurement sensors consists of a fine wire resistor that changes resistance value depending on the temperature variation; the RTD wire is often a pure material such as platinum, which gives a good accuracy and a long-term stability.

²platinum probe with a resistance of 100 Ω at 0°C .

probes have a measurement error of ± 0.2 °C.

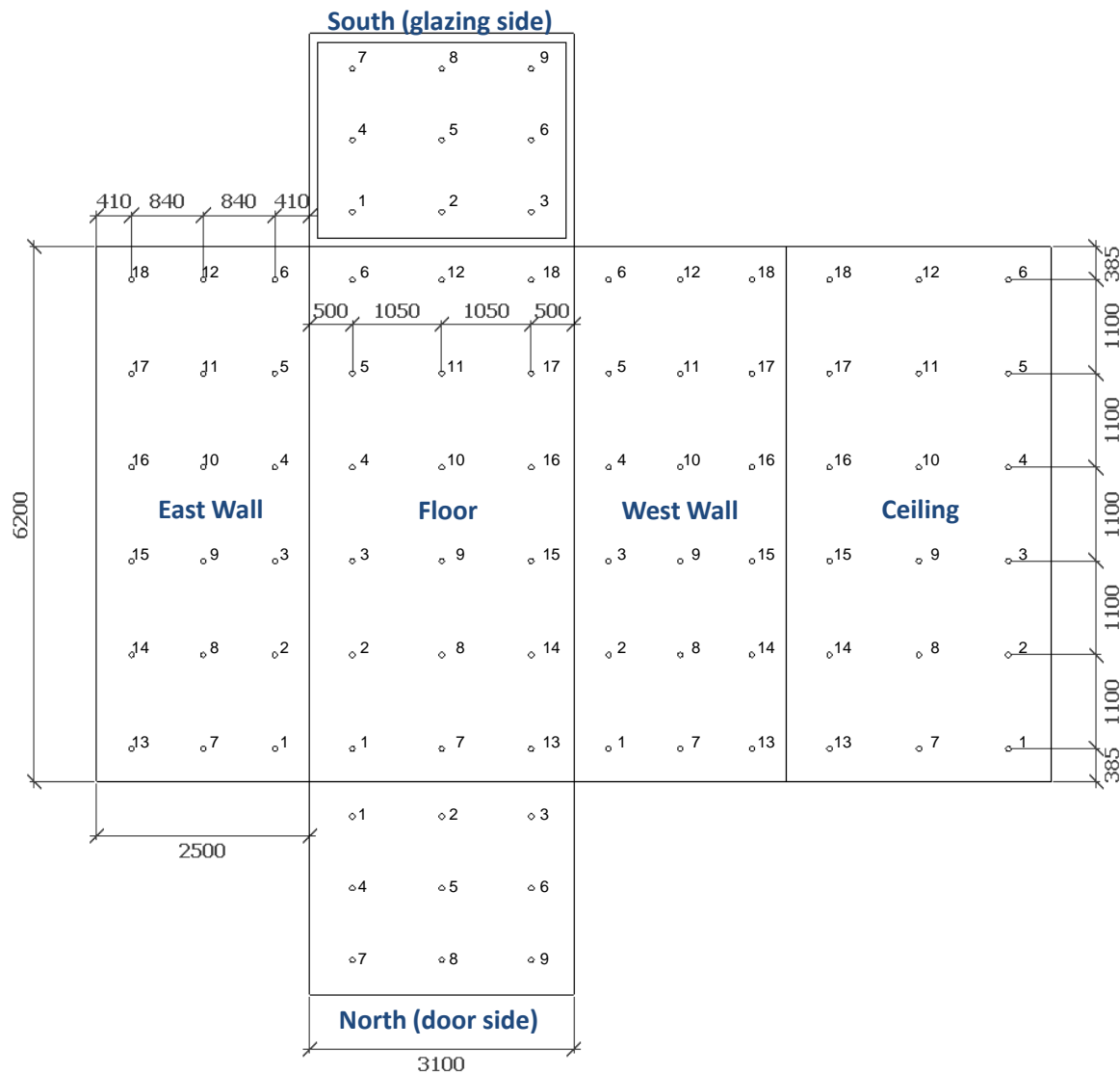


Figure 2.4 – Pt100 probes repartition in the test cell envelope

CLIMATIC CHAMBER AND THERMAL BUFFER ZONE AIR TEMPERATURE

Air temperature inside the climatic chamber and inside the thermal buffer zone are recorded continuously with 5 Pt100 probes: 2 probes are installed inside the climatic chamber and 3 probes inside the thermal buffer zone. The exact position of these probes are given in the Figure 2.5.

All the Pt100 probes (including those for the wall surface temperature measurement) are connected to a Keithley 7200 central multiplexing station. This station comprises 11 acquisition boards with 39 input channels each. Measurements are obtained thanks to a Keithley 2700 multimeter. The data acquisition is piloted by a LabVIEW software program.

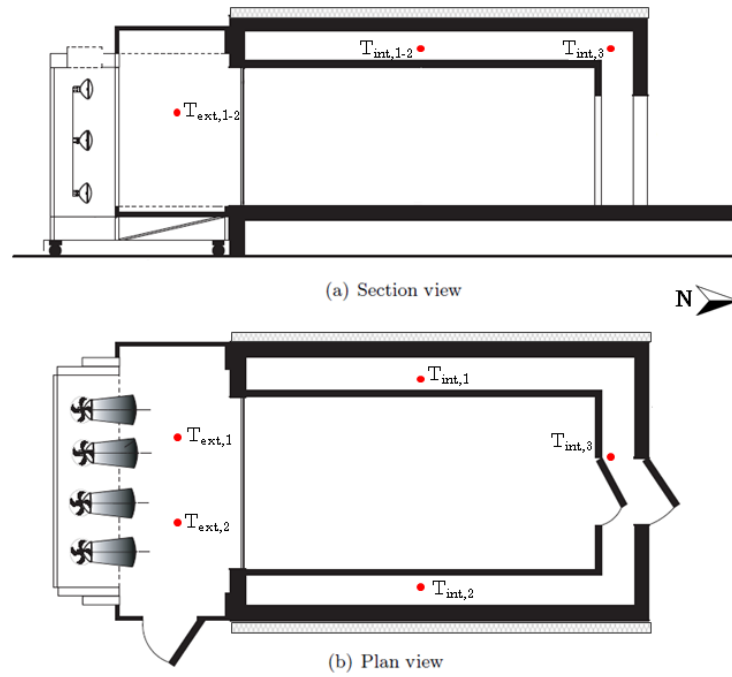


Figure 2.5 – Pt100 probes location inside the climatic chamber and the thermal buffer zone

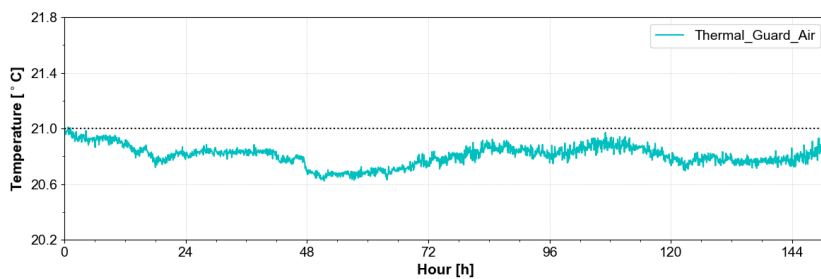
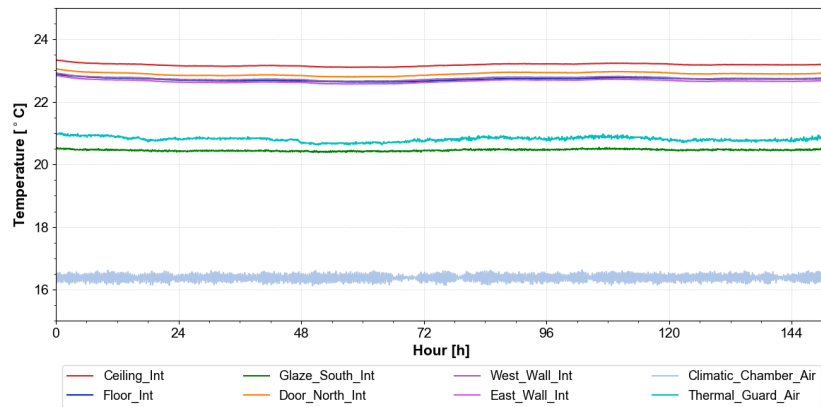


Figure 2.6 – MINIBAT temperature evolution over a period of 144 hours

2.2.3.4 Performance test of MINIBAT

Some preliminary measurements were performed to assess the stability and the precision of the temperature boundary conditions generated by the experimental facility.

We present here a measurement of a heating configuration. The temperature set-point in the thermal buffer zone was set to 21 °C, and the temperature set-point in the climatic chamber was set to 15 °C. The temperature in the hall was approximately equal to 11 °C. The Figure 2.6(a) presents the evolution of the surface temperature of the six test cell walls, in the climatic chamber, and in the thermal buffer zone, over a period of 144 hours. The Figure 2.6(b) focus on the evolution of the thermal buffer zone air temperature.

The result showed a satisfying stability during the preliminary measurement. The wall temperatures show a mean standard deviation of ± 0.05 °C, which is below the probes accuracy. The mean amplitude of the temperature fluctuation in the thermal buffer zone is ± 0.2 °C; the maximum fluctuation amplitude is ± 0.4 °C around the temperature set point.

2.3 Test cell adapted configuration for the study

The primary objective of the present PhD work is to study the temperature and velocity distribution in a room due to a mixing ventilation system. We remind that, in realistic conditions, the ventilation system is not located on a symmetrical plane of the room; the jet is disturbed by the geometry of the grill diffuser, by the shape of the ducts before the grill diffuser, by the proximity of walls near the air supply, by the temperature of the walls and by the location of the air exhausts. The ventilation system of MINIBAT test cell was designed to reproduce all those perturbations on a mixing ventilation air jet.

The ventilation system was designed to allow very stable air conditions at the air inlet (flow rate, temperature and humidity). It was essential that we could reproduce a stationary regime in order to have the time to measure the temperature and velocity fields in the room.

An additional constrain was taken into account during the design of the ventilation system: the whole system (test room + ventilation ducts near the room) should be easy to model in CFD simulation tools. Thus, we avoided complex curved surfaces, and we ensured that it was possible to estimate the boundary conditions on every external surface of the system.

2.3.1 Airflow configuration for the test cell

The Figure 2.7 presents the schematic of the test cell with the airflow configuration. The figure highlights the architectural elements which might disturb the air jet development: the near side wall, the plenum geometry, the grille diffuser geometry, and the location of the air exhausts.

2.3.1.1 Air supply and air exhaust mouths

The air is introduced into the test cell via an air diffuser located on the ceiling; the air jet issued from the diffuser is vertical and descendant. The air is extracted from the test cell by means of two air exhausts located on the North wall. This disposition increases the homogeneity of the air distribution within the test cell. On the inlet side, the ventilation network includes a horizontal duct, a plenum box, a vertical duct and an air diffuser.

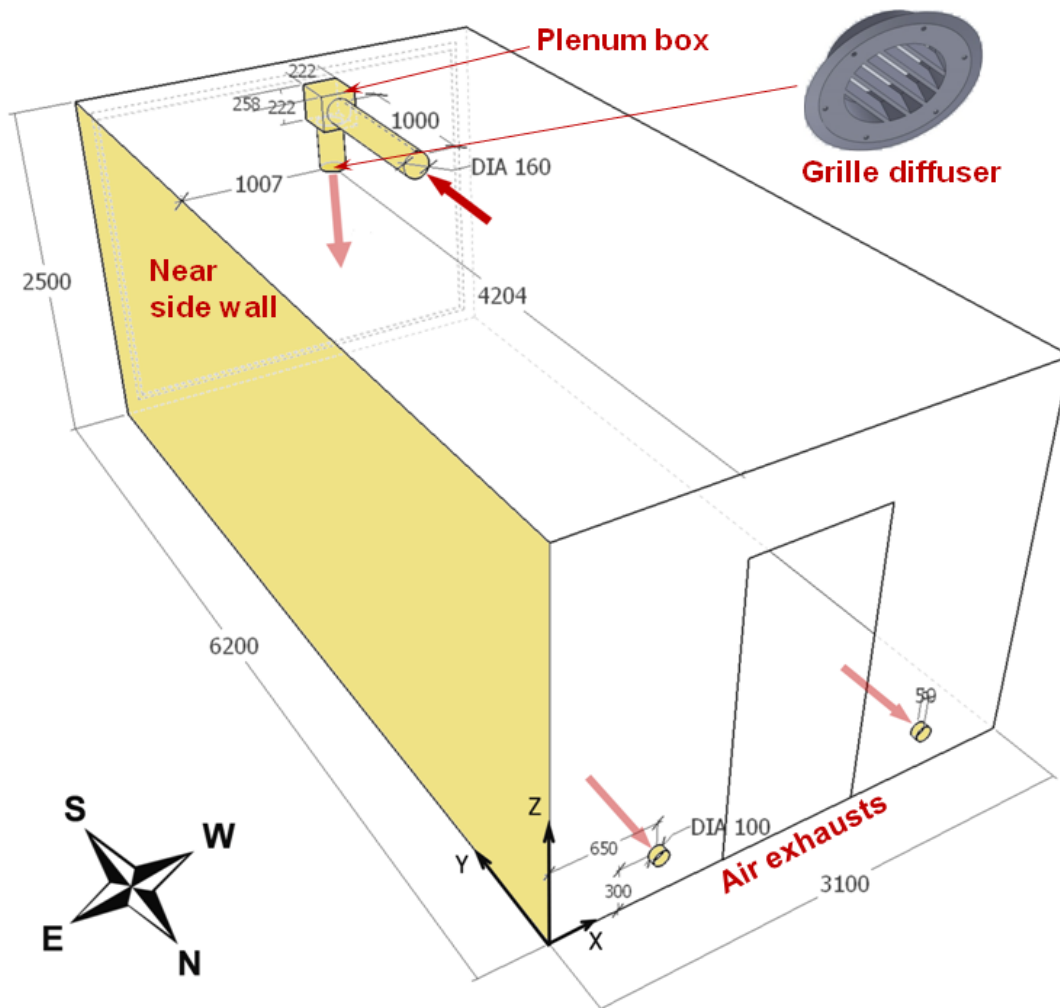


Figure 2.7 – Test cell schematic with airflow configuration (millimeter unit)

The various red arrows show the airflow directions within the test cell. The center of the air inlet is located 1.0 m from the East wall and 4.2 m from the North wall ($\varnothing 160$ mm). The distance between the near wall East and the supply air inlet is large enough so that the air jet would not be attached to the wall. Calculations are based on (Awbi, 2003). The two air exhausts are located on the North wall. They are distanced by 0.3 m from the floor and 0.65 m from the adjacent vertical East and West walls ($\varnothing 100$ mm). The two air exhausts opening are balanced in order to reach the same exhaust flow rate in each duct.

2.3.1.2 Plenum box

As illustrated in Figure 2.7, a plenum box is added inside the thermal buffer zone, just before the air inlet. Its dimension is 258 x 222 x 222 mm (c.f. Figure 2.8). According to Smoljan and Balen (2010), a major advantage of this component is that it offers better uniformity of the outflow velocity from the air supply diffuser (if a duct elbow had been used instead of a plenum box, the outflow velocity would follow a nearly Poiseuille's profile). Besides, in practice, the plenum box usually offers a much lower noise level compared to the conventional duct elbow.

2.3.1.3 Grille diffuser

As can be seen in the Figure 2.8 (A-A section), a grille diffuser is mounted at the supply air inlet. The grille is not a commercial model. It is a generic model, which was 3D printed at our laboratory. It was specifically designed to ease the numerical modeling.

A scheme of the grille diffuser is given in the Figure 2.9. The grille has an inner diameter of 160 mm and is equipped with five fixed grille fins. It has an effective area/free area ratio of 76%. This ratio is defined according to (ASHRAE, 2017); for which the effective area is the net area of an inlet device through which air can pass; the free area is the total minimum area of openings in an air inlet through which air can pass. The direction of the grille fins is parallel to the X-direction, as can be seen in the section-view in the Figure 2.8.

2.3.2 Southern wall

The first design criterion for the South facade was a low thermal resistance. A low thermal resistance allows us to get strong wall temperature gradients between the South surface and the other surfaces of the test cell. The other design criterion were motivated by the fact that we planned to perform condensation experiments with this facade. Thus, the facade had to have a very smooth surface to allow a homogeneous initiation of the

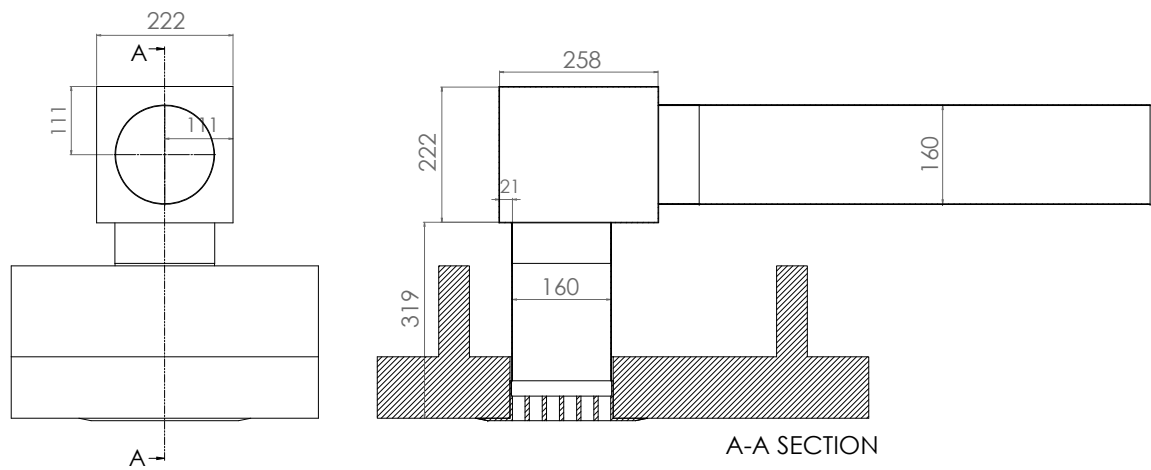


Figure 2.8 – Plenum box scheme (millimeter units)

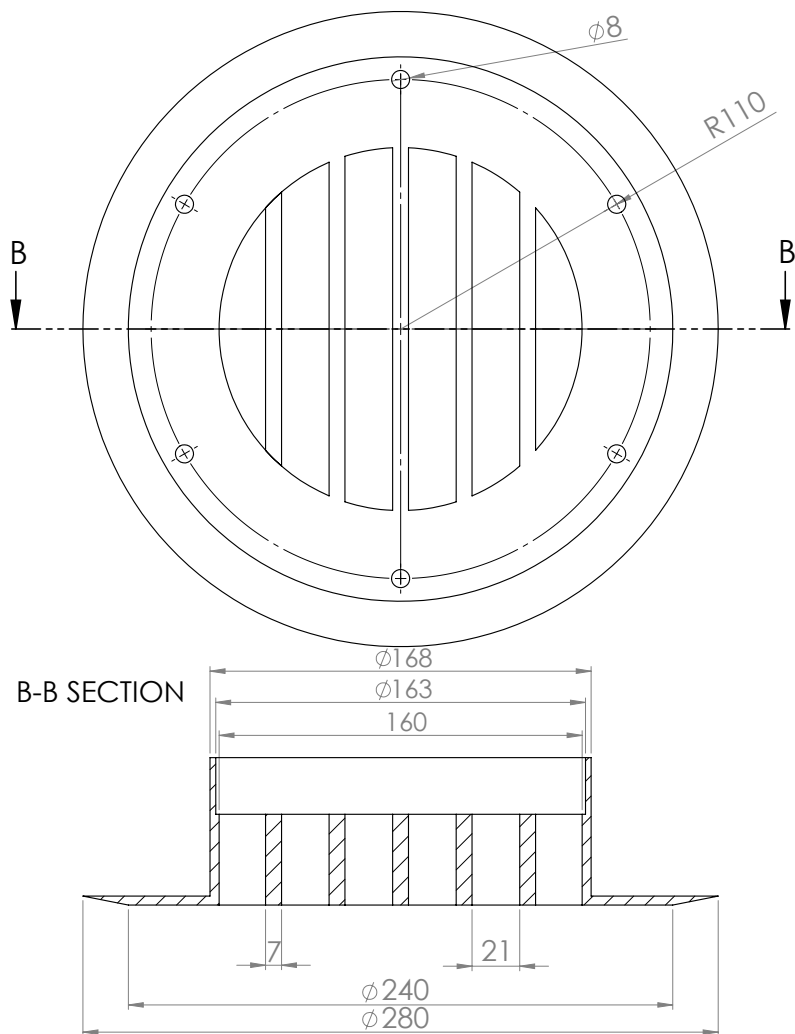


Figure 2.9 – Grille diffuser scheme (millimeter units)

condensation, and to ease the visualization of water vapor droplets.

Hence, the selected design was a fully glazed facade, made with a 1.2 cm thick laminated glazing. Its dimension is $W \times H = 2.90 \times 2.30 \text{ m}$. The resulting surface to surface thermal resistance is $R = 0.012 \text{ m}^2.K/W$.

2.3.3 Air handling unit for the test cell

2.3.3.1 Air handling unit description

The temperature, the humidity and the flow rate of the ventilation airflow are controlled by an air handling unit installed on the roof of an adjacent local. A 3D schematic and a photo of the air handling unit are given in the Figure 2.10(a) and the Figure 2.10(b). The ductwork which conducts airflow from the air handling unit to the MINIBAT test cell is shown in the Figure 2.10(c).

The dimensions of the AHU are $L \times W \times H = 2.40 \times 1.00 \times 0.77 \text{ m}$. Its envelope is made of double-skin panels, insulated by 5 cm thick of rockwool. As shown in the Figure 2.10(a), the air handling unit comprises, in the direction of airflow:

- an air filter;
- a cooling coil with a refrigerating capacity of 3.2 kW;
- a centrifugal plug fan with an air flow rate range from 70 to 400 m^3/h ;
- an electrical resistance with a heating capacity of 2.6 kW;
- a steam injection nozzle connected to a humidity generator;
- an auxiliary heating of a capacity of 0.5 kW, which is located inside the thermal buffer zone, near the air inlet into the MINIBAT test cell.

A 15 m of ducts network was needed to connect the AHU to the cell (as shown in the Figure 2.10(c)); the ducts are thermally insulated to reduce heat loss throughout the network. The AHU is operating in closed-loop to reduce fluctuations due to external conditions.

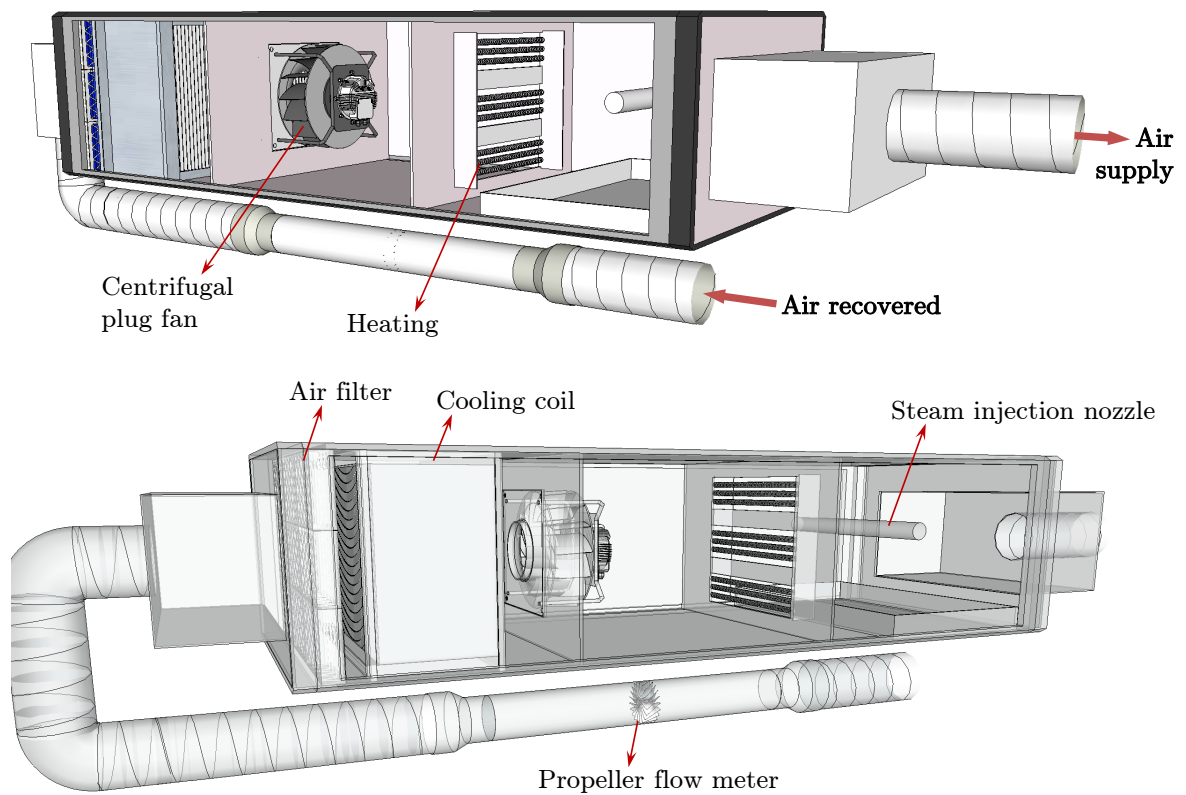
2.3.3.2 Air handling unit metrology and regulation

SUPPLY AIRFLOW RATE

The airflow rate is measured and regulated thanks to a propeller flow meter with an accuracy of $\pm 0.5 \text{ m}^3/\text{h}$. Its calibration was carried out by the CETIAT³ in 2015.

The flow meter is located at the air entrance of the air handling unit. Therefore, the flow

³Centre Technique des Industries Aéronautiques et Thermiques



(a) 3D scheme



(b) AHU photo



(c) Ductwork

Figure 2.10 – AHU system for the test cell

meter measures the airflow rate at the air outlet from the test cell. Some measurements were performed to assess the air tightness of the ventilation circuit between the flow meter and the air supply. The procedure we followed is described in the Appendix D. We followed this procedure for two flow rate set points: $200 \text{ m}^3/\text{h}$ and $100 \text{ m}^3/\text{h}$. We found that the air flow rate difference between the air flow meter and the air supply did not exceed 2%.

The regulation of the airflow rate is carried out with a PID controller⁴ programmed in a LabVIEW program.

SUPPLY AIR TEMPERATURE AND HUMIDITY

Air temperature and humidity measurements along the air handling unit and the ducts network are carried out by using Pt100 probes and Sensirion SHT75 probes. The location of the probes are shown in the Figure 2.11. The Pt100 probes are the 4-wire miniaturized type ($2 \text{ mm} \times 2.3 \text{ mm}$), with an accuracy of $\pm 0.1 \text{ }^\circ\text{C}$.

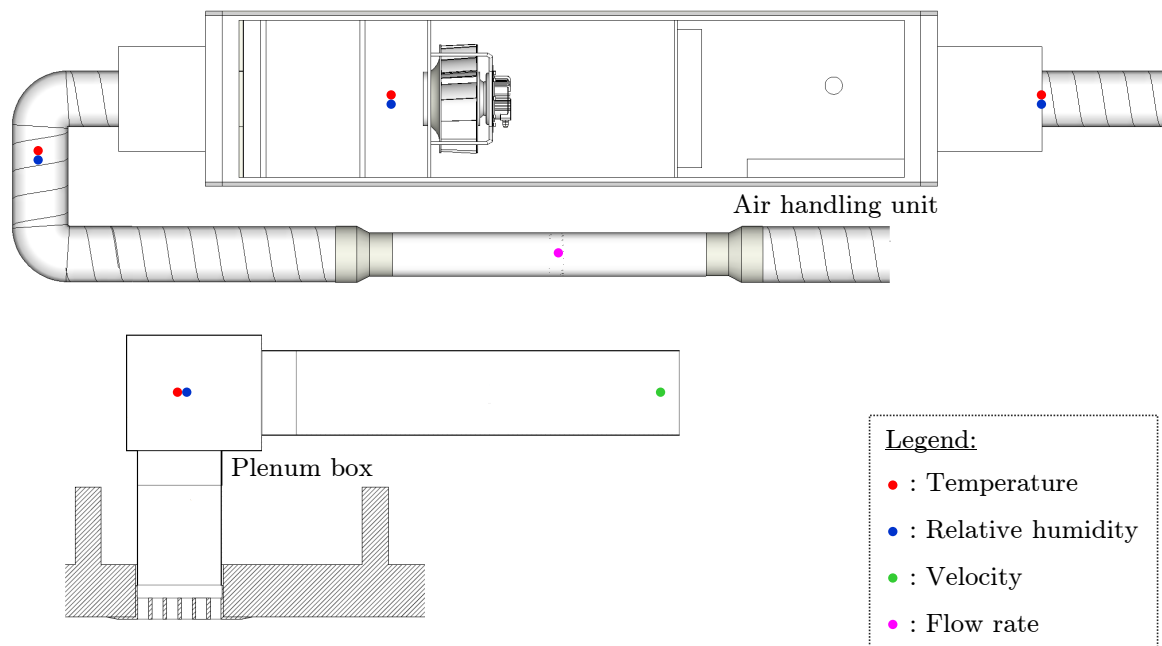


Figure 2.11 – Probes location within the air handling unit and along the ductwork

The SHT75 probes measure the air relative humidity (with an accuracy of $\pm 1.8 \%RH$) and the air temperature (accuracy of $\pm 0.3 \text{ }^\circ\text{C}$). The specific humidity is computed with the temperature data from the Pt100 probes, and the relative humidity data from the SHT75 probes. Those SHT75 probes are calibrated by the manufacturer.

The temperature of the cooling coil is set to be constant. Thus, the cooling coil cools down

⁴A proportional-integral-derivative controller is a control loop feedback mechanism widely used in industrial control systems and a variety of other applications requiring continuously modulated control. It continuously calculates an error value as the difference between a desired set point and a measured process variable and applies a correction based on proportional, integral, and derivative terms.

and dries out the air constantly. The AHU outlet temperature and specific humidity are regulated with two PID controllers. The first PID controller acts on the steam generator to regulate the specific humidity. The second PID controller acts on the resistances to adjust the air temperature. This regulation scheme avoids dead regulation zones. The temperature of the air is adjusted just before the plenum with the auxiliary heater.

SUPPLY AIR VELOCITY

A thermoelectric anemometer was added in the duct located just before the plenum, to perform fast measurements of the inlet air velocity. Those fast measurements are used to determine the inlet turbulence characteristics.

The probe employed is a Schiltknecht ThermoAir64 omnidirectional hot-sphere anemometer. Its description will be discussed further in the section 3.2.1.4. The probe velocity range goes from 0.15 to 5 m/s, with an accuracy of $\pm 0.5\%$ of full-scale and $\pm 1.5\%$ of the reading value. The location of the anemometer is shown in the Figure 2.11.

2.3.3.3 Steam generator for the air handling unit

The humidity generator for the air handling unit is a precise steam generator E-3000 from Cellkraft. A picture of the unit is given in the Figure 2.12.



Figure 2.12 – Precise steam generator unit for the air handling unit

It is a "ready-to-use" complete system, which comprises a precision pump and an evaporator. Its steam flow rate range goes from 1 to 50 g/min. The steam flow rate is regulated by the pump control, which precisely adjusts the water supply to the evaporator with high resolution and stability. The flow accuracy is $\pm 2\%$ of full scale at steady state. Its steam temperature range goes from 100 to 200 °C with an accuracy of ± 2 °C.

2.4 Summary: boundary conditions of the system

This section summarizes the nature of the boundary conditions within our configuration study. Those boundary conditions are reproduced and measured thanks to the MINIBAT configuration presented here above. The summary of the boundary conditions might be helpful for the CFD researchers who will try to simulate our configuration to validate their model.

The Table 2.3 and the Table 2.4 describe the nature of the boundary conditions applied on each surface of MINIBAT test cell along with the ventilation system.

Each boundary condition is associated with some parameters, which is measured during the experimental campaign. The names of the parameters are also given in the tables.

There are two options for modeling the walls around the cell. In the Table 2.3, we consider that the walls are modeled with a temperature boundary condition. In that case, we provide the temperature measured on the inner surface of the walls. In the Table 2.4, we consider that the walls are modeled with a mixed boundary condition with the thermal resistance of the wall and the temperature measured on the outer surface of the wall. The tables also provide a color code to identify the various surfaces of the system on the Figure 2.13.

An illustration of the boundary condition type associated to the plenum box and the grille diffuser, as well as the air exhaust mouths is given in the Figure 2.14.

Surface name	Color code	Thermal BC		Dynamic BC	
		Type	Parameter	Type	Parameter
Ceiling		T	$T_{SI,C}$	SW	-
Floor		T	$T_{SI,F}$	SW	-
East wall		T	$T_{SI,EW}$	SW	-
West wall		T	$T_{SI,WW}$	SW	-
North wall (door)		T	$T_{SI,NW}$	SW	-
South wall (glazing)		T	$T_{SI,GL}$	SW	-
Plenum box		T	AD	SW	-
Air inlet		T	T_0	QV	Q_0, TI_0
Air exhausts		T	AD	-	-

Table 2.3 – MINIBAT boundary conditions using inner surface

Surface name	Color code	Thermal BC		Dynamic BC	
		Type	Parameter	Type	Parameter
Ceiling		T+R	$T_{SE,C} + R_{S2S,C}$	SW	-
Floor		T+R	$T_{SE,F} + R_{S2S,F}$	SW	-
East wall		T+R	$T_{SE,EW} + R_{S2S,EW}$	SW	-
West wall		T+R	$T_{SE,WW} + R_{S2S,WW}$	SW	-
North wall (door)		T+R	$T_{SE,NW} + R_{S2S,NW}$	SW	-
South wall (glazing)		T+R	$T_{SE,GL} + R_{S2S,GL}$	SW	-
Plenum box		T	AD	SW	-
Air inlet		T	T_0	QV	Q_0, TI_0
Air exhausts		T	AD	-	-

Table 2.4 – MINIBAT boundary conditions using outer surface

Thermal boundary condition types: T - Imposed temperature;

R - Imposed thermal resistance; AD - Adiabatic

Dynamic boundary condition types: SW - Solid wall; QV - Volume flow rate

Parameter name nomenclature: SI - inner surface; SE - outer surface;

TI - turbulence intensity

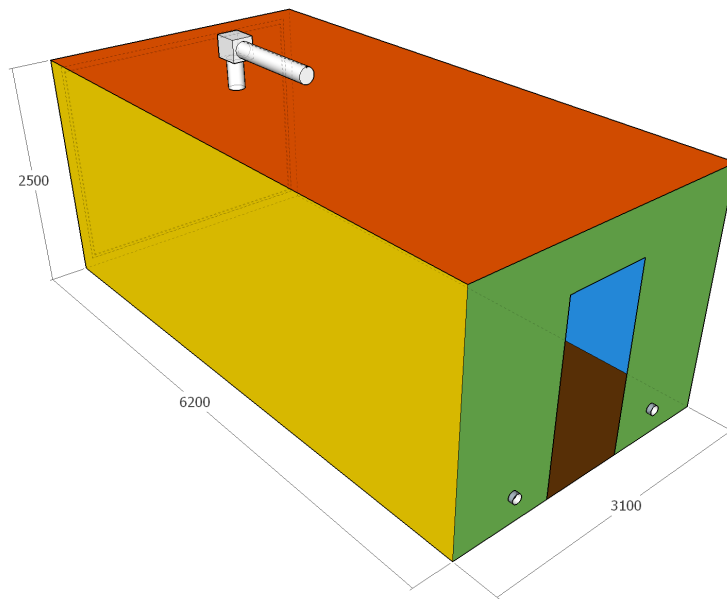
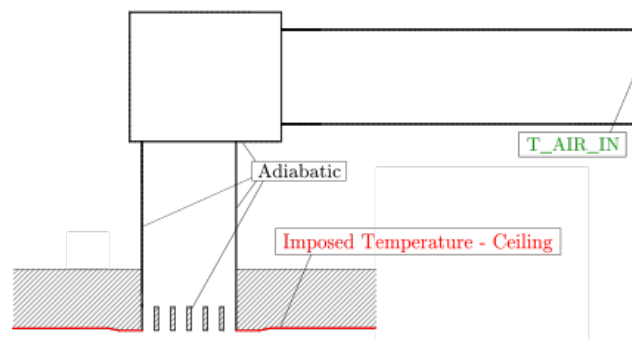
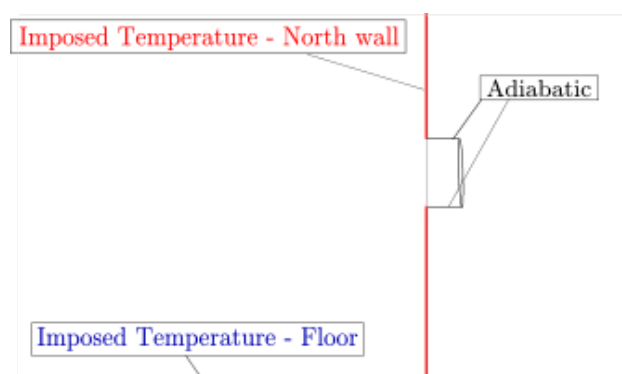


Figure 2.13 – The test cell wall boundary conditions with color code



(a) Plenum box and grille diffuser



(b) Air exhaust mouths

Figure 2.14 – Boundary conditions type associated to the ventilation ductwork within the test cell

Indoor air metrology and experimental protocol

3.1 Introduction

A detailed study of the indoor hygrothermal and airflow characteristics, especially the turbulent characteristics, requires accurate measurements in the interior volume. The measurements comprise measurements of the air velocity (instantaneous and mean value), the air temperature and the air humidity.

Therefore, this chapter presents the indoor test cell metrology as follows:

- section 3.2 describes the different sensors used to measure the air fields in the test cell;
- section 3.3 describes the mobile robot developed to scan the volume of the test cell;
- section 3.4 presents the experimental protocol for the air jet studies.

3.2 Metrology for indoor air fields measurements

3.2.1 Indoor air velocity

3.2.1.1 Airflow parameters and characteristics

The indoor airflow is characterized by the following magnitudes:

- the instantaneous velocity u_i , where i represents the direction of velocity component (i.e. x, y, z);
- the mean velocity $\overline{u_i}$;
- the standard deviation of the velocity σ_u ;

- and the turbulence intensity TI .

The indoor airflow within a mechanically ventilated room is characterized by a relatively low mean velocity (0.01 - 2 m/s) and by relative high turbulence intensity (10% - 70%), according to Hanzawa et al. (1987). The velocity fluctuations with frequencies between 1 Hz and 2 Hz contribute by 90% of the RMS of the fluctuating component (Popiolek et al., 2007). Therefore, flow measurement systems need to be carefully chosen to obtain reliable and accurate information of the airflow pattern along with velocity and turbulence intensity distributions.

In our configuration, we have a relatively large space ($L \times W \times H = 6.20 \times 3.10 \times 2.50$ m), mechanically ventilated by a turbulent vertical descendant air jet through a grille diffuser of $\varnothing 160$ mm. The AHU airflow rate ranges from 70 to 400 m³/h, which means that the air velocity supplied through the diffuser ranges from 0.9 to 5.5 m/s. However, as preconized by ISO and ASHRAE Handbook Fundamentals (ASHRAE, 2017), the indoor mean air velocity should not exceed 0.5 m/s in the occupied region and 2 m/s in the jet region. Therefore, the AHU airflow rate range will be restricted to 70 - 150 m³/h.

A study by Loomans (1998) gives an overview of the expected mean velocity and turbulence intensity values in different zones of a mechanically ventilated room. An illustration which is extracted from his study is given in the Figure 3.1. According to the author, the mean velocity (in m/s) and turbulence intensity (in %) values are distributed as follows:

- source-zone: $\overline{u_i} \in [0.1; 2.0]$; $TI \in [5; 25]$
- boundary-zone: $\overline{u_i} \in [0.05; 0.3]$; $TI \in [10; 30]$
- free-zone: $\overline{u_i} \in [0.01; 0.15]$; $TI \in [10; 100]$

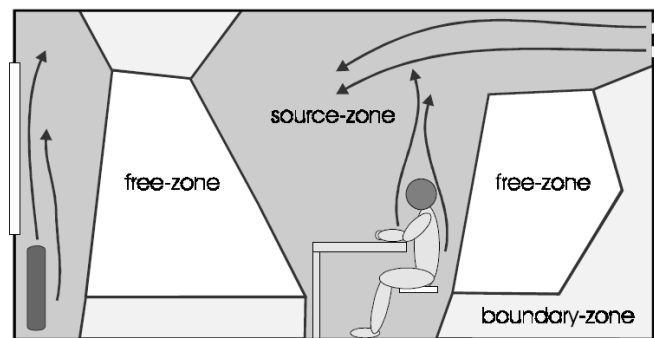


Figure 3.1 – Room air flow zones division following flow regimes (Loomans, 1998)

It is obvious that the flow measurement system should have an appropriate velocity measurement range (0.01 - 2 m/s) with a high spatial resolution. It must have a high dynamic (frequency) response to be able to access to most of the flow turbulence information. Furthermore, the three-dimensional characterization of the air jet pattern is required.

Two measurement techniques were candidate for the velocity field measurement in this study: the hot-sphere anemometer and the particle image velocimetry (PIV). A short review of flow measurement techniques used in the literature is given in the section 3.2.1.2. Two techniques mentioned above will be described in detail. Their advantages and their limitations will be analyzed to justify our decision.

3.2.1.2 Flow measurement techniques

Different techniques for indoor flow measurement along with their applications and their limitations have been reviewed by [Sun and Zhang \(2007\)](#). They can be divided into two categories: point-wise technique which can only give the velocity data at the measured point of the probe, and global-wise technique which can measure a whole-field velocity data. For instance, point-wise techniques include: rotating vane anemometer, hot-wire anemometer, hot-sphere anemometer, ultrasonic anemometer, Laser-Doppler velocimetry (LDV); and global-wise techniques include: particle image velocimetry (PIV), stereoscopic PIV (SPIV) and particle tracking velocimetry (PTV).

Point-wise techniques

Rotating vane anemometer and ultrasonic anemometer have a low spatial resolution (3.5 - 10 cm) and a significant intrusiveness. They are not suitable for low room air velocity measurement and thus not appropriate for our study.

Hot-wire anemometer and LDV techniques, despite their intrusiveness, support three dimensional velocity components measurement with a high spatial resolution (1 mm) and a high time resolution (0.1 to 10 ms). Besides, three-dimensional hot-wire anemometers had been used before by [Kuznik et al. \(2007\)](#) for his experimental study within the MINIBAT test cell. Their probes had an accuracy of ± 0.05 m/s and $\pm 3\%$ of the reading value. According to the author, the results were relevant, the probes showed a good performance. Thus, they are suitable for our need but however, these techniques mentioned above are finally excluded due to its excessive high cost.

Hot-sphere anemometers are omnidirectional, which mean they are not sensitive to the airflow direction and thus can only measure the air total speed (velocity magnitude). They offer a high spatial resolution (1 mm) and a good time resolution (0.1 s to 2 s). Their price is also reasonable, which make the hot-sphere anemometer a good candidate in the point-wise measurement technique category.

Global-wise techniques

The particle image velocimetry (PIV) and particle tracking velocimetry (PTV) techniques consist of a visualization method with a digital image processing technique. They are capable to provide both qualitative fluid information (airflow pattern) and quantitative fluid information (velocity data).

Both techniques are based on seeding tracer particles to the indoor airflow with an ap-

appropriate particle concentration. These particles, which ideally have the same physical density as the ambient air, are illuminated by a pulsed light source and recorded within a short time interval thanks to one or multiple high-speed digital camera. For the PIV and SPIV techniques, the displacement of a group of tracer particles is recorded in a specific plane to get instantaneous air velocity values. In the case of the PTV technique, the displacement of a single particle is recorded and tracked to get the 3D air trajectories. To get the turbulence flow data, a high sequence of airflow field image must be captured within a short time interval by increasing the image acquisition frequency. More details about the measurement principle and the data processing of the PIV and SPIV techniques can be found in a comprehensive book by Raffel (2007).

These techniques, partially-intrusive, offer a high time resolution (dependent on the pulse interval, from less than 1 *ms* to 500 *ms*) and a high spatial resolution (dependent on the tracer particle size) with a low limit of velocity detection (Sun and Zhang, 2007).

A complete summary and review of the PIV and the PTV applications for indoor air-flow measurements are given by (Cao et al., 2014c) and by (Fu et al., 2015). This study only focuses on the applications achieved in full-scale experiments.

Hosni and Jones (2002) used the PIV to measure the local airflow distribution within a volume of 2.3 x 2.3 x 2.3 *m* around a thermal manikin. The latter is placed in a real size room whose dimension is 7.3 x 4.9 x 2.7 *m*. They concluded that the flow pattern, as well as accurate velocity and turbulence intensity magnitudes and directions, can be measured using the PIV technique.

An American research group from University of Illinois has intensively studied indoor airflow distribution using the PIV technique in a full-scale test room of dimension 5.5 x 3.7 x 2.4 *m*. They have developed and tested both two-dimensional PIV technique (Zhao et al., 1999), (Zhao et al., 2001) and three-dimensional SPIV technique (Sun et al., 2001), (Sun and Zhang, 2003) and (Sun et al., 2004b).

According to the author, these techniques are capable to recognize clearly small differences in airflow patterns and velocity distributions. There is no limitation for the PIV method to detect low air velocity, in theory. The lowest velocity resolution can be detected is of order of 0.02 *m/s*.

A research group from Germany have built a highly developed PIV and PTV techniques (Bosbach et al., 2006), which are able to measure strongly turbulent 3D airflow in an area as large as 12.6 *m*². In fact, the biggest challenge concerning the PIV and the PTV development is about the equipment technology limitations. For example, a low tracer particle generating rate impacts the seeding density and thus leads to a poor spatial density. As pointed out by Bosbach et al. (2009), the critical factor in full-scale airflow investigation using these techniques is that a much higher seeding density is mandatory to determine the flow velocity and the turbulence data. Therefore, using helium filled soap bubbles (HFSBs) as tracer particles, they have developed a multi-channel generator

with a nozzle orifice, which is capable to generate up to several thousand HFSBs per second.

They have conducted full-scale experiments in their cylindrical convection cell whose dimensions are $\varnothing 7.15 \times H 6.3 \text{ m}$. Using their newly built bubble generator, combined with a high power pulsed laser illuminate source, a measurement plane of $4 \times 3.5 \text{ m}$ can be recorded with the SPIV technique (Resagk et al., 2004). Later in 2010, using the 3D PTV technique, they were capable to perform an airflow measurement within a zone of $7 \times 3 \text{ m}$ (Lobutova et al., 2010). For this study, their 3D PTV technique requires four high-speed camera recording system, a powerful full-volume illumination system and latex balloons as tracer particles.

Biwole (2009); Biwole et al. (2009) have developed a complete large-scale 3D PTV algorithm that can be fully applied to measure the indoor air velocity. He has conducted several experiments within large-scale rooms, such as MINIBAT ($3.1 \times 3.1 \times 2.5 \text{ m}$) and a $5.5 \times 3.7 \times 2.4 \text{ m}$ test room. Their results showed that the algorithm can track more than 1400 tracer particles in a volume up to $3 \times 3 \times 1.2 \text{ m}$.

3.2.1.3 Choice of technique for the present study

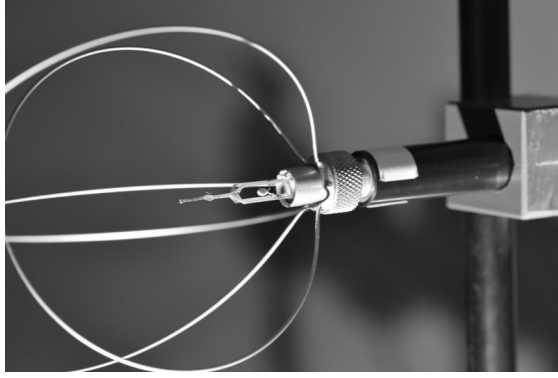
Indoor airflow measurements in large-scale enclosures as MINIBAT are technically achievable using PIV/PTV techniques. We have conducted a feasibility test in MINIBAT with our existing PIV system. As a result, a significant investment is required for a system that allows to obtain 3D airflow data. In addition, a rail support system is required to displace the camera recording system in MINIBAT. Its intrusiveness potentially disturbs the airflow.

The investigation presented here above led to the decision to use the hot-sphere anemometer. Despite the fact that this is a point-wise and intrusive technique, it still offers a good compromise between the performance and the cost. According to Sun and Zhang (2007), the hot-sphere anemometer is specially designed for indoor airflow applications with a measured speed (velocity magnitude) range from 0.05 to 5 m/s.

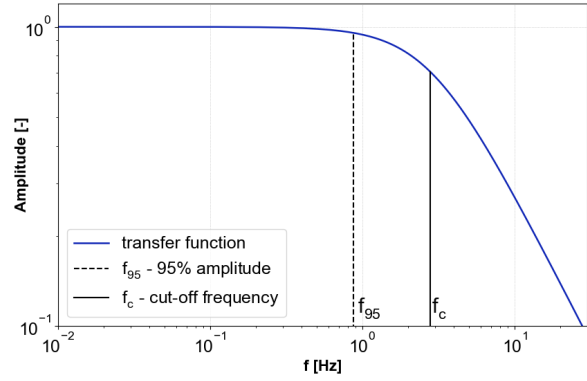
3.2.1.4 Hot-sphere anemometer description

The anemometer selected is an omnidirectional hot-sphere anemometer ThermoAir64 developed by a Swiss manufacturer, Schiltknecht. The Figure 3.2(a) presents a picture of the hot-sphere anemometer.

As mentioned in the section 3.2.1.1, the indoor velocity fluctuation may reach a frequency up to 2 Hz. The hot-sphere anemometer has an acquisition frequency of 10 Hz (with undamped option). The diameter of the sphere (sensing element) is about $d_{\text{sphere}} = 200 \mu\text{m}$. This low size may allow us to capture indoor velocity fluctuations. Lack of information from the manufacturer, we suppose that the material of the probe is



(a) Hot-sphere anemometer picture



(b) First-order transfer function

Figure 3.2 – Omnidirectional hot-sphere anemometer Schiltknecht ThermoAir64

Nickel: $\rho = 8900 \text{ kg/m}^3$, $C_p = 105 \text{ J/kg.K}$, $\lambda = 90.5 \text{ W/m.K}$ (at 20°C). The convection coefficient around the sphere can be evaluated: $h_{air} = 473.52 \text{ W/m}^2.\text{K}$. Further details on the calculation can be found in the Appendix C.

If we consider an airflow velocity of 0.5 m/s , the time constant τ of the probe is:

$$\tau = \frac{\rho C_p V_{sphere}}{h_{air} S_{sphere}} \simeq 0.057 \text{ s} \quad (3.1)$$

Assuming a first-order transfer function of the probe, its amplitude can be expressed as follows:

$$|TF(f)| = \frac{1}{\sqrt{1 + (2\pi f \tau)^2}} \quad (3.2)$$

This transfer function is shown in the Figure 3.2(b). We note f_{95} , the frequency for which 95% of the fluctuation amplitude can be captured by the anemometer. We have $f_{95} \simeq \frac{1}{20\tau} \simeq 0.88 \text{ Hz}$. Hence, it is possible to capture a part of the velocity fluctuations with the anemometer selected.

Besides, we note f_c , the cut-off frequency for which the signal amplitude through the anemometer begins to attenuated. We have $f_c = \frac{1}{2\pi\tau} \simeq 2.79 \text{ Hz}$.

Shilknecht proposes two measurement ranges for their anemometer: $0.01\text{-}1 \text{ m/s}$ and $0.015\text{-}5 \text{ m/s}$. The anemometer probes were calibrated by the manufacturer. We did not recalibrate them in the laboratory. The manufacturer provides the following information about the probes accuracy:

- $0.01 - 1 \text{ m/s}$ with an accuracy of $\pm 1\%$ fs. and $\pm 1.5\%$ rdg.
 - $0.015 - 5 \text{ m/s}$ with an accuracy of $\pm 0.5\%$ fs. and $\pm 1.5\%$ rdg.
- (fs. = full-scale ; rdg. = reading value)

The absolute accuracy of the probes are shown in the Figure 3.3. For an anemometer with a measuring range of $0.01 - 1 \text{ m/s}$, the accuracy vary from ± 0.01 to $\pm 0.025 \text{ m/s}$. For

an anemometer with a measuring range of 0.15 - 5 m/s, the accuracy vary from ± 0.027 to ± 0.1 m/s.

However, one should be paid attention with regard to the various factors which can potentially impact the hot-sphere anemometer measurement uncertainty, as presented by Melikov et al. (2007). Their detailed study consists in testing four different type of low-velocity hot-sphere anemometer and analyzing the impact of error sources on the accuracy of the mean air velocity and the turbulence intensity. They identified 11 important error sources affecting the measurement:

1. Natural convection
2. Directional sensitivity
3. Frequency response
4. Calibration reference
5. Conversion and reproducibility
6. Velocity gradient
7. Temperature compensation
8. Temperature gradient
9. Air temperature fluctuations
10. Barometric pressure variations
11. Humidity variations

Afterward, they were able to quantify the absolute expanded accuracy¹ of the measured velocity introduced by the combined effect of all error sources. They defined an equation in which the absolute expanded accuracy of mean air velocity is determined as a function of the mean air velocity. Other equations for the absolute expanded accuracy of the velocity fluctuation and the turbulence intensity are also defined. These equations are given below:

$$\Delta \bar{u}(\bar{u}) = \pm(0.025 + 0.025\bar{u}) \quad (3.3)$$

$$\Delta \sigma_u(\sigma_u) = \pm(0.007 + 0.15\sigma_u) \quad (3.4)$$

$$\Delta TI(TI) = \pm(4 + 0.23TI) \quad (3.5)$$

It is beyond our scope to perform such a detailed study as they did. Therefore, we recalculated the absolute accuracy of our hot-sphere anemometer for mean velocity measurement with their formulas. The expanded absolute accuracy are shown in the Figure 3.3. We should keep in mind that the hot-sphere anemometer actually measures air speed (velocity magnitude) but not real air velocity. Anyway, since "velocity" is a more common term and is widely used (Popiolek et al., 2007), the term "velocity" will be used through-

¹According to the authors, their expanded accuracy was defined at 95% confidence level in accordance with the Guide for the Expression of Uncertainty in Measurement (EN 1995b) accepted by the International Organization for Standardization (ISO).

out this manuscript instead of the more correct term "speed", for the sake of simplicity.

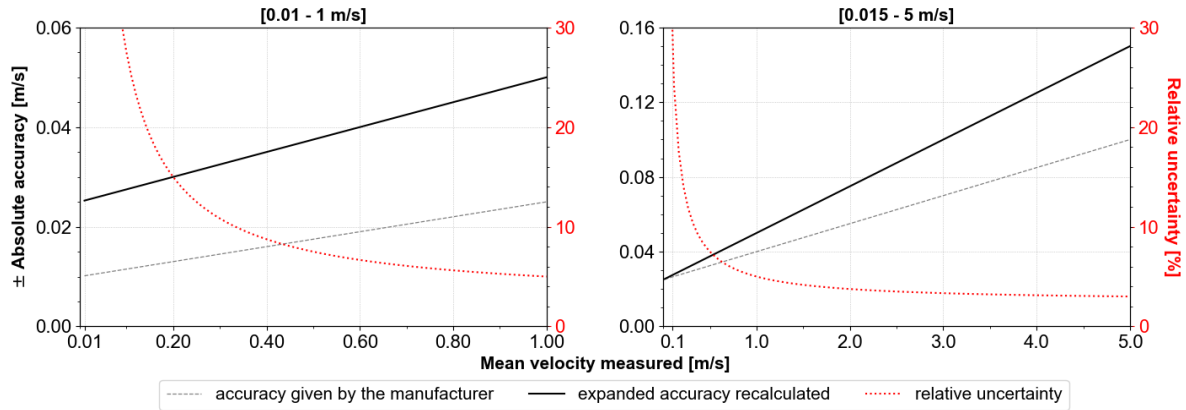


Figure 3.3 – Anemometer absolute accuracy as function of mean velocity measured

For low velocity measurements (i.e. between 0.01 and 1 m/s), the expanded accuracy recalculated is twice higher than the accuracy given by the manufacturer. A mean velocity value of 1 m/s measured has an absolute accuracy of $\pm 0.05 m/s$ instead of $\pm 0.025 m/s$. More surprisingly, a mean velocity measured as low as 0.01 m/s could have an expanded accuracy of $\pm 0.025 m/s$, which is greater than the value itself. As for the hot-sphere anemometer with the measuring range of 0.015 - 5 m/s , their expanded absolute accuracy vary between ± 0.028 and $\pm 0.15 m/s$.

For the present study, we used five anemometers with a range 0.01-1 m/s and five anemometers with a range 0.015-5 m/s . The position of the probes on the mobile robot will be described in the section 3.3.

3.2.2 Indoor air temperature

3.2.2.1 Temperature measurement techniques

The temperature measurement techniques for HVAC and building applications can also be divided into two categories, which are whole-field and point-wise techniques.

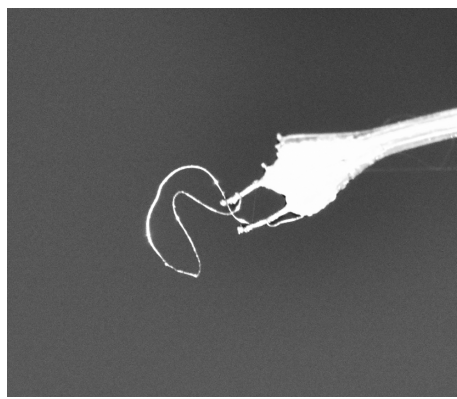
Whole-field air temperature measurement can be achieved by using the infrared thermography (Sandberg, 2007). However, air is transparent to infrared radiation. Thus, a measuring screen needs to be installed within the indoor volume. The infrared (IR) camera actually measures the temperature of the screen that adopts the air temperature. The problem is the measuring screen disturbs significantly the airflow motion. Besides, the IR camera has an absolute accuracy of about $\pm 2 ^\circ C$, which is unacceptable for our study.

As for the air temperature measurement using point-wise technique, two sensor types are commonly used: the RTD Pt100 probe and the thermocouple. Here we used thermocouples in order to get faster dynamic response time.

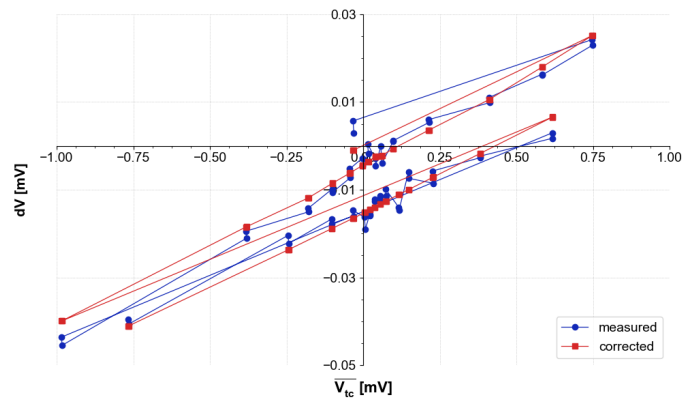
3.2.2.2 Thermocouples for the present study

In our configuration, we can have a temperature gradient up to 8 °C between the air supply temperature and the zone near the simulated outdoor environment. We used 17 K-type thermocouples $\varnothing 25 \mu m$ to scan the temperature field in the test cell. The thermocouples were welded at the CETHIL.

The Figure 3.4(a) presents an image captured of our thermocouples (scale 40:1). Given the very small size of the hot weld, these thermocouples allow a very fast response time. For instance, for the airflow with the air velocity ranging from 0.03 m/s to 2.1 m/s, their response time vary from 8.80 ms down to 6.19 ms. The description of the thermocouple response time determination is given in the appendix C.



(a) Picture at scale 40:1



(b) Calibration curve

Figure 3.4 – K-type thermocouple $\varnothing 25 \mu m$

A precise calibration process is required to guarantee a good accuracy of the thermocouple. The thermocouples were calibrated in-situ at our laboratory. The calibration device consists of a reflux thermostatic bath Lauda RM6T with constant fluid temperature and a reference sensor Pt100 AOIP AN 5847, which is connected to a thermometer AOIP PHP61. More details on the calibration procedure and the uncertainty determination can be found in the appendices A and B. A calibration curve of one of these thermocouples is shown in the Figure 3.4(b) for example. Results issued by the calibration process give an absolute accuracy of approximately ± 0.06 °C (on the mean measured value).

3.2.3 Indoor air humidity

The measurement of the indoor air humidity are performed using SHT75 probes manufactured by Sensirion.

The SHT75 probe, whose dimensions are $L \times W = 5.08 \times 3.1$ mm, is able to measure the air relative humidity and the air temperature. Pictures of the SHT75 probe are given

in the Figure 3.5.

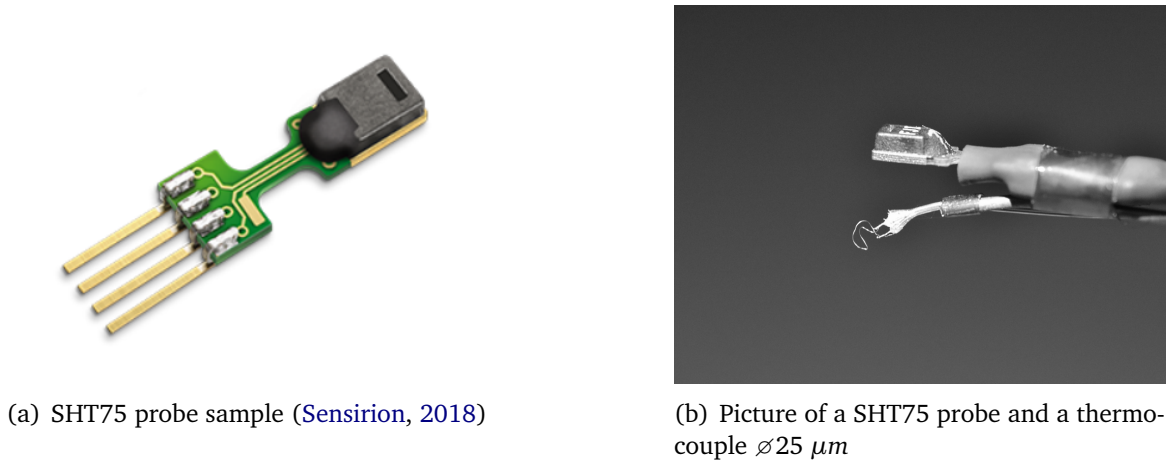


Figure 3.5 – Sensirion SHT75 humidity/temperature probe

The SHT75 probes were calibrated by the manufacturer. We did not recalibrate them in the laboratory. The manufacturer provides the following information about the probes accuracy (c.f. Figure 3.6):

- for the relative humidity: $\pm 1.8\%RH$ within the measurement range of $[10; 90]\%RH$;
- for the temperature: $\pm 0.3\text{ }^{\circ}C$ within the measurement range of $[10; 40]\text{ }^{\circ}C$.

Besides, the SHT75 probes have a relative slow response time of 8 s, according to the manufacturer.

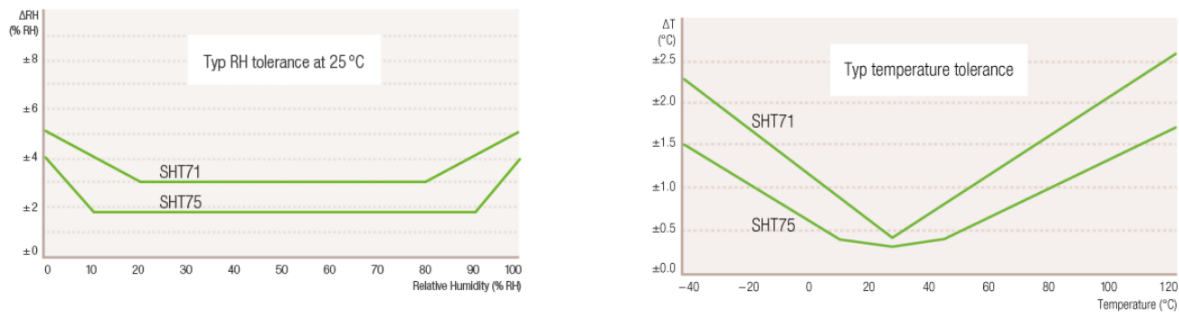


Figure 3.6 – Accuracy limits of the SHT75 probe (Sensirion, 2018)

3.3 MINIBAT mobile robot description

3.3.1 Mobile robot system and sensors

In order to determine indoor air velocity, temperature and humidity fields, we have designed and programmed a mobile robot equipped with the sensors described above. A

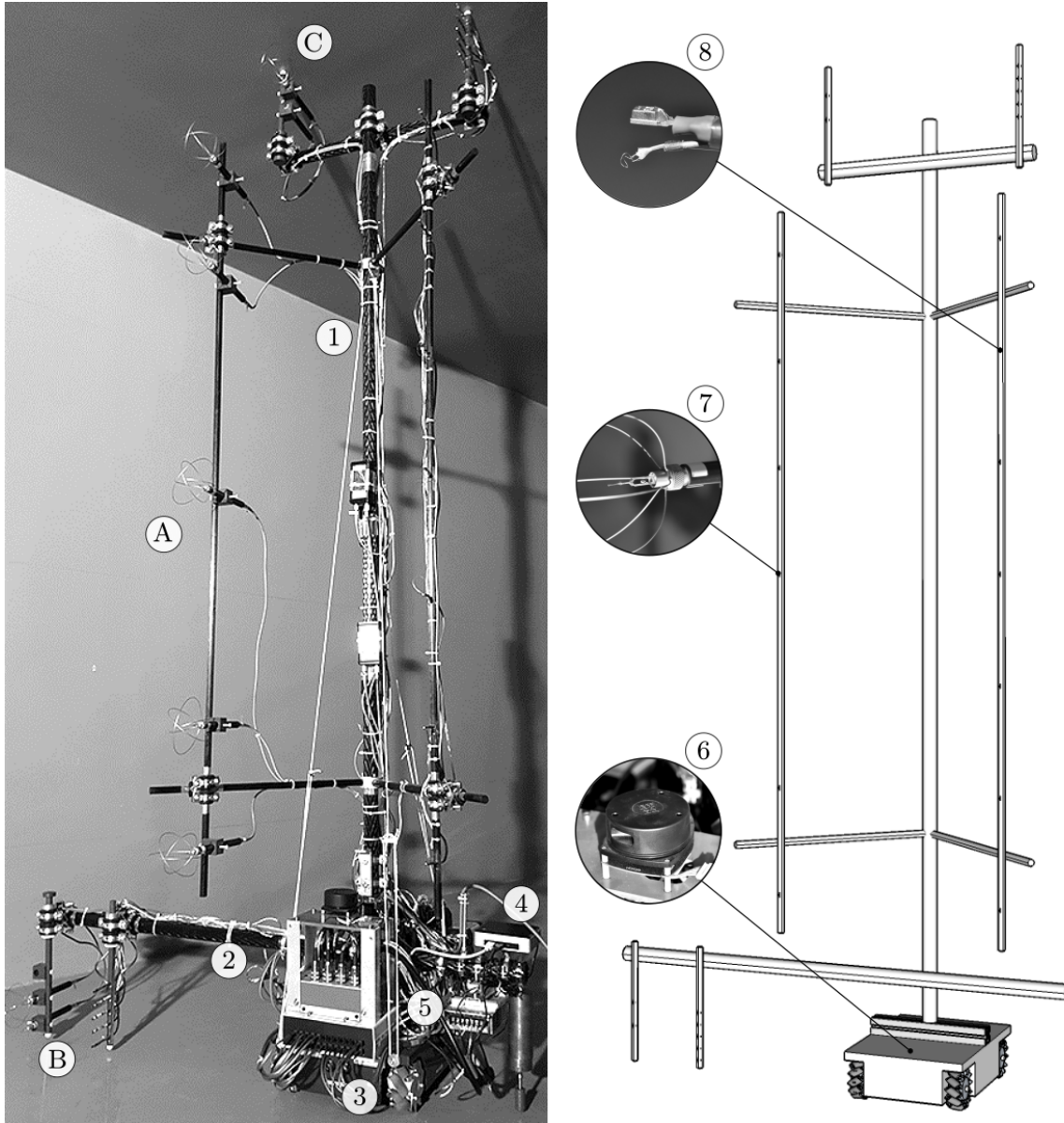


Figure 3.7 – MINIBAT mobile robot scheme

- (1, 2) - main masts; (3) - Mecanum wheel;
 (4) - Mini-PC remote controlled; (5) - data acquisition systems; (6) - LiDAR;
 (7) - hot-sphere anemometer ThermoAir64;
 (8) - K-type thermocouple $\varnothing 25 \mu\text{m}$ and SHT75 probe;
 (A, B, C) - central, near-floor, near-ceiling measurement profiles

picture of the robot is given in the Figure 3.7.

The robot chassis is made of aluminum alloy whose dimensions are $L \times W \times H = 400 \times 300 \times 120 \text{ mm}$. The chassis can support a maximum load of 15 kg . The main masts (1) and (2) are made of carbon fiber. The robot is equipped with 4 Mecanum wheels ($\varnothing 100 \text{ mm}$) (3); each of these wheels has its own geared DC motor and its own rotary encoder. This configuration makes it possible to independently control the movement of

each wheel. The four motors are driven by one ArduinoTM microcontroller board, which is located inside the robot chassis. Different schemes of the robot chassis along with additional information on technical specifications can be found in the Appendix G.

A mini-PC Intel[®] NUC (4) is installed on the horizontal mast. It controls the ArduinoTM board and the various data acquisition systems (5). The mini-PC communicates with a computer located outside of the test cell through Wi-fi communication.

The Figure 3.8 shows the location of temperature sensors (17 thermocouples), humidity sensors (17 SHT 75 sensors) and velocity sensors (10 hot-sphere anemometers). These sensors are implemented along three vertical profiles.

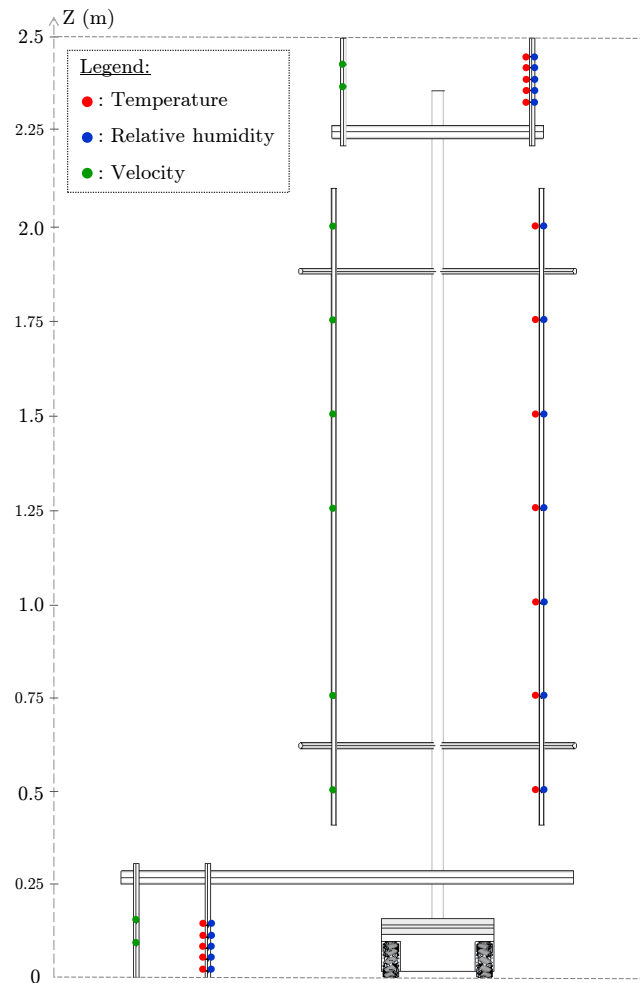


Figure 3.8 – Sensors position on the mobile robot

There are two profiles located near the floor (B) and near the ceiling (C). They have a vertical amplitude of 0.05 m. Each of these profiles contains five temperature and humidity probes, and two anemometers. They capture high gradients, which make it possible to distinguish the different types of boundary conditions at the walls.

The central profile (A) has a vertical amplitude of 1.5 m, which extends from 0.5 m to 2.0 m in height. The main purpose of this profile is to measure airflow characteristics

within this zone. It includes 7 measurements of air temperature and humidity, and 6 measurements of air velocity. It is the data from this profile which will be analyzed in the further sections.

The mobile robot total cost is evaluated approximately 27,000 euros tax-excluded. It took two years to accomplish, from the design stage to assemblage and programming stage. Compared to the mobile arm on rail system used previously by Hohota (2003) and Kuznik (2005), there are two main advantages of using the mobile robot system: (1) air flow disturbances reduction given the limited volume of materials installed inside the test cell; (2) data measurements in any area of interest, avoiding regular measurement meshes as it was happened before. In addition, the total heat gain due to the microcontroller, the mini PC, the LiDAR and data acquisition systems is of order of 10 W, airflow characteristics disturbance due to natural convection is minimal.

3.3.2 Evaluation of measurement positions

The absolute coordinates of a sensors in the MINIBAT system of coordinates are a combination of:

1. The coordinates of the sensors in the Robot system of coordinates;
2. The coordinate of the Robot in the MINIBAT system of coordinates.

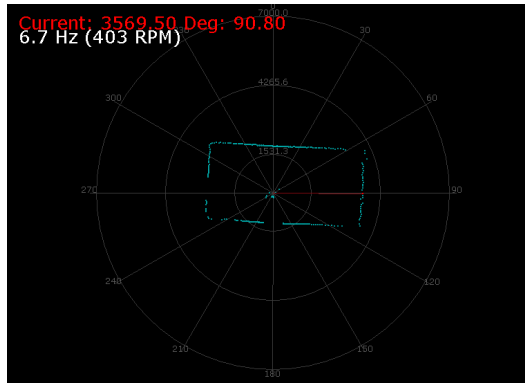
The coordinates of the sensors in the Robot system of coordinates are constant. They were evaluated beforehand. We used a laser level to projected the location of the sensors on a vertical scale (for the Z coordinate) and on a millimeter paper located on the ground (for the X and the Y coordinates).

The center of the robot system of coordinates is located on the rotation axis of the Lidar (Laser Detection And Ranging) system². The Lidar is shown in the Figure 3.7 (6). This system is used to locate the mobile robot within the test cell. Its accuracy is evaluated at ± 2 mm.

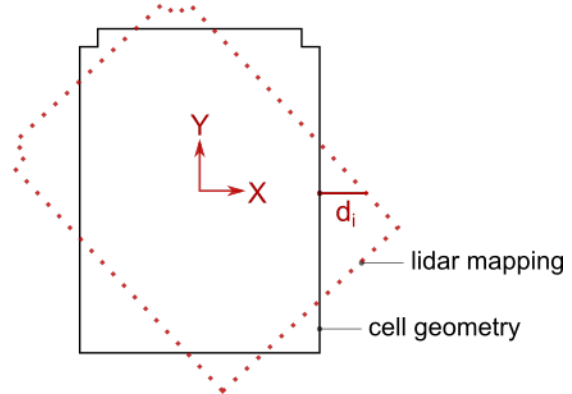
The Figure 3.9(a) shows a screenshot of the Lidar mapping software in MINIBAT. The Lidar functions at a rate of 6.7 Hz and gives instantly the distance to obstacles within 360°. A Scilab script is used to convert data from the robot coordinate to the test cell system of coordinates, whose origin was defined previously (c.f. section 2.2.3.1). The Figure 3.9(b) shows the principle schematic for Lidar data processing. Assuming a function that gives the distance between the series of points and the test cell:

$$f(X, Y, \theta) = \sqrt{\sum d_i^2(X, Y, \theta)} \quad (3.6)$$

²It is a technique using pulsed laser light to measure distance to an obstacle in every direction.



(a) Screenshot of the Lidar software



(b) Data processing

Figure 3.9 – Lidar system for the mobile robot

where (X, Y, θ) represents the Lidar coordinate regarding the test cell coordinate. The process consists in minimizing the function $f(X, Y, \theta)$ with a predefined initial parameters (X_0, Y_0, θ_0) . The Scilab script is given in the Appendix F.

3.3.3 Data acquisition system

The temperature, and velocity signals are recorded through data acquisition cards placed in a National InstrumentsTM NI cRIO-9074³ data acquisition chassis.

The thermocouples are connected to a cold weld junction box. This box consists in a heavily insulated copper cylinder in which the cold weld junctions of the thermocouples are concentrated. The temperature of the cylinder is measured by two high precision Pt100 probes. The cold junction box redirects the voltage signals of the thermocouple toward two NI-9205 data acquisition cards, and the signal of the Pt100 probes toward one NI-9217 data acquisition card. The anemometers are plugged in a box which distribute their electrical power supply, and redirect their signal toward two NI-9203 data acquisition cards. The SHT75 signals are processed in a laboratory-made electrical circuit which then redirects the signal to a Raspberry Pi⁴ control card. The Figure 3.10 presents a scheme of the complete data acquisition network.

The cRIO is connected to the mini-PC, which is remote controlled using Wi-fi data transmission. The mobile robot displacement is piloted using a program executed in the Arduino software. For each robot position, a LabVIEW program is used to collect indoor air measurements via the cRIO controller.

³CompactRIO (or cRIO) is a real-time embedded controller, with re-configurable input/output modules, and a FPGA (Field-Programmable Gate Array) module, which allows implementing high-speed response time control, custom timing and triggering directly in hardware.

⁴Raspberry Pi is a credit-card sized single-board computer

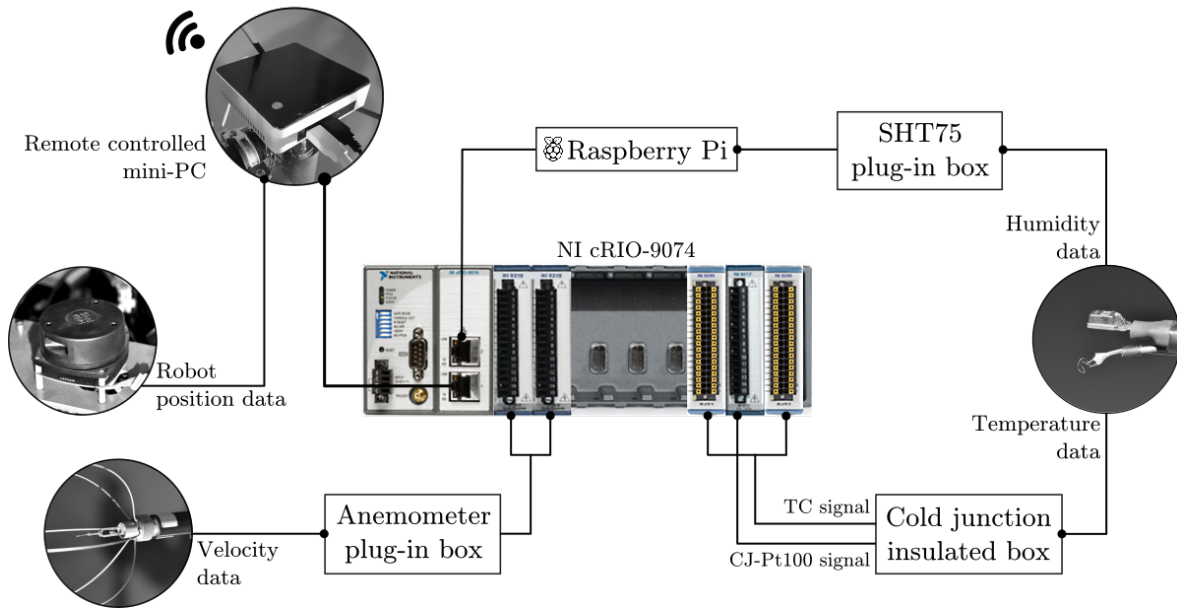


Figure 3.10 – Data acquisition systems schematic

3.4 Experimental protocol

For each measurement campaign, the very first step consists in establishing the steady state within the MINIBAT test cell. During this stage, the set points of the test cell ventilation system, of the thermal buffer zone ventilation system and of the climatic chamber ventilation system are kept constant.

According to the observation we made during various experiments conducted before in MINIBAT, a minimum of three days are required to obtain the steady state. During this stabilization period, the wall surface temperatures and the inlet air velocity, temperature and humidity are recorded every five minutes.

3.4.1 Examining planes

Once the steady state is reached, the mobile robot is used to scan an indoor airflow volume of 12 m^3 ($L \times W \times H = 4 \times 2 \times 1.5 \text{ m}$), divided into 6 horizontal planes (for velocity measurements) and 7 planes (for temperature and humidity measurements). The height of the plane corresponds to the height of the sensors. We distinguish 3 scanning areas in the test cell volume, as shown in the Figure 3.11.

- In the volume defined by a $1 \times 1 \text{ m}^2$ around the diffuser axis, the distance between the measurement points is 0.05 m . This is the air jet region that captures a high gradient in air velocity and temperature;
- In the surrounding volume defined by a $2 \times 2 \text{ m}^2$ around the diffuser axis, the distance between the measurement points is 0.1 m . This area corresponds to the

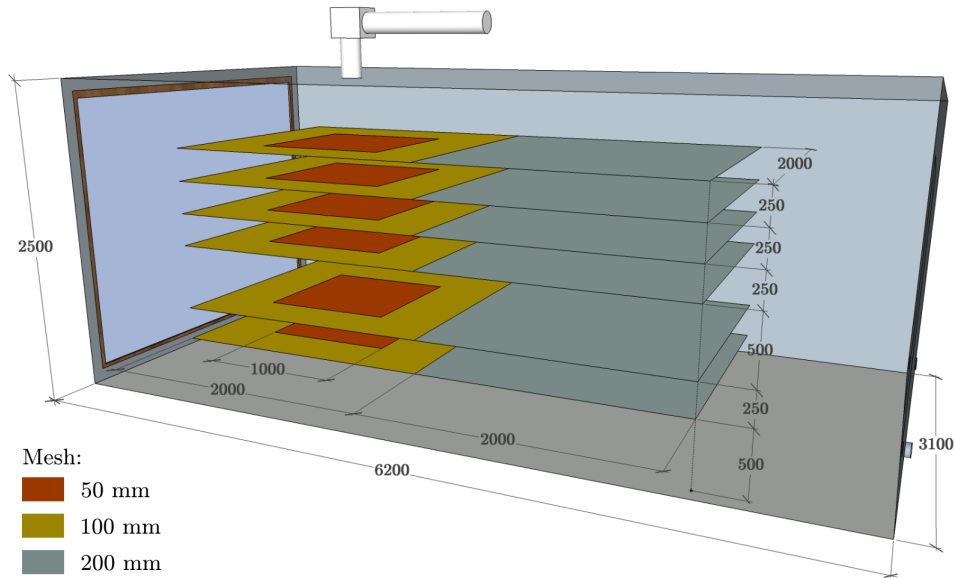


Figure 3.11 – Scanning planes within the test room

area in which the air is well mixed between the air supply and the ambient air;

- The remaining region is a $2 \times 2 \text{ m}$ volume located on the north side. In this region, the distance between the measurement points is 0.2 m . This region is considered as the occupied zone, since it is far enough from the air jet zone. This zone can also be considered as the free-zone according to the flow regimes division, as described in the section 3.2.1.1.

3.4.2 Data acquisition parameters

The indoor instantaneous air velocity and temperature are measured with an acquisition frequency of 10 Hz (100 ms between each measure). Recorded values are then averaged over 2000 samples, i.e. in 200 s , to obtain the mean air velocity and the mean air temperature. The averaging allows to reduce the fluctuation error.

The indoor air relative humidity is measured with an acquisition frequency of 0.5 Hz , averaged over 100 samples (200 s).

The time required between two positions of the mobile robot is about 5 minutes. It includes the time for the robot displacement, the waiting time before starting the data acquisition and the time for data acquisition mentioned above (3 minutes and 20 seconds).

During the experimental campaign, the boundary conditions data were recorded with a reduced time interval of two minutes. It allows us to follow their evolution and to detect an eventual non-steady behaviors. It took about 1 week, steady state establishment included, to accomplish each experimental campaign.

3.5 Summary

- *Two main matters have been detailed in this chapter: the indoor air fields metrology and the experimental protocol.*
- *In order to determine the indoor air velocity, temperature and humidity fields, a mobile robot equipped with various sensors has been designed and programmed. The choice of the hot-sphere anemometer for the indoor air velocity measurement and the thermocouple $\varnothing 25\ \mu\text{m}$ for the air temperature measurement are justified in detail. The absolute accuracy associated with each sensor is also determined.*
- *Finally the experimental protocol for the indoor air jet study is presented, which includes an initial period for steady state establishment and a test period with a well-defined scanning procedure.*

Turbulent vertical axisymmetric free jet - Empirical model

4.1 Introduction

An air jet can be considered as a free jet if his development is not affected and obstructed by any neighboring room architecture elements such as a ceiling, a floor, walls or any other surfaces. This section presents the empirical model for characterizing an axisymmetric free air jet. This empirical model was widely used in the literature for both academic research and practical design (Goodfellow, 2001; Awbi, 2003; ASHRAE, 2017; Rajaratnam, 1976).

The empirical model of an axisymmetric free jet will be presented as follows:

- section 4.2 gives a short description of the different zones within an air jet;
- section 4.3 treats the cases of an idealized isothermal air jet, where the temperature of the supply air is equal to the temperature of the room ambient air;
- section 4.4 treats the cases of a non-isothermal air jet, where the temperature of the supply air is different from that of the room ambient air. In reality, it is frequently the case. Depending upon the outdoor weather scenario, i.e. winter or summer, the supply air jet could be a heated (hot) air jet or a cooled (cold) air jet, accordingly;
- section 4.5 presents a short discussion on the axisymmetric free jet empirical model.
- section 4.6 describes briefly the different characteristics of the turbulent airflow;
- in the concluding section 4.7, the author describes the procedure that will be used to characterize the experimental jet.

4.2 Jet zones decomposition

According to ASHRAE Handbook Fundamentals ASHRAE (2017), the zones decomposition of a full length air jet is based on the flow development and on the maximum velocity decay along the jet axis. As illustrated in the Figure 4.1(a), one could divide a jet into four zones as follows:

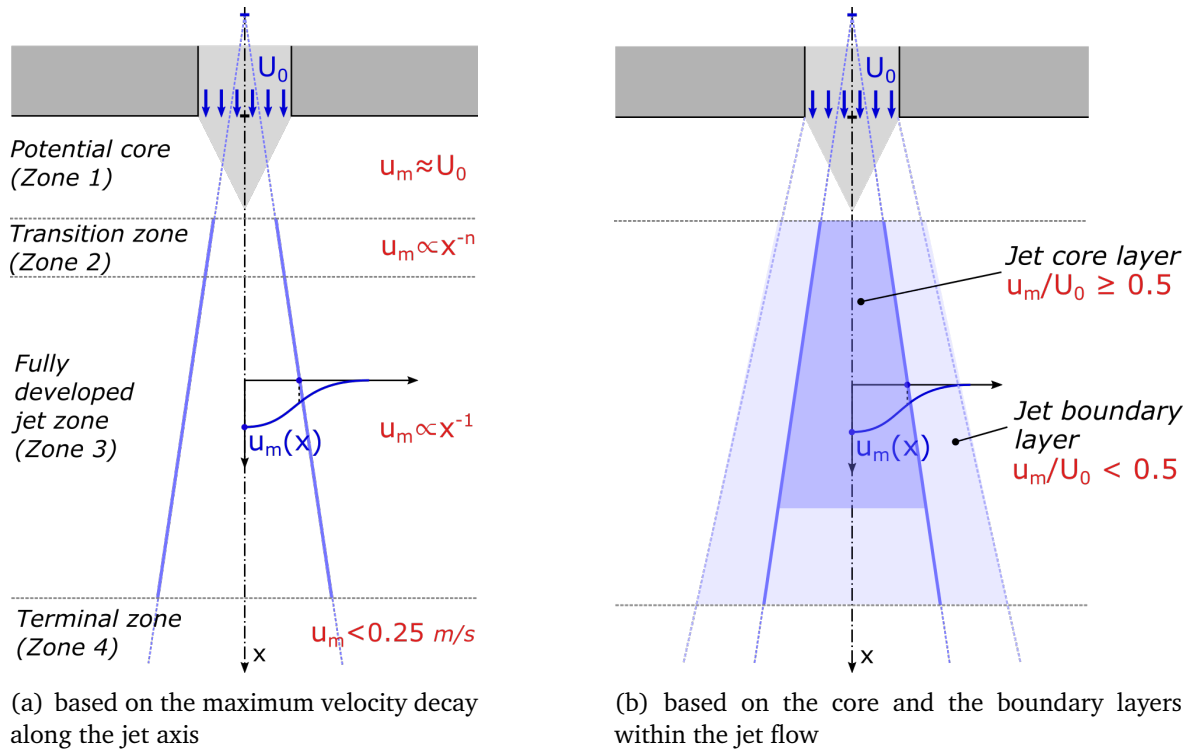


Figure 4.1 – Jet zones decomposition

- Zone 1: the *potential core* is the zone located near the diffuser outlet. In this zone, the centerline velocity u_m remains practically unchanged and is equal to the outlet velocity U_0 ;
- Zone 2: the *transition zone* is the zone where the centerline velocity u_m begins to decrease and is assumed to be proportional to $1/x^n$, where n depends on the outlet characteristics such as its geometry or its aspect ratio. The length of the zone 2 is usually very short. For a circular jet, this zone can be considered as having a negligible length (Awbi, 2003; Kuznik, 2005);
- Zone 3: the zone of *fully developed jet* is the zone where the centerline velocity u_m is often approximated as proportional to $1/x$ and where the jet cross-sectional profiles are found to be similar. In this zone, the heat and mass transfers between the air jet and the room ambient air strongly occur and the airflow has a high turbulence;

- Zone 4: the *terminal zone* is the zone where the residual velocity decreases rapidly into large-scale turbulent eddies. It is often assumed that the beginning of this zone is located where the centerline velocity goes below 0.25 m/s.

The zone 3 is the zone of the fully established turbulent flow. From a technical point of view, zone 3 is the most important area since, in most cases, it is the part of the jet that enters the occupied region. It is the zone which has the most influence on the occupant thermal comfort and the indoor air quality.

According to [ASHRAE \(2009\)](#), an air jet can be decomposed into two layers, which are the core layer and the boundary layer. An illustration is given in the Figure 4.1(b). In this figure, the airflow is divided into two color code:

- the dark blue envelope represents the jet *core layer* (primary air zone) where the air velocity ratio u_m/U_0 is greater than 0.5;
- and the light blue envelope represents the jet *boundary layer* (total air zone) where the ratio u_m/U_0 is greater than 0.5.

[ASHRAE \(2009\)](#) also pointed out that the primary air zone can be treated analytically, whereas the total air zone is "*not subjected to precise analytical treatment*".

4.3 Isothermal axisymmetric free air jet characteristics

A simplified schematic of an axisymmetric free jet development is presented in the Figure 4.2. The different magnitudes used for the characterization are also indicated. The empirical model is based on a jet with an outlet homogeneous velocity equal to U_0 across the outlet mouth surface.

4.3.1 Centerline velocity decay

For an axisymmetric free air jet, the maximum velocity in the cross-section is located on the jet axis. The maximum velocity decay is also the centerline velocity decay.

It is possible to calculate the centerline velocity decay in zone 3 from equations based on the principle of momentum conservation along the jet. The calculation is described in detail in ([Malmström et al., 1997](#)). The centerline velocity decay in zone 3 is given by the following equation:

$$\frac{u_m(x)}{U_0} = K_1 \frac{\sqrt{A_0}}{x + \bar{x}} \quad (4.1)$$

with:

- U_0 : the averaged initial velocity at the diffuser outlet [m/s]
- $u_m(x)$: the centerline velocity at distance x from the diffuser outlet face [m/s]

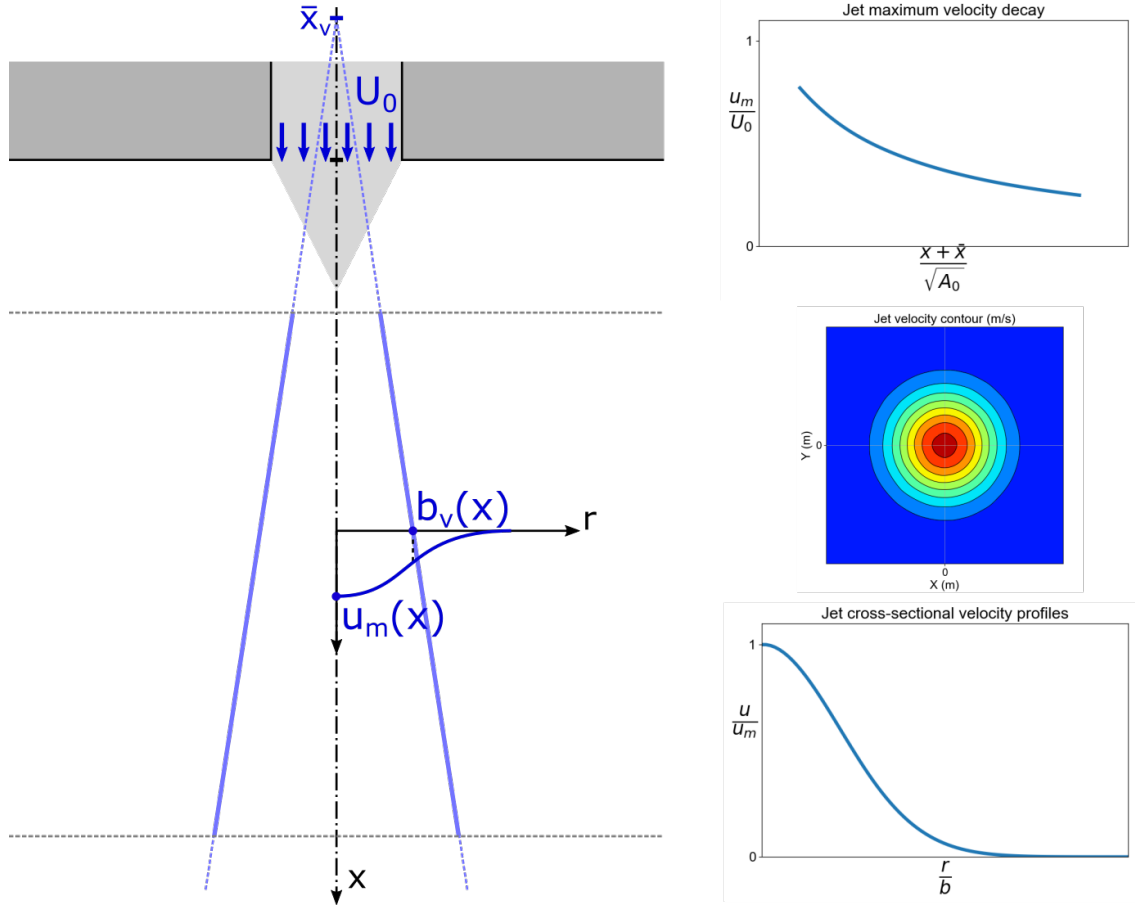


Figure 4.2 – Isothermal axisymmetric free air jet simplified schematic with characteristics graphs

- K_1 : the maximum velocity decay coefficient [-]
- A_0 : the diffuser effective area through which air can pass [m^2]
- \bar{x} : the virtual origin of the air jet [m]

This formula includes two empirical constants: the maximum velocity decay coefficient K_1 and the virtual origin \bar{x} . These two parameters, which are interdependent according to (Zou, 2002), depend mainly upon the type of jets, the type of diffuser outlet, the jet initial velocity and the temperature difference between the air supply and them room ambient air. In other words, K_1 and \bar{x} need to be evaluate experimentally, there is no universal value of these empirical coefficients.

According to Tuve's experimental studies (Tuve, 1953), K_1 varies between 5.7 and 7 for a circular jet depending upon the supply air velocity and the type of outlet. Malmström et al. (1997) suggests that K_1 depends on the jet initial velocity at the diffuser outlet face: it varies between 3 and 6 for $U_0 < 5m/s$ and remains equal to 6 for $U_0 > 5m/s$. Kuznik (2005) defined the K_1 -value as a function of the initial Reynolds number Re_0 : $K_1 = -3.10^{-5}Re_0 + 5.424$. Chassaing (2000) summarizes all the K_1 -value found in the literature

in his book. For an initial velocity between 14 m/s and 230 m/s: $K_1 = 5.91 \pm 0.15$.

For a vertical circular jet, [Li et al. \(1993b\)](#) found $K_1 = 5.7$ for a diffuser effective area $A_0 = 0.4f t^2 \simeq 0.03716m^2$. [ASHRAE \(2013\)](#) advised a K_1 -value of 4.7 for air jets issued from a floor grille diffuser (i.e. vertical ascendant jets). ([Awbi, 2003](#)) divided supply air diffusers into 4 classes. The class 1 comprises diffusers from which the jet is essentially three-dimensional, e.g. nozzles and grilles. He suggested a value of 4.6 for grilles having free area >40% and $U_0 < 5m/s$.

Some researchers ([Rajaratnam, 1976](#); [Goodfellow, 2001](#)) set the virtual origin $\bar{x} = 0$, for practical reason. [Abramovich \(1963\)](#) found that the virtual origin ranges from $0.6d$ to $2.2d$ behind the nozzle, where d is the nozzle diameter. According to Zou's study ([Zou, 2001](#)), for $U_0 < 5m/s$, the virtual origin varies between 0 and 4 times the diffuser outlet diameter.

Besides, in the case of an air outlet equipped with a diffuser, U_0 is actually the averaged air velocity at the diffuser outlet face. In fact, it is difficult to evaluate U_0 in a representative manner. There is no single outlet velocity U_0 in the case of a diffuser, but rather multiple local air velocities within a big interval. Therefore, one traditional and simple way to determine the value of U_0 is by averaging the air velocity over the opening section of the diffuser:

$$U_0 = \frac{Q_0}{A_0} \quad (4.2)$$

with Q_0 is the measured supply airflow rate [m^3/h].

4.3.2 Jet dynamic thickness

According to [Rajaratnam \(1976\)](#), the dynamic thickness¹ of the jet can be obtained using this equation:

$$b_v(x) = K_2(x + \bar{x}) \quad (4.3)$$

with:

- $b_v(x)$: the radial distance from the jet axis to the point where velocity is one-half the centerline velocity: $u(x, r = b_v) = 0.5u_m(x)$ [m]
- K_2 : the jet spread coefficient [-]

K_2 -value depends on the type of diffusers (circular, rectangular opening, etc.) the and initial velocity of the jet. It has been evaluated by various researchers in the literature for a circular jet: $K_2 = 0.097$ according to ([Abramovich, 1963](#)), 0.151 according to ([Tollmien, 1926](#)), and 0.1 according to ([Rajaratnam, 1976](#)).

¹there are several other names for the jet boundary: jet spread, jet growth, jet expansion, etc.

4.3.3 Velocity profiles in the jet cross-section

Rajaratnam (1976), Goodfellow (2001) and Awbi (2003) demonstrated that, in the fully developed jet region, cross-sectional velocity distribution profiles at different heights of the jet were found to have a similar shape. These profiles could be approximated by the following Gauss error-function:

$$\frac{u}{u_m(x)} = \exp\left(-\ln 2 \cdot \left(\frac{r}{b_v(x)}\right)^2\right) \quad (4.4)$$

where u is the jet velocity corresponding to the radial distance r .

4.3.4 Jet throw

Using the and the definition of the jet zones listed above in the section 4.2, it is possible to determine the diffuser jet throw.

The diffuser jet throw L_{throw} is a parameter which is commonly used in air diffuser sizing. It is the distance between the diffuser outlet and the beginning of the terminal zone (where $u_m < 0.25 \text{ m/s}$). From the equation (4.1), the jet throw is expressed as follows:

$$L_{throw} = K_1 \sqrt{A_0} \frac{U_0}{u_t} - \bar{x} \quad (4.5)$$

where u_t is the velocity in the terminal zone, assumed to be 0.25 m/s .

4.4 Non-isothermal axisymmetrical free air jet characteristics

4.4.1 Criteria for vertical non-isothermal air jets

In ventilation for buildings, the temperature of the air jet is often higher or lower than the room ambient air temperature. In these cases, the temperature difference between the supplied air and room air generates buoyancy forces in the jet, affecting the trajectory, the spread as well as the throw of the jet (Chen and Rodi, 1980; Koestel, 1954). The Figure 4.3 presents a scheme of what the airflow behavior from vertical non-isothermal jets should look like in the case of a cold jet and in the case of a hot jet.

Physically, the jet flow behavior is governed by both the buoyancy forces (due to the temperature difference) and the inertia forces (due to the jet momentum). Non-isothermal air jets can be classified as follows (Goodfellow, 2001):

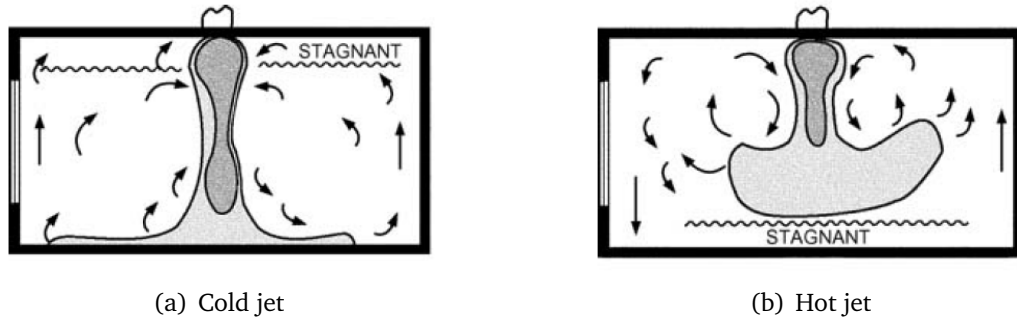


Figure 4.3 – Scheme of vertical non-isothermal jets behavior (extract of (ASHRAE, 2009))

- Buoyant jet: buoyancy forces act in the same direction as the inertia forces. This is the case for a downward cold air jet;
- Negative buoyant jet: buoyancy forces act in the opposite direction with the inertia forces. This is the case for a downward hot air jet;
- Plume: the buoyancy forces completely dominate the inertia forces;
- Non-buoyant jet: the effect of buoyancy is negligible, i.e. an isothermal air jet.

The significance of such effects is conditioned by the ratio of the thermal buoyancy to the inertia force within the air jet. This ratio is referred as the Archimedes number. At the diffuser outlet face level, the Archimedes number can be expressed by the following formula:

$$Ar_0 = \frac{g \sqrt{A_0} (T_0 - T_{amb})}{U_0^2 T_{amb}} \quad (4.6)$$

with:

- g : the gravitational acceleration [m/s^2]
- T_0 : the air temperature at the diffuser face [$^{\circ}C$]
- T_{amb} : the room ambient air temperature [$^{\circ}C$]
- U_0 : the averaged initial velocity at the diffuser outlet [m/s]
- A_0 : the diffuser effective area through which air can pass [m^2]

In this formula, the buoyancy force and the inertia force are represented by the terms g and the terms $U_0^2 / \sqrt{A_0}$, respectively. The Archimedes number is an algebraic number: a negative value corresponds to a cold air jet situation, whereas a positive value corresponds to a hot air jet.

In general, in the region near the supply air diffuser, the inertia forces dominate the flow since the air jet always has an initial momentum. Hence, it behaves like a non-buoyant jet. There follows an intermediate region where the the buoyancy forces begin to dominate the inertia forces. In the final region, the initial momentum is nullified and the

air jet behaves like a plume. The knowledge about the transition between those regions is important for an air jet characterization, in terms of both velocity and temperature.

4.4.1.1 Local Archimedes number

Given a non-isothermal axisymmetric free air jet, Grimitlyn and Pozin (1993) has defined a local Archimedes number, in order to characterize the relationship between the buoyancy forces and the inertia forces in different cross-sections of the jet:

$$Ar_x = Ar_0 \frac{K_T}{K_1^2} \left(\frac{x + \bar{x}}{\sqrt{A_0}} \right)^2 \quad (4.7)$$

with:

- K_T : the jet temperature decay coefficient [-]
- K_1 : the jet velocity decay coefficient [-]
- x : the distance to the diffuser face [m]
- \bar{x} : the virtual origin of the air jet [m]

After intensive experimental investigations, Grimitlyn proposes a threshold value of Archimedes number for which non-isothermal jets can be described by the empirical model:

- $Ar_x \leq 0.25$: the jet velocity and temperature characteristics can be predictable by applying a correction coefficient K_n ;
- $Ar_x > 0.25$: the jet characteristics are unpredictable by empirical model, experimental data should be used instead.

Besides, the air jet can be considered as unaffected by buoyancy forces if Archimedes number ≤ 0.1 .

4.4.1.2 Coefficient of non-isothermality

As mentioned previously, Grimitlyn defined a correction coefficient K_n , named coefficient of non-isothermality. This coefficient can be used to determine the velocity and temperature distributions, as long as the criterion of $Ar_x \leq 0.25$ is satisfied.

For an axisymmetric free jet, the coefficient of non-isothermality K_n is expressed as follows:

$$K_n(x) = \sqrt[3]{1 \pm 2.5Ar_x} = \sqrt[3]{1 \pm 2.5Ar_0 \frac{K_T}{K_1^2} \left(\frac{x + \bar{x}}{\sqrt{A_0}} \right)^2} \quad (4.8)$$

In this equation, the plus-sign corresponds to the situation in which the directions of the buoyancy and the inertia forces coincide, whereas the minus-sign will be used if they

do not. In other words, the plus-sign will be applied for a downward cooled air jet, and the minus-sign for a downward heated air jet.

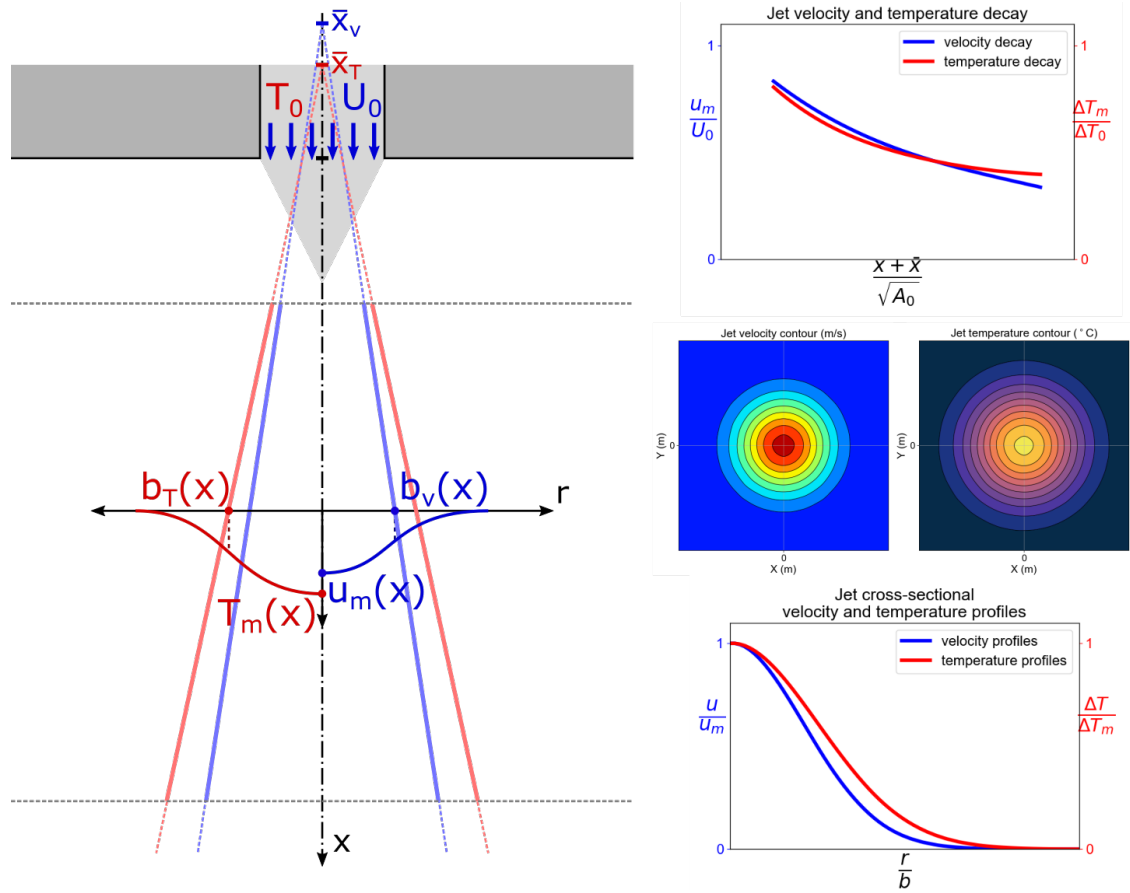


Figure 4.4 – Non-isothermal axisymmetric free air jet simplified schematic with characteristics graphs

4.4.2 Velocity and temperature characteristics in a non-isothermal vertical air jet

A simplified schematic of a non-isothermal vertical axisymmetric free jet is presented in the Figure 4.4. The different magnitudes used for the characterization are indicated. As illustrated in the schematic, along with a constant velocity potential core (Zone 1), there is also a constant temperature core zone in a jet. Considering the more intensive heat diffusion than the momentum diffusion, the core of constant temperatures fades away faster than that of constant velocities; and the temperature profile is subsequently flatter than the velocity profile (Goodfellow, 2001; Awbi, 2003).

Before entering into details about the various equations of the empirical model, it would be appropriate to mention the governed assumptions:

- the non-isothermal air jet is supplied into a room in which the ambient air is still and the air temperature is uniform;
- the buoyancy forces are the only force opposing to the inertia forces (in the case of a heated air jet);
- the shape of the temperature and velocity profiles along the jet cross-section still follow a Gaussian curve.

The following sections only describe the equations which are added or modified when we take into account the buoyancy effects in the jet: the jet centerline velocity and temperature decays, the jet throw. The other characteristics remain unchanged.

4.4.2.1 Centerline velocity and temperature decay

For an axisymmetric free air jet, the maximum velocity and the extremum temperature in the cross-section are all located on the jet centerline axis.

The centerline velocity decay and temperature decay² are determined by the following equations:

$$\frac{u_m}{U_0} = K_1 \frac{\sqrt{A_0}}{x + \bar{x}} \cdot K_n(x) \quad (4.9)$$

$$\frac{\Delta T_m}{\Delta T_0} = K_T \frac{\sqrt{A_0}}{x + \bar{x}} \cdot \frac{1}{K_n(x)} \quad (4.10)$$

with:

- $\frac{\Delta T_m}{\Delta T_0} = \frac{T_m - T_{amb}}{T_0 - T_{amb}}$
- U_0 : the averaged initial velocity at the diffuser face [m/s]
- u_m : the centerline velocity of the jet at distance x from the diffuser face [m/s]
- T_m : the centerline temperature of the jet at distance x [°C]
- T_{amb} : the room ambient air temperature [°C]
- T_0 : the averaged initial temperature at the diffuser face [°C]

The equation (4.10) involves another empirical coefficient, K_T , for characterizing the jet temperature decay. As in the case of the velocity decay coefficient K_1 , values of K_T depend upon the air supply conditions, i.e. the diffuser type, the jet supply velocity and more importantly, the temperature difference between the air supply and the room ambient air.

According to [Shepelev \(1961\)](#); [Grimitlyn and Pozin \(1993\)](#), there is a relation between

²it is actually the excessive temperature decay, but the term "temperature decay" is used for the sake of simplicity ([Li et al., 1993b](#); [Goodfellow, 2001](#))

the K_1 and K_T coefficients. They suggest the following formula:

$$K_T = K_1 \sqrt{\frac{1 + Pr}{2}} \quad (4.11)$$

where Pr is the Prandtl number, which is the ratio between the air momentum diffusivity and the air thermal diffusivity. The Prandtl number actually gives the relative thickness of the momentum and thermal boundary layers. When Pr is small, it means that the heat diffuses more than the momentum, so the thermal boundary layer is thicker than the momentum boundary layer.

Typical values for Pr are around 0.7 - 0.8 for air (Incropera and Dewitt, 2007). A Prandtl number of 0.7 has been suggested, according to many researchers in the literature and as reported by Goodfellow (2001).

4.4.2.2 Velocity and temperature profiles in the jet cross-section

The jet spread coefficient K_2 is supposed to be unaffected by the buoyancy forces ($K_2 = \text{const}$). The equation for the jet dynamic thickness b_v remains unchanged (c.f. equation (4.3)).

It is supposed that the buoyancy forces do not disturb the jet cross-sectional velocity and temperature profiles even if the momentum increases or decreases due to the buoyancy forces. Hence, it would be appropriate to approximate these profiles by the following Gauss error-function:

$$\frac{u}{u_m} = \exp\left(-\ln 2 \cdot \left(\frac{r}{b_v}\right)^2\right) \quad (4.12)$$

$$\frac{\Delta T}{\Delta T_m} = \left(\frac{u}{u_m}\right)^{Pr} \quad (4.13)$$

with: $\frac{\Delta T}{\Delta T_m} = \frac{T - T_{amb}}{T_m - T_{amb}}$.

It turned out that the jet cross-sectional temperature profiles can also be related directly to the velocity profiles by the Prandtl number without passing by the jet thermal thickness b_T .

We can derive the relation between b_T and b_v from the equation (4.13):

$$b_T = b_v \sqrt{\frac{1}{Pr}} \quad (4.14)$$

4.4.2.3 Non-isothermal jet throw

In the case of a downward cold air jet, the jet throw is determined using the equation (4.5) presented in the previous chapter. As for the case of a hot air jet supplied downward,

the buoyancy forces become dominating at this stage and strongly disturb the jet flow development. In fact, due to momentum losses, warm air begin to escape in the radial direction, and rise upward due to the convective transfer. This escaping warm air then rises and causes a change in ambient conditions for the upper part of the jet, like a plume. By taking into account the initial Archimedes number, the maximum throw of a downward-projected hot air jet can be determined as follows (Grimitlyn and Pozin, 1993):

$$L_{throw} = \frac{0.63K_1\sqrt{A_0}}{\sqrt{K_TAr_0}} - \bar{x} \quad (4.15)$$

4.5 Free air jet empirical model: Discussions

The empirical model of an axisymmetric free air jet has been presented in this chapter. The ability of this model to predict the air jet performance was discussed by Chen (2009). The centerline velocity decay coefficient K_1 and the virtual origin \bar{x} are key factors for describing the performance of a free air jet since they are directly proportional to the velocity decay along the jet axis. Hence, the determination of their values has received a great attention in the literature (Li et al., 1993b).

K_1 and \bar{x} are often estimated experimentally based on the linear fitting of the function $U_0/u_m = f(x/\sqrt{A_0})$ (Zou, 2001). The slope of the line gives the coefficient K_1 (or rather $1/K_1$). The intersection of the line and the x-axis gives information on \bar{x} .

On the other hand, K_2 and \bar{x} can be estimated based on the linear fitting of the function $b(x) = K_2(x + \bar{x})$. The slope of the line gives K_2 ; the intersection of the line and the x-axis gives \bar{x} . Nevertheless, this approach was rarely used in the literature.

Since the length of the Zone 3 of the air jet is not well-defined beforehand, decisions about which measured points should be comprised in the fitting line might have a great influence on the estimated values of K_1 , K_2 and \bar{x} . As described previously in the section 3.3, we decided to have 6 measurements of air velocity and 7 measurements of air temperature, humidity in this zone.

Briefly, the free air jet empirical model is a parametric model with three empirical coefficients: the maximum velocity decay K_1 , the jet growth coefficient K_2 and the virtual origin \bar{x} . Since those coefficients vary upon the diffuser outlet type, the jet initial velocity, their values need to be estimated individually by experimental study according to each test configuration (Grimitlyn and Pozin, 1993). No universal values were found in the literature. Hence, it is obvious that there is no fixing reference case, but rather a fitting empirical model that could be adjusted upon the test configuration.

4.6 Turbulent characteristics of the indoor airflow

In mechanically ventilated enclosures supplied by mixing ventilation air jets, the indoor airflow is rarely laminar. The relatively high velocity within the jet region implies a turbulent airflow. The indoor turbulence airflow has a high random feature. Its characterization involves statistical analysis of time-series signals of the air velocity.

The turbulence airflow can be characterized by the following magnitudes:

- the instantaneous velocity u_i , where i represents the direction of velocity component (i.e. x, y, z);
- the mean velocity $\overline{u_i}$;
- the standard deviation of the velocity σ_u ;
- the turbulence intensity TI ;
- and the turbulent kinetic energy k .

The instantaneous velocity u_i can be Reynolds decomposed as follows:

$$u_i = \overline{u_i} + u'_i \quad (4.16)$$

where $\overline{u_i}$ is the mean velocity component and u'_i is the velocity fluctuation component. It should be noticed that u'_i represents the velocity fluctuation in the main flow direction considering the hot-sphere anemometer employed is omnidirectional. The mean velocity is the average of the instantaneous velocity over an interval of time Δt . Its means the averaged value of the velocity fluctuation is statistically supposed to be equal to zero.

The standard deviation of the velocity is the root-mean-square (RMS) of the fluctuating component. It shows the average dispersion of the velocity fluctuation over Δt :

$$\sigma_u = \sqrt{\overline{u_i'^2}} \quad (4.17)$$

The turbulence intensity TI is defined as the standard deviation divided by the mean velocity. The result is usually expressed as percentage:

$$TI(\%) = \frac{\sqrt{\overline{u_i'^2}}}{\overline{u_i}} \cdot 100 \quad (4.18)$$

The turbulent kinetic energy per unit mass can be calculated from:

$$k = \frac{1}{2} \overline{u_i'^2} \quad (4.19)$$

where $\overline{u_i'^2}$ represents the variance of the total energy of the velocity fluctuation.

The energy spectral density function can be defined from the velocity fluctuation by the following relation:

$$\int_0^{\infty} E(f) df = \overline{u_i'^2} \quad (4.20)$$

$E(f)$ provides information about the distribution of the turbulent kinetic energy over a range of frequencies.

The turbulence intensity TI is useful to predict the sensation of draught, which is believed to provoke the local discomfort due to turbulent flow (Fanger et al., 1988; Melikov et al., 2007). Nevertheless, the turbulence intensity is not sufficient to characterize the turbulent flow. According to Hanzawa et al. (1987), we can find turbulent flows with the same mean velocity and turbulence intensity but having different frequencies in terms of the velocity fluctuation. In addition, Zhou and Melikov (2002) has pointed out that the main responsible factor for occupants' draught sensation are velocity fluctuations having frequencies between 0.2 and 0.6 Hz.

Hence, the present study will address in particular the energy spectra and the turbulent kinetic energy of the turbulent airflow.

4.7 Summary: Criteria for characterizing an interacting air jet

The existing empirical coefficients can be served as criteria for describing and quantifying the characteristics of the interacting air jet. K_1 coefficient describes the centerline velocity decay, which is also the maximum velocity decay for an axisymmetric free jet. But this is not necessarily the case for an interacting and deviated jet. Hence, to avoid such confusion, the coefficient K_2 appears to be a more relevant criterion for characterizing such air jets.

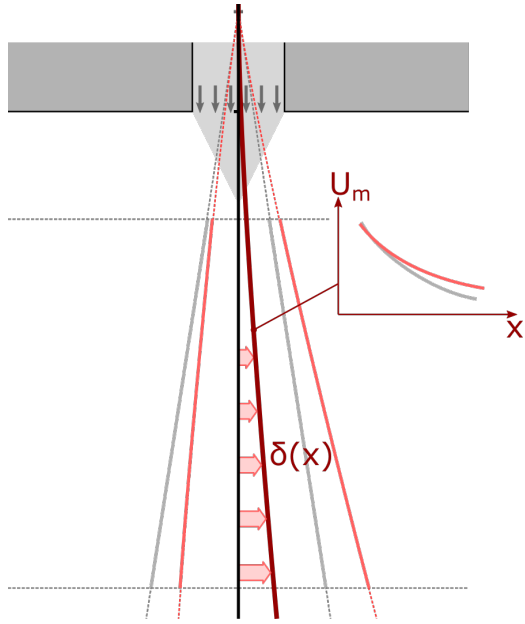
On the other hand, for the virtual origin \bar{x} , its location is affected by the air jet initials conditions. If the air jet flow is disturbed at the diffuser outlet (i.e. by the presence of grilles, etc.), it will cause an increased room air entrainment with the air jet. This influence can be described as an upstream shift of the virtual origin distance, which make the apparent source of the air jet can be located behind the diffuser outlet face (Malmström and Zou, 2000). For practical reason, some researchers neglect this distance, since the length of the fully developed jet zone is usually preponderant with regard to the length of the virtual origin (Rajaratnam, 1976). But in our present study, since the length of the jet is limited by the height of the test cell (2.5 m), taking into account the virtual origin will potentially allow a correction of the jet development.

Under local interaction effects and non-isothermal effects within a realistic configu-

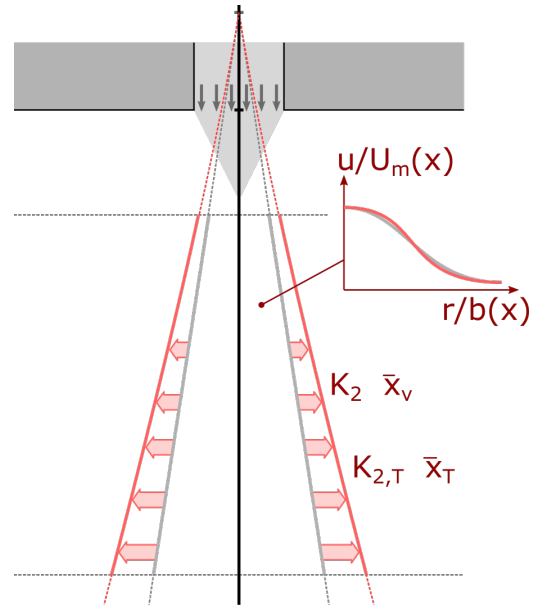
ration, a trajectory deviation of the experimental jet is expected. The shape of the jet is expected to be asymmetrical and deformed. Hence, to characterize such an air jet, the data analysis should be able to respond to the following questions. An illustration schematic is given in the Figure 4.5.

- (1) The *deviation of the jet trajectory* from the diffuser axis? The *maximum velocity and temperature decays*?
- (2) The *distribution of velocity and temperature cross-sectional profiles*? The *spread rate of the dynamic and thermal layers* in the jet?
- (3) The characterization of the *shape deformation* of those cross-sectional profiles?
- (4) The *turbulent flow characteristics*? (energy spectral distribution, turbulent kinetic energy)

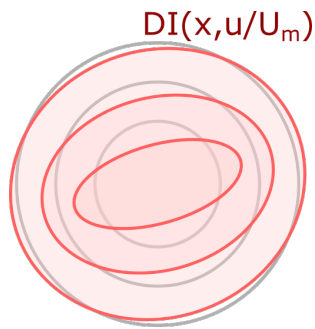
One can notice in the Figure 4.5(b) the presence of two new coefficients $K_{2,T}$ and \bar{x}_T . In the case of an interacting jet, the velocity and temperature profiles do not necessarily correlated to each other. Hence, $K_{2,T}$ and \bar{x}_T are introduced to characterize the spread rate and the virtual origin of jet thermal layer.



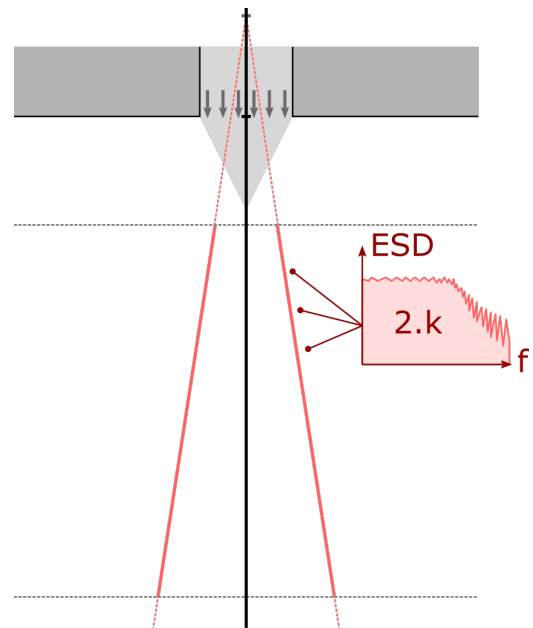
(a) Jet trajectory deviation



(b) Jet dynamic and thermal spread



(c) Cross-sectional profiles deformation



(d) Turbulent flow characteristics

Figure 4.5 – Criteria for characterizing an interacting asymmetric jet

Interacting air jet - Experimental results and analysis

5.1 Introduction

The experimental results of the interacting asymmetric jets are shown and analyzed in the following order:

- section 5.2 describes the different test cases which have been investigated. For each test case, we present the set points applied to MINIBAT, and we expose the measured values of the test cell boundary conditions;
- section 5.3 presents the indoor velocity and temperature fields;
- in section 5.4, the air jet characteristics are computed from the measurement results;
- section 5.5 analyses the turbulence characteristics of the air jet.

5.2 Test cases description

In the present chapter, we present and analyze the results of one measurement campaign which consists in three test cases: one isothermal jet, one cold jet and one hot jet.

This is the final measurement campaign of the thesis. It was preceded by preliminary measurement campaigns whose measurement results were used to adjust the density of the field measurement mesh, to fit the regulation parameters, and to define the way to analyze the experimental data.

For all the test cases of the present measurement campaign, the supply airflow rate of the ventilation system is $120 \text{ m}^3/\text{h}$. The three test cases are named "iso_120" for the

isothermal jet, "cold_120" for the cold jet, and "hot_120" for the hot jet.

Configuration	Symbol	Set points			
		$Q_{0,sp}$ [m^3/h]	$T_{0,sp}$ [$^{\circ}C$]	$T_{cc,sp}$ [$^{\circ}C$]	$T_{tbz,sp}$ [$^{\circ}C$]
Isothermal jet	iso_120	120	20	20	20
Cold jet	cold_120	120	16	22	22
Hot jet	hot_120	120	30	16	20

Table 5.1 – Set points for the three test cases

Where: $Q_{0,sp}$ - airflow rate set point; $T_{0,sp}$ - supply air temperature set point;
 $T_{cc,sp}$ - climatic chamber temperature set point;
 $T_{tbz,sp}$ - thermal buffer zone temperature set point

The set points for those three test cases are summarized in the Table 5.1. For the "iso_120" test case, the ventilation, thermal buffer zone and climatic chamber temperature set points are all equal to 20 °C. For the "cold_120" test case, the MINIBAT configuration corresponds to a summer climate configuration: the temperature set point in the climatic chamber is 22 °C, the temperature set point of the ventilation is 16 °C, and the temperature set point of the thermal buffer zone is 22 °C. For the "hot_120" test case, the MINIBAT configuration corresponds to a winter climate configuration: the temperature set point in the climatic chamber is 16 °C, the temperature set point of the ventilation is 30 °C, and the temperature set point of the thermal buffer zone is 20 °C.

The measured boundary conditions for each test case are summarized in the Table 5.2 and 5.3. In those tables, the standard deviation quantifies the fluctuations of the measured values over the time during the steady state regime. Let Y be a measured quantity, the standard deviation s^Y is given by the equation:

$$s^Y = \sqrt{\frac{\sum_{i=1}^{N_Y} (Y_i - \bar{Y})^2}{N_Y - 1}} \quad (5.1)$$

where Y_i are the measured values, \bar{Y} is the mean value and N_Y is the number of measurement samples.

For the "iso_120" test case, the walls mean temperatures are close to each other. It would be appropriate to consider an isothermal condition. However, the standard deviation of the temperature is high (an order of 0.20 °C). This is probably due to the high temperature fluctuations of the outdoor environment during the days the experimental campaign took place. In the contrast, the "cold_120" and "hot_120" test cases show lower temperature standard deviations. The temperatures of the walls are quite stabilized over the time.

The air temperatures in the thermal buffer zone and in the climatic chamber do not differ

Category - Name		Symbol	iso_120		cold_120		hot_120	
			Mean	SDEV	Mean	SDEV	Mean	SDEV
Wall temperature	Ceiling	$T_{SI,C}$	20.81	0.18	20.97	0.09	23.18	0.04
	Floor	$T_{SI,F}$	21.02	0.15	20.86	0.10	20.86	0.05
	South	$T_{SI,GL}$	20.99	0.12	21.25	0.06	20.46	0.03
	North	$T_{SI,F}$	20.73	0.21	21.56	0.09	22.89	0.05
	East	$T_{SI,EW}$	20.59	0.20	20.80	0.08	22.66	0.05
	West	$T_{SI,WW}$	20.62	0.20	20.78	0.09	22.75	0.05
Air temperature	Ambient air	T_{amb}	20.35	0.08	19.74	0.06	23.25	0.06
	CC	T_{cc}	20.45	0.28	21.21	0.16	16.38	0.11
	TBZ	T_{tbz}	19.86	0.30	20.86	0.11	20.81	0.07

Table 5.2 – Measured boundary conditions within the MINIBAT test cell

Where: Mean - mean temperature; SDEV - standard deviation;
CC - climatic chamber; TBZ - thermal buffer zone

much from the temperature set points. The temperature standard deviation is higher in the climatic chamber. This is due to the regulation of the climatic chamber air handling unit.

Parameters	Symbol	iso_120		cold_120		hot_120	
		Mean	SDEV	Mean	SDEV	Mean	SDEV
Airflow rate	$Q_0 [m^3/h]$	119.99	0.72	119.99	0.97	119.98	1.37
Air velocity	$U_0 [m/s]$	2.18	-	2.18	-	2.18	-
Air temperature	$T_0 [^{\circ}C]$	19.97	0.07	16.00	0.04	30.00	0.08
Reynolds number	$Re_0 [-]$	17268	-	17268	-	17268	-
Archimedes number	$Ar_0 [-]$	0	-	-0.0033	-	0.0058	-

Table 5.3 – Air supply characteristics

The table 5.3 provides values for the air supply characteristics. The Archimedes number is calculated using the equation (4.6). The Reynolds number is computed using the following equation:

$$Re_0 = \frac{U_0 \sqrt{A_0}}{\nu} \quad (5.2)$$

where ν is the kinematic viscosity of the air supply [m^2/s].

The measured airflow rate is close to the set point. The control is correct; a standard deviation of about $1 \text{ m}^3/\text{h}$ is observed (0.83% with regard to the mean value). The air velocity at the diffuser outlet is calculated using the equation (4.2), there is no standard deviation associated. The mean air temperature is regulated accurately with respect to the set point; the standard deviation is low (about $0.06 \text{ }^\circ\text{C}$).

The graphs representing the evolution of the measured boundary conditions for the three test cases are given in the Appendix E.

5.3 Indoor velocity and temperature fields

In this section, we present the measured mean velocity and mean temperature fields. We remind that the mean values are the values which were averaged over 200 seconds of measurement.

5.3.1 Data processing

The first step consists in interpolating the experimental data obtained on each horizontal measurement plane. This interpolation process allows to visualize the data contour map. It also allows to determine the location and the value of the maximum velocity and temperature points ($u_m, \Delta T_m$) (c.f. section 5.4.1.1).

The interpolation was performed using Python language. We use the function *interpolate.griddata* from the library *Scipy*. The associated interpolation scheme is the Clough-Tocher scheme (Alfeld, 1984). It is a second order, two dimensional interpolation method. It uses 2D Bezier polynomials as interpolation functions. The resulting interpolant is piecewise cubic and continuously differentiable.

The interpolations were first performed on the horizontal measurement planes (Figure 5.1(a) for the velocity and Figure 5.1(b) for the temperature). The interpolated domains formed $0.8 \times 0.8 \text{ m}$ squares around the jet centerline. The interpolated values were computed on a $2 \times 2 \text{ mm}$ regular squared mesh (c.f. Table 5.4). The Figure 5.1(c) illustrates a horizontal plane view from the top. It includes the location of the plenum box and the grille diffuser. The coordinates $(X, Y) = (0; 0)$ corresponds to the diffuser axis.

Then, interpolations were performed over two cross-section vertical planes (c.f. Figure 5.1(d)). Interpolated values were computed on a rectangular mesh with a 2 mm size in the X, Y directions and a 125 mm size in the Z-direction.

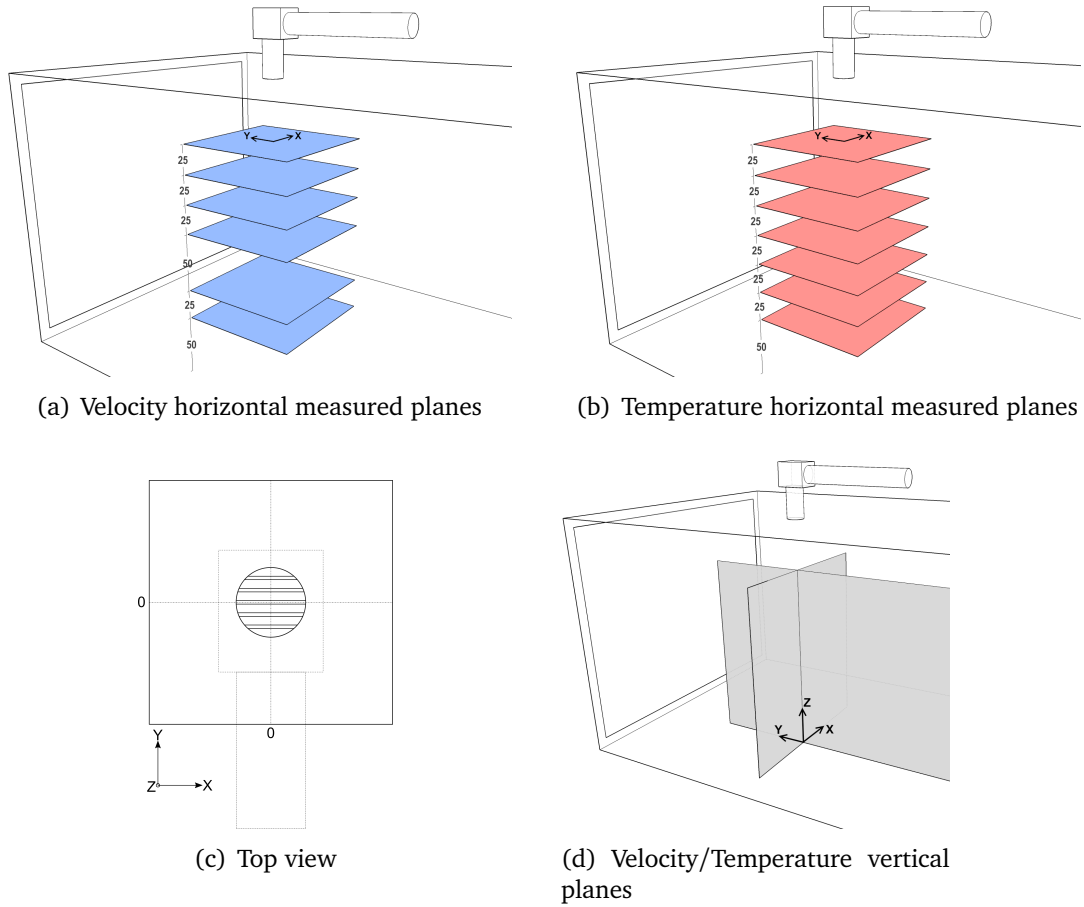


Figure 5.1 – Schematic of the various section-planes plotted

	X	Y	Z
Interpolation plane size [m]	[-0.8 ; 0.8]	[-0.8 ; 0.8]	[0.1 ; 2.0]
Interpolation step [m]	0.002	0.002	0.125

Table 5.4 – Grid size and interpolation step

5.3.2 Velocity fields

In the following mean velocity contour maps, the air velocities below 0.2 m/s are not plotted. This threshold value was chosen based on recommendations found in the literature (Hurnik et al., 2015; Nastase and Meslem, 2010). The authors stated that such small velocities did not take part of the dynamic of the jet. Moreover, our hot-sphere anemometers have a relative high uncertainty at the low velocity range. A value measured lower than 0.15 m/s (uncertainty included) can be treated as not reliable (c.f. Figure 3.3).

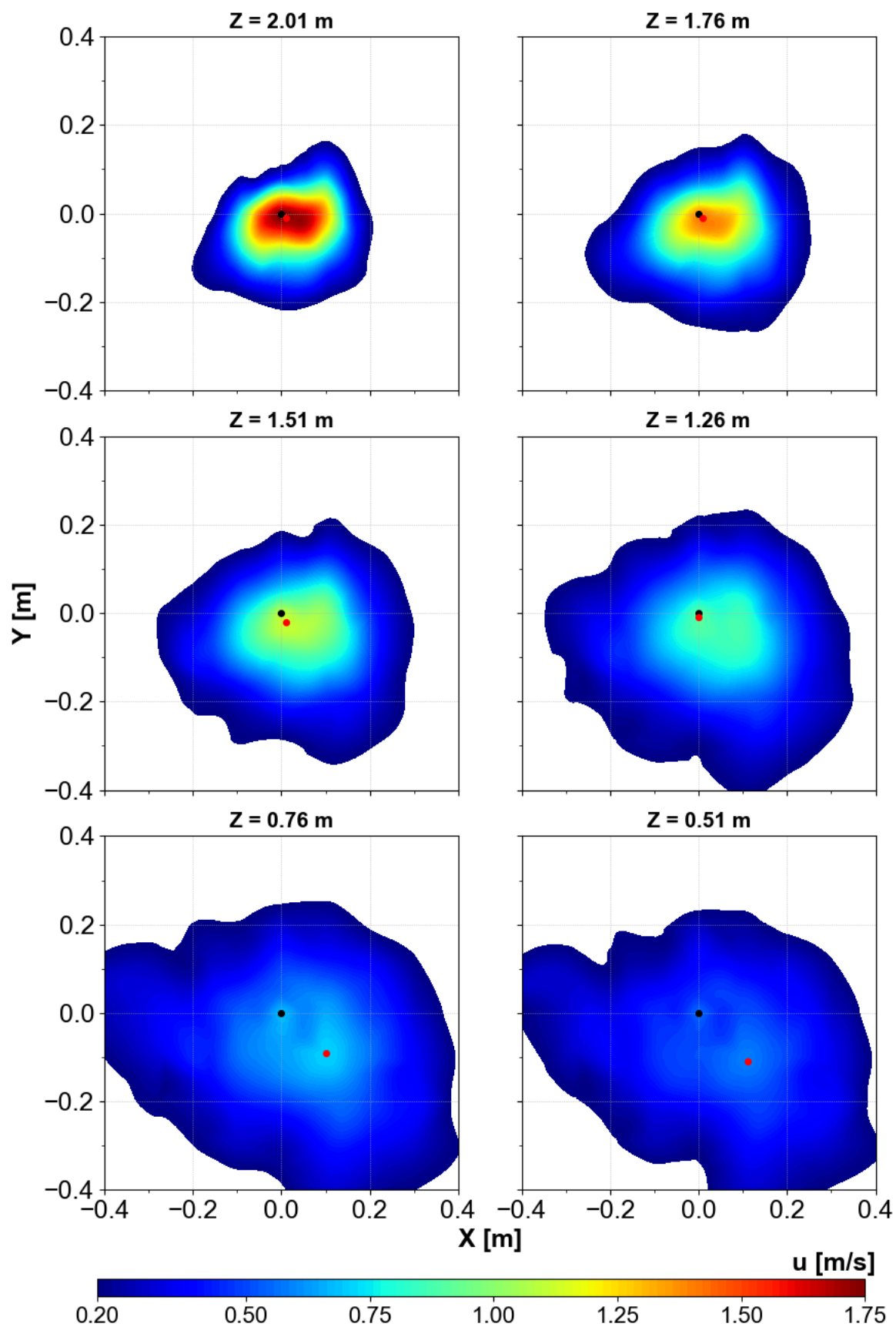


Figure 5.2 – iso_120 - Jet mean velocity contours over the horizontal planes
Black dot: diffuser center ; Red dot: maximum velocity location

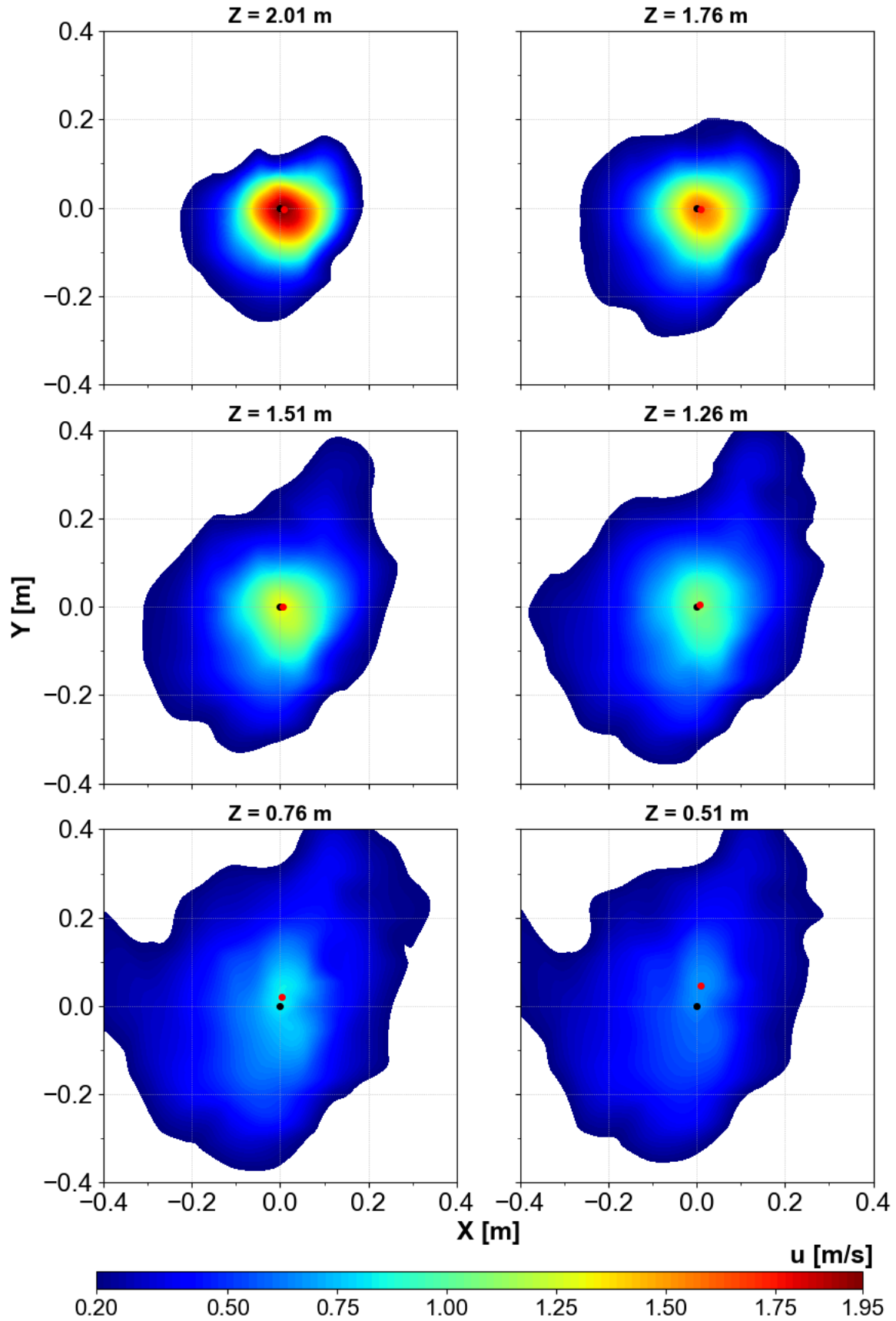


Figure 5.3 – cold_120 - Mean velocity contours map over the horizontal planes

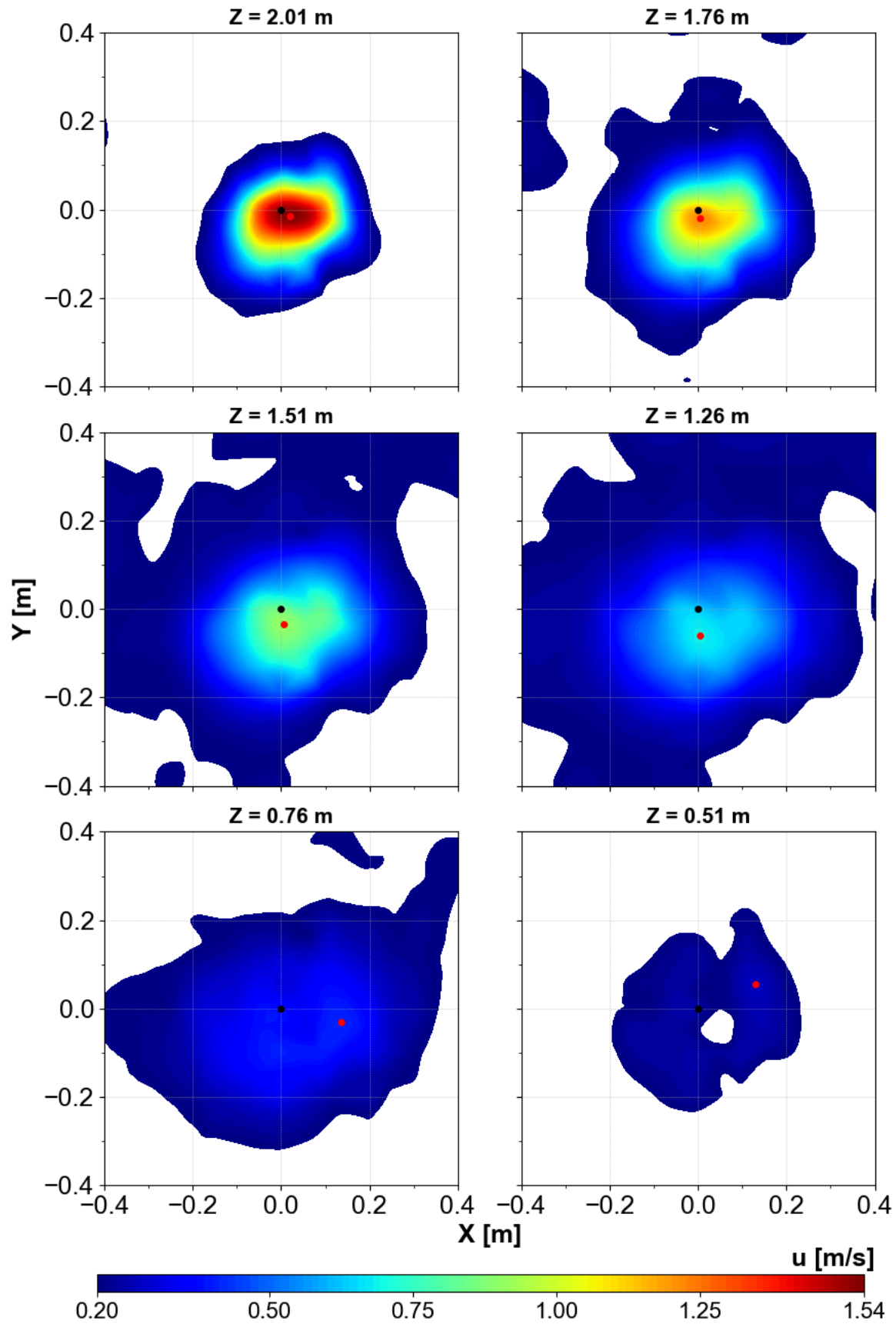


Figure 5.4 – hot_120 - Mean velocity contours map over the horizontal planes

5.3.2.1 Description of the velocity fields over the horizontal planes

The Figures 5.2, 5.3 and 5.4 present the contours maps of mean velocity fields over the horizontal planes (c.f. Figure 5.1(a)). The center of the diffuser is marked by a black dot. The maximum velocity value of each plane is marked by a red dot.

In general, we can notice that the jet flow is developed asymmetrically. As described previously, the jet dynamic core layer is characterized by a mean velocity value over 0.75 m/s . For the isothermal and the hot jet, the core layer has an oval form. This might be explained by the direction of the grille fins, as shown in the Figure 5.1(c). However, in the cold jet case, the direction of the grille fins seems to have much less impact on the velocity core distribution. The velocity contours remain quasi-circular.

The jet dynamic boundary layer can be characterized by a mean velocity value between 0.2 and 0.75 m/s . The shape of the jet boundary layer seems to be deformed by the room geometry, especially by the aspiration of exhausts mouths and by the glazing (temperature gradient between the glazing and the air jet). The diffuser geometry seems to have much less impacts on the jet boundary layer than on the jet core layer. For the hot jet, the jet boundary layer cannot be well defined¹, since the recirculated airflow are also captured by the anemometers.

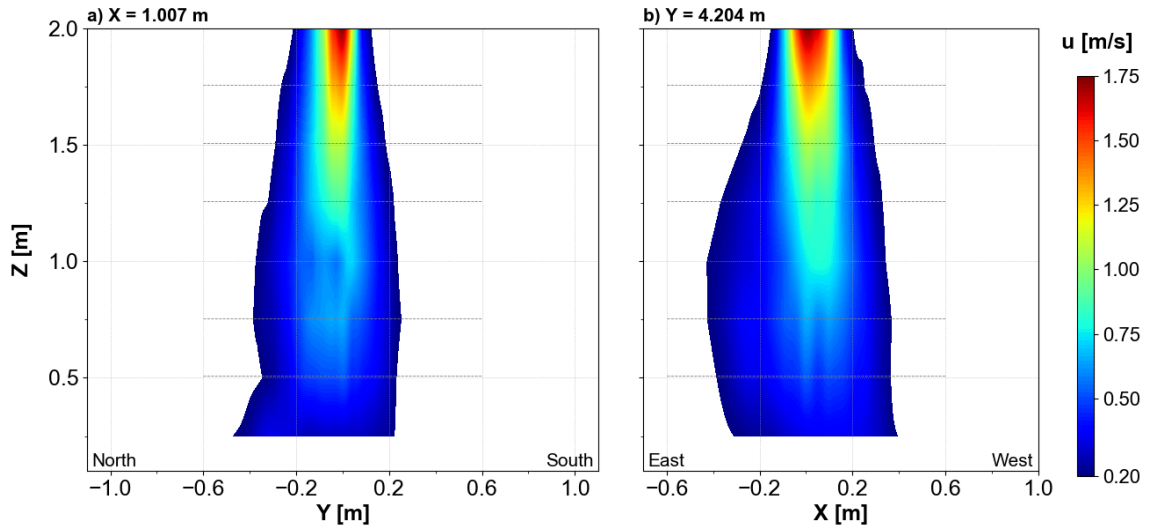
For the first four planes, the maximum velocity locations are not deviated much from the diffuser axis comparing to the downstream region. Considering the hot jet case, the mean velocity values have decreased to the range of $0.2\text{...}0.3\text{ m/s}$ at the downstream region. In this region, the amplitude of the velocity distribution is small and the velocity measurement uncertainty is not negligible. Hence, the computed maximum velocity value is not reliable at this level.

5.3.2.2 Description of the velocity fields over the vertical planes

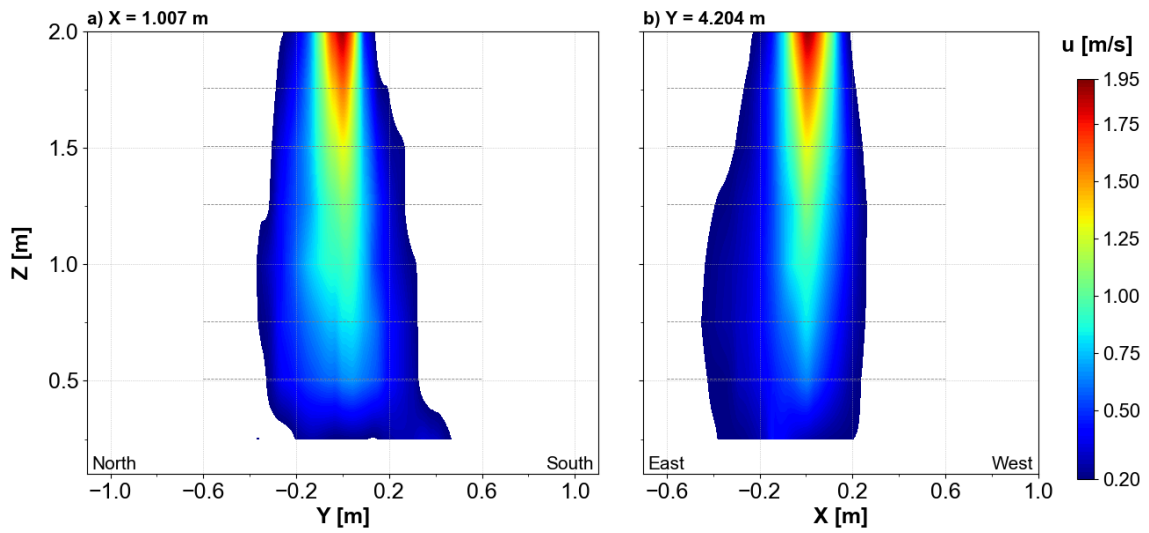
The Figure 5.5 presents the contours map of mean velocity fields over the vertical planes. The low threshold value is fixed at 0.2 m/s . The four directions NSEW are given in the figure for a better comprehension. The six measurement planes are indicated by horizontal dashed lines.

The jet boundary layer tends to spread in the direction of the nearest side wall (East wall), after entering the room for a distance of about 0.8 m from the diffuser ($Z = 1.7\text{ m}$). This tendency is observed for all test cases (figures on the right). This behavior could be explained by a pressure difference across the jet caused by the near side wall. In fact, as the air jet develops, the turbulent mixing layer entrains room

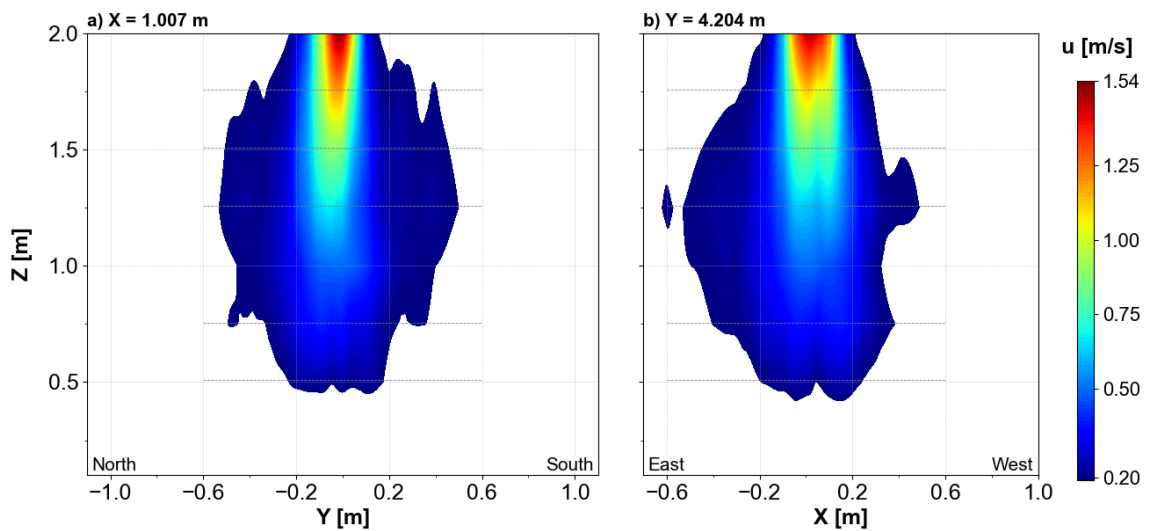
¹the plot was also based on the lower threshold velocity value of 0.20 m/s to guarantee the uniform scale within the three test cases



(a) iso_120



(b) cold_120



(c) hot_120

Figure 5.5 – Jet mean velocity contours over the vertical planes

air from both sides of the jet. A lower static pressure due to the disturbance of the near side wall, creates a deflection of the air flow toward the wall. This phenomenon is a kind of the Coanda effect. It can be observed typically in ceiling horizontal wall jets² (Awbi, 2003; Zou, 2002; Kuznik, 2005).

Awbi (2003) defined a critical distance D_c between the diffuser outlet and the near wall, below which the attachment of the air jet will occurs. For an axisymmetric free jet, D_c was found to equal to $6\sqrt{A_0}$. In our case, $D_c = 0.74\text{ m}$ while the diffuser center is located 1.007 m from the East wall. Hence, the jet flow develops without reaching the wall surface.

For the isothermal jet, the dynamic core layer reaches $Z = 1.2\text{ m}$ (1.3 m far from the outlet). For the cold jet, the direction of the buoyancy forces and the inertia forces coincide and thus they help the velocity core reaching $Z = 0.8\text{ m}$ (1.7 m far from the outlet). For the hot jet, the buoyancy forces act in the opposite direction of the jet inertia forces. The velocity core cannot reach farther than $Z = 1.5\text{ m}$ (1.0 m far from the outlet).

Besides, for the hot jet case, we notice that the jet has a wide spread between $Z = 0.8$ and $Z = 1.7\text{ m}$. This behavior is due probably to the recirculated airflow. Under the effect of the buoyancy forces, the latter acts in the uprising direction (c.f. Figure 5.5(c)). The jet flow on the East side seems to be influenced by both the Coanda effect and the uprising recirculated flow.

As stated earlier in the metrology section 3.2.1.4, the hot-sphere anemometers are omnidirectional; they are able to measure the velocity magnitude but not the velocity direction. It is therefore not possible, in this case, to distinguish the impact of each effect on the jet flow development. From what have been shown in the literature, the real flow pattern of a downward-projected hot jet is very much like an inverted-mushroom (Chen and Rodi, 1980).

5.3.3 Temperature fields

The mean air temperature fields are plotted in this section. Here we plot the contour maps of the temperature difference between the jet and the room ambient air temperature, i.e. $\Delta T = T - T_{amb}$.

The Figures 5.6 and 5.7 present the temperature difference contour maps over the seven horizontal planes (c.f. Figure 5.1(b)). The Figure 5.8 presents the temperature difference contours map over the vertical planes (c.f. Figure 5.1(d)). The room ambient air temperature T_{amb} for the cold and the hot jet are respectively 19.74°C and 23.25°C .

A narrow development of the air temperature in the jet core can be observed for

²The Coanda effect is an useful practice in mixing ventilation for which the the high-velocity region in a wall jet is restricted to the ceiling thus freeing the occupied zone from discomfort due to draft.

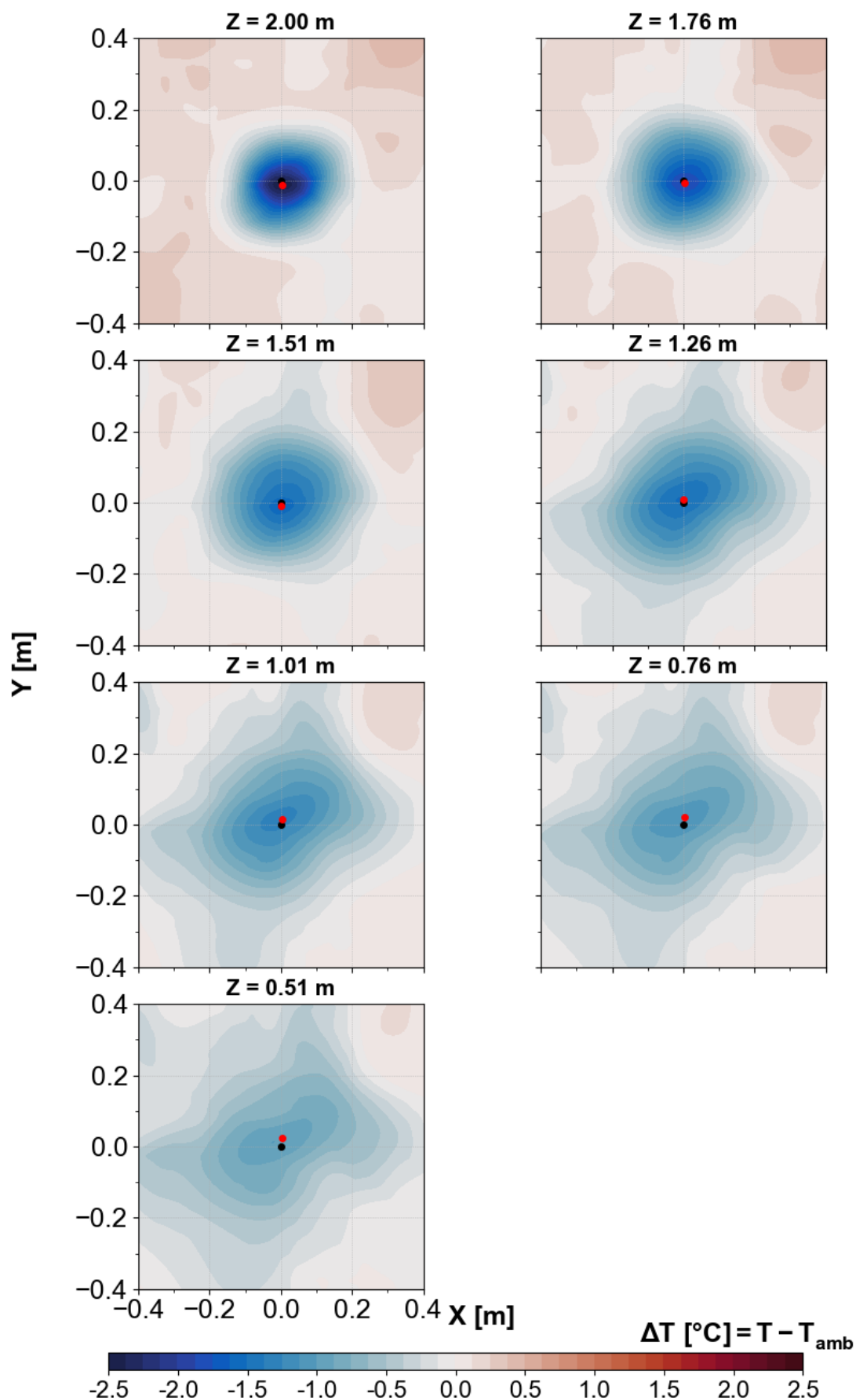


Figure 5.6 – cold_120 - Mean temperature contours map over the horizontal planes

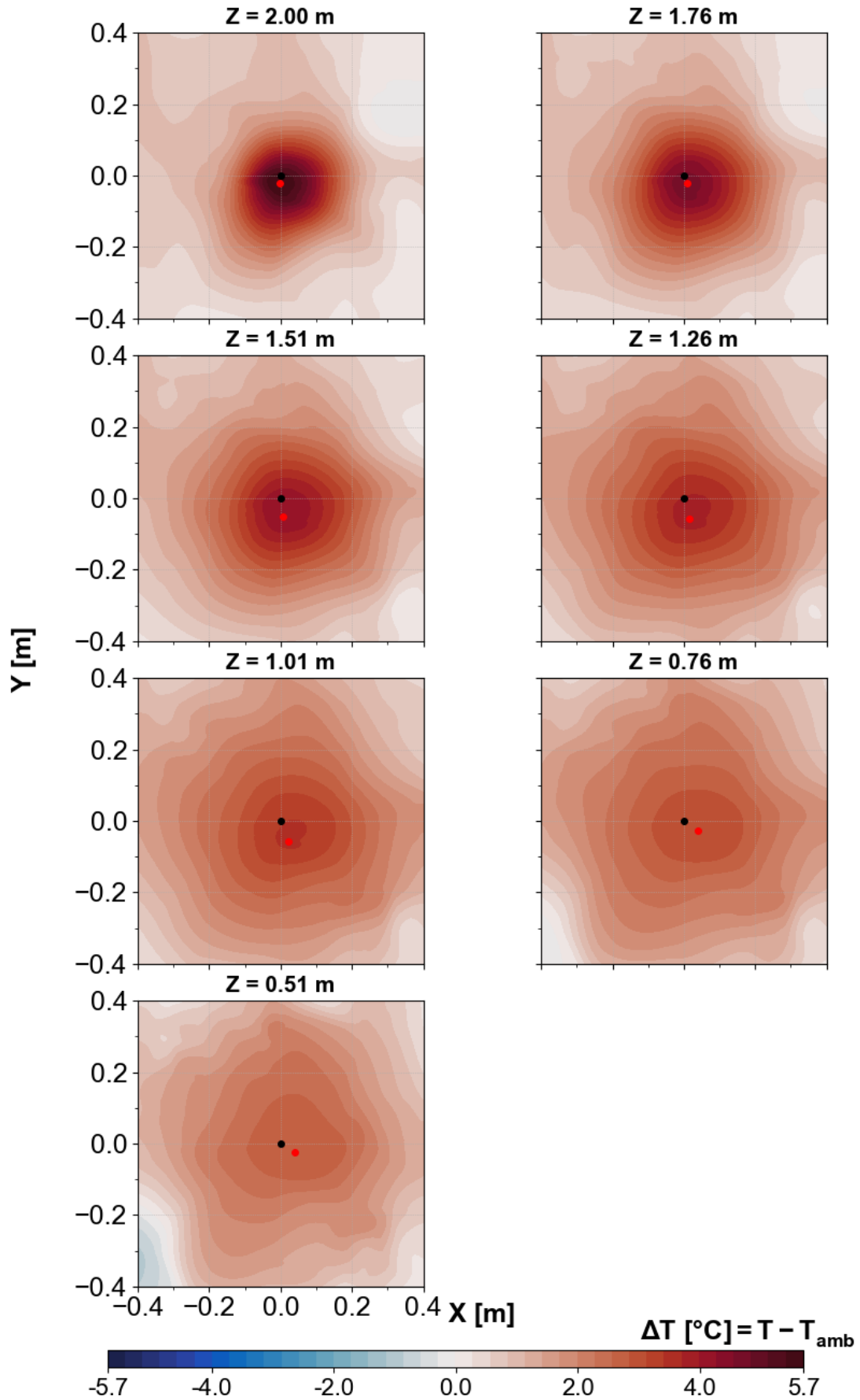


Figure 5.7 – hot_120 - Mean temperature contours map over the horizontal planes

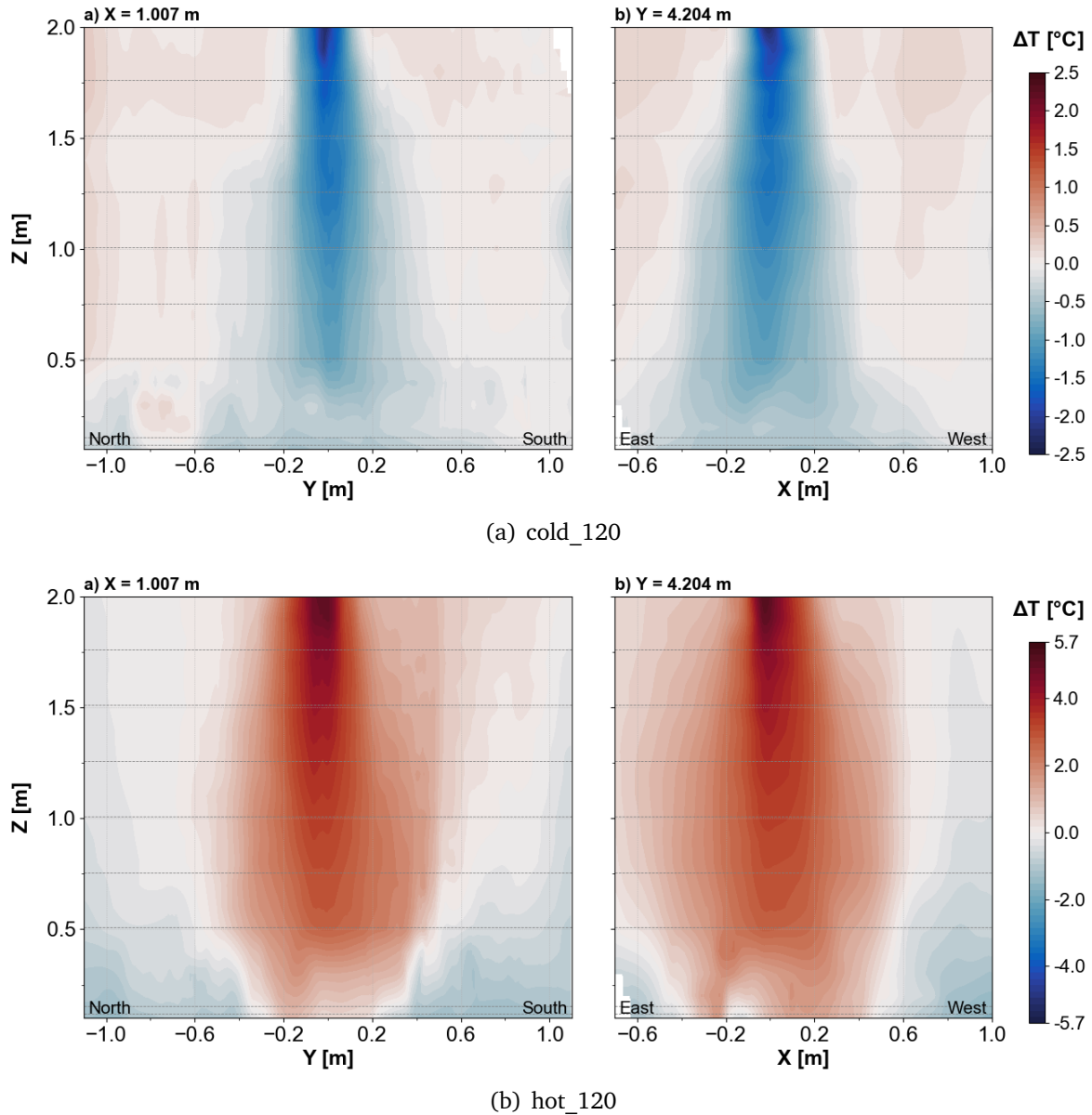


Figure 5.8 – Non-isothermal jets - Temperature contours map following X and Y direction

the cold jet. This distribution is in agreement with that of the air velocity contours (c.f. Figure 5.5(b)).

For the hot jet, the jet temperature contours develop widely in the radial direction, which is in agreement with the velocity distribution. Nevertheless, the interesting point is that the thermal layer continues to develop in the axial Z-direction up to $Z = 0.2$ m, while the dynamic layer has already disintegrated at about $Z = 0.5$ m. The buoyancy forces have indeed supported the convective heat transfers at these levels.

5.4 Interacting asymmetric jet characterization

5.4.1 Deviation of the interacting jet trajectory

5.4.1.1 Data processing

This section gives the quantitative description of the trajectory deviation of the interacting jet with regard to an axisymmetric free jet. To do so, we compute the location of the extremum velocity and temperature value on each horizontal measurements plane. The distance between the diffuser axis and the maximum value locations is named δ [m]. The angle of deviation (0° is the North direction, positive values toward the East direction) is named θ [°].

The extremum velocity (or temperature) points are the points where the interpolated velocity (or temperature) values are the maximum over the interpolated planes. We recall that the interpolation scheme we used is a second order interpolation scheme. This scheme allows us to get a subgrid precision on the extremum velocity (and temperature) values and position. This effect is illustrated on a 1D example in the Figure 5.9. Let $x_i, x_{i+1} \dots x_{i+3}$ be four measurement locations, on which we measure the quantities $y_i, y_{i+1} \dots y_{i+3}$.

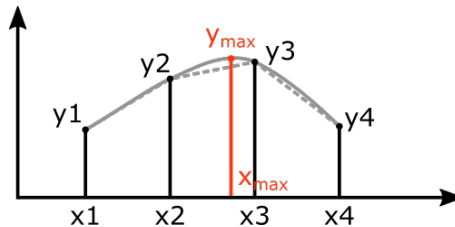


Figure 5.9 – Data interpolation principle

If we use a first order interpolation scheme, straight lines link the measurement values. The maximum value location must be one of the measurement locations. If we use a second order interpolation scheme, the measurement points are linked by cubic interpolants, which allow local maximums between the measurement points. The maximum value location can be located between the measurement points. Thus, the precision on the maximum value and the maximum value location are improved by the 2nd order interpolation.

Since the mesh size of the interpolation points is 2×2 mm, we can expect a minimum 2 mm uncertainty on the maximum point locations.

We provide in this section 3D visualisations of the jet trajectories. The visualizations were performed on ParaView software. The 3D visualizations also show iso-velocity surfaces at 0.25 m/s to provide a first impression of the jet spreads.

5.4.1.2 Amplitude and angle of deviation of the jet trajectory

The jet trajectories for the isothermal jet, the cold jet and the hot jet cases are displayed in 3D views in Figures 5.10, 5.12 and 5.14. The (a) figures show a closer visualization of the jet behavior. Visualizations in X and Y-direction are given in (b) and (c) figures.

The quantitative descriptions of the jet deviation from the diffuser axis are given in the Figure 5.11, 5.13 and 5.15 for the three cases accordingly. The (a) figures are plotted in local polar coordinates $(0, \delta, \theta)$: the center $(0; 0)$ corresponds to the diffuser axis; the NSEW-directions are the same as those shown previously in the Figure 2.7, the North-direction points to the exhausts mouths while the South direction points to the glazing. In the (b) figures, the deviation amplitudes δ are plotted against the room height Z .

In the isothermal case, the downstream flow is deviated toward the North-West (NW) direction. The North side is where the exhausts are located: the jet is attracted by the exhaust mouth. The West side is the side where the jet has more space to spread on the East-West direction. The presence of the plenum box may also have an impact on this deviation: the jet flow at the upstream is shifted toward the North side. The plenum box imposes an abrupt change of the inlet airflow and tends to deviate the jet flow at the diffuser face.

As shown in Fig. 5.11, at the upstream region, the deviation amplitude remains minimal (1 cm to 2 cm). At the downstream region ($Z = 0.76$ m and 0.51 m), the deviation is much more visible with an amplitude reaching 15 cm and an angle of 45° (NW-direction).

In the summer scenario (cold jet), the deviation of the jet trajectory is much smaller. It is concentrated at the lower part of the jet where the jet seems to be attracted in the South direction. The higher temperature of the glazing causes an aspiration at the ground level due to natural convection flows. The maximum velocity decay curve and the minimum temperature decay curves seem to inline to each other. This alignment shows the coherence between the core dynamic layer and the core thermal layer within the air jet. The velocity contours in Figure 5.12(b) and 5.12(c) show that the jets tends to spread over the South direction (due to the aspiration of the glazing) and the East direction (due to the Coanda effect).

The velocity curve deviates slightly to the West direction at the upstream region (c.f. Fig. 5.13). However, the deviation amplitude remains minimal, $r < 1$ cm. Then, the amplitude reach 2 cm at $Z = 0.76$ m and 5 cm at $Z = 0.51$ m. The velocity curve deviates toward the South side under the aspiration effect of the temperature gradient at the glazing.

The minimum temperature curve develops more narrowly; the deviation amplitude does not exceed 2 cm. The first three points deviate slightly to the NW-direction and the four others to the South direction, which are in coherence with the velocity curve. The mean and maximum absolute difference between the two curves are respectively 0.5 cm and

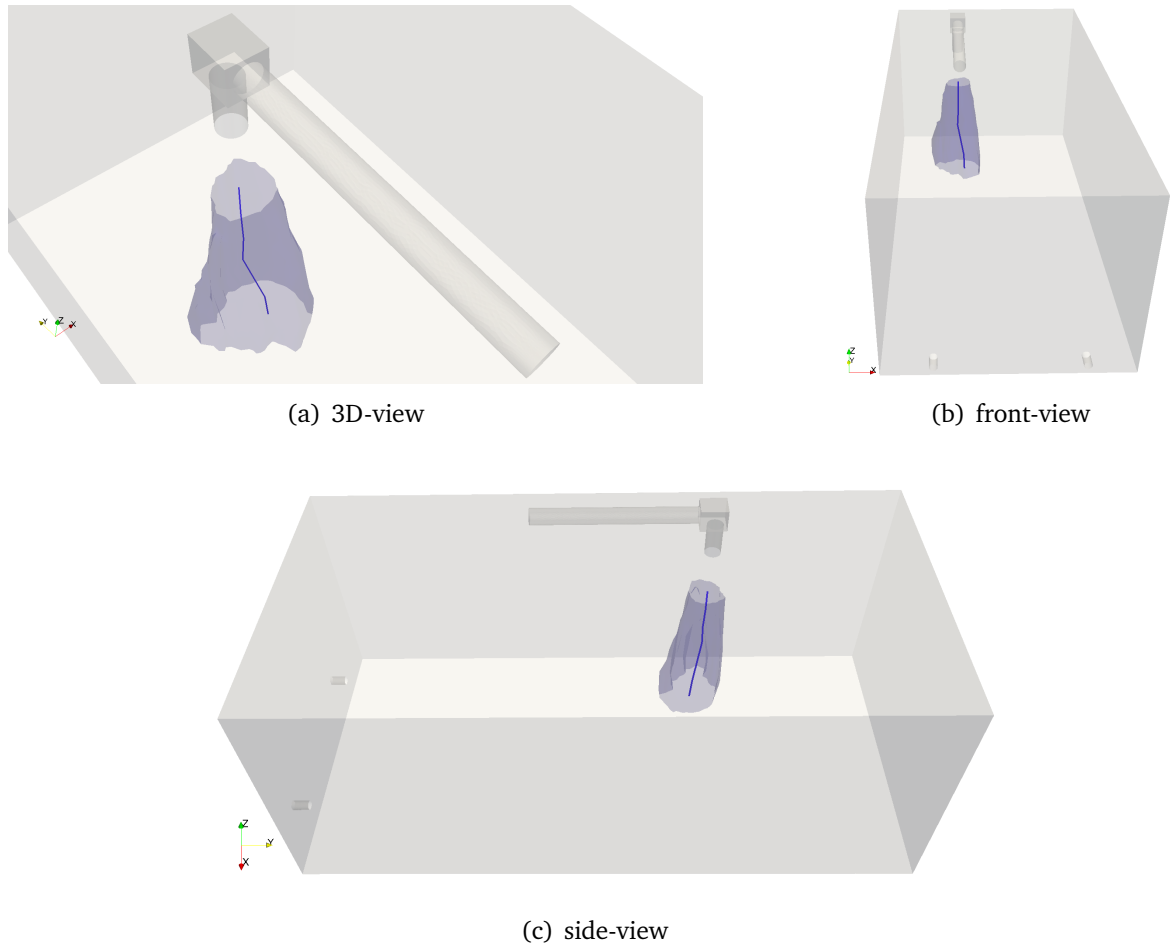


Figure 5.10 – iso_120 - Maximum velocity trajectory

Where: *Blue contour* - interacting jet; *Blue curve* - maximum velocity decay;

Value taken for contour drawing: 0.25 m/s

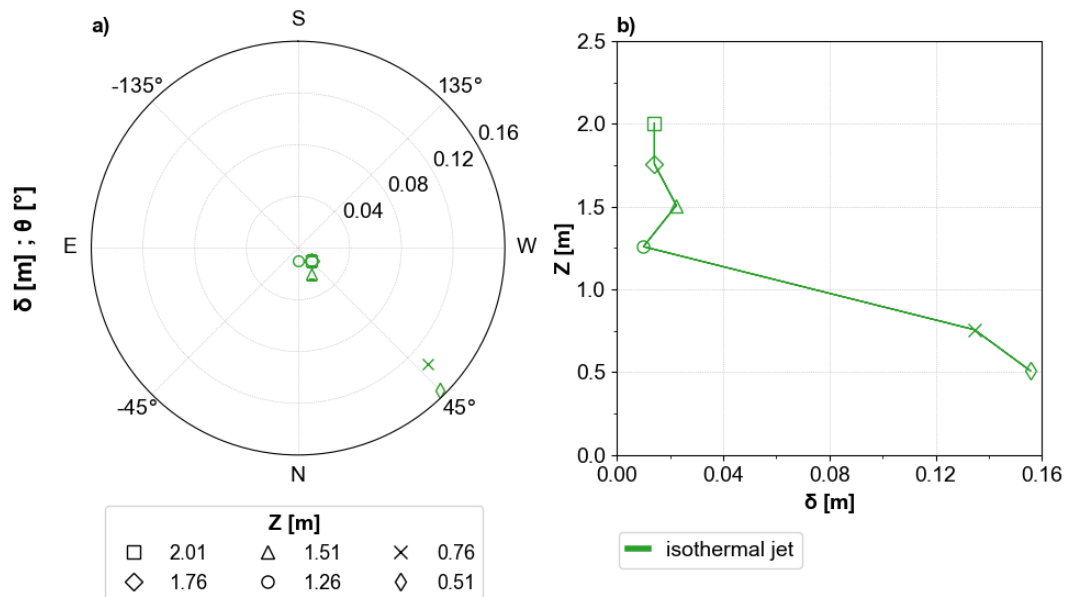


Figure 5.11 – iso_120 - Jet deviation: (a) in polar coordinates; (b) following Z

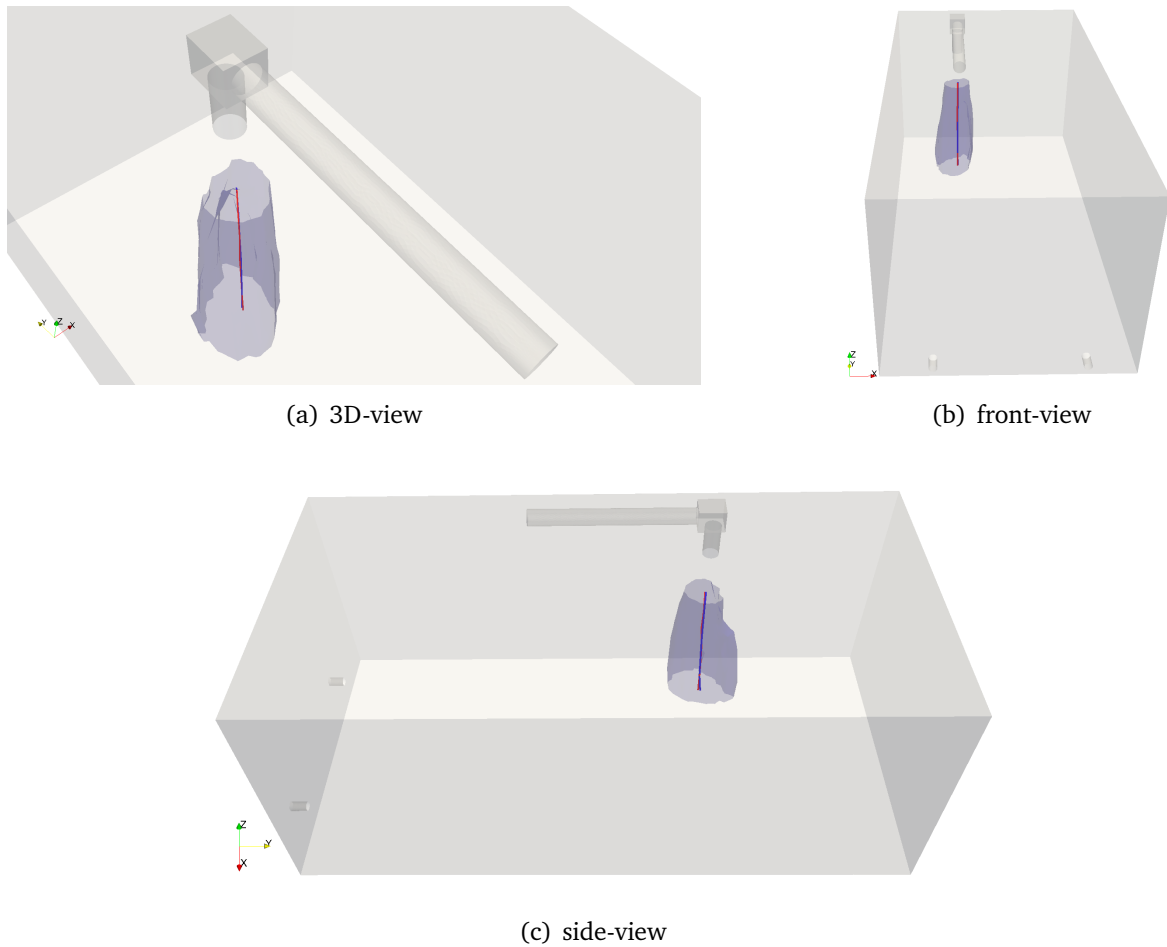


Figure 5.12 – cold_120 - Extremum velocity and temperature trajectories
 Where: *Blue contour* - interacting jet; Contour drawing: 0.25 m/s
Blue curve - velocity decay; *Red curve* - temperature decay

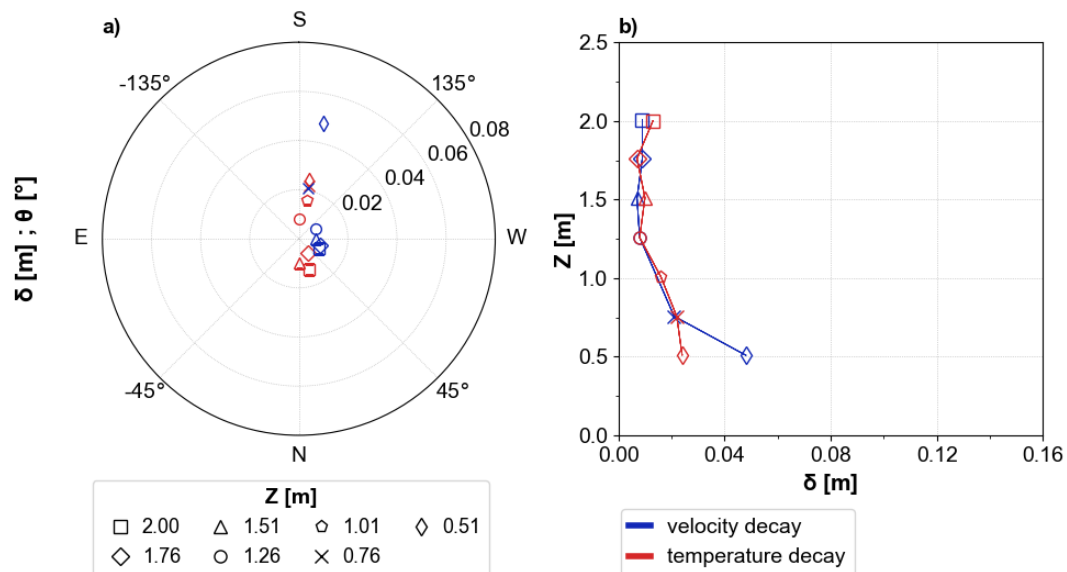


Figure 5.13 – cold_120 - Jet deviation: (a) in polar coordinates; (b) following Z

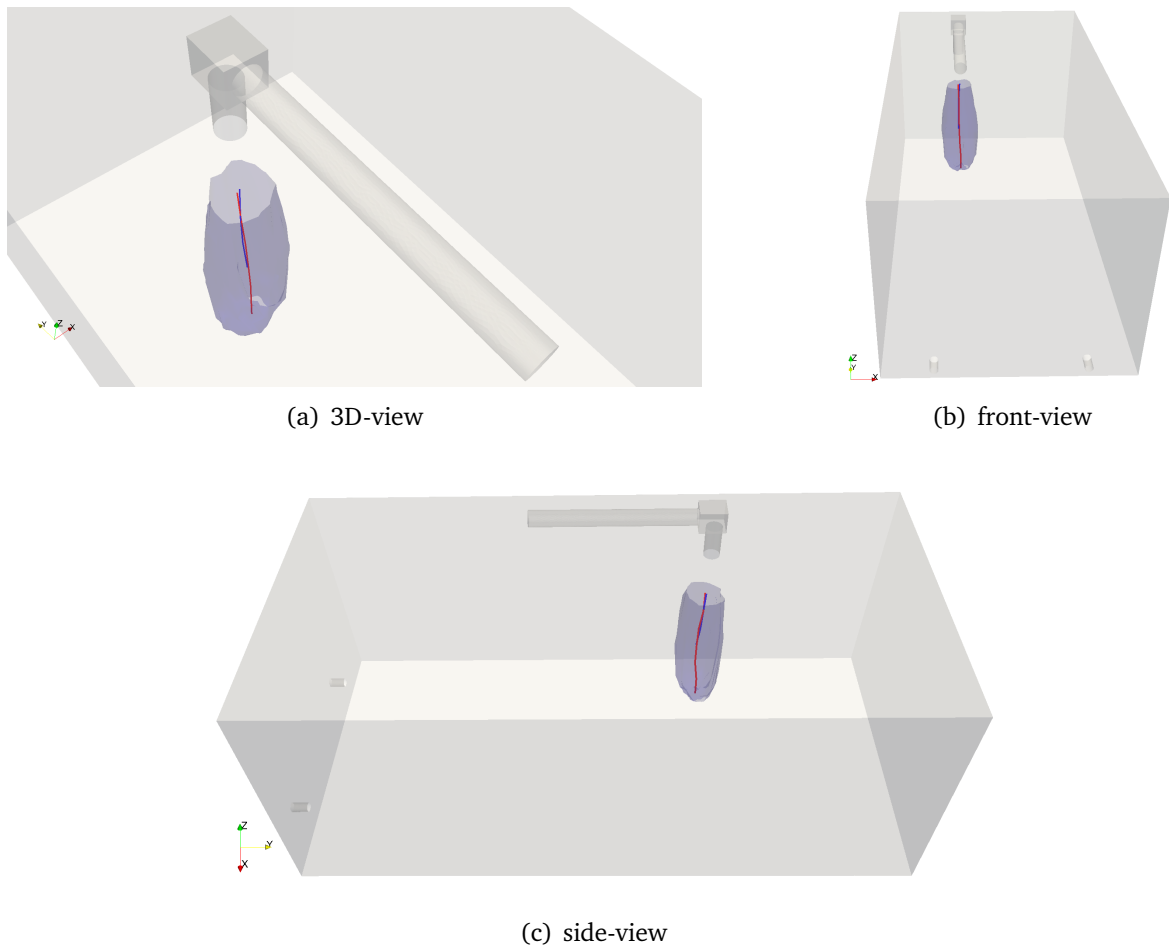


Figure 5.14 – hot_120 - Extremum velocity and temperature trajectories

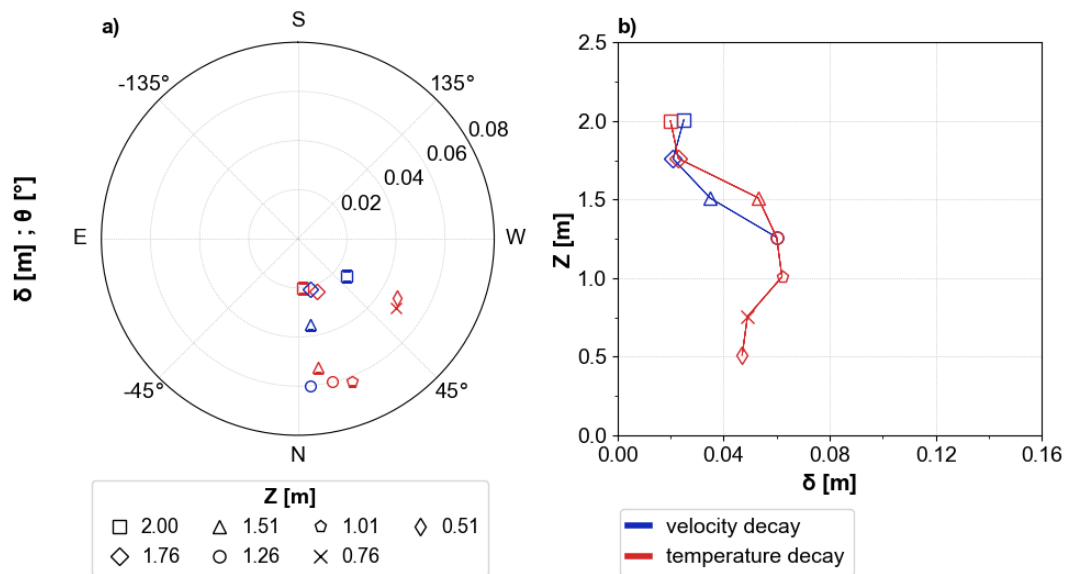


Figure 5.15 – hot_120 - Jet deviation: (a) in polar coordinates; (b) following Z

2.4 cm.

In the winter scenario (hot jet), the hot jet shows a large spread right after leaving the diffuser (c.f. Figure 5.14(a)). The jet trajectory seems to curve towards the West direction at the region near the floor. However, it could not reach the floor and seems to disintegrate earlier than the two other cases.

The velocity and temperature decay curves are aligned in the upstream region (c.f. Fig. 5.15). They deviate generally in the NW-direction. The mean absolute difference is about 0.8 cm. The maximum velocity values in the last two planes are not plotted due to its questionable reliability.

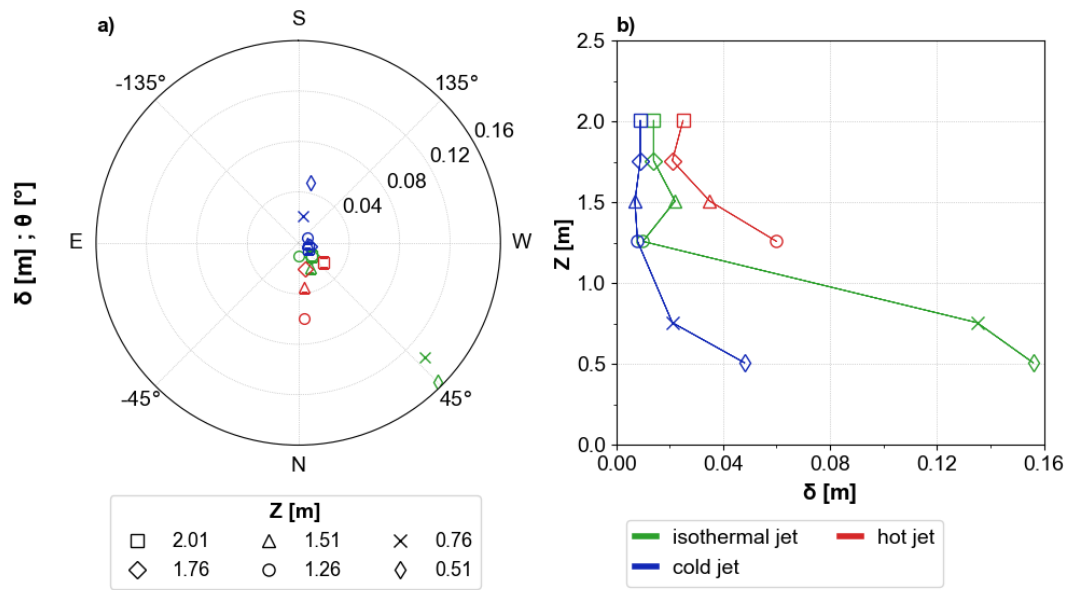


Figure 5.16 – Comparison of the jet deviation in three test cases

The Figure 5.16 summarizes the velocity trajectory deviations for the three test cases. There is an agreement between the jet behavior in the first four measurement planes. In this region, the influence of the temperature gradients in the room is weaker and the jet behavior mainly depends on the upstream flow. All the jets deviated in the quarter formed by the North and the West directions, with a deviation amplitudes which do not exceed 6 cm. Due to the effect of the buoyancy forces, the cold air jet trajectory is the least deviated while the hot air jet trajectory is the most deviated.

5.4.2 Jet cross-sectional distributions

For characterizing the jet cross-sectional distributions, it is common to represent the velocity and temperature fields in terms of dimensionless values $\frac{u}{u_m}$, $\frac{\Delta T}{\Delta T_m}$ (Rajaratnam, 1976; Awbi, 2003; ASHRAE, 2017).

The theory predicts that the velocity and the temperature distributions in the jet cross-section are axisymmetric and follow a Gaussian curve along the radial direction. In this section, we visualize the radial distributions of the velocity and the temperature to check if we retrieve the Gaussian distributions.

5.4.2.1 Data processing

The measured temperature and velocity distributions are not centered around the jet axis (due to the deviation of the jet) and are not axisymmetric. It is then irrelevant to plot the velocity and temperature evolution along the X and the Y directions to have an idea of their distributions. We would risk a loss of information with such an analysis. To visualize the velocity and temperature evolution across the jet, we plot the velocity and temperature values as functions of the disk-equivalent radius r_{Deq} .

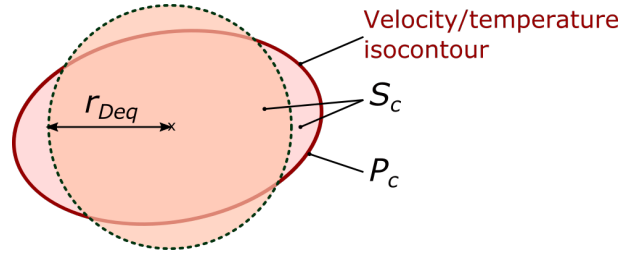


Figure 5.17 – Area and disk-equivalent radius of an isocontour

To get the disk-equivalent radius for a specific velocity or temperature value, we first draw the corresponding isocontour on the selected measurement plane (c.f. Figure 5.17). Then we compute the area S_c [m²] inside the isocontour. The disk-equivalent radius is the radius of a circular contour which would have the same area:

$$r_{Deq} = \sqrt{\frac{S_c}{\pi}} \quad (5.3)$$

The disk-equivalent radius is inspired from the "equivalent diameter" employed in duct sizing³. This approach was addressed in the book of Goodfellow (2001), but it was rarely used in the literature.

We first plotted the dimensionless velocity values u/u_m as functions of the disk-equivalent radius r_{Deq} . We got one curve for each measurement plane. From each curve, we identified the jet dynamic thickness b_v . This is the value of the disk-equivalent radius where u/u_m is equal to 0.5:

$$b_v = r_{Deq} \left(\frac{u}{u_m} = 0.5 \right) \quad (5.4)$$

³the equivalent diameter is the diameter of a circular duct or pipe that gives the same pressure loss or resistance as an equivalent duct or pipe with non-circular shape (e.g. rectangular, oval, oblong, etc.).

The same procedure was used to determine the jet thermal thickness b_T . We first plotted the dimensionless temperature difference $\Delta T / \Delta T_m$ as functions of the disk-equivalent radius r_{Deq} . We got one curve for each measurement plane. On each curve, the jet thermal thickness is the value of the disk-equivalent radius where:

$$b_T = r_{Deq} \left(\frac{\Delta T}{\Delta T_m} = 0.5 \right) \quad (5.5)$$

Finally, the dimensionless velocity and temperature distributions are plotted as functions of the dimensionless disk-equivalent radius r_{Deq}/b_v and r_{Deq}/b_T .

5.4.2.2 Velocity and temperature distributions in the jet cross-section

The contour maps of the dimensionless velocity and temperature distribution are given in the Appendix H. Those graphs are used to compute the disk-equivalent radius of each isocontour in the horizontal measurement planes.

The dimensionless values u/u_m and $\Delta T / \Delta T_m$ following the dimensionless radial distance r_{Deq}/b_v and r_{Deq}/b_T are presented in the figures from 5.18 to 5.20. Values within a range of [0.2 - 1.0] are plotted; the profile of value 0.1 is excluded since it was qualified as not reliable. The reference profile is expressed by a single Gauss error-function curve according to equation (4.4).

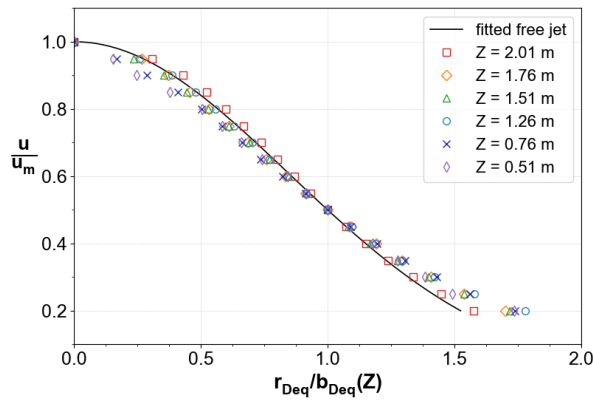


Figure 5.18 – iso_120 - Dimensionless velocity profiles distribution

There is a remarkable self-similarity between all the profiles despite the asymmetric spreading. The measurement points located above the reference curve indicate a larger spread. Otherwise, the points located below the reference curve indicate a smaller spread.

For the isothermal jet (c.f. Fig. 5.18), the jet spreads roughly with the same rate as the reference profile at the core zone ($u/u_m > 0.5$). At the jet boundary layer ($u/u_m < 0.3$), the jet spreads about 18% larger than the reference profile. The cross-sectional

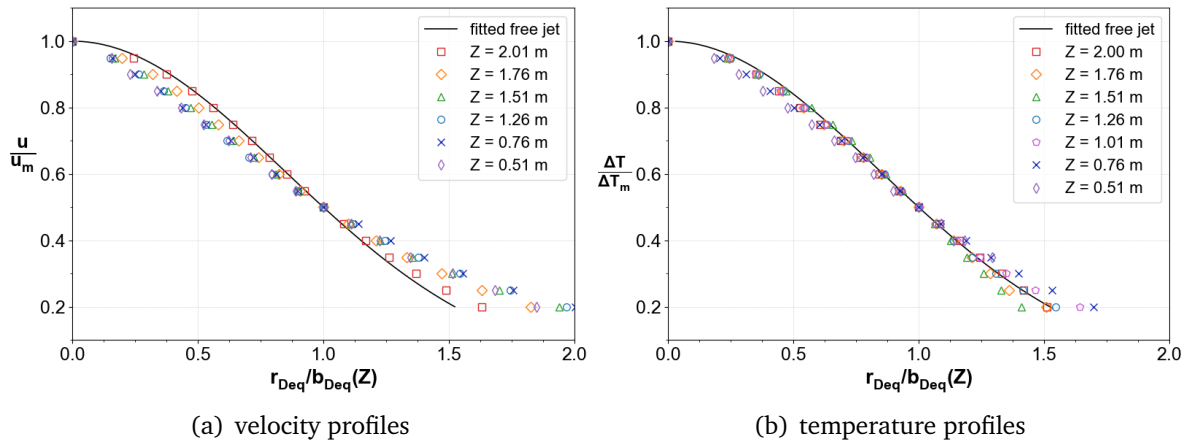


Figure 5.19 – cold_120 - Dimensionless velocity and temperature profiles distribution

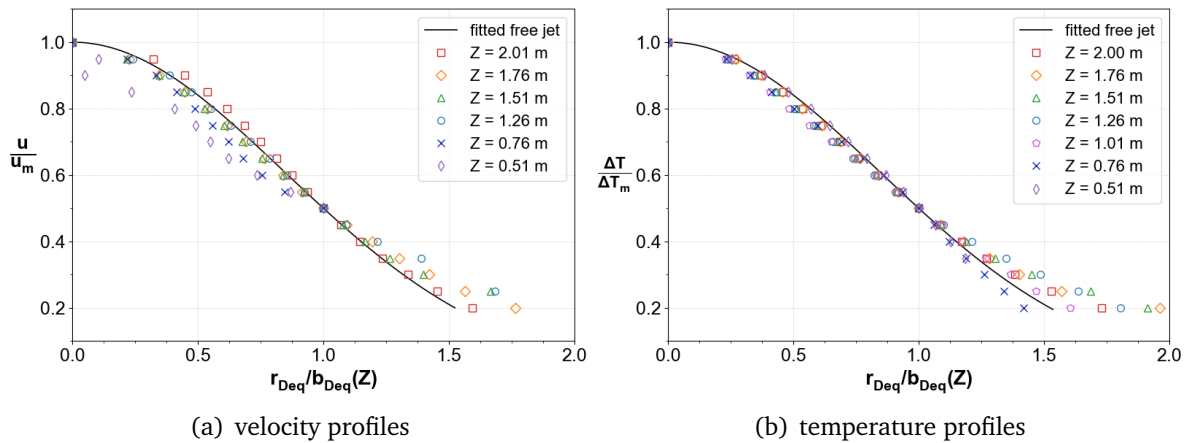


Figure 5.20 – hot_120 - Dimensionless velocity and temperature profiles distribution

velocity distributions tend to become more linear when the jet approaches the floor (for low Z values).

The same conclusions can be drawn for the non-isothermal jets. The figures 5.19 and 5.20 highlight the self-similarity of both the cross-sectional velocity and temperature profiles.

In the core zone of the cold jet, the velocity and temperature profiles have a smaller spread than the reference profile. It is assumed that this behavior is due to the coincided inertia and buoyancy forces which have the opposite effect on the heat transfer. The profiles have a larger spread in the jet boundary zone where the airflow is constrained by both the turbulence and the convective heat transfer. The profiles at the downstream flow seem to be distributed linearly rather than normally.

The same tendency is observed for the hot air jet. The velocity profiles at $Z = 0.76$ and 0.51 m show some dispersion compared to the other profiles. However, the results at this level are subjected to uncertainty due to the low velocity values. The dimensionless

velocity value below 0.5 of the planes $Z = 0.76$ and 0.51 m are not plotted.

5.4.3 Jet thickness and spread rate

One of the most important criteria for characterizing an air jet is the jet dynamic spread rate K_2 . This is the rate of the evolution of the jet dynamic thickness b_v along the x-direction (the x-direction is the axial distance from the diffuser face). We recall that the equation for $b_v(x)$ is (c.f. section 4.3.2):

$$b_v(x) = K_2(x + \bar{x}) \quad (5.6)$$

where \bar{x} is the virtual origin of the jet dynamic layer.

For non-isothermal jets, we also define the jet thermal spread rate $K_{2,T}$ as the rate of evolution of the jet thermal thickness along the x-direction:

$$b_T(x) = K_{2,T}(x + \bar{x}_T) \quad (5.7)$$

where \bar{x}_T is the virtual origin of the jet thermal layer.

We recall that, from a theoretical point of view, the relations between $b_v(x)$ and $b_T(x)$ should be (c.f. section 4.4.2.2):

$$b_T = b_v \sqrt{\frac{1}{Pr}} \quad (5.8)$$

5.4.3.1 Data processing

To determine the values of K_2 and \bar{x} , we first plot the values of b_v determined by the procedure described in section 5.4.2, as functions of $x = H - Z$ where Z is the height of the measurement plane, and $H = 2.5$ m is the height of the room.

Then we perform a linear regression to estimate the relationship between these points. The slope and the x-intercept of the line correspond respectively to the jet spread coefficient K_2 and the virtual origin \bar{x} .

The linear regressions were performed with the function *stats.linregress* from the *Scipy* library of Python.

The procedure above-mentioned was also applied on the jet thermal thickness to get the jet thermal spread rate $K_{2,T}$ and the virtual origin of the jet thermal layer \bar{x}_T .

5.4.3.2 Jet dynamic and thermal spread

The Figure 5.21 presents the linear regression graphs of the jet dynamic thickness of the three test cases. The Figure 5.22 presents the linear regression graphs on the jet

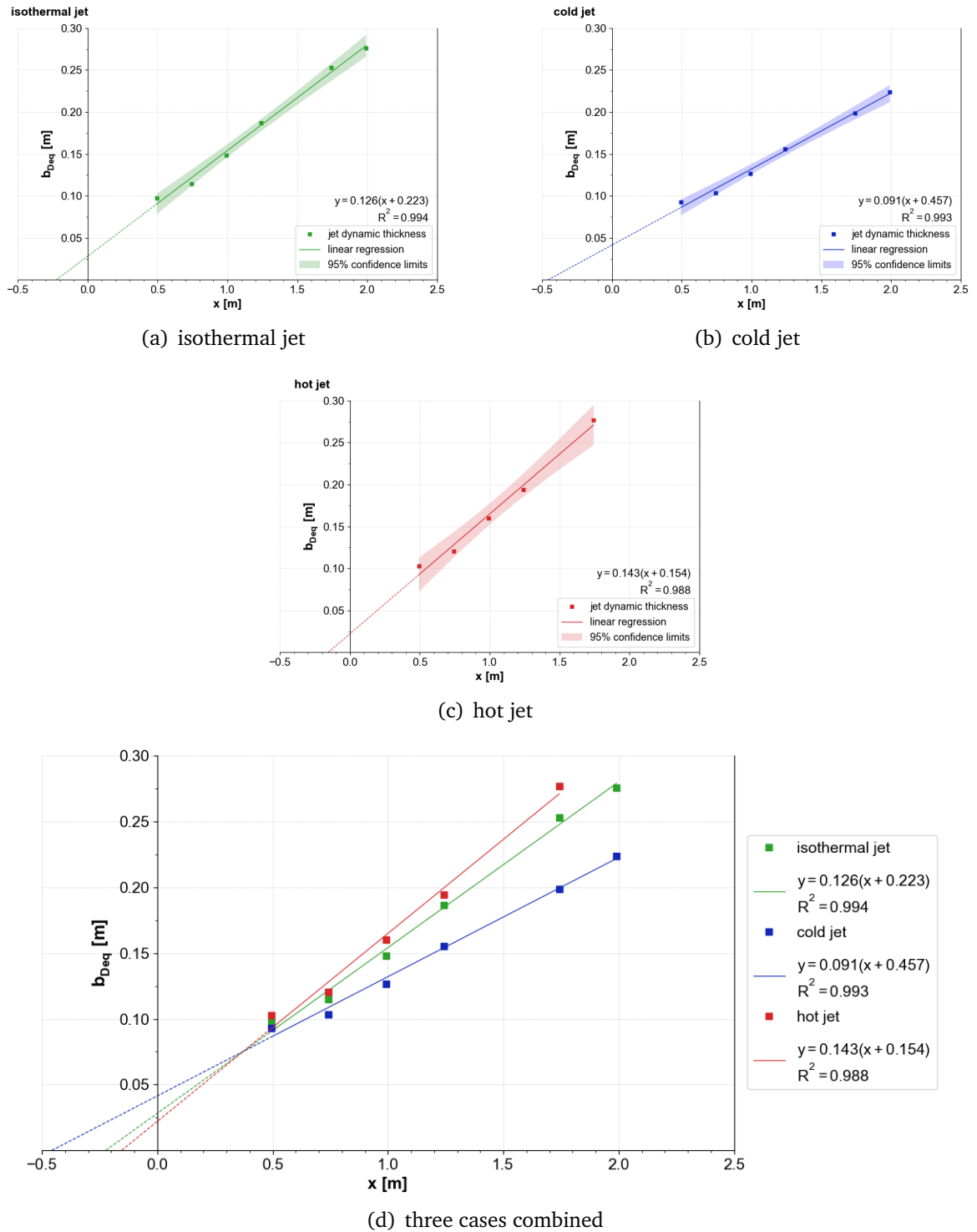
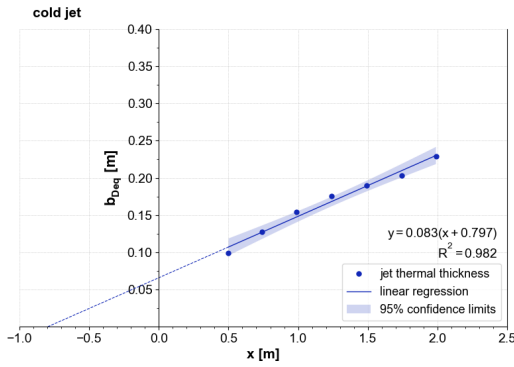
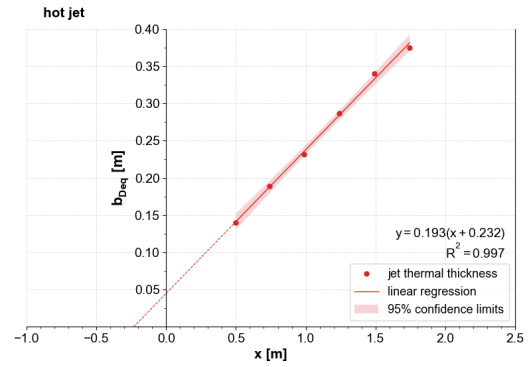


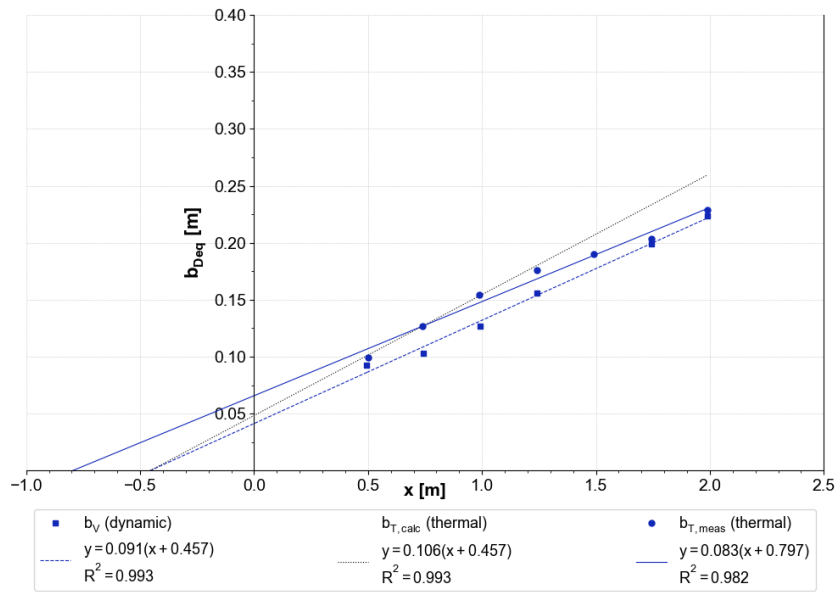
Figure 5.21 – Jet dynamic thickness and spread



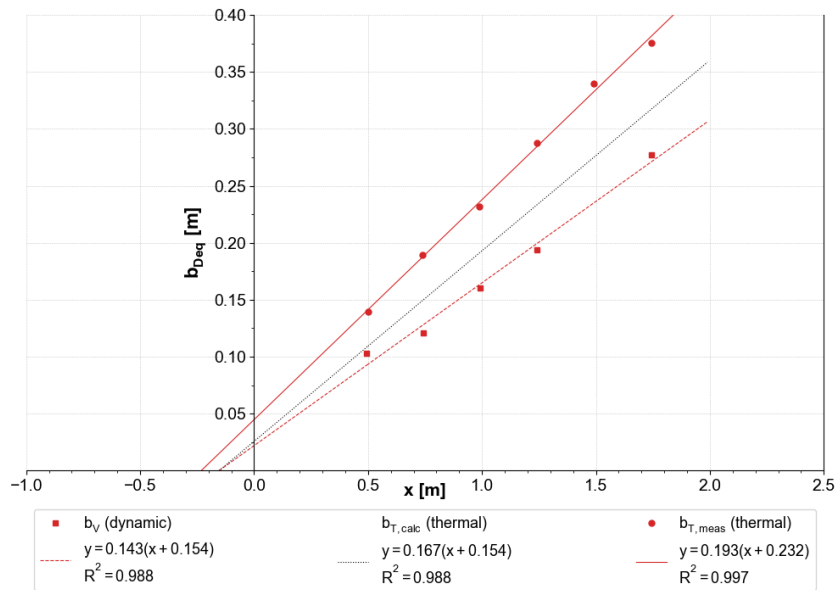
(a) cold jet



(b) hot jet



(c) cold jet - comparison with empirical profiles



(d) hot jet - comparison with empirical profiles

Figure 5.22 – Jet thermal thickness and spread

thermal thickness of the non-isothermal jets. The line equations and their coefficient of determination R^2 are given. The colored-band shows the 95% confidence interval on the line. It should be noted that errors related to the regression are assumed to be normally distributed. They are calculated based on the Student's t-distribution given the small sample size.

For the jet dynamic thickness, individual results of the three cases are combined into one single graph for a better comparison (c.f. Figure 5.21(d)). The three coefficient of determination R^2 obtained are all higher than 0.98. This coefficient represents the goodness of a fit: $R^2 = 1$ means a perfect fit and $0 < R^2 < 0.6$ means a poor fit. Hence, it is possible to assume a linear spread of the interacting asymmetrical jet considered. The jet dynamic spread rates increase in the following order: cold < isothermal < hot ($K_2 = 0.091, 0.126, 0.143$ accordingly). This result is in agreement with remarks noticed on the effect of buoyancy forces. The coincidence of inertia and buoyancy forces makes the cold jet spreads more narrowly, whereas the reversed buoyancy forces make the hot jet spreads more widely. Besides, the jet dynamic virtual origin, issued from the linear fitting, increases in the reverse order: hot < isothermal < cold ($\bar{x} = 0.154, 0.223, 0.457$ m accordingly). The dynamic virtual origin of the jet is located further from the diffuser surface when the jet is colder.

For the jet thermal thickness, results of both the jet dynamic and thermal spread are combined into one graph (c.f. Figure 5.22(c) for the cold jet and Figure 5.22(d) for the hot jet). In those graphs, the square markers represent the jet dynamic thickness and the dot markers represent the jet thermal thickness issued from measured data. The dashed-lines show the jet dynamic spreads, the solid-lines show the jet thermal spreads obtained experimentally and the dotted-lines give the jet thermal spreads deducted empirically using the equation (5.8).

Given the relative high coefficient R^2 obtained, we can assume a linear spread of the jet thermal layer. The jet thermal spread is smaller than the jet dynamic spread ($K_{2,T} = 0.083 < 0.091 = K_2$) for the cold jet, while the reverse order is observed for the hot jet ($K_{2,T} = 0.193 > 0.143 = K_2$).

Besides, we can notice a discrepancy between the jet thermal thickness obtained experimentally and empirically. For the cold jet, the experimental thermal layer tends to spread larger than the empirical one at the upstream but then spreads more narrowly at the downstream. Their relative mean difference is about 5%. For the hot jet, the experimental thermal layer always has a large spread compared to the empirical one with a difference of 25%.

These parameters for characterizing the jet spread are summarized in the Table 5.5. Their uncertainties (at 95% confidence interval) are also reported. The results on the hot jet dynamic layer show a largest uncertainty compared to other cases. For instance, the virtual origin of the dynamic layer could actually located in front of the diffuser face

and not behind it ($\bar{x} < 0$). This is because the linear regression for the hot jet case was performed on 5 points (instead of 6). The last point was excluded given its questionable reliability as mentioned previously. That explains the relative large width of the confidence limits band obtained (c.f. Figure 5.21(c)).

For the isothermal jet, the jet spread coefficient is found to equal to 0.126, which lies between the interval $[0.085 - 0.151]$ found in the literature for an isothermal axisymmetric free jet (Goodfellow, 2001).

Characteristics	Symbol	iso_120	cold_120	hot_120
Jet dynamic spread	K_2 [-]	0.126 ± 0.014	0.091 ± 0.010	0.143 ± 0.029
Virtual origin (dynamic)	\bar{x} [m]	0.223 ± 0.165	0.457 ± 0.209	0.154 ± 0.261
Jet thermal spread	$K_{2,T}$ [-]	-	0.083 ± 0.013	0.193 ± 0.014
Virtual origin (thermal)	\bar{x}_T [m]	-	0.797 ± 0.331	0.232 ± 0.106

Table 5.5 – Jet spread coefficients and virtual origin

5.4.4 Maximum velocity and temperature decay

The maximum velocity and temperature decays are widely used in the literature to describe the behavior of a free jet (Zou, 2000; Awbi, 2003). Those decays are theoretically predicted by equations (4.9) and (4.10). Those equations involve two empirical coefficients: K_1 , K_T and their corresponding virtual origin \bar{x} , \bar{x}_T .

Here, we will determine the values of those coefficients for our measured velocity and temperature decays.

5.4.4.1 Data processing

We recall the equations the theory used for predicting the decays of a free jet:

$$\frac{u_m}{U_0} = K_1 \frac{\sqrt{A_0}}{x + \bar{x}} \quad (5.9a)$$

$$\frac{u_m}{U_0} = K_1 \frac{\sqrt{A_0}}{x + \bar{x}} \cdot K_n(x) \quad (5.9b)$$

$$\frac{\Delta T_m}{\Delta T_0} = K_T \frac{\sqrt{A_0}}{x + \bar{x}} \cdot \frac{1}{K_n(x)} \quad (5.9c)$$

For isothermal jets (eq. (5.9a)), K_1 and \bar{x} are estimated based on the linear regression of the function $U_0/u_m = f(x/\sqrt{A_0})$. The slope and the x-intercept of the fitted line

correspond to $1/K_1$ and $\bar{x}/\sqrt{A_0}$.

For non-isothermal jets (eq. (5.9b), (5.9c)), the theory predicts that the value of K_1 remains the same between an isothermal and a non-isothermal jet (with the same inlet flow rate). The effects of the non-isothermality are taken into account by the coefficient $K_n(x)$ (c.f. section 4.4.1.2). The relationship between U_0/u_m (or $\Delta T_0/\Delta T_m$) and $x/\sqrt{A_0}$ is not necessarily linear since $K_n(x)$ depends on $x/\sqrt{A_0}$ to the power of $2/3$.

In this section, we will assume that the non-linearity due to the temperature gradient is weak and that we can express the jet maximum velocity and temperature decays with the equations (5.10a) and (5.10b). Those equations involve the four coefficients K_1 , K_T , \bar{x} and \bar{x}_T that we will determine from the linear regression.

$$\frac{u_m}{U_0} = K_1 \frac{\sqrt{A_0}}{x + \bar{x}} \quad (5.10a)$$

$$\frac{\Delta T_m}{\Delta T_0} = K_T \frac{\sqrt{A_0}}{x + \bar{x}_T} \quad (5.10b)$$

5.4.4.2 Evaluation of the jet decays

The graphs of the jet velocity and temperature decay are presented in Figures 5.23 and 5.24. The jet maximum velocity and temperature decays u_m/U_0 and $\Delta T_m/\Delta T_0$ are plotted as functions of the dimensionless jet axial distance $x/\sqrt{A_0}$. Values of U_0 and ΔT_0 ($=T_0 - T_{amb}$) in the three test cases are recapitulated in the Table 5.6.

	iso_120	cold_120	hot_120
U_0 [m/s]	2.18		
ΔT_0 [°C]	-	-3.74	6.75

Table 5.6 – Values of U_0 and ΔT_0 in the three test cases

For the maximum velocity decay (Fig. 5.23(b)), we can observe a same tendency between the three curves corresponding to the three test cases. In each measurement plane, the velocity values decrease in the following order: cold > isothermal > hot. Compared to the isothermal jet, the cold jet has a slower decay (u_m/U_0 increases by 15.6%); the hot jet has a quicker decay (u_m/U_0 decreases by 22.4%).

The Figure 5.23(a) presents the maximum velocity decay of the isothermal jet that taken into account the virtual origin. A curve of the empirical free jet is presented for reference. This curve is computed using the equation (5.9a) with $K_1 = 4.7$ (ASHRAE, 2017) and $\bar{x} = 0.223$ m (c.f. Table 5.5). The maximum velocity decay of the isothermal jet does not differ much from that of the free jet (0.6% of mean relative difference).

For the maximum temperature decay (Fig. 5.24), in the contrast with the velocity

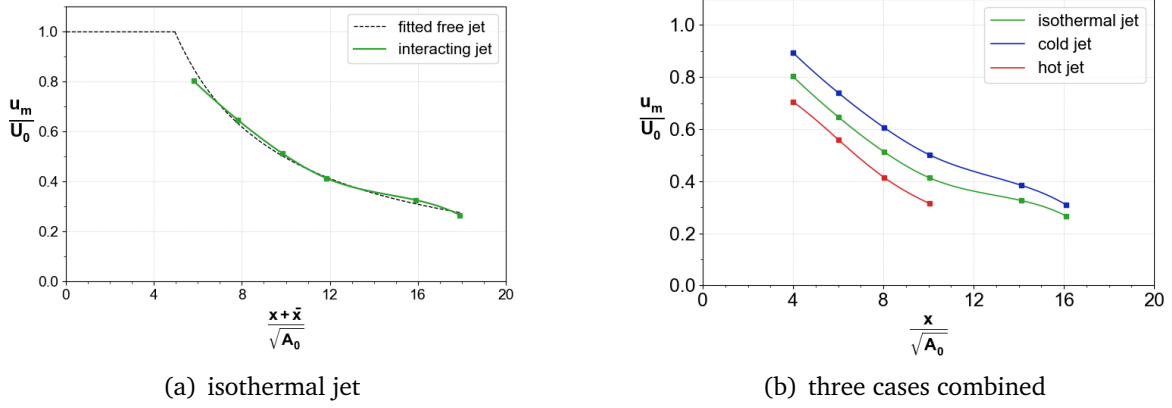


Figure 5.23 – Jet maximum velocity decays

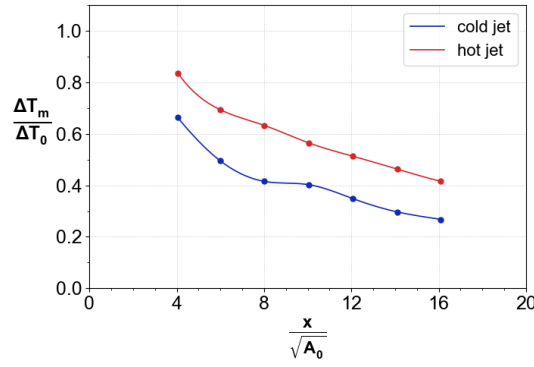


Figure 5.24 – Jet maximum temperature decays

decay, the hot jet experiences a much slower temperature decay compared to that of the cold jet ($\Delta T_m/\Delta T_0$ increases by 42.3%). The temperature decay of the hot jet is quasi-linear.

This contrast result between the cold and hot jet can be reasonably explained by the buoyancy effects, which have opposite impacts on those two jet cases. Besides, it is possible to deduct that the architectural elements might deviate the jet trajectory but due to the mass conservation, the free jet and the interacting jet have about the same maximum velocity decay, at least in the isothermal condition.

5.4.4.3 Regression results

The Figure 5.25 and 5.26 present the results of the linear regression which were used to determine the coefficients characterizing the maximum velocity and temperature decay of the experimental jet. The estimated equations, their coefficient of determination and their associated confidence limits band are given.

In all those graphs, the coefficient of determination R^2 are all higher than 0.97. A

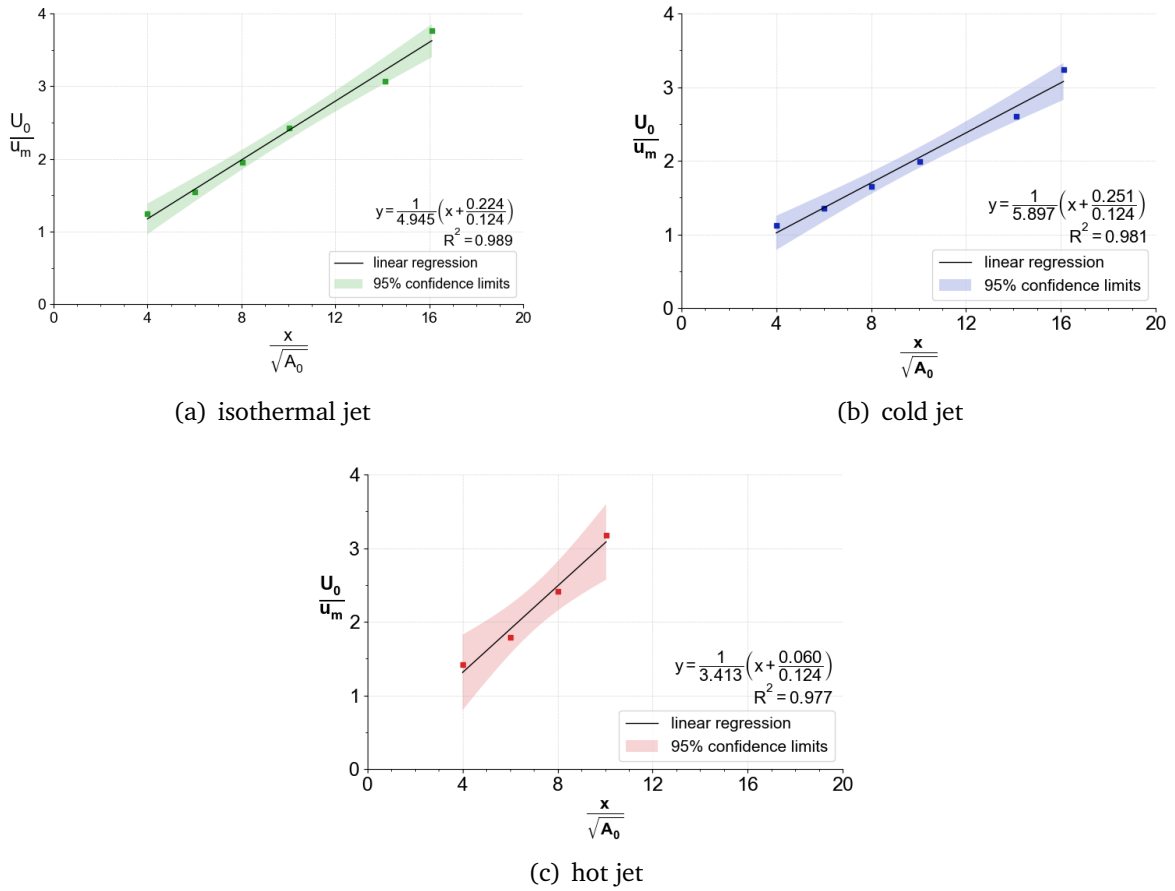


Figure 5.25 – Linear regression of the maximum velocity decay

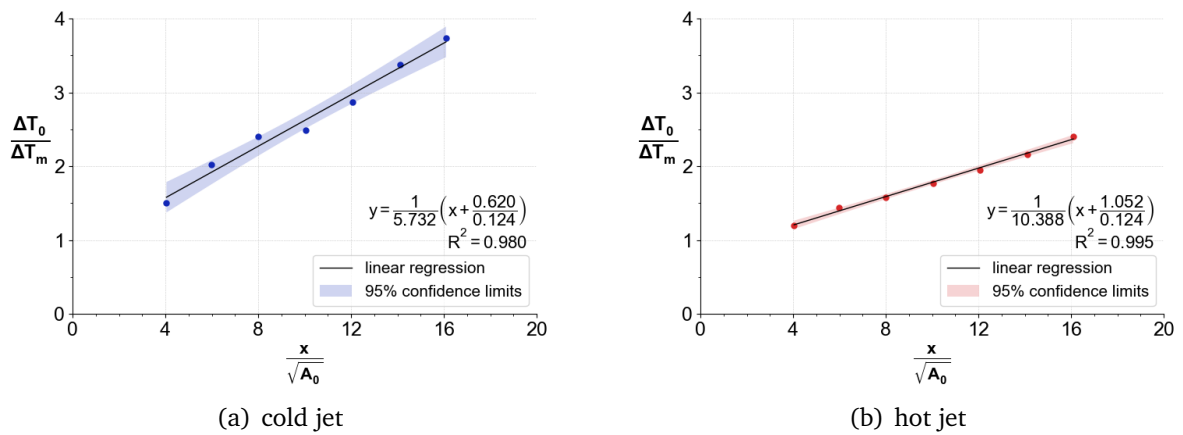


Figure 5.26 – Linear regression of the maximum temperature decay

linear decay can be assumed for the jet maximum velocity and temperature. The regression of the hot jet velocity decay is only based on four points; thus, the confidence limits band is broader compared to other graphs. The regression of the hot jet temperature decay gives the best fit ($R^2 = 0.995$), and the confidence limits band is much smaller. The coefficients deducted from the linear regression are summarized in the Table 5.7.

Characteristics	Symbol	iso_120	cold_120	hot_120
Velocity decay coeff.	K_1 [-]	4.945 ± 0.628	5.897 ± 1.129	3.413 ± 1.581
Virtual origin (dynamic)	\bar{x} [m]	0.224 ± 0.223	0.251 ± 0.298	0.060 ± 0.450
Temperature decay coeff.	K_T [-]	-	5.732 ± 0.935	10.388 ± 0.836
Virtual origin (thermal)	\bar{x}_T [m]	-	0.620 ± 0.320	1.052 ± 0.192

Table 5.7 – Empirical coefficients determination

For the isothermal jet, a value of 4.945 is found for the velocity decay coefficient K_1 . This value is not far from the values found in the literature for a vertical grille diffuser: 4.7 for a floor grille (ASHRAE, 2017), 4.6 for a grille with free area >40% (Awbi, 2003). A value of 0.224 m is found for the virtual origin \bar{x} . This value is in agreement with the value found previously in the section 5.4.3.2.

For the non-isothermal jet, if we assume that the decays are linear, the cold jet has a highest K_1 -value while the hot jet has the lowest. The dynamic virtual origin \bar{x} found for this part are not in very consistency with that found in the previous section. The uncertainties associated to \bar{x} are larger due to the less goodness of the linear fitting compared to the previous one. On the other side, the hot jet has a K_T -value twice as high as that of the cold jet. The thermal virtual origin \bar{x}_T of the cold jet is in agreement with what found previously (uncertainty included). The hot jet has a \bar{x}_T reaching up to 1 m, which is 5 times higher than that found previously. This length is not physically true since it is even located outside of the supply air circuit.

5.4.5 Quantification of jet profiles deformation

5.4.5.1 Deformation indicator definition

For quantifying the deformation of the jet cross-sectional profiles, we define a deformation indicator, noted DI . For a given jet cross-section, this indicator can be used to describe how much the jet is deformed with respect to a circular spread (i.e. an axisym-

metric free jet). The deformation indicator is given by the following formula:

$$DI = \frac{r_h}{r_{Deq}} \quad (5.11)$$

The deformation indicator is computed for each measurement plane, for a set of velocity (and temperature) values. Let's consider a particular velocity value. We saw in the section 5.4.2.1 how to compute the disk-equivalent radius r_{Deq} for that velocity value from the area S_c inside its isocontour. The hydraulic radius⁴ r_h depends on the area S_c inside the isocontour, and on the perimeter P_c of the isocontour (c.f. Figure 5.17):

$$r_h = \frac{2S_c}{P_c} \quad (5.12)$$

The hydraulic radius takes into account the isocontour perimeter, and thus can represent the effective radius corresponding to a given isocontour shape. As shown in the Figure 5.27, for a circular isocontour, we get $r_h = r_{Deq}$, so $DI = 1$. For a distorted isocontour with the same area, the hydraulic radius decreases, so DI gets values below 1.

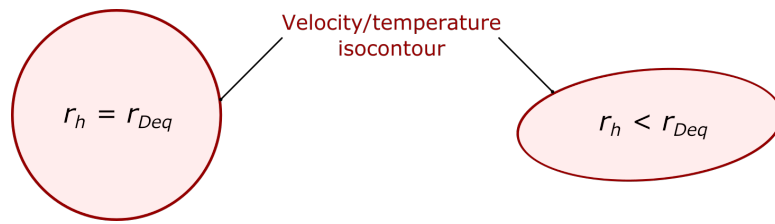


Figure 5.27 – Hydraulic radius and disk-equivalent radius of an isocontour

Hence, DI has an interval value between $[0; 1]$. $DI = 1$ means zero-deformation, a circular contour is obtained. A DI -value near zero means the contour is strongly deformed; but it is rarely the case, at least for an air jet issued from a diffuser with circular opening.

5.4.5.2 Jet profiles deformation evaluation

The DI -values are calculated for different dimensionless velocity and temperature values u/u_m and $\Delta T/\Delta T_m$. Their values are plotted in the Figure 5.28, 5.29 and 5.30 for the isothermal, cold and hot jet case. The scatter points give us the variation of DI of different dimensionless velocity and temperature values. The curve presents the mean value of DI according to each cross-sectional plane.

⁴it should not be confused with the hydraulic radius used in fluid dynamics engineering, which is equal to S/P . In that context, the hydraulic radius is defined as the ratio of the cross-sectional area of a channel or pipe in which a fluid is flowing to the wetted perimeter of the conduit.

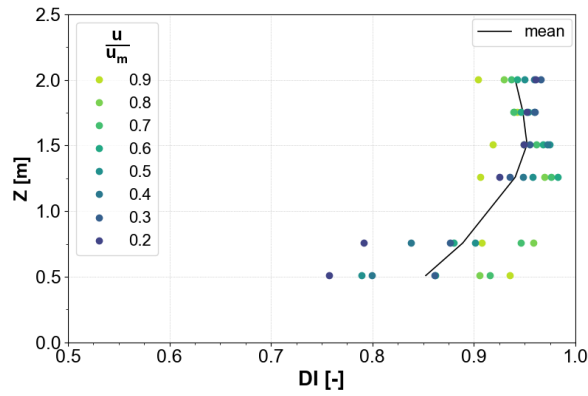
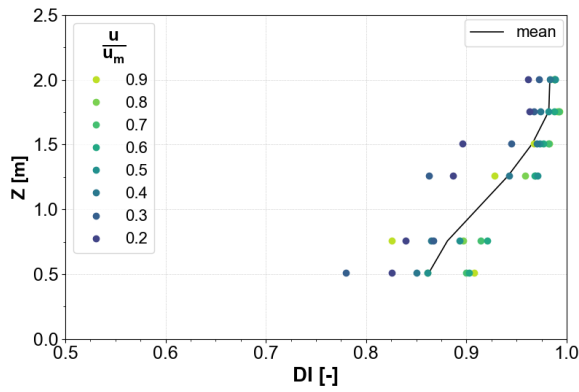
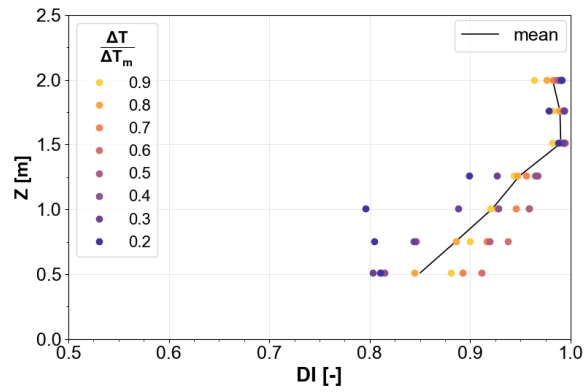


Figure 5.28 – iso_120 - Deformation indicator of velocity profiles

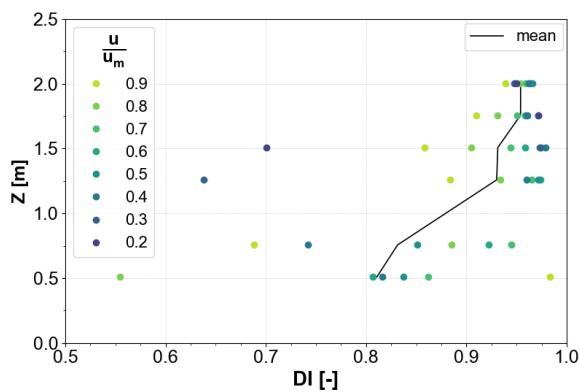


(a) velocity profiles

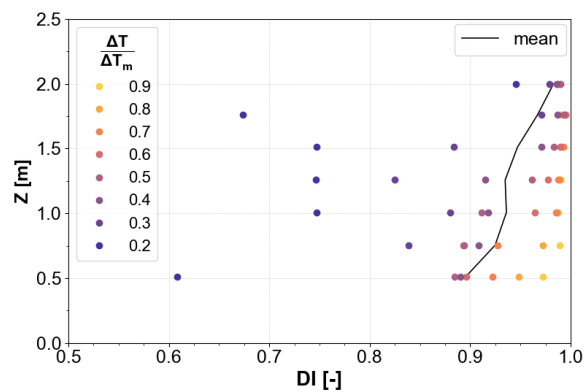


(b) temperature profiles

Figure 5.29 – cold_120 - Deformation indicator of velocity and temperature profiles



(a) velocity profiles



(b) temperature profiles

Figure 5.30 – hot_120 - Deformation indicator of velocity and temperature profiles

For the isothermal jet (Fig. 5.28), the mean-value curves show generally that profiles in the upstream are less deformed than that in the downstream. The plane $Z = 1.5\text{ m}$ is the least deformed with $DI = 0.95$. Then DI decreases from 0.95 to 0.85 when Z decreases from 1.5 to 0.5 m.

Now let's take a closer look to the scatter points in each cross-sectional profile. In the upstream, the jet shows a larger deformation in the core zone than in the boundary zone: the dimensionless velocity value 0.9 is the most deformed in the first four planes. This is the jet core velocity, which is mainly deformed because of the diffuser geometry. Contrariwise, in the two lowest planes, the profile 0.2 is the most deformed due to its interaction with room architectural elements. This is the jet boundary layer which is distorted at this level.

For the cold jet (Fig. 5.29), a same tendency is observed for the mean curve. The velocity profiles show that DI mean values decrease from 0.98 to 0.86 when Z decrease from 2 to 0.5 m. The temperature profiles show a general concordance of DI mean values with the velocity profiles, except for the profile $Z = 1.50\text{ m}$. At this height, the velocity profile at the boundary has already spread out and deformed while the temperature profile still stay closed to the circular shape.

In each cross-section plane, the DI -value tends to decrease when u/u_m and $\Delta T/\Delta T_m$ decrease, i.e. from the jet core zone to the boundary zone. The velocity profiles in the core layer and in the jet upstream are the least deformed due to the effect of buoyancy forces. At the boundary zone, the interaction effects with architectural elements dominate the airflow. These effects include the aspirations of the exhaust mouths, the near side-wall and the gradient temperature at the glazing. Hence, the profiles are likely to be more deformed.

For the hot jet (Fig. 5.30), the mean curves show a similar tendency: less deformed in the upstream and more deformed in the downstream. Following the room height, the DI mean values decrease from about 0.95 to 0.81 when Z decreases. The temperature profiles are less deformed with a mean value decreasing from 0.98 to 0.90.

In each cross-section plane, for the velocity profiles, the DI -value tends to increase when u/u_m decreases. It is the same tendency as the isothermal jet case. The profile 0.2 at $Z = 1.5$ and 1.25 m seem to largely deformed. The profiles below 0.5 at $Z = 0.75$ and 0.5 m have DI -values greater than 1 and are not shown in the graph. This is due to the fact that those contours are not fully connected, as shown in the Fig. H.3. Hence, the DI -value obtained are not exact. For the temperature profiles, the DI -value increases when u/u_m increases. The thermal core layer is the least deformed while the boundary is the most deformed. This result is reasonable given the strong convective transfer at this zone.

5.5 Characterization of the indoor flow turbulence

In this section, we present the characteristics of the turbulence of the airflow. These characteristics were introduced previously in the section 4.6.

5.5.1 Energy spectral density analysis

5.5.1.1 Data processing

A spectral analysis of the turbulent flow implies a treatment of time-series air velocity data signals. In order to obtain a relevant energy spectral density function, we should take into account the two following factors:

- the probe performance: the transfer function and the frequency f_{95} , for which 95% of the fluctuation amplitude can be captured by the probe (c.f. section 3.2.1.4);
- the algorithm used for discrete-time signal processing.

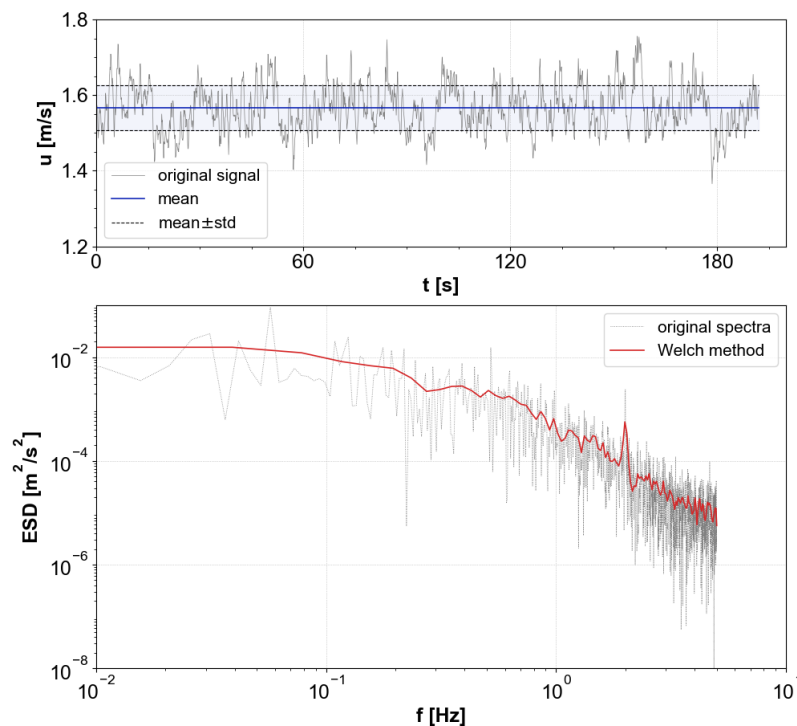


Figure 5.31 – Instantaneous air velocity signals and its energy spectra

The Figure 5.31 shows a preliminary test on an air velocity signal. The first graph plots the instantaneous velocity over time. The mean velocity and the velocity standard deviation are shown. The acquisition frequency was set at $f_s = 10 \text{ Hz}$, the measurement was performed over 190 s. The second graph plots the energy spectral density function of the velocity fluctuation over a range of frequencies.

To express the velocity fluctuation in the frequency-domain, a Fast Fourier Transform

(FFT) method is used. The original spectra is computed using a Discrete Fourier Transform (DFT). The output is Hermitian-symmetric: the negative frequency terms are redundant since they are just the complex conjugates values of the corresponding positive-frequency terms. The transformation is computed up to the Nyquist frequency, which corresponds to $f_s/2 = 5 \text{ Hz}$ in this case.

The spectra using a simple DFT appears to be noisy. This noise is mainly due to the finite data sample. It is not quite useful for the interpretation. Hence, an improvement is performed using the Welch's method (Welch, 1967). Here is the principle of the Welch's method:

1. the data is divided into overlapping segments;
2. a non-rectangular window function is applied to the overlapping segments. This process helps avoiding redundant information due to overlapping data;
3. the energy spectral density of each windowed segment is computed using the DFT, and is then averaged.

The method reduces the variance of the estimated energy spectra, as shown in the Figure 5.31.

The data computing was performed using Python programming language and the *Scipy* library. The functions *signal.periodogram* and *signal.welch* were used to compute the original spectra and the spectra with the Welch method, respectively.

We cannot analyze the energy spectra of all the measurement points in the present document. It would be fastidious and most of the information would be redundant. So we restricted our analysis of the turbulent spectra to three (X,Y) positions. For each (X,Y) position, we will plot the turbulence spectra which correspond to the 6 velocity measurement heights.

The corresponding vertical lines are shown in the Figure 5.32. They are representative for the three zones in the room. The position (1), located right in the diffuser axis, represents the jet core zone; the position (2), located 0.2 m from the diffuser axis, represents the jet boundary zone; and the position (3), located 2 m from the diffuser axis, represents the occupied zone.

5.5.1.2 Energy spectra of the turbulent flow

The Figure 5.33 presents the energy spectra of the velocity fluctuation for the hot jet case, for the three (X,Y) positions mentioned previously. For each figure, the four graphs (a), (b), (c) and (d) show respectively the energy spectra at the air inlet, in the jet core zone, in the jet boundary zone and in the occupied zone. The graph "Air inlet" corresponds to the supply air velocity measured by the anemometer in the inlet circuit (c.f. Fig. 2.11). The same tendencies are observed for the graphs of the two other test cases. Those graphs are given in the Figure H.6, H.7 in the Appendix H to avoid overloading the section.

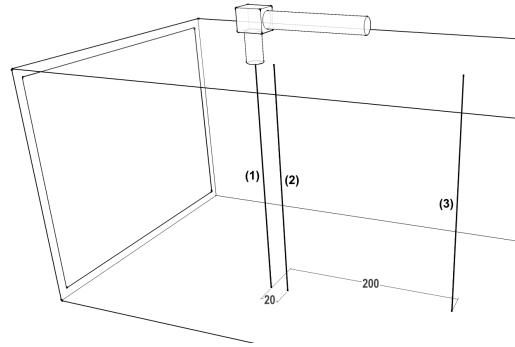


Figure 5.32 – Location of points analyzed

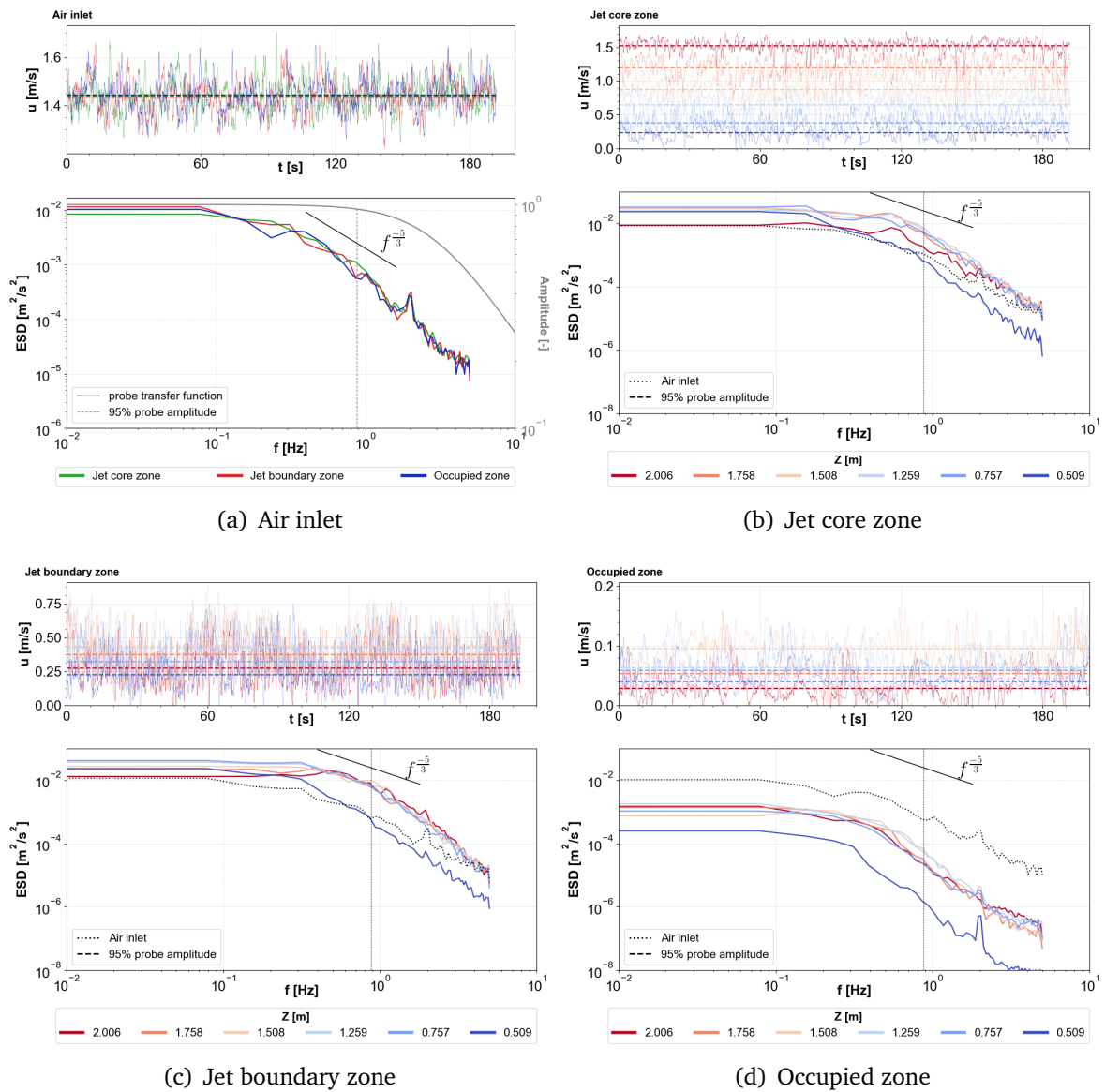


Figure 5.33 – hot_120 - Energy spectral distribution

In the first graph, the transfer function of our probe and the dashed-line corresponding to the frequency f_{95} are shown. But in the other graphs, only the f_{95} -line is shown. We remind that the energy spectral density function describes the distribution of the turbulent kinetic energy with respect to a frequency range. The low-frequency components correspond to large eddies and the higher to smaller eddies. We should note that only a part of the turbulent kinetic energy can be captured with our anemometers. We assume that the data located on the left of the dashed-line are not yet damped by the probe.

In general, all the spectra show that the large eddies are the main contribution to the total turbulent kinetic energy. At the air inlet, the curves have roughly the same distribution, and tend to follow the $f^{-5/3}$ Kolmogorov law (Hanzawa et al., 1987) in the frequency above 0.3 Hz.

At the jet core zone and the jet boundary zone, the velocities contain higher levels of the turbulent kinetic energy compared to those in the air inlet (represented by the dotted-curve). The curves tend to decrease quicker than the $f^{-5/3}$ law. High fluctuations in the high-frequency range can be observed in the core zone compared to the boundary zone. This indicates that more small eddies are generated due to the large velocity gradients in the core zone. At the occupied zone, the distribution of the turbulent kinetic energy is significantly reduced.

In most of the cases, we can observe a peak frequency at about 2 Hz, whose origin remains unknown.

5.5.2 Turbulence intensity and turbulent kinetic energy

5.5.2.1 Data processing

For the same three (X,Y) positions presented above, the Figure 5.34 presents the characteristics of the turbulent flow following the room height, in the three cases. Those characteristics are: the standard deviation of velocity σ_u (a), the turbulent kinetic energy k (b) and the turbulence intensity TI (c). We recall that the equations used for computing those characteristics are (c.f. section 4.6):

$$\sigma_u = \sqrt{\overline{u'^2}} \quad (5.13a)$$

$$k = 0.5\overline{u'^2} \quad (5.13b)$$

$$TI = 100.\sigma_u/\bar{u} \quad (5.13c)$$

where \bar{u} is the mean velocity and u' is the velocity fluctuation.

The standard deviation of the velocity represents the average dispersion of the velocity fluctuation over an interval of time. The turbulent kinetic energy represents the kinetic energy contained in turbulent eddies. The turbulence intensity represents the degree of

turbulence in percentage.

The absolute uncertainty associated to each characteristic is presented in the graph. The calculation is based on the equations (3.3). They are the minimum realistic expanded uncertainty at 95% confidence, proposed by Melikov et al. (2007) which takes into account the various error sources.

5.5.2.2 Results analysis

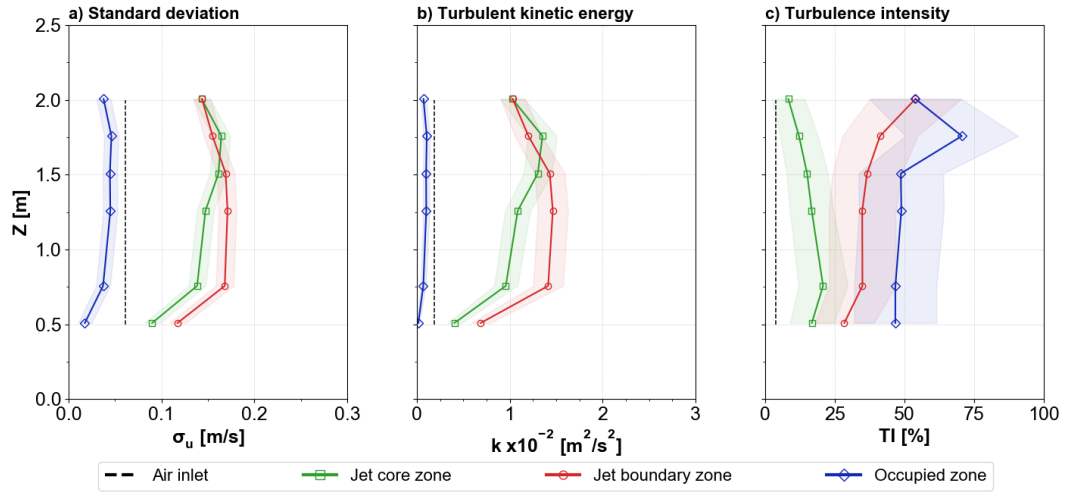
For the standard deviation of the air velocity σ_u and the turbulent kinetic energy k , we can observe a similar tendency for all the three cases. The uncertainty band associated to the turbulent kinetic energy is broader since k is correlated to σ_u by the equation (4.19). Its absolute uncertainty is evaluated to equal to $\pm 2 \cdot \sigma_u \cdot \Delta \sigma_u$.

Between the three zones, the core zone and the boundary zone have the σ_u and k much higher than that in the occupied zone and the air inlet. In the air inlet, the averaged standard deviation is $\sigma_u = 0.066 \text{ m/s}$, the averaged turbulent kinetic energy is $k = 0.22 \times 10^{-2} \text{ m}^2/\text{s}^2$. With regard to the air inlet, we have:

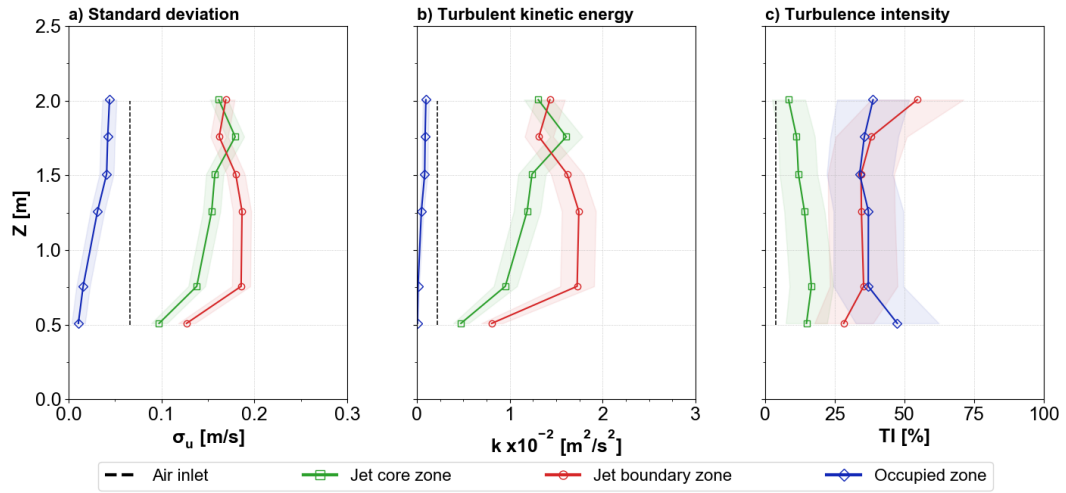
- in the jet core zone: $\sigma_u = 0.148 \text{ m/s}$ (increased by 125%); $k = 1.13 \times 10^{-2} \text{ m}^2/\text{s}^2$ (increased by 400%);
- in the boundary zone: $\sigma_u = 0.168 \text{ m/s}$ (increased by 155%); $k = 1.44 \times 10^{-2} \text{ m}^2/\text{s}^2$ (increased by 550%);
- in the occupied zone: $\sigma_u = 0.031 \text{ m/s}$ (decreased by 50%); $k = 0.06 \times 10^{-2} \text{ m}^2/\text{s}^2$ (decreased by 70%).

A high standard deviation indicates a high velocity fluctuation. According to the turbulence theory (Hinze, 1975), the velocity fluctuation are responsible for the generation of turbulence. At the jet zone, the turbulence is generated due to the mixing interaction between the jet air and the room air and between the jet and the local architectural elements. The turbulence is subsequently transported from the jet zone to the occupied zone by the convection but it is also dissipated by the viscous effect. This may explain the significant lower turbulent kinetic energy of the airflow in the occupied zone compared to the jet zone. These observations are in agreement with results from (Li et al., 1993b). For the averaged turbulence intensity, we have $TI = 14.95\%$ in the jet core zone. In the jet boundary zone, we have $TI = 38.31\%$ (increased by 160%); and in the occupied zone, $TI = 52.58\%$ (increased by 250%). For information, we have $TI = 3.86\%$ in the air inlet.

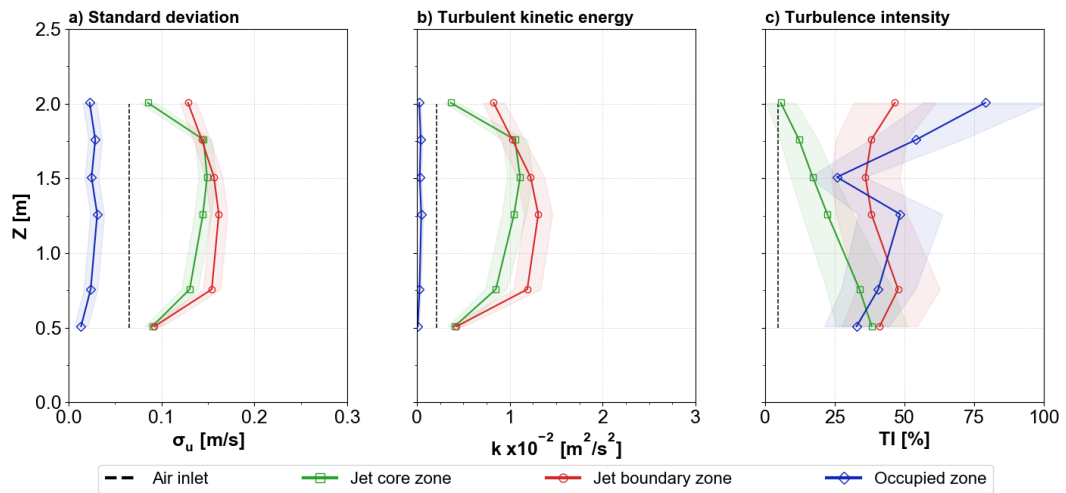
In the contrast with the turbulent kinetic energy, the turbulence intensity is the highest in the occupied zone and the lowest in the jet core zone. This can be explained by the fact that the turbulence intensity is the ratio between the standard deviation and the mean velocity. The mean velocity is much lower in the occupied zone than in the core zone, e.g. an averaged value of 0.07 m/s compared to 1.04 m/s . The mean velocity is increased by



(a) isothermal jet



(b) cold jet



(c) hot jet

Figure 5.34 – Standard deviation of the velocity, turbulent kinetic energy and turbulence intensity

14 times while the standard deviation is only increased by 4 times. Zhang et al. (1992b) concluded that the turbulent kinetic energy is "a more appropriate term to represent the importance of the turbulence effect on the room air motion than the turbulence intensity". The turbulence intensity is required to characterize the draught sensation, though (Fanger et al., 1988, 1989).

Now we analyze the graphs over the room height Z . For the jet core zone, σ_u and k increase by 36% from $Z = 2.0$ m to 1.75 m. They decrease progressively by 30% between $Z = 1.75$ and 0.75 m. Then they decrease drastically by 60% from 0.75 m to 0.5 m. The same tendency is observed for the jet boundary zone, except that σ_u and k are the most higher between $Z = 1.5$ and 0.75 m. In the occupied zone, σ_u and k also decrease with the room height, but not significantly since their magnitude are already too low. For the turbulence intensity, the three cases show a different tendency if we don't take into account the uncertainty bands. In the jet core zone, TI seems to increase when Z decreases. In the jet boundary zone, the isothermal jet and the cold jet show that TI also decrease with Z , but the hot jet does not follow this tendency. In the occupied zone, the mean velocity is too low that we can see a TI reaching up to 80% at some location.

5.5.3 Turbulent kinetic energy spatial distribution

5.5.3.1 Data processing

Here we used the interpolation technique described in section 5.3.1 to interpolate the values of turbulent kinetic energy. The size of the grid and the interpolation step for each direction are given in the Table 5.8.

	X	Y	Z
Interpolation plane size [m]	[-0.7 ; 1.0]	[-1.3 ; 1.0]	[0.1 ; 2.0]
Interpolation step [m]	0.002	0.002	0.125

Table 5.8 – Grid size and interpolation step

5.5.3.2 Description of the turbulent kinetic energy fields over the horizontal planes

The Figure 5.35, 5.36 and 5.37 present the spatial distribution of the turbulent kinetic energy over the horizontal planes, for the three test cases. The center of the diffuser is marked by a black dot. The maximum turbulent kinetic energy value of each plane determined by the interpolation is marked by a red dot. We don't display turbulent kinetic energy values below $k = 0.1 \times 10^{-2} \text{ m}^2/\text{s}^2$ for a better visualization of the transport process.

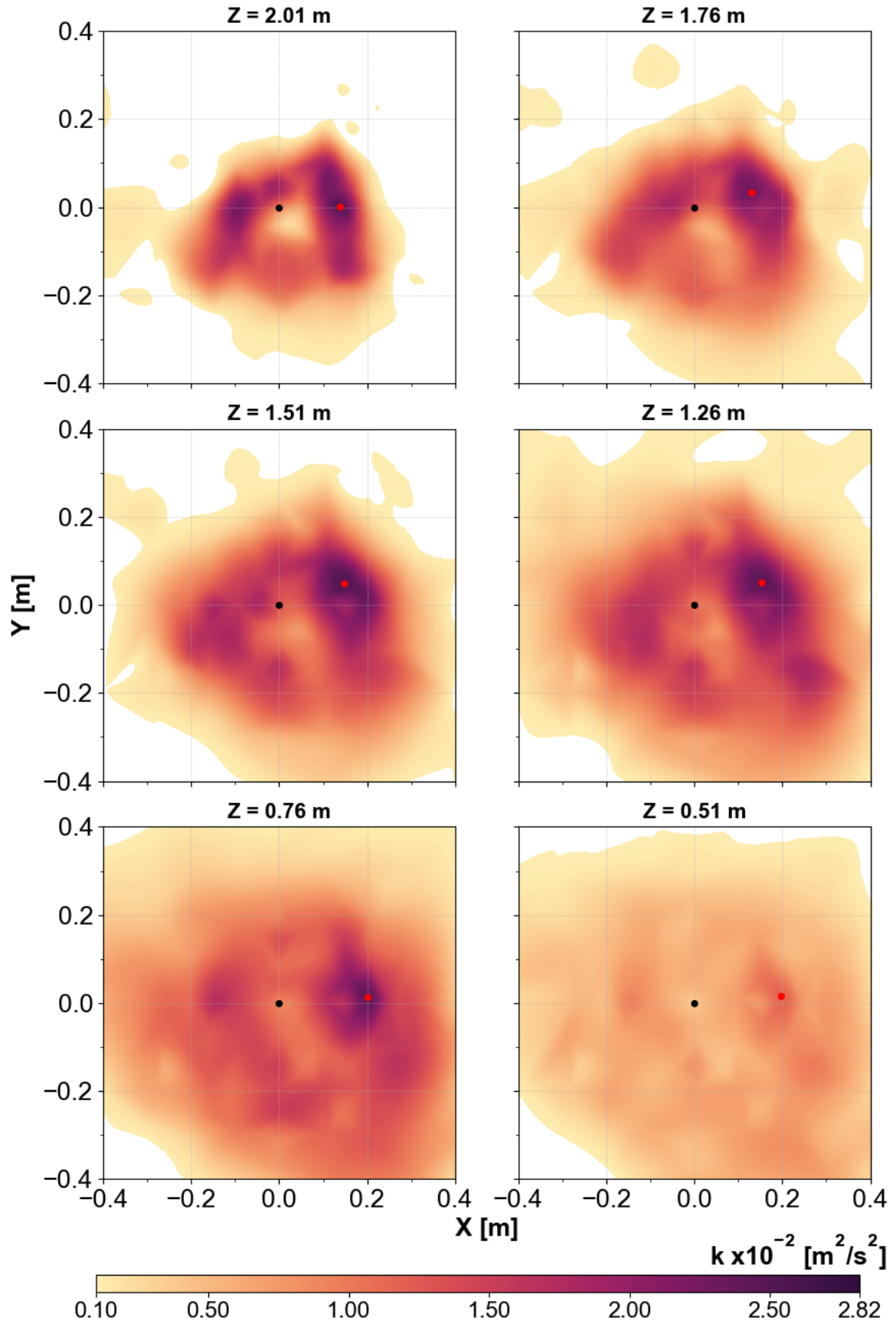


Figure 5.35 – iso_120 - Turbulent kinetic energy fields over the horizontal planes

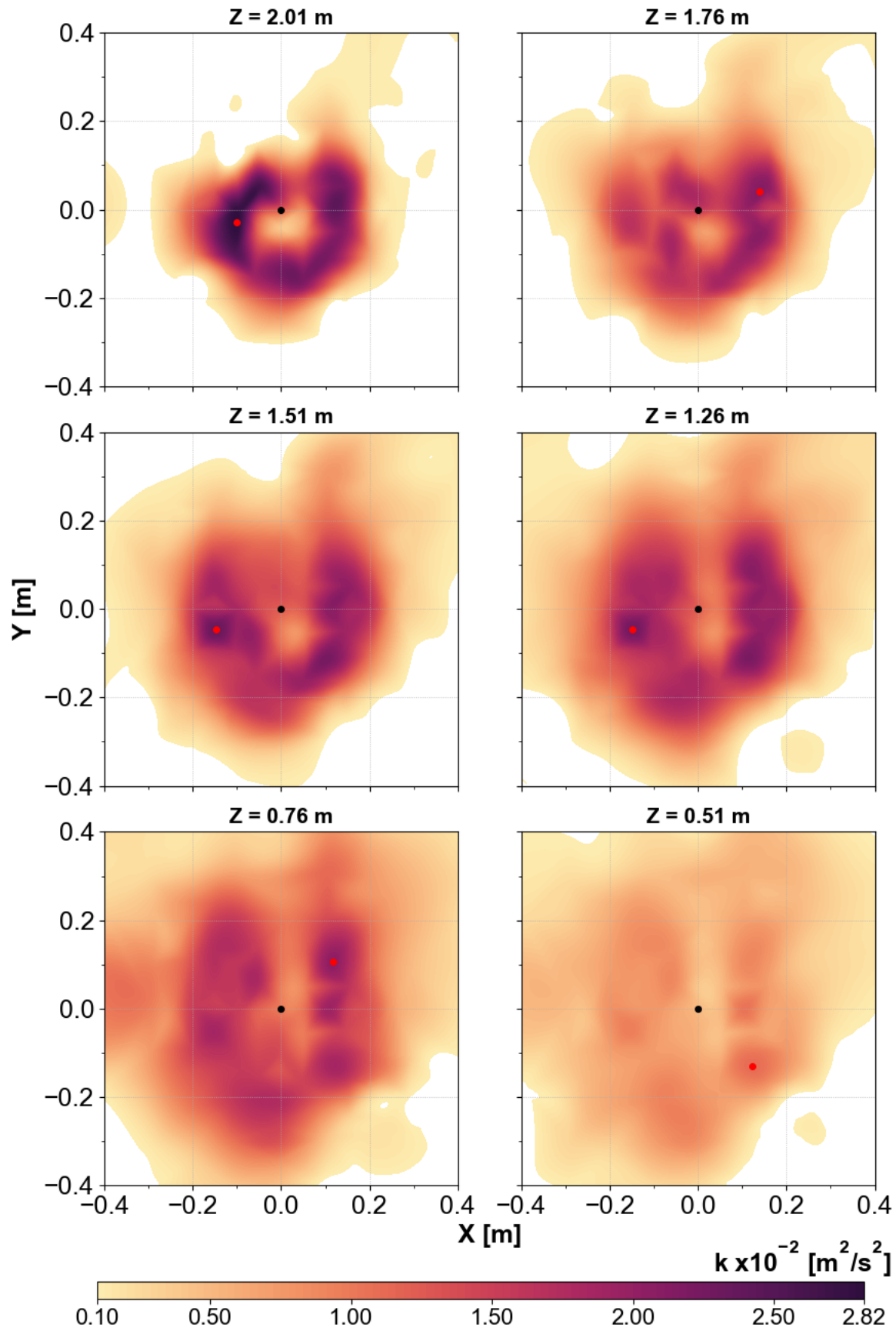


Figure 5.36 – cold_120 - Turbulent kinetic energy fields over the horizontal planes

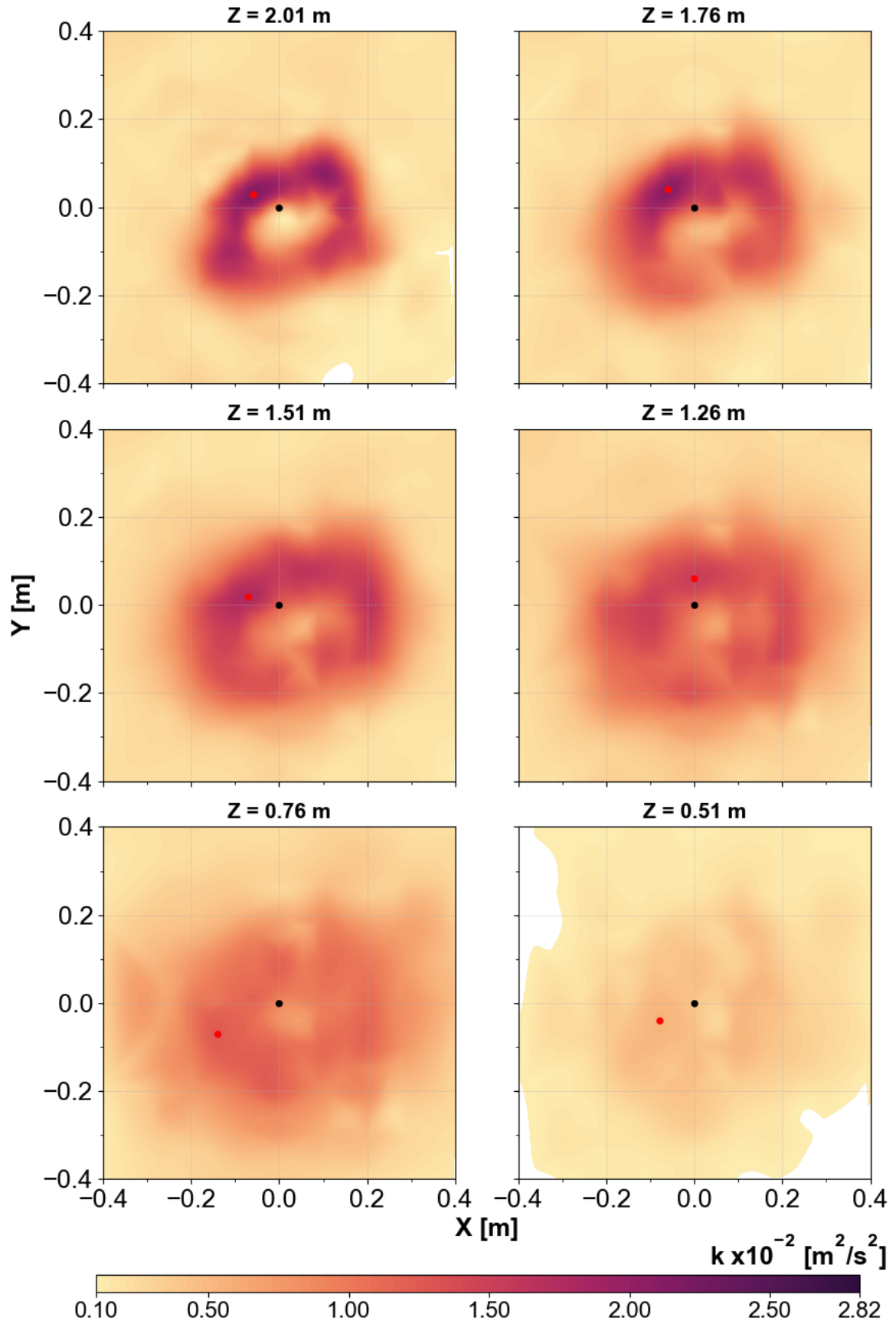


Figure 5.37 – hot_120 - Turbulent kinetic energy fields over the horizontal planes

In general, the same tendency is observed for the three test cases. Around the diffuser axis, a small zone (a diameter of about 0.1 m) is formed, in which the turbulent kinetic energy is low (about $0.3 \times 10^{-2} \text{ m}^2/\text{s}^2$). It is the jet core zone. Around this zone, a zone in the form of a ring contains significantly higher values of the turbulent kinetic energy k . This zone, with an outer diameter reaching 0.2 m, corresponds to the jet boundary zone.

The maximum value of k for each plane is always located in this zone, and it decreases with the room height Z :

- for the isothermal jet: k decreases from $2.48 \times 10^{-2} \text{ m}^2/\text{s}^2$ down to $1.17 \times 10^{-2} \text{ m}^2/\text{s}^2$ (1.1 times lower);
- for the cold jet: k decreases from $2.82 \times 10^{-2} \text{ m}^2/\text{s}^2$ down to $1.11 \times 10^{-2} \text{ m}^2/\text{s}^2$ (2.5 times lower);
- for the hot jet: k decreases from $2.15 \times 10^{-2} \text{ m}^2/\text{s}^2$ down to $0.54 \times 10^{-2} \text{ m}^2/\text{s}^2$ (4 times lower);

The highest turbulent kinetic energy value is found in the cold jet case while the lowest is found in the hot jet case. This observation shows an agreement with a previous statement: the larger the velocity gradient in the jet, the higher the value of the turbulent kinetic energy. Besides, the hot jet seems to have the largest spread among the three cases.

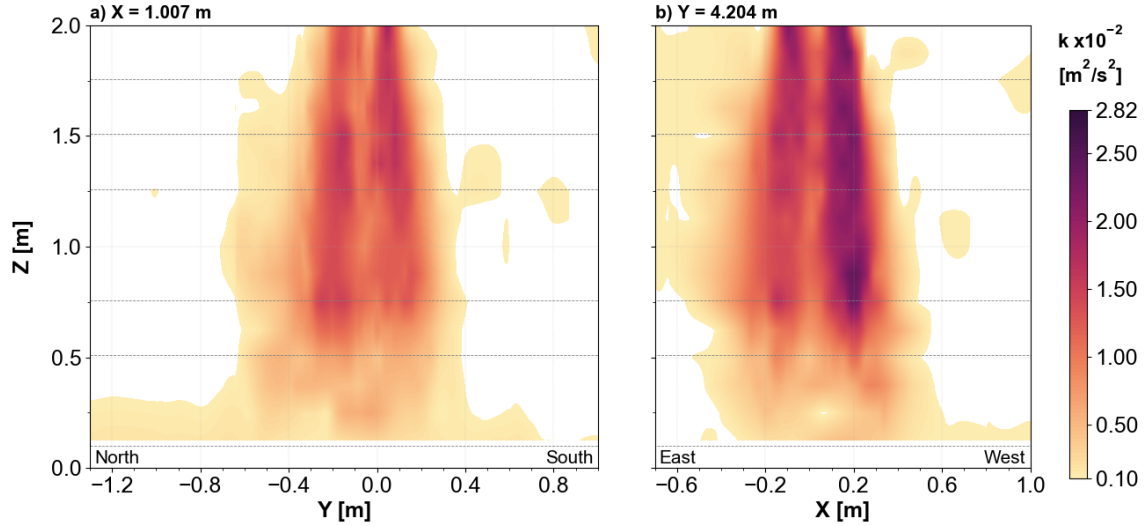
5.5.3.3 Description of the turbulent kinetic energy fields over the vertical planes

The Figure 5.38 present the spatial distribution of the turbulent kinetic energy over the vertical planes, for the three test cases. The two vertical planes shown are those passing through the diffuser axis. The low threshold value is fixed at $k = 0.1 \times 10^{-2} \text{ m}^2/\text{s}^2$. The four directions NSEW and the six measured planes are also indicated.

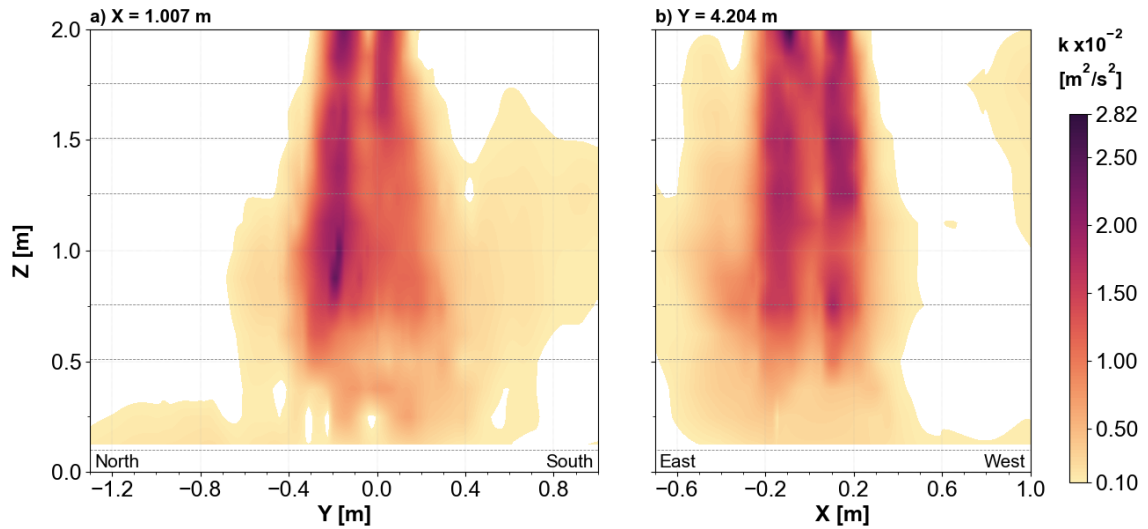
The column near the diffuser axis that captures lower turbulent kinetic energy might be the jet core zone. The neighboring columns that capture much higher turbulent kinetic energy might be the jet boundary zone. Here in these figures, the transport process of the turbulence can be observed.

For the isothermal jet (c.f. Fig. 5.38(a)), the turbulent kinetic energy is transported mainly toward the North side at the floor level and toward the near side East wall at the upper level. On the right figure, in the jet boundary zone, we can observe that the turbulent kinetic energy on the East side is lower than that on the West side. This is due to the transport of the turbulence to the near side wall. The interaction between the jet and the local architectural elements is probably responsible for this tendency of turbulence transport.

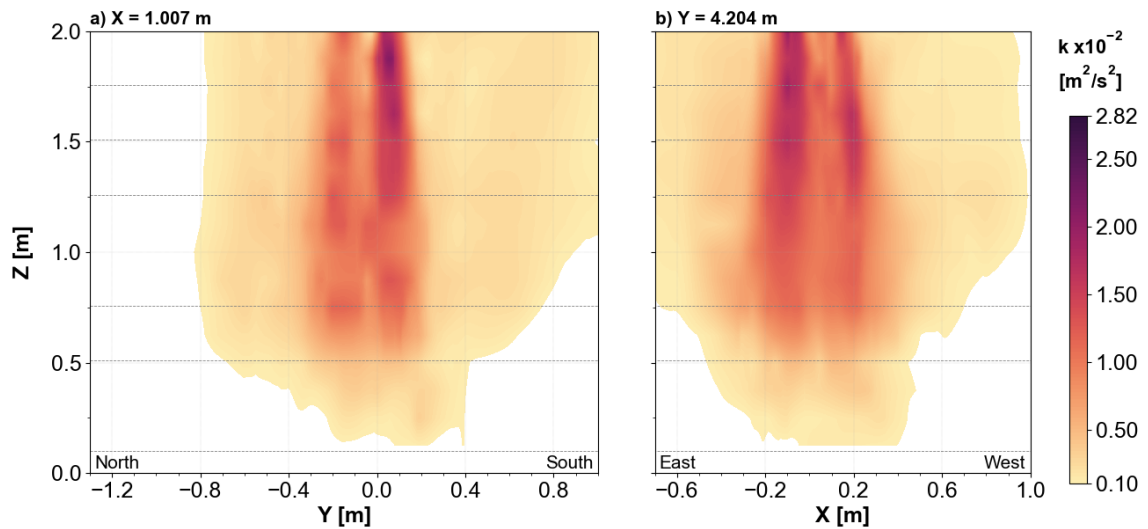
For the cold jet (c.f. Fig. 5.38(b)), a same tendency can be observed with regard to the isothermal case. Furthermore, the turbulent kinetic energy is transported toward



(a) isothermal jet



(b) cold jet



(c) hot jet

Figure 5.38 – Turbulent kinetic energy fields over the vertical planes

the South side. This might be explained by the aspiration effect due to the temperature gradient at the glazing.

For the hot jet (c.f. Fig. 5.38(c)), the spreading of the turbulent kinetic energy is much wider. In the contrast with the two other cases, the turbulent kinetic energy is transported as soon as the air jet entering the room. The turbulent kinetic energy is transported over all directions, but relatively smaller to the North side. The negative-buoyancy effects have indeed supported the convective transfer of the turbulent flow. This turbulence transport might be responsible for the large spread of the hot jet.

5.6 Summary

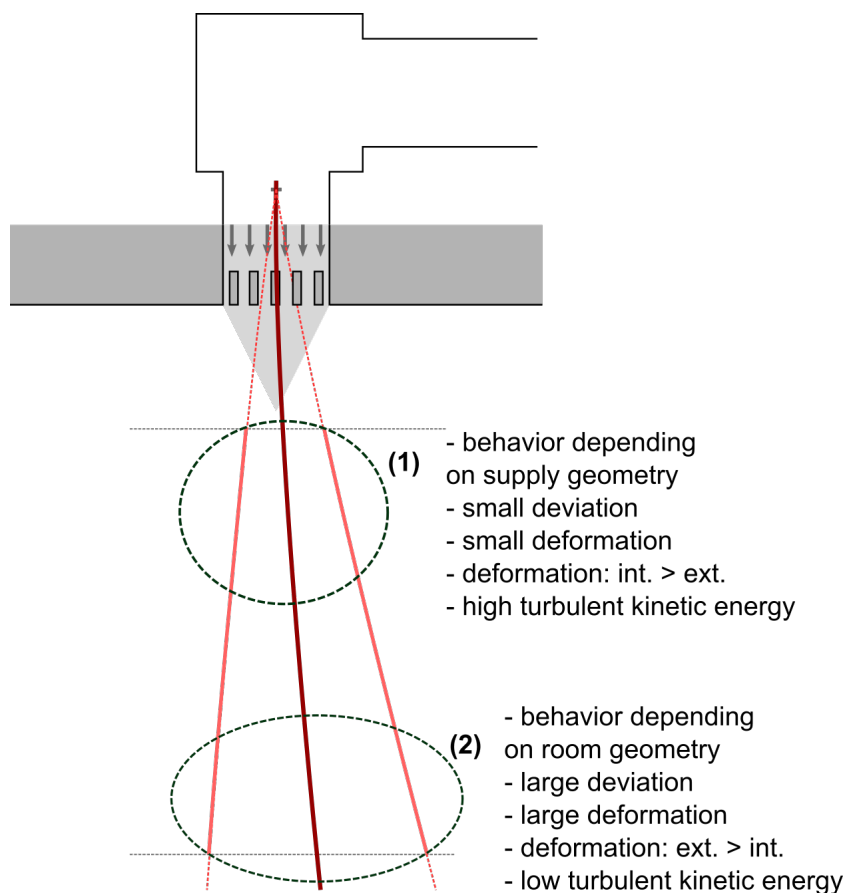


Figure 5.39 – Summary of the jet characterization

In this chapter, we have characterized an asymmetric interacting air jet under three scenarios: isothermal jet, cold jet and hot jet. It is a three-dimensional vertical jet having interaction with local architectural elements.

The behavior and the flow structure of the air jet are visualized. The different characteristics of the air jet are analyzed. Here are some statements that could be made. An illustration is given in the Figure 5.39.

In the jet upstream region (1):

- *the jet behavior is mainly influenced by the supply conditions (plenum, diffuser geometry);*
- *the deviation of the jet trajectory is minimal due to inertia forces;*
- *the distribution of jet cross-sectional profiles is self-similar despite an asymmetric shape;*
- *the cross-sectional velocity and temperature profiles have their DI-value close to 1, the shape deformation is minimal;*
- *the jet is more deformed in the inner zone than the outer zone;*
- *the turbulent kinetic energy is the strongest in the jet boundary zone in this region.*

In the jet downstream region (2):

- *the jet behavior is mainly influenced by the architectural elements such as the near side wall, the glazing and the exhaust mouths; in this region, the hot jet is already disintegrated due to "negative" buoyancy forces;*
- *the isothermal jet trajectory is largely deviated due to the aspiration of exhaust mouths; the cold jet trajectory is the least deviated due to "positive" buoyancy forces;*
- *the jet cross-sectional profiles tend to have a linear distribution instead of a Gaussian distribution;*
- *the jet cross-sectional profiles have their DI-value scattering between 0.6 and 0.95, the shape deformation is more visible;*
- *the jet is more deformed in the outer zone than the inner zone;*
- *the turbulent kinetic energy is already attenuated in this region due to the transport/dissipation process of the turbulence.*

In general for the whole jet, the jet spread coefficients and the jet decay coefficients are quantified:

- *we can assume a linear spreading for both the jet dynamic and thermal layers; the cold jet has the smallest spread whereas the hot jet has the largest spread;*
- *we can also assume a linear decay for both the maximum velocity and the extremum temperature of the air jet.*

Quantification of the condensation rate on cold wall surface

6.1 Introduction

This chapter treats the problem of surface condensation on a cold glazing within a ventilated room. The contents will be presented in the following order:

- section 6.2 presents the physical backgrounds of the condensation phenomenon in general and the dropwise condensation in particular;
- section 6.3 describes the experimental set-up, the metrology and the experimental protocol for the study;
- in section 6.4, the experimental results are presented and discussed.

6.2 Condensation phenomenon: physical backgrounds

Condensation is a thermodynamic phenomenon where fluid in the vapor state changes into the liquid state. It can be seen easily in the nature. For example: after the rain, the vapor of water condenses on the leaves surfaces which have a lower temperature. Or even in your house, when you boil water you may see some droplets of water formed after the condensing the vapor, that is condensation.

The condensation occurs when the temperature of the fluid drops down below the saturation temperature, or when the pressure decreases. The change of pressure affects the temperature of saturation. Scientists have done many researches for years about this phenomenon and tried to apply it in industry and house appliances. There are two modes of condensation: homogeneous condensation and heterogeneous condensation.

6.2.1 Homogeneous and heterogeneous condensation

Homogeneous condensation refers to the condensation of a vapor at the surface of a liquid film, or the condensation of a vapor which forms droplets in the bulk vapor. For this type of condensation, there is usually no foreign particles with a lower temperature which would act as a nucleating agent (dust particles for instance). The lack of the nucleating agent causes difficulties for the vapor to condense at the temperature just below the saturation temperature. It requires a certain level of super-cooling to condensate (cooling below the saturation temperature). The droplet formation will happen when the nucleation site is surrounded by super-cooled vapor.

Heterogeneous condensation refers to the condensation of vapor on a cooled solid surface whose temperature is lower than the saturation temperature of the vapor. For this type of condensation, there are foreign particles of a lower temperature to act as nucleating agents. Thanks to the nucleating agents, this mode of condensation is triggered more easily. Thus, heterogeneous condensation is significantly more common than the homogeneous condensation. The heterogeneous condensation can be divided into two types of condensation: filmwise condensation and dropwise condensation.

A schematic of these two condensation types is given in the Figure 6.1. Filmwise condensation (Fig. 6.1(a)) occurs when the condensate forms a thin liquid film on the cold surface which is well wetted by the liquid. Dropwise condensation (Fig. 6.1(b)) occurs when the condensate forms liquid droplets on the cold surface, which is not well wetted. A well-wetted surface is called a hydrophilic surface while a less or non-wetted surface is called a hydrophobic surface. In the nature, the filmwise type could be more easily observed than the dropwise type since hydrophilic surfaces are more common than hydrophobic surfaces.

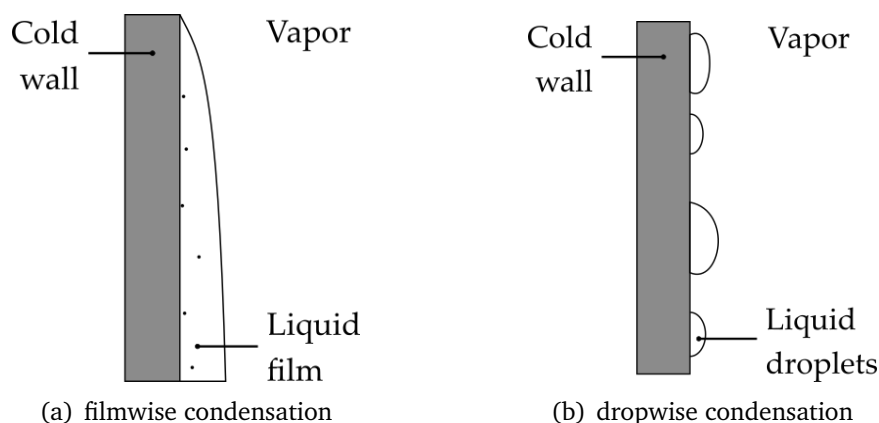


Figure 6.1 – Two types of heterogeneous condensation

6.2.2 Filmwise condensation (FWC)

Nusselt (1916) was the first researcher who built a filmwise condensation model. FWC occurs when a cold wall surface is in contact with a vapor which is near saturation conditions. FWC on a vertical surface occurs when the liquid phase fully wets the surface (in the case of a hydrophilic surface). The liquid film then begins to flow downward due to the gravity. As the condensation proceeds, more and more condensate liquid is added. The film becomes thicker when the condensate moves downward. If the vertical wall is long enough, three different regimes could be observed: the laminar regime, the wavy regime and turbulent regime (Faghri and Zhang, 2006). The local flow regime is determined by the local Reynolds number:

$$Re_{\delta} = \frac{4\dot{m}}{\mu_l} \quad (6.1)$$

where \dot{m} is the mass flow rate of condensate per unit width; μ_l is the dynamic viscosity of the liquid; and δ is the thickness of the film at the region of interest.

The laminar flow regime is always present on the upper part of the surface, when Re_{δ} is approximately below 30. The wavy and turbulent flows may be present depending on a number of properties such as the height of the plate and the thermo-physical properties of the condensing fluid. Kapitza and Kapitza (1949) detailed that the wavy regime can be found when the value for Re is greater than 33. The wavy films may have higher heat transfer coefficients because there is an increase of interfacial area, and furthermore the liquid film can be thinner in some places. If the surface is long enough we could see the turbulent regime which was investigated by McAdams (1954). He found that the regime occurs when the Reynolds number reaches the threshold value of 1800 and if the vapor is stagnant. It should be noted that the critical Reynolds number is smaller if the vapor shear stress is significant. In the turbulent flow, the heat transfer coefficient is even higher than in the wavy because of the increase of interfacial surface and the thinner thickness of the film at some area.

FWC is widely used in industry thanks to its good heat transfer coefficients and its easy promotion (the other modes of condensation may require surface coatings or treatments, which increases the cost). Nevertheless, due to the basic mechanism of FWC, the film acts as a thermal boundary between the wall and the vapor. Thus, the condensation no longer occurs at the cool surface but at the liquid-vapor interface. When the vapor condenses at the interface, the latent heat of the vapor is transferred into the film. This heat energy is then transferred across the thickness of the film, towards the condenser surface. Therefore the rate of condensation and the overall rate of heat transfer are both related to the rate of the heat transfer across the thickness of the film, and as such linked to the thermal conductivity of the liquid and the thickness of the film (Faghri and Zhang,

2006).

6.2.3 Dropwise condensation (DWC)

In contrast with FWC, if the near-saturated vapor is in contact with a not wetted cold wall surface, it may condense in the form of droplets. Having an initial diameter of 10 - 100 μm (Graham and Griffith, 1973), droplets continue to growth in size. Once the droplets reach a certain size, it will roll off of the surface due to the gravity force (in case of a vertical wall).

According to Rose (2002), the dropwise condensation (DWC) was believed to be discovered and analyzed for the first time by Schmidt et al. (1930). Since then, several studies have been undertaken to improve the understanding on the physical theory behind this type of condensation. Here is a list non-exhaustive of those studies:

- the dynamic mechanism of DWC (Umur and Griffith, 1965; Rose, 1967; Mikic, 1969; Yongji et al., 1991; Beysens, 2006; Mei et al., 2011; Hu and Tang, 2014; Castillo et al., 2015)
- the overall heat transfer in DWC (Le Fevre and Rose, 1965; Rose, 1981, 1998; Ma et al., 2001; Vemuri and Kim, 2006; Niu et al., 2017)
- the drop size distributions (Le Fevre and Rose, 1966; Graham and Griffith, 1973; Rose and Glicksman, 1973; Tanaka, 1975; Rose, 1976; Kim and Kim, 2011; Mei et al., 2015)
- the effect of droplet contact angle (Kwok and Neumann, 1999; Cao et al., 2003; Kim and Kim, 2011; Nahavandi and Mehrabani-Zeinabad, 2012)
- the effect of condensing surface properties (McCormick and Westwater, 1965; Griffith and Man Suk Lee, 1967; Aksan and Rose, 1973; Hannemann and Mikic, 1976; Lara and Holtzapple, 2011b)

Until now, the dynamic mechanism and the heat transfer in DWC are of main interests among research concerns. Researchers have found that DWC leads to significantly higher heat transfer coefficient compared to FWC. For example, Lara and Holtzapple (2011a) found that DWC had heat transfer coefficients in the range of 1.6 - 28.6 times greater than FWC. Hannemann and Mikic (1976) found that the DWC heat transfer coefficients were actually in the range of 30 - 40 times greater than in FWC. The magnitude of the ratio between the FWC and DWC heat transfer coefficients seems to be argued, but everyone agreed that the DWC heat transfer coefficients are much higher.

The first model to calculate the heat transfer rate of DWC was proposed by Fatica and Katz (1949) (as mentioned by Vemuri and Kim (2006)). The authors assumed that all the droplets had the same size, were arranged uniformly, and grew by direct condensation in a given area. The uniform spacing assumption was not well consistent. It has been

dealt lately by different researchers, for example: [Le Fevre and Rose \(1965\)](#) derived a time averaged distribution for droplets. However this model only described accurate behaviour for very small and very large droplets. Further details on the overall heat transfer in condensation can be found in this reference ([Carey, 2017](#)).

Droplet formation can be promoted by foreign impurities such as particles. Droplets tend to form at cavities on the surface, whether these cavities are natural or artificially produced by the use of needles or scratches. These impurities act as triggers for droplet nucleation. The amount of nucleation sites on the condensing surface clearly influences the heat transfer. A higher number of nucleation sites leads to a higher amount of droplet growth and therefore increases condensation heat transfer ([Rose, 2002](#)).

Upon formation in the nucleation sites, droplets grow only if they form with a radius that exceeds a certain radius, called minimum equilibrium radius. If a droplet forms with a smaller radius, it will spontaneously destruct. [Faghri and Zhang \(2006\)](#) defined this minimum equilibrium radius r_{min} as follows:

$$r_{min} = \frac{2\sigma_l T_{vap}}{\rho_l h_{lv}(T_{vap} - T_w)} \quad (6.2)$$

where:

- σ_l : the surface tension of the condensing fluid $[N/m]$;
- ρ_l : the liquid droplet density $[kg/m^3]$;
- h_{lv} : the latent heat of condensation (or vaporization) $[J/kg]$;
- T_{vap} : the vapor temperature $[K]$;
- T_w : the cold wall temperature $[K]$;
- and r_{min} is the minimum radius of droplet formation which allows droplets growth $[m]$.

As DWC occurs when a surface does not get wet, the wettability of a surface plays an important role on this type of condensation. The wettability of the surface influences directly the contact angle of a droplet with a surface. These matters will be described in the next section 6.2.4. In practical, surfaces are often coated (often with oils or waxes) in order to promote DWC.

6.2.4 Wettability and contact angle

Wettability is the ability of a solid surface to reduce the surface tension of a liquid in contact with it, so that it spreads over the surface and wets it. The wettability of a surface depends on the free energy of the surface, of the condensate and of the vapor.

The wettability is not a property of just the surface, but also the liquid that composes the condensate and the vapor.

6.2.4.1 Contact angle definition

The wettability of a surface is characterized by the contact angle. It is the angle between the droplet surface and the solid surface along the triple line (i.e. the line at the intersection of the three phases). The liquid droplet is assumed to be in equilibrium state with the solid surface. An illustration of the contact angle is given in the Figure 6.2.

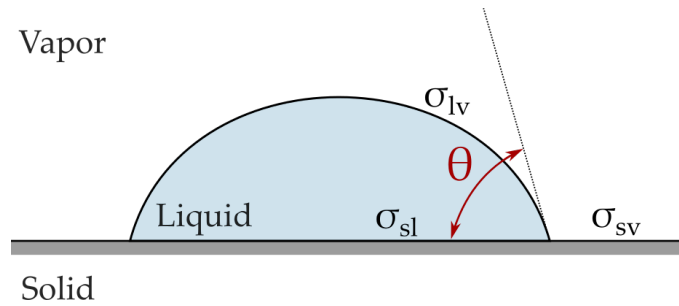


Figure 6.2 – Contact angle and equilibrium of surface tensions of a single droplet

As shown in the figure, the (equilibrium) contact angle, named θ , is the angle through the liquid between the tangent to the liquid-vapor interface and the tangent to the solid surface. The contact angle can be determined based on the three interfacial surface tensions according to the Young's equation (Faghri and Zhang, 2006):

$$\cos \theta = \frac{\sigma_{sv} - \sigma_{sl}}{\sigma_{lv}} \quad (6.3)$$

where σ_{sv} , σ_{sl} and σ_{lv} are respectively the surface tension at the solid-vapor interface, the solid-liquid interface and the liquid-vapor interface. This equation is valid for a liquid droplet on a smooth, insoluble, and homogeneous solid in equilibrium condition.

When there is a relative motion of the liquid droplet over the solid surface, a different contact angle can be expected. When the relative motion stops, an angle different from the apparent (equilibrium) contact angle is seen; it depends upon the direction of the previous motion, i.e. whether it was a receding or advancing surface.

In general, the larger is the contact angle, the lower the wettability of the surface. If the contact angle is smaller than 90° , the surface is hydrophilic, and the FWC is likely to occur. Inversely, if the contact angle is above 90° , the surface is hydrophobic, and the DWC is likely to take place.

It is possible to observe a mixed type of condensation, i.e. DWC and FWC, at the same time. Cao et al. (2003) found experimentally that for contact angles below 70.67° , FWC appears more frequently (as expected for a hydrophilic surface) and for contact angles

above 90° , DWC appears more frequently (as expected for hydrophobic surfaces). A combination of FWC and DWC tends to appear for contact angles between 70.67° and 90° . If the contact angle is near 0° , the surface is considered to be superhydrophilic, while if the contact angle is over 150° , it is considered to be superhydrophobic (Lafuma and Quéré, 2003; Wang and Jiang, 2007).

6.2.4.2 Contact angle measurement

A contact angle in equilibrium condition can be measured from a static drop on a horizontal surface. There are many ways to measure static contact angles such as: the half-angle method, the captive bubble method or the Telescope-Goniometer (Yuan and Lee, 2013; Kyowa, 2018). With the half-angle method (or $\theta/2$ method), the contact angle is determined by the following equation (c.f. Figure 6.3):

$$\theta = 2 \arctan\left(\frac{h}{r}\right) \quad (6.4)$$

where h and r are respectively the height at the droplet apex and the droplet radius. According to Yuan and Lee (2013), this method yields reasonable results for small droplets that are assumed to be unaffected by the effect of the gravitational force. The half-angle method is widely used in practical due to its simplicity (Kyowa, 2018).

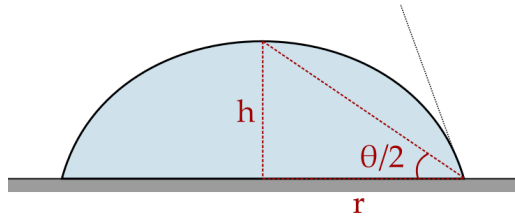


Figure 6.3 – Contact angle measurement using the half-angle method

Examining the contact angle hysteresis is another method of determining the wettability of a surface (Kwok and Neumann, 1999). The contact angle hysteresis is defined as the difference between the advancing contact angle and the receding contact angle. This method is useful for characterizing the surface wettability. There are two ways to measure the contact angle hysteresis:

- The first method is to change the mass of the droplet, by adding or subtracting the liquid in a droplet with a syringe. In the case of adding liquid, firstly we will see an increase of the size of the droplet but the radius of the droplet on the surface remains unchanged. The radius starts to increase slowly after that. The advancing angle is the maximum angle observed during the two phenomenon which are mentioned above. To measure the receding contact, we will do reversely by decreasing the mass of the droplet. The radius of the droplet on the surface will remain con-

stant and then will decrease slowly. The receding angle is the contact angle of the droplet just before the radius starts to decrease.

- The second method is called "Tilting Plate" method. It can be done by looking at the droplet on an inclined surface. We increase the surface angle until the droplet starts to slide. The advancing contact angle is the largest contact angle (the lowest point of the droplet or downward position). The receding contact angle is the smallest angle (the highest position of the droplet or upward position).

Hydrophobic surfaces promote a small contact angle hysteresis while hydrophilic surfaces promote large contact angle hysteresis. The increase of the surface roughness can result in an increase of the surface hydrophobicity, which promotes DWC and increase drastically the heat transfer coefficient of the surface. However, it is not that simple to increase the heat transfer coefficient. [Zhong et al. \(2010\)](#) has observed an opposite trend, the increase of the surface's roughness can actually decrease the rate of heat transfer. This is because of the large contact angle hysteresis which appears. When a droplet falls by the force of gravity it leaves traces behind which are liquid (maybe lines or dots) instead of being wiped. It adds additional thermal resistance to the surface.

Further details on the various techniques that are commonly used to measure contact angles, ranging from the basic one to the most advanced one, can be found in this reference ([Yuan and Lee, 2013](#)).

6.2.5 Thermal resistances in condensation process

When condensation occurs, the heat transfer between the vapor and the solid may be modeled with a series of thermal resistances. Several of these resistances are common for both DWC and FWC, though they have different formal expressions. [Faghri and Zhang \(2006\)](#) pointed out that these thermal resistances are: two conduction resistances in the solid and in the liquid phase, a resistance in the vapor phase, a resistance caused by capillary depression and two interfacial resistances. There are two more resistances that only apply in the case of DWC: a convective resistance and a constriction resistance. Only the case of the DWC will be described in detail, a schematic of these above-mentioned resistances is given in the Figure [6.4](#) for a DWC process.

As shown in the Figure [6.4](#), the thermal resistances, which are associated to the process, comprise:

- R_w : the conductive thermal resistance through the cold wall;
- R_{liq} : the conductive thermal resistance through the liquid droplet;
- R_{cap} : the thermal resistance due to the capillary depression of the equilibrium saturation temperature at the interface;

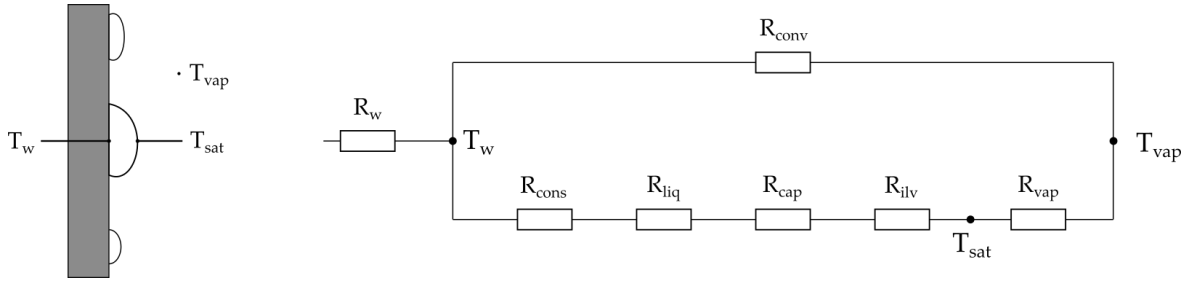


Figure 6.4 – Thermal resistances in a dropwise condensation process

- R_{ilv} : the (interfacial) resistance at the liquid-vapor interface;
- R_{vap} : the resistance in the vapor phase;
- R_{conv} : the convective resistance for the area uncovered by the droplets;
- R_{cons} : the constriction resistance which is due to the non-uniform distribution of the condensate on the surface, and the resulting constriction of the heat flux.

If one assumes that the wall surface temperature T_w is constant over time, the overall temperature difference between the wall surface and the vapor can be expressed as follows:

$$\Delta T_{total} = T_{sat} - T_w = \Delta T_{vap} + \Delta T_{ilv} + \Delta T_{cap} + \Delta T_{liq} + \Delta T_{cons} \quad (6.5)$$

6.2.5.1 Conductive resistance through a droplet

Let's consider a single condensed droplet with radius r_d and contact angle θ on a vertical glazing surface. The latter is not coated and is assumed to be thin enough to have a unique temperature T_w . The contact angle is assumed to be fixed regardless the droplet radius r_d , the vapor temperature T_{vap} and the glazing surface temperature T_w .

Conduction through an individual liquid droplet is a function of the size of the droplet, as well as the thickness of the droplet. The latter, in turn, depends on where the heat enters (at the apex or the base). [Graham and Griffith \(1973\)](#) proposed taking the variable thickness of the liquid into account. The temperature drop ΔT_{liq} that is caused by the resistance of a single droplet, which form a contact angle θ can be determined by the following equation ([Kim and Kim, 2011](#)):

$$\Delta T_{liq} = \frac{q_d \theta}{\lambda_l \cdot 4\pi r_d \sin \theta} \quad (6.6)$$

where:

- q_d : the heat transfer rate through a single droplet [W];
- λ_l : the liquid thermal conductivity [W/m.K];
- r_d : the radius of the droplet [m].

6.2.5.2 Resistance in the vapor

The thermal resistance in the vapor phase is usually ignored in both FWC and DWC because its magnitude is negligible regarding the other resistances. There are some special cases in which the thermal resistance of the vapor would have to be taken into account. Typically, it is the case of a superheated vapor, or the case of condensations of vapor mixtures.

Hence, the temperature drop ΔT_{vap} can be assumed to equal to 0.

6.2.5.3 Interfacial resistance

This resistance is found at the liquid-vapor interface during the condensation process. According to several theoretical and experimental investigations on the condensation heat and mass transfer rate (Rose, 2002), the corresponding heat transfer coefficient across the interface h_{ilv} can be expressed by the following equation:

$$h_{ilv} = \left(\frac{2\alpha}{2-\alpha} \right) \left(\frac{\rho_v h_{lv}^2}{T_{vap}} \right) \sqrt{\frac{M_{vap}}{2\pi R T_{vap}}} \quad (6.7)$$

where:

- α : the accommodation coefficient [-];
- ρ_v : the vapor density [kg/m^3];
- M_{vap} : the molecular mass of the vapor [kg];
- R : the specific gas constant [$J/kg.K$].

The accommodation coefficient α is defined as the fraction of molecules that condense on the interface with respect to the total amount of molecules that act upon the interface. The accommodation coefficient of pure water is close to unity, i.e. $\alpha \simeq 1$. Hence, the temperature drop ΔT_{ilv} across the interface of the considered droplet is obtained by the following relation:

$$\Delta T_{ilv} = \frac{q_d}{h_{ilv} \cdot 2\pi r_d^2 (1 - \cos \theta)} \quad (6.8)$$

Rose (1998) stated that in the case of FWC, when the accommodation coefficient is close to 1, the temperature drop, and the heat transfer resistance as well, are negligible compared to the temperature difference across the liquid film. Liquid metals have accommodation coefficient significantly smaller than 1, so this is the only case where this interfacial resistance must be taken into account.

6.2.5.4 Capillary depression resistance

(Graham and Griffith, 1973) reported the existence of a thermal resistance due to the slight depression of the equilibrium temperature at the interface. The latter falls below the temperature of saturation for a droplet of radius r_d . Therefore, the temperature drop ΔT_{cap} across the capillary depression can be expressed and rearranged as follows (Faghri and Zhang, 2006):

$$\Delta T_{cap} = \frac{2\sigma_l T_{sat}}{\rho_l h_{lv} r_d} = \frac{r_{min}}{r_d} (T_{sat} - T_w) \quad (6.9)$$

where T_{sat} is the vapor temperature of saturation [K], and the equation rearrangement is resulting from combining with the eq. (6.2).

6.2.5.5 Convective resistance

The convective resistance is caused by the vapor that exchanges heat with the cold surface without condensing, i.e. along the liquid-free area between droplets. The heat flux by convection is assumed to be negligible compared to the heat exchanged by the latent heat of vaporization. It could therefore be assumed that this resistance is very large, however as it is parallel with the other resistances previously listed. The contribution of convection to heat transfer can generally be neglected.

6.2.5.6 Constriction resistance

For practical reason, the temperature at the contact surface between the solid and the droplets was assumed as uniformed. In reality, the non-uniform distribution of the droplet-sizes causes a non-uniform distribution of the condensing surface temperature. More precisely, the heat flux will be greater in the areas where the droplets are smaller (Mikic, 1969). Due to the liquid thickness acting as a relatively large thermal resistance, Mikic referred to large-diameter droplets as being "inactive", which create an inactive area. He pointed out that the constriction resistance depends on the surface materials especially on the surface thermal conductivity λ_s . For a copper surface ($\lambda_s = 400 \text{ W/m.K}$), Mikic showed that the constriction resistance represents 20% of the global resistance; while for stainless steel ($\lambda_s = 16 \text{ W/m.K}$), it contributes up to 84% of the global resistance. Takaharu et al. (1991) confirmed experimentally that the constriction resistance rise when the surface thermal conductivity reduces.

Mikic (1969) found that the constriction resistance also depends upon the orientation of the surface. Its value is significantly lower in the case of a vertical condensing surface. Because, in these cases, there are less large droplets as they roll off due to the force of gravity; and as a result, the inactive area reduces consequently. Hence, the temperature drop ΔT_{cons} can be assumed to equal to 0.

6.2.6 Overall heat transfer coefficient and condensation rate

6.2.6.1 Overall heat transfer rate

By substituting the expressions for temperature drops of the various terms, i.e. eq. (6.6), eq. (6.8), eq. (6.9), into the equation (6.5), the overall temperature difference through one droplet during the condensation process can be expressed as follows:

$$\Delta T_{total} = T_{sat} - T_w = \frac{q_d \theta}{\lambda_l \cdot 4\pi r_d \sin \theta} + \frac{q_d}{h_{ilv} \cdot 2\pi r_d^2 (1 - \cos \theta)} + \frac{r_{min}}{r_d} (T_{sat} - T_w) \quad (6.10)$$

(one assumes that the temperature drop in the vapor phase and due to the constriction are neglected compared to the other terms).

The heat transfer rate through a single droplet q_d , formed on a condensing surface with a contact angle θ , can be then deducted as follows:

$$q_d = \Delta T_{total} \cdot 2\pi r_d^2 \frac{1 - \frac{r_{min}}{r_d}}{\frac{r_d \theta}{2\lambda_l} + \frac{1}{h_{ilv}(1 - \cos \theta)}} \quad (6.11)$$

In order to obtain the overall heat transfer rate through all droplets, an integration of q_d over the whole range of droplet size distribution is required (Carey, 2017):

$$q_{tot} = 2\pi \Delta T_{total} \int_{r_{min}}^{r_{max}} N(r_d) r_d^2 \frac{1 - r_{min}/r_d}{\frac{r_d \theta}{2\lambda_l} + \frac{1}{h_{ilv}(1 - \cos \theta)}} d(r_d) \quad (6.12)$$

where $N(r_d)$ represents the droplet size distribution [m^{-3}] and r_{max} is the droplet radius necessary for its fall (fall-off radius).

6.2.6.2 Drop size distribution

As shown in the eq. (6.12), the drop size distribution $N(r_d)$ is the key factor to obtain the overall heat transfer coefficient and the overall heat flux in the DWC process. Yet, its determination is not that simple, especially for droplets having a diameter smaller than 10 μm (Graham and Griffith, 1973). Those droplets are major contributors to the heat transfer in dropwise condensation.

Many researchers have dealt with this topic, as listed previously in the section 6.2.3. According to Kim and Kim (2011), the drop size distribution can be divided into two sub-types: $n(r_d)$ for small droplets and $N(r_d)$ for large droplets. For small droplets that grow mainly by direct condensation, the drop size distribution $n(r_d)$ can be evaluated

with a population balance theory (Tanaka, 1975). For large droplets, since they grow by both direct condensation and coalescence between droplets, an empirical equation can be used to determine the drop size distribution $N(r_d)$ (Le Fevre and Rose, 1966). Kim pointed out that the boundary between $n(r_d)$ and $N(r_d)$ can be defined by an effective radius r_e . They suggested a value of $r_d = r_e = 1 \mu m$ ¹.

Le Fevre and Rose (1966) have established an empirical equation for determining the drop size distribution $N(r_d)$ for larger droplets. This correlation is widely used in the literature:

$$N(r_d) = \frac{1}{3\pi r_d^2 r_{max}} \left(\frac{r_d}{r_{max}} \right)^{\frac{-2}{3}} \quad (6.13)$$

6.2.6.3 Overall heat transfer coefficient

The overall heat transfer coefficient h_{tot} [$W/m^2.K$] can be deduced from the eq. (6.12):

$$h_{tot} = 2\pi \int_{r_{min}}^{r_{max}} N(r_d) r_d^2 \frac{1 - r_{min}/r_d}{\frac{r_d \theta}{2\lambda_l} + \frac{1}{h_{ilv}(1 - \cos \theta)}} d(r_d) \quad (6.14)$$

Substituting the eq. (6.13) into the eq. (6.14), the overall heat transfer coefficient through all the larger droplets in the dropwise condensation process is given by the following equation:

$$h_{tot} = 2\pi \int_{r_{min}}^{r_{max}} \frac{1}{3\pi r_{max}^2} \left(\frac{r_d}{r_{max}} \right)^{\frac{-2}{3}} \frac{1 - r_{min}/r_d}{\frac{r_d \theta}{2\lambda_l} + \frac{1}{h_{ilv}(1 - \cos \theta)}} d(r_d) \quad (6.15)$$

In practice, this theoretical model is rarely used to predict the heat transfer coefficient in DWC process unless we know the droplet size distribution $N(r_d)$. In the case that the studied fluid is water vapor (or steam), Griffith (1983) recommended the following correlation to predict the overall heat transfer coefficient h_{tot} during the DWC process:

$$h_{tot,corr} = \begin{cases} 51104 + 2044.T_{sat} & \text{if } 22^\circ C < T_{sat} < 100^\circ C \\ 255510 & \text{if } T_{sat} > 100^\circ C \end{cases} \quad (6.16)$$

where T_{sat} is the dew point of the vapor.

¹this value falls well below the camera resolution employed for our experimental study, which is about $5 \mu m/px$. Hence, the evaluation of $n(r_d)$ will not be addressed. Further details on the theory of population balance can be found in the following references (Tanaka, 1975; Kim and Kim, 2011)

6.2.6.4 Condensation rate

The condensation rate can be obtained using the following equation (Faghri and Zhang, 2006):

$$\dot{m} = \frac{q_{tot}}{h_{lv}} = \frac{h_{tot}(T_{sat} - T_w)}{h_{lv}} \quad (6.17)$$

where \dot{m} is the time-dependent condensation mass flow rate per unit area of wall surface during the condensation process [$kg/m^2.s$].

6.3 Experimental apparatus and protocol

Here we present the measurement devices used to evaluate the condensation rate on the South facade of the MINIBAT test cell. We remind that this South facade is a vertical glazing whose dimensions are $W \times H = 2.90 \times 2.30 \text{ m}$. Condensation appears on the inner surface of this glazing when the temperature in the climatic chamber is sufficiently cold, and when the relative humidity in the test cell is sufficiently high.

6.3.1 Measurement devices

6.3.1.1 Digital camera

A digital camera equipped with a macro lens was installed inside the test cell. The camera allowed us to capture with precision pictures of condensate droplets on the glazing. The camera is a Nikon D810 digital single-lens reflex (DSLR). Its image sensor has a size of $35.9 \times 24.0 \text{ mm}$ and a resolution of 7360×4912 pixels (36.3 million effective pixels). The ratio pixel/mm is therefore equal to approximately 205 px/mm in both directions.

Dedicated to macro-photography, the lens we used is a $105 \text{ mm f}/2.8$ with a reproduction ratio of 1:1. This ratio means that the size of the image on the sensor is identical to that of the captured object. The minimum focus distance between the object and the image sensor of the DSLR is 314 mm . The lens is equipped with 4 synchronized speed-light flash system designed especially for macro-photography. A picture of the camera is given in the Figure 6.5(a).

The camera is installed inside the test cell, at the South-East lower corner. It is mounted on a tripod and is set to be perpendicular to the glazing. To guarantee the 1:1 reproduction ratio, the camera needs to aim the glazing at the minimum focus distance, i.e. 314 mm precisely. For this purpose, a micrometric positioning sliding plate is used. The plate is installed between the tripod and the camera, as shown in the Figure 6.5(c). It allows to precisely position the camera system with regard to the glazing. The glazing area being captured by the camera is given in the Figure 6.5(d). It has the

dimension of the camera image sensor, which is 35.9 x 24.0 mm.



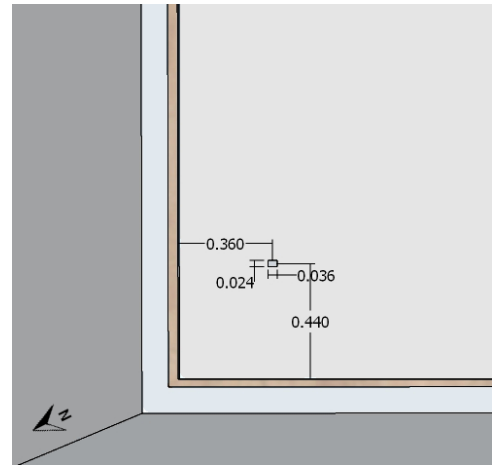
(a) DSLR equipped with macro lens and speed-light flash system



(b) DSLR set-up position



(c) Micrometric positioning sliding plate



(d) captured area (meter unit)

Figure 6.5 – Digital camera system for the condensation study

6.3.1.2 Infrared camera

The glazing area captured has a relative small size. An infrared (IR) camera is installed to monitor the surface temperature of the corresponding glazing area during the condensation test. The IR camera we used is a FLIR T420bx. It supports a temperature measuring range between -20 °C and 350 °C. According to the manufacturer, the IR camera has an absolute accuracy of ± 2 °C. The IR camera is mounted on a tripod and is set up inside the climatic chamber, as shown in the Figure 6.6(a).

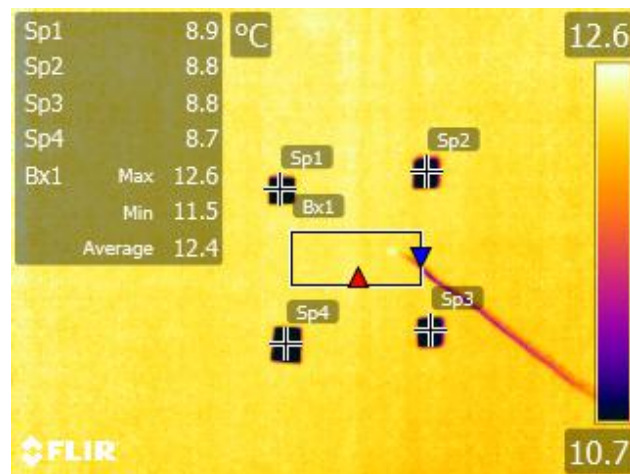
Despite its advantageous characteristic of whole-field measurements, the infrared measurement technique is constrained by its high uncertainty (Sandberg, 2007), and by its sensitivity to the reflected flux radiation (Datcu et al., 2005). More precisely, in our case, the IR camera was used to measure the surface temperature of a glazing, which reflects part of the radiation received. This reflected flux radiation is subsequently detected back by the camera sensor and thus the resulting temperature data is erroneous.

Hence, a procedure for data correction is performed, as suggested by Rodler (2014). Four small pieces of aluminum foil tape were fixed at the four corner, as can be seen in the upper left of the Figure 6.6(a). They were used as correction materials for determining the real temperature of the glazing surface, as shown in the Figure 6.6(b). Besides, a reference K-type thermocouple $\varnothing 80 \mu m$ is used to deduct the relative error between the temperature data obtained by the IR camera and the thermocouple.

A sample of the image captured by the IR camera is given in the Figure 6.6(b). The surface temperatures of the four aluminum foils are given by the four points from *Sp1* to *Sp4*. The corrected surface temperature of the glazing area is given by the zone *Bx1*. Here in this figure, an error source is introduced because the IR camera also captures the temperature of the thermocouple wire. That is why the IR camera is fixed in inclined position to reduce the measurement error.



(a) IR camera set-up position



(b) image captured by the IR camera

Figure 6.6 – Location of the IR camera and a photo captured sample

6.3.1.3 Supervision camera

A supervision camera is installed in the climatic chamber to detect the appearance and the evolution of the condensation on the glazing. The camera we used is a TRENDnet TV-IP320PI. A picture of the supervision camera is given in the Figure 6.7(a).

The camera has a near-infrared illumination, which allows it to operate in complete dark-

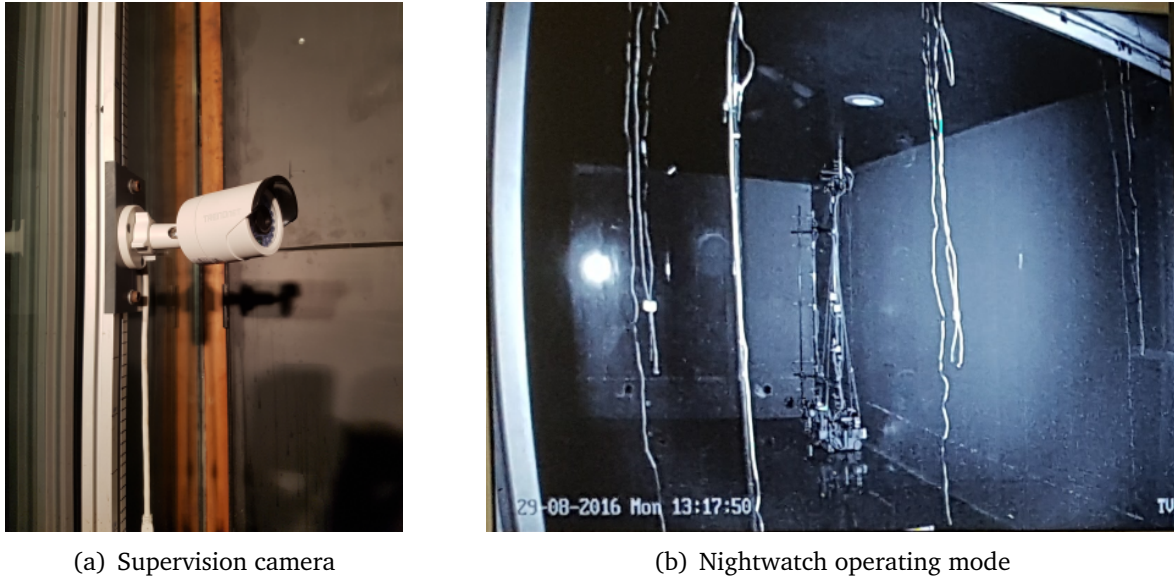


Figure 6.7 – Supervision camera system for the test cell

ness, and to see through the glazing, as shown in the Figure 6.7(b). Besides, the camera has an IP66² outdoor weather rating, which allows it to operate in a temperature range from -30 to 60 °C.

6.3.2 Experimental protocol

For this study, MINIBAT was put under a winter scenario, i.e. an outdoor low temperature along with an indoor heated air. The test cell was put on a few days for establishing a steady state without condensation. At this initial condition, steam was already injected into the test cell, but was kept at appropriate level to avoid condensation.

Afterward, the air supply set point was changed to the test condition, for which the air humidity level is higher. As presented previously in the section 2.3.3.3, steam was produced using a humidity generator, and was injected into the room ambient air through the hot air jet. This configuration allows to promote significantly the apparition of the condensation on the glazing surface, which is in contact with both the outdoor cold air and the indoor humid hot air.

From this time, the DSLR camera and the IR camera began capturing the glazing surface area, at a regular time interval. The IR camera was controlled remotely using a software named FLIR Tools. The temperature acquisition time step was fixed at 5 minutes. The DSLR camera was controlled remotely using a software named Nikon Camera Control Pro 2. The photo acquisition time step was fixed at 60 seconds. A post-treatment of these photos allows us to quantify the condensate rate of droplets on the glazing.

²International Protection marking

For the indoor air metrology, the mobile robot was kept immobilized. It was placed close to the glazing in order to record the evolution of the air velocity, temperature and humidity over time. The data recording time step was set at 60 seconds. The data recording begun 15 minutes before setting up the test condition. The location of the robot can be seen in the Figure 6.5(b).

6.3.3 Data post-treatment using image processing methods

6.3.3.1 Condensation rate

The post treatment aims to determine the condensation rate over the glazing surface from the series of condensation pictures taken by the camera.

The condensation rate \dot{m} is the time evolution of the mass of condensed fluid attached to the glazing per unit of area. It is expressed in $kg/m^2.s$. To determine experimentally the condensation rate we must evaluate the mass of water vapor formed on the glazing for each picture. This section describes how we proceed to evaluate this mass.

The condensate mass over a portion of glazing surface is the sum of the droplet mass on this area. The mass of a single droplet is:

$$m_d = \rho_w V_d \quad (6.18)$$

The water density at the atmospheric pressure ρ_w is given in tables as a function of the water temperature. We must determine the volume of the droplets from the pictures.

6.3.3.2 Droplet volume as a function of the contact surface

Let's assume that the shape of a droplet is a perfect truncated sphere. The Figure 6.8 presents the different variables used to determine the droplet volume.

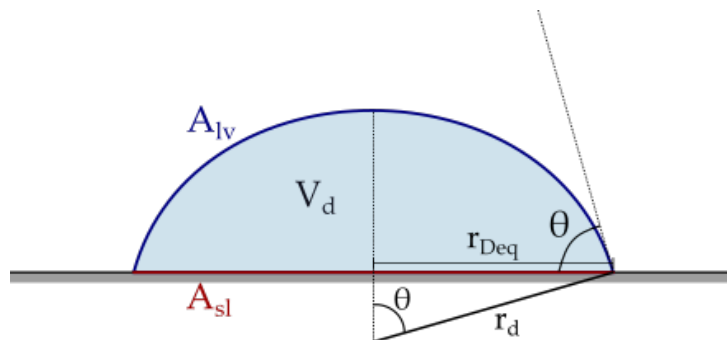


Figure 6.8 – Contact angle and droplet radius

In the figure, we have:

- A_{lv} : the surface area shared by the solid-liquid interface [m^2];
- A_{sl} : the surface area shared by the solid-liquid interface [m^2];
- r_{Deq} : the equivalent radius of the surface area A_{sl} [m];
- r_d : the droplet radius [m];
- θ : the droplet contact angle [$^\circ$].

The above-mentioned surface area can be determined as follows:

$$A_{sl} = \pi r_{Deq}^2 = \pi r_d^2 (1 - \cos^2 \theta) \quad (6.19a)$$

$$A_{lv} = 2\pi r_d^2 (1 - \cos \theta) \quad (6.19b)$$

Let's assume that we know the area of the contact surface between the droplet and the solid surface A_{sl} . The shape of this surface is a perfect disk whose radius is equal to r_{Deq} . The volume of the truncated sphere, V_d [m^3], is given by the following equation (Faghri and Zhang, 2006):

$$V_d = \frac{\pi r_d^3}{3} (2 - 3 \cos \theta + \cos^3 \theta) \quad (6.20)$$

where $r_d = r_{Deq} / \sin \theta$. The main assumption of our data treatment is that we consider that this equation is also valid for droplets whose shape is not a perfect truncated sphere.

Thus, once we know the contact angle between the glazing and water droplet, we just need to determine the contact surface of each droplet present in the picture, and we get the volume of each droplet from the equation (6.20).

6.3.3.3 Determination of the contact angle

As mentioned previously, the contact angle, formed by a liquid droplet and a solid surface, depends only on the properties of the surface and the condensed liquid (c.f. section 6.2.4). In our case, these are glazing surface and condensed water vapor. Hence, it seems reasonable to assume that the contact angle remains constant regardless of the droplet size and the surface and vapor temperatures.

Based on this assumption, a side test was conducted to achieve the contact angle information. For this test, we use a glazing sample, which has the same characteristics with the glazing installed in the test cell. Its surface is also cleaned with the same acetone product used to clean the glazing surface in the test cell.

The glazing sample is fixed initially at the horizontal position. We use a pipette to drop off some droplet samples onto the surface. Then the glazing surface is put at the vertical position. The DSLR is fixed at the side view position to capture images of the droplet. The contact angle is computed using the half-angle method (c.f. section 6.2.4.2). The whole test is repeated for a several time to deduct an averaged value of the contact angle.

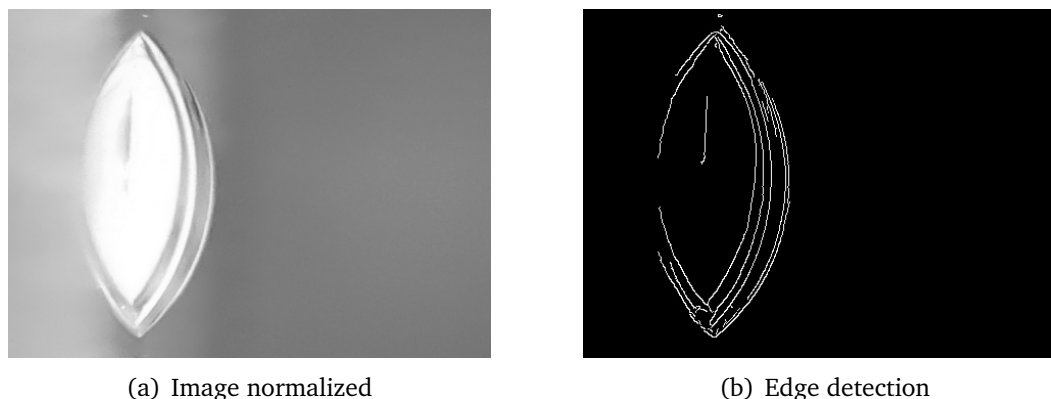


Figure 6.9 – Determination of the contact angle

The Figure 6.9(a) presents an example of the droplet captured. The function `cv2.Canny()` (OpenCV³ for Python) is used to detect edges in the image. The Figure 6.9(b) presents the image processed. In this example, the contact angle is about 59.5° . This value is in agreement with Kwok and Neumann (1999) study's. In general, without surface treatment, a glazing surface is rather hydrophilic than hydrophobic. Hence, a contact angle smaller than 90° should be obtained.

6.3.3.4 Determination of the contact surface between the droplets and the solid surface: image processing

The total volume of condensed droplets can be determined experimentally using the image acquisition technique. For each test campaign, image series of the evolution of condensed droplets over time are obtained. A post-treatment computing method is then employed to extract the necessary information to calculate the droplets volume. An example of an image captured is given in the Figure 6.10.

On the left we can observe thousands of droplets of various size on a glazing surface of $35.9 \times 24 \text{ mm}^2$. To obtain a closer look of droplets, the right photo shows a cropped image of area $5 \times 5 \text{ mm}^2$. We can notice the coexistence of the very small droplets and the larger droplets. The small droplets, which grow by direct condensation, have a quasi-circular shape. The large droplets, which form by the coalescence between neighboring droplets, have approximately an oval shape.

The image processing method for finding and analyzing the droplet contours include the following steps. An illustration of these steps are given in the Figure 6.11. The raw image taken as example is the one with dimension $5 \times 5 \text{ mm}$ presented above.

1. Images histogram equalization

³Open Source Computer Vision

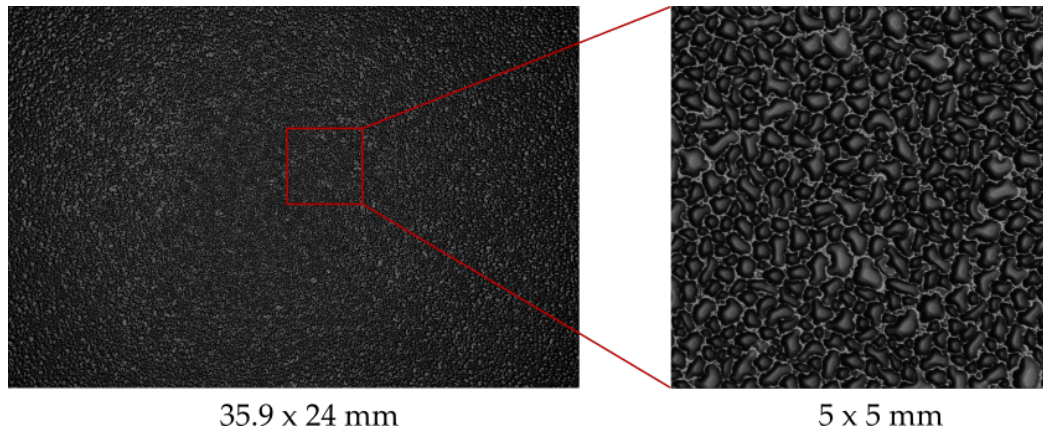


Figure 6.10 – Example of captured image of droplets on cold glazing

2. Images noise filtering
3. Images binarization (thresholding)
4. Images contours finding
5. Contours area and equivalent radius calculation.

(a) *Histogram equalization* (Fig. 6.11(a)): the raw image shown in the Figure 6.10 has a brighter zone in the center and a darker zone in the corner, i.e. a non-homogeneous contrast. This is due to the flash-lights system that was not able to illuminate the whole captured area. Hence, the histogram equalization method allows to adjust the image global contrast so that areas of lower local contrast can gain a higher contrast (Russ and Neal, 2017). The resulting image is given in the Figure 6.11(a), which show a clear difference in terms of global contrast compared to the raw image (Fig. 6.10). Through this adjustment, the luminous intensities can be better distributed on the image's histogram, as shown in the Figure 6.12(a).

(b) *Noise filtering* (Fig. 6.11(b)): a filter can be applied to reduce the noise content, which can potentially be detected later as droplets edges. Nevertheless, since high frequency contents comprises both edges and noises, a simple Gaussian low-pass filter will help removing noises but also undesirably blurring the edges (OpenCV, 2018c). Hence, the benefit of the bilateral filter, whose current name has been given by Tomasi and Manduchi (1998). The bilateral filtering technique is basically a non-linear Gaussian filter, which demonstrates its highly effectiveness in noise removal while preserving sharp edges; as shown in the Figure 6.11(b). Further readings on this technique can be found in this comprehensive reference (Paris et al., 2007).

(c) *Image thresholding* (Fig. 6.11(c)): the filtered image goes through the thresholding process. This technique is used for image binarization, i.e. for reducing grayscale images into binary image with only two levels: black or white. This process is essential for increasing the accuracy of the next step, which is the contours finding. There exist several

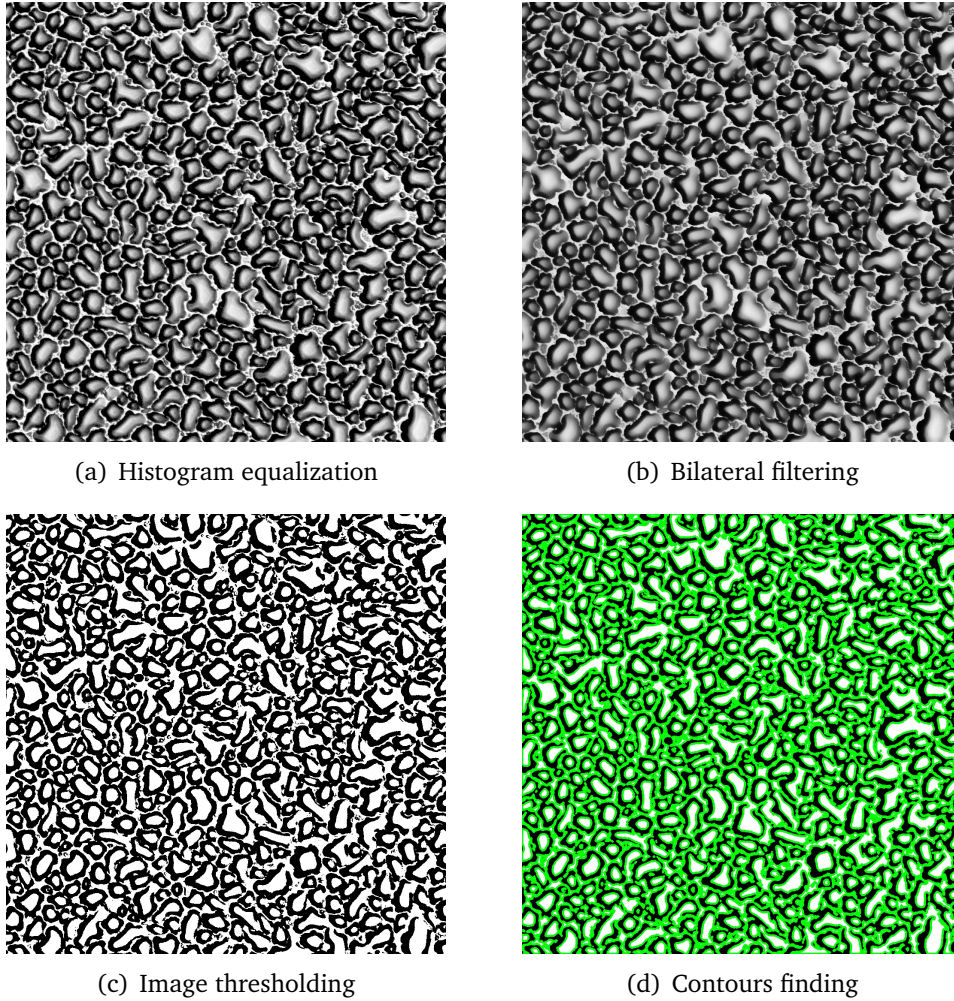


Figure 6.11 – Image processing steps for droplets contours finding

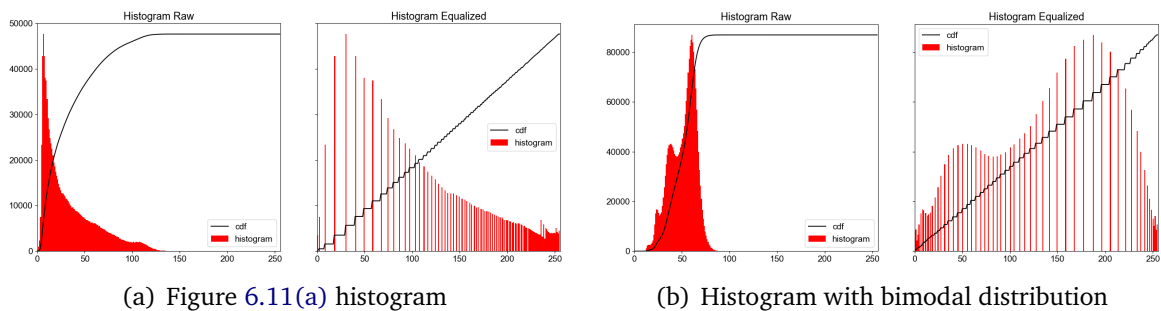


Figure 6.12 – Image histogram before and after equalization

methods for thresholding an image (OpenCV, 2018b):

- the simplest one is to assign an unique "user-defined" value as threshold value for the whole image, so this is called the "Global (or Simple) Thresholding";
- when the illuminating conditions vary from an image to another, an adaptive thresholding method might be more relevant. For this, the threshold value is calculated

locally for small regions of the image while taking into account the neighborhood region. The OpenCV package proposes two adaptive threshold algorithm:

- (1) the threshold value $T(x, y)$ at an image coordinate (x, y) is a mean of the "user-defined" area size in the neighborhood;
- (2) the threshold value $T(x, y)$ is a weighted sum (cross-correlation with a Gaussian window) of the "user-defined" area size in the neighborhood. These two methods are called "Adaptive Mean Thresholding" and "Adaptive Gaussian Thresholding" respectively;

- now let's consider a bimodal image, i.e. an image whose histogram distribution possesses two peaks after being equalized, as can be seen in the Figure 6.12(b). Dealing with such kind of images, a thresholding technique called Otsu's binarization method (Otsu, 1979) appears to be quite relevant and effective. For this, the threshold value is calculated based on the bimodal image histogram as the middle value between the two peaks, approximately.

(d) *Contours finding* (Fig. 6.11(d)): the final step consists in finding all the possible contours in the given image (OpenCV, 2018a). The contours detected are colored in green color for a better visualization. Once these contours retrieved, the following information can be extracted: the number of contours detected that correspond to the total number of droplets; the area and the equivalent radius of each droplet; as well as the minimum and maximum equivalent radius of all these droplets.

The whole process are computed using the OpenCV package for Python. In this example, the function `cv2.bilateralFilter()` is used to filter the image noise. We perform the image binarization with the Adaptive Gaussian thresholding method: the function `cv2.adaptiveThreshold()` with the `cv2.ADAPTIVE_THRESH_GAUSSIAN_C` argument is used. The function `cv2.findContours()` is used to find the image contours. Optionally, those contours can be drawn using the function `cv2.drawContours()`. The area of each contour is computed using the function `cv2.contourArea()`.

6.4 Experimental results and discussions

6.4.1 Experimental conditions

6.4.1.1 Description of the test case

Some preliminary tests were carried out to determine the appropriate test condition. We recall that the condensation measurements comprise an initial steady state without condensation, followed by an increase of the supply air humidity set point. The set points for the initial condition and the test condition are listed in the Table 6.1.

The supply airflow rate was set at $100 \text{ m}^3/\text{h}$. The condensation occurred quite slowly, as well as the condensate growth rate. For instance, a series of ten images captured every 60 seconds showed no significant change. Hence, we opted for test cases with the supply airflow rate of $150 \text{ m}^3/\text{h}$, which gives the maximum restricted indoor air velocity in the jet region (c.f. section 3.2.1.1). The air supply temperature set point is fixed at 28°C . The vapor specific humidity set point increases from 9 g/kg_{as} to 14 g/kg_{as} between the two conditions. The vapor specific humidity set point cannot go further than 14 g/kg_{as} , otherwise significant fluctuations can be observed due to the limited performance of the steam generator.

Five test cases have been undertaken, but only one is analyzed and discussed in detail in this chapter. It will be noted "cond_150" from now on, for the sake of simplicity.

6.4.1.2 Measurement of the boundary conditions

The boundary conditions were measured during the whole duration of the test. The measurement results are listed in the Table 6.2 and the Table 6.3. The Figure 6.13 presents the boundary conditions evolution over time, only for the period of the condensation test. More details on the evolution over time of the experimental conditions are given in the Appendix E.

For the temperature evolution (c.f. Figure 6.13(a)), the low standard deviations reveal a reasonable stability of the temperature boundary conditions around the test cell. On the south facade, the standard deviation is much higher (0.46°C). Its temperature is slightly increased (about 1°C) during the test. This is due to the condensation process which increase the temperature (c.f. section 6.2.3).

For the air supply characteristics (c.f. Figure 6.13(b)), the set points for the airflow rate and the air temperature remain unchanged for the test. The mean air specific humidity increase from 9.06 g/kg_{as} to 14.07 g/kg_{as} with a respective standard deviation of 1.20 g/kg_{as} and 1.66 g/kg_{as} .

	Set points				
	$Q_{0,sp}$ [m^3/h]	$T_{0,sp}$ [$^{\circ}C$]	$r_{0,sp}$ [g/kg_{as}]	$T_{cc,sp}$ [$^{\circ}C$]	$T_{tbz,sp}$ [$^{\circ}C$]
Initial condition	150	28	9	6	21
Test condition	150	28	14	6	21

Table 6.1 – MINIBAT set points for the condensation test

Where: $Q_{0,sp}$ - airflow rate set point; $T_{0,sp}$ - supply air temperature set point;

$r_{0,sp}$ - supply air specific humidity set point;

$T_{cc,sp}$ - climatic chamber ventilation temperature set point;

$T_{tbz,sp}$ - thermal buffer zone ventilation temperature set point

Category - Name		Symbol	cond_150	
			Mean	SDEV
Wall temperature	Ceiling	$T_{SI,C}$	21.38	0.20
	Floor	$T_{SI,F}$	21.09	0.19
	South	$T_{SI,GL}$	15.29	0.46
	North	$T_{SI,NW}$	21.29	0.21
	East	$T_{SI,EW}$	21.05	0.18
	West	$T_{SI,WW}$	21.15	0.21
Air temperature	Test cell	T_{amb}	21.19	0.08
	CC	T_{cc}	7.63	0.08
	TBZ	T_{tbz}	21.38	0.07

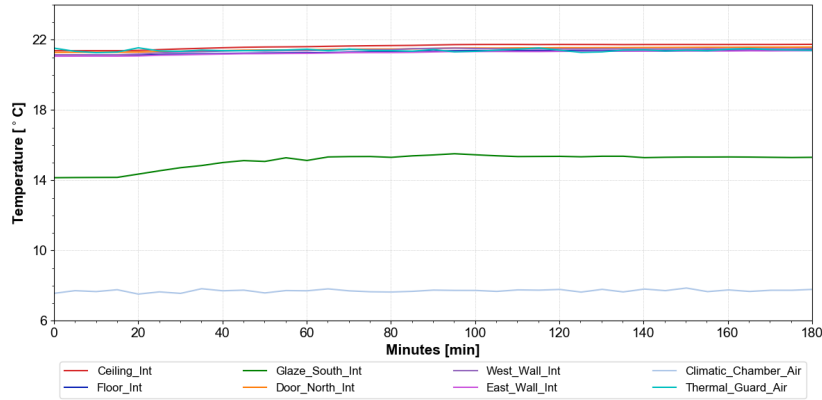
Table 6.2 – Measured temperature boundary conditions for the condensation test

Where: Mean - mean temperature; SDEV - standard deviation;

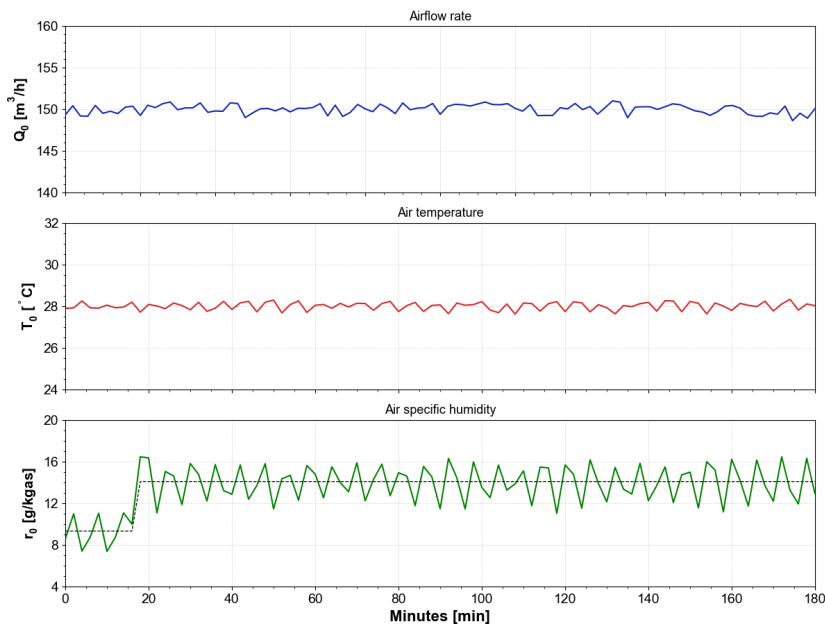
CC - climatic chamber; TBZ - thermal buffer zone

		Q_0 [m^3/h]	U_0 [m/s]	T_0 [$^{\circ}C$]	Re_0 [-]	Ar_0 [-]	r_0 [g/kg_{as}]	HR_0 [%]
Initial	Mean	149.99	2.52	28.00	19962	0.0044	9.06	38.65
	SDEV	0.58	-	0.10	-	-	1.20	4.93
Test	Mean	150.05	2.52	28.01	19962	0.0044	14.07	59.54
	SDEV	0.55	-	0.19	-	-	1.66	6.49

Table 6.3 – Air supply characteristics for the condensation test



(a) Wall inner surface temperature



(b) Air supply parameters

Figure 6.13 – Boundary conditions evolution during the test period

6.4.1.3 Air velocity, temperature and humidity evolution within the test cell

The air velocity, temperature and humidity within the test cell are obtained using the mobile robot fixed near the test area (c.f. section 6.3.2). The evolution of the indoor moist air just before and during the condensation test is presented in the Figure 6.14. The time given in the x-axis is in perfect synchronization with the time shown in the boundary conditions (c.f. Figure 6.13).

For the air velocity, the moist air velocity at different height is not greater than 0.25 m/s , the influence of convection can be considered as negligible.

For the air temperature, a temperature stratification of approximately 2°C is observed between the floor and the room upper part ($Z = 2.0 \text{ m}$). This stratification appears to be

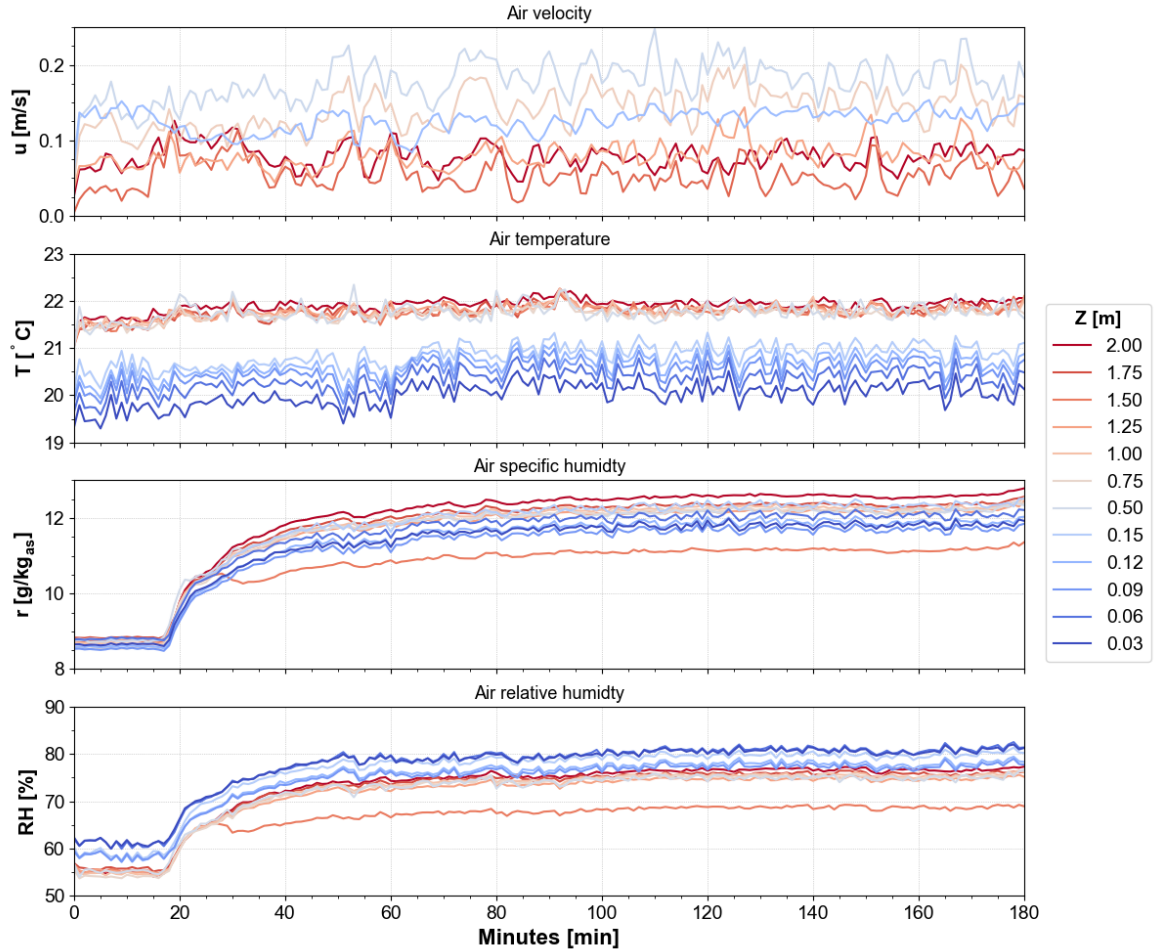


Figure 6.14 – Evolution of the indoor moist air velocity-temperature-humidity just before and during the test

comprehensible given the measurement location. This is a stagnant zone where the air velocity can be as low as 0.05 m/s , thus the airflow can not be homogeneously mixed.

The last two graphs present the evolution of the moist air specific humidity and relative humidity over time. As soon as the humidity conditions in the air supply circuit switch quasi-instantaneously from the initial to the test condition, the indoor moist air humidity level begins to increase. The transient regime lasts for approximately 40 minutes. From the newly established quasi-steady state regime, the air humidity vary from 11.5 to 12.5 g/kg_{as} (80 \%RH to 72 \%RH) between the floor and the room upper part⁴. This stratification could be reasonably explained by the fact that the water vapor injected was actually high-temperature steam, which reduces the moist air density and creates this stratification.

⁴the humidity sensor at $Z = 1.5 \text{ m}$ seems to be defective since its recorded values differ largely from the others; thus it will be excluded for the data analysis

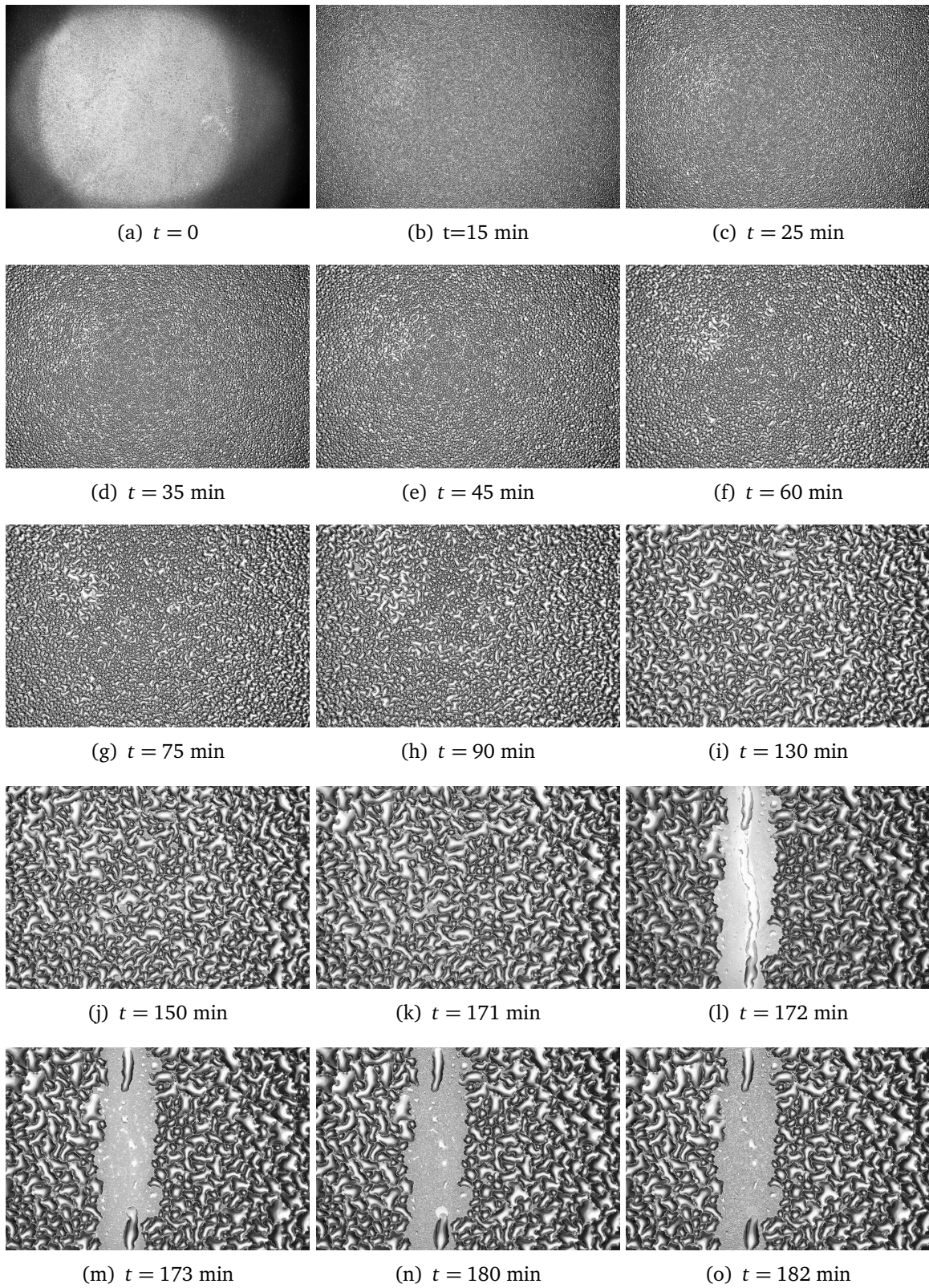


Figure 6.15 – Dropwise condensation dynamic mechanism

6.4.2 Pictures of the condensation process

The Figure 6.15 presents a series of images captured over time, which could show clearly the formation, the growth, the coalescence as well as the fall-off and the re-nucleation of droplets along the glazing. We note that all the images shown in the figure are not the raw image. They have been equalized according to the method above-mentioned in the section 6.3.3.4, to ensure a better vision.

As shown in the Figure 6.15(a), in the beginning ($t = 0$), droplets form at the same time at nucleation sites with a very small initial radius. Their initial size is so small that the camera device is not able to do an object-focus properly. As a result, the vignetting effect (darker zone at the image periphery) can be observed. It is actually the failure of the synchronization between the out-of-focus shooting and illuminating. At this early stage, the droplets grow mainly by direct deposition of condensed saturated vapor onto the glazing surface.

From the time $t = 15$ min, the camera device starts to perform a proper focus, the droplets edges are clearly defined on the pictures. For this reason, this is also the moment for which the image series are used for post-processing. As the droplets become larger in size and as the distances between neighboring droplets become smaller, the coalescence effect begins. Smaller droplets fuse into bigger droplets. The coalescence process seems to be the dominating mechanism for the droplet growth since it lasts for the longest time of the whole process: from $t = 15$ min up until $t = 171$ min (from Fig. 6.15(b) to Fig. 6.15(k)), which means about two hours and a half.

Once the droplets reach a certain size, called "fall-off size", they roll off the glazing surface. In fact, as the droplets grow by coalescence and increase to the departure size, the gravity forces exceed the capillary force within the droplets. They cause them to fall and sweep away other droplets in its path, as can be seen in the Figure 6.15(l) at the moment $t = 172$ min.

Just one minute later (i.e. at $t = 173$ min), right at the freshly cleared glazing surface, new droplets form rapidly at the nucleation sites. As shown in the last two figures 6.15(n) and 6.15(o), the re-nucleation starts over and the growth process cycle repeats, next to the other droplets which still undergo the coalescence process.

6.4.3 Quantification of the condensation rate

In this section, we are interested in the condensation rate of the water vapor droplet on the glazing.

As shown earlier in the section 6.2.6, the condensation rate is strongly related to the overall heat transfer coefficient during the condensation process. Hence, four different methods are identified in order to determine the condensation rate:

1. experimentally using the image processing method (c.f. section 6.3.3);
2. analytically using the Griffith's correlation (eq. (6.16));
3. analytically re-evaluating the overall heat transfer coefficient using the theoretical equation (6.15) and the experimental data;
4. numerically by CFD simulations (Ilie, 2017); this task was undertaken by the Romanian partners, as part of the joint research ANR project.

6.4.3.1 Vapor dew point and glazing surface temperature

Except for the first method, computing the three other models require some input data, which include the glazing surface temperature, the indoor moist air temperature, humidity and eventually velocity. In fact, once the moist air temperature and humidity are known, the vapor partial pressure, the dew point as well as the thermophysical properties of the water droplets can be deduced using tables and approximation formulas.

The evolution of the indoor moist air temperature, the corresponding dew point and the glazing surface temperature are given in the Figure 6.16.

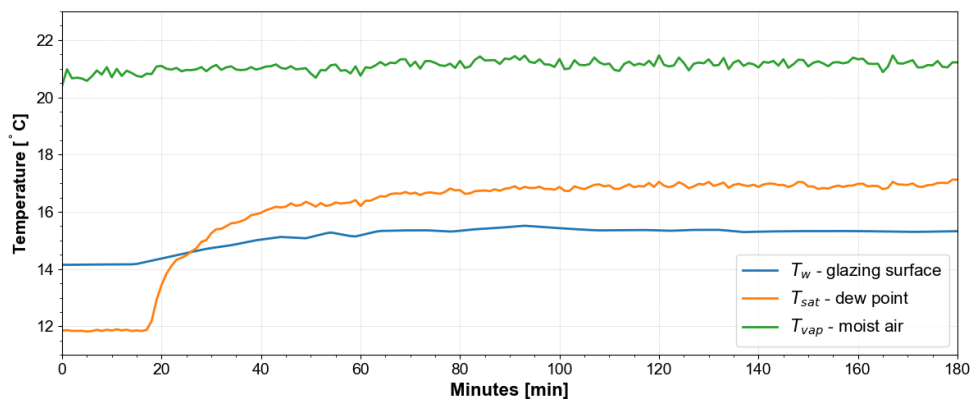


Figure 6.16 – Temperature evolution of the moist air, the dew point and the glazing surface just before and during the test

The five consecutive temperature profiles ($Z = 0.75...0.09$ m) shown in the Figure 6.14 are averaged to obtain a representative moist air temperature. The same average process was applied for the air specific humidity. Having the air specific humidity, the atmospheric pressure as inputs, the actual partial pressure of the water vapor and the corresponding dew point can be deduced using approximation formulas. The temperature of the glazing inner surface where the image capturing takes place was extrapolated using the Pt100 data which measure both inner and outer glazing surfaces temperature and the IR camera data which measure the glazing outer surface temperature.

The representative moist air temperature is quasi-stable over time. The dew point remains at about 12 °C during the initial condition. With the increasing indoor air hu-

midity, i.e. the water vapor content, the corresponding dew point also begin to increase from about 12 °C to 16.5 °C. The glazing surface temperature increases from 14.1 °C to 15.3 °C approximately, as a result of the increasing heat transfer coefficient promoted by the dropwise condensation process.

6.4.3.2 Condensation rate

The time-evolution of the condensation rate is given in the Figure 6.17. The timeline shown in the x-axis is also in perfect synchronization with all the previous graphs. Results issued from four methods above-mentioned are presented.

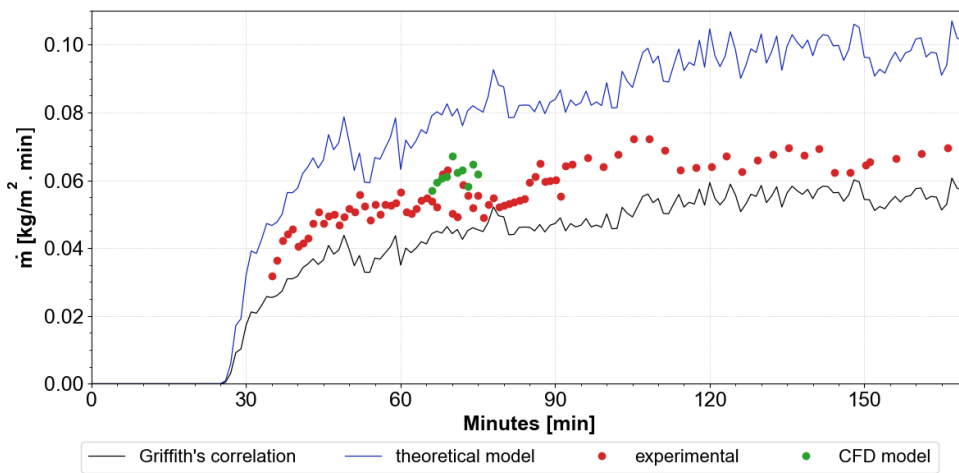


Figure 6.17 – Evolution of the condensate mass flow rate just before and during the test

The two solid curves in black and blue colors represent the condensation rate computed using the Griffith's correlation and the theoretical equation, respectively. For the two scatter plot series, the green dots represent the CFD numerical results extracted from (Ilie, 2017), and the red dots represent the experimental results issued from the image processing method, described previously in the section 6.3.3.4.

To determine the condensation rate, the two solid curves are computed using the same equation (6.17). The overall heat transfer coefficient $h_{tot,corr}$ using the Griffith's correlation (eq. (6.16)) is computed with the vapor dew point temperature determined just above.

The overall heat transfer coefficient h_{tot} using the theoretical equation (6.15) is the result of a definite integral. This integral requires information on the droplet minimum equilibrium radius r_{min} , the droplet fall-off radius r_{max} and the droplet contact angle θ . Those information are listed in the Table 6.4. The minimum equilibrium radius r_{min} is computed using the equation (6.2). The fall-off radius r_{max} is assumed based on the Figure 6.15(I). The contact angle θ is obtained experimentally. It is an averaged value determined following the test described in section 6.3.3.3.

We note that the results shown here are computed using a combination of two adaptive thresholding methods regarding the binarization step. This matter will be addressed further in the section 6.4.4.

	Symbol	Value
Droplets contact angle	θ [°]	56.88
Minimum equilibrium radius (eq. (6.2))	r_{min} [μm]	0.0115
Fall-off radius	r_{max} [mm]	2.0

Table 6.4 – Droplets minimum equilibrium radius, fall-off radius and contact angle

For the condensation rate (c.f. Fig.6.17), the dropwise condensation occurs as soon as the dew point exceeds the glazing surface temperature (c.f. Fig. 6.16); and thus the condensation rate increases. The comparison of the experimental results with the theoretical model indicates a mean relative difference of approximately 18%, which implies an overall good agreement. Nevertheless, the uncertainty of experimental results is still not evaluated.

Furthermore, the CFD numerical results seem to follow the same trend as the experimental and theoretical results. However, we regret that their study (Ilie, 2017) have published results within only 10 minutes (with a time step of 1 minute). According to them, the transient simulations require an initialization of the variables specific to each parameter (indoor air velocity, temperature, moisture content) related to the studied field. If these variables are initialized with the stationary regime initial values, a great number of simulations for each time step are involved, which leads to a significant increase in the computation time.

6.4.4 Discussions on the image post-treatment

As stated previously, the experimental results are computed using combined methods for the image binarization. This is a crucial step since finding droplet contours are based on binarized images.

OpenCV proposes four different methods for binarizing an image (c.f. section 6.3.3.4):

- Global thresholding;
- Otsu's method;
- Adaptive Mean thresholding;
- Adaptive Gaussian thresholding.

For the global thresholding method, it might be complicated to choose manually an optimal threshold value for each image. The Otsu's method is an alternative simple method thanks to its capacity to determine automatically the threshold value for each

image. However, this method's accuracy is significantly limited if the histogram of the image in question does not have a significant bimodal distribution (Gonzalez and Woods, 2018). The adaptive thresholding methods are relevant choices for images with varying illumination. But those methods also require input parameters that need to be defined by the users.

In our case, the droplets are illuminated differently depending on the size. The more the droplets increase in size, the more the light reflection increases. Thus, a series of droplet images do not receive an uniform illumination. Two examples of small and large droplets are given in the Figure 6.18. The image size is 5 x 5 mm.

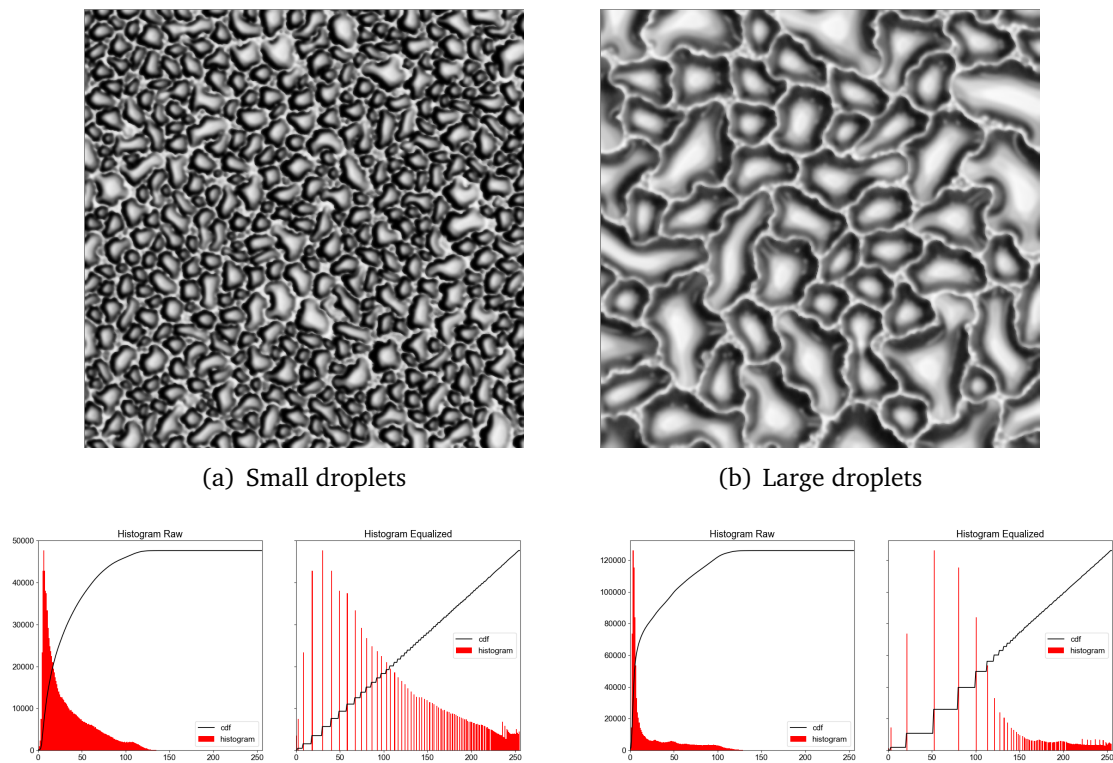


Figure 6.18 – Image samples of small and large droplets (5 x 5 mm) with their corresponding histograms

The image on the left is the same as the sample shown earlier (c.f. Fig. 6.10). The image on the right is extracted from the Figure 6.15(i). Both samples have their histogram equalized and their noise filtered with the same parameter. We can notice that the image sample of large droplets is brighter, and the contour edges of the droplets are not illuminated uniformly from one direction to another.

Those two image samples are binarized using three different methods, which are the Otsu's method, the Adaptive Mean thresholding and the Adaptive Gaussian thresholding. The results are given in Figures 6.19 and 6.20.

Globally, we can observe on all those figures that some droplet edges are very well connected and form closed contours. Some others, with less uniform illumination re-

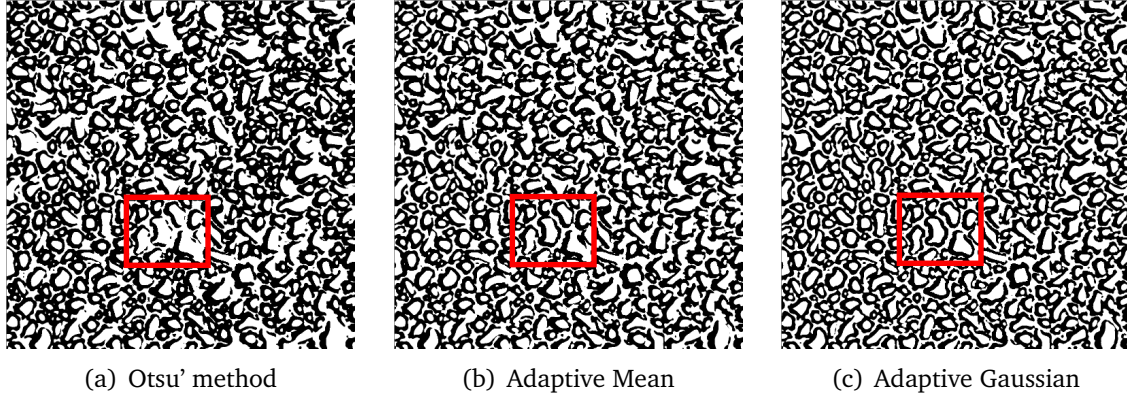


Figure 6.19 – Image thresholding for the image sample of small droplets

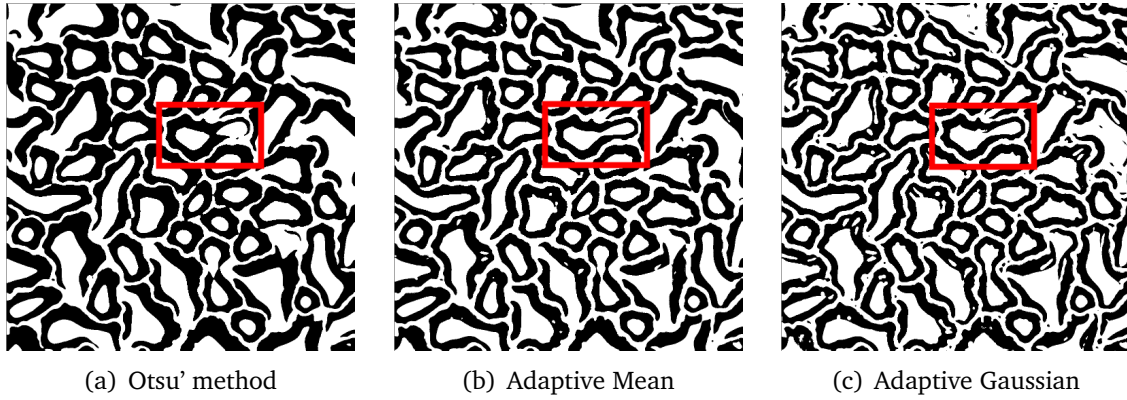


Figure 6.20 – Image thresholding for the image sample of large droplets

ceived during the image capturing, could not be connected. The Otsu's method is the least effective among the three methods. This is predictable since the histograms of the two images do not have a bimodal distribution (c.f. Fig. 6.18).

For the image sample of small droplets (Fig. 6.19), the Adaptive Gaussian thresholding (Fig. 6.19(c)) is significantly more effective than the Adaptive Mean method. For the image sample of large droplets (Fig. 6.20), both methods show about the same performance. But the Adaptive Mean thresholding (Fig. 6.20(b)) appears to be more suitable since the resulting image is less noisy than the other one.

Regardless of the method chosen, there are still some droplet contours that cannot be properly connected. Since this constitutes a loss of information, great attention should be made regarding the image thresholding step.

The treatment of the two samples shown above are not representative for the whole population of small and large droplets. To define the "transition" radius and the optimized parameters for thresholding, the method for now is trial and error.

For the treatment of each image, we compute the averaged equivalent radius of all the droplets $\overline{r_d}$. By repeated tests, we find the transition radius $\overline{r_{d,tr}} = 100 \mu m$. If $\overline{r_d} < \overline{r_{d,tr}}$,

the Adaptive Gaussian method is used for image thresholding; otherwise the Adaptive Mean thresholding method is used.

6.5 Summary

In this chapter, the problem of surface condensation on a cold glazing within a ventilated room is treated. The main intention is to determine the condensation mass flow rate during the condensation process.

- Given the instantaneous and transient characteristics of this phase-change phenomenon, it is important to know the mechanism of droplet formation as well as the heat and mass transfer involved during the phenomenon. The physical background of the condensation and the literature are reviewed. Two theoretical models are identified to determine the condensation rate.*
- A method of measurement is proposed to estimate the condensation rate experimentally. The measurement is based on the close-up imaging technique (macro-photography). The image post-treatment process allows to determine the condensation rate over the glazing surface.*
- Comparisons between experimental and theoretical results show some agreement, which could validate the feasibility of the imaging techniques in full-scale condensation studies.*

Conclusions and perspectives

General summary

In view of the current context about the building energy efficiency and the occupants' comfort and health, it is essential to ensure a proper design of ventilation systems. Despite abundant studies conducted on the mixing ventilation system in the past decades, there are still some issues that need to be considered, which are: (1) an air jet in a realistic airflow configuration; (2) the indoor heat-air-moisture transfer including the surface condensation phenomenon.

First, by full-scale experiments, we aim to get improved the knowledge concerning the behavior and the characteristics of a realistic asymmetric air jet having interaction with room architectural elements. Second, under indoor airflow conditions that promote the surface condensation, we intend to measure the condensation rate of the water vapor deposited on a glazing surface.

For the jet study, we have investigated the air jet under three scenario: isothermal jet, cold jet (summer) and hot jet (winter). In total, twelve different test cases were conducted with three of them having the finest measured data. These experimental campaigns allow a precise visualization of the distribution of the indoor air velocity and temperature fields. Through data computing, those measurements allow to better understand the jet behavior, and to analyze the different characteristics of the air jet.

Besides, the author's intention is to provide a detailed set of experimental data for further use. The experiments are fully described (the configuration geometry, the metrology, the boundary conditions) so that the results can be used for further analysis or for the validation purpose. Although this full-scale experimental study is restricted to one single configuration, the detailed experimental data accompanied by well-known boundary conditions can serve as a benchmark test to validate and to improve CFD numerical models, especially for airflow configurations with rupture of symmetry.

For the condensation study, a method of measurement is proposed to deal with the quantification of the condensation phenomenon on a cold glazing surface. The measurement is based on the close-up imaging technique (macro-photography). The image post treatment allows to determine the condensation rate over the glazing surface from the series of condensation pictures taken by the camera.

We can therefore confirm the feasibility of the imaging techniques in full-scale condensation studies. The experimental results on the surface condensation rate could be extremely valuable for the validation purpose since there was no similar studies in the literature at such the scale.

Last but not least, for the laboratory CETHIL, through this thesis, we have developed an original and realistic configuration and a mobile robot equipped with sensors within

the experimental test cell that can be served for further research project.

Perspectives

This thesis improves the current knowledge on the realistic air jet and the surface condensation. Nevertheless, some future work is needed to consolidate the findings and expand the analysis.

Regarding the jet study, additional measurements with finer mesh around the diffuser would be useful to improve the results precision on the jet characteristics. In the present study, a mesh of 5 cm was chosen in the volume defined by a 1 x 1 m² around the diffuser axis. We suggest a mesh of 2 cm or lower in this zone, which captures the highest gradient in air velocity and temperature.

The impact of internal obstructions and internal heat sources such as mannequins, furniture should be studied to better represent a realistic airflow configuration. Additional sensors can also be considered to assess the indoor thermal comfort and the ventilation effectiveness of the ventilation system.

Besides, as mentioned earlier, the detailed experimental data issued from this thesis can serve as a benchmark test to validate and to improve CFD numerical models. We have established an "User Guide" providing a description of the procedure to compare simulation results with experimental data. The comparison procedure is based on Python scripts and Paraview visualization. This package is believed to ease the work of CFD modelers.

Regarding the condensation study, it is concluded that the imaging techniques are feasible for estimating the surface condensation rate. However, our method is limited in terms of the accuracy and the precision of the experimental results. We suggest two ways to surpass this problem.

First, in terms of the experimental apparatus, we can upgrade the whole camera system, i.e. the body and the lens, to get a higher resolution and a reproduction ratio greater than 1. Another option, the camera lens can be replaced by a telescope. The precision of the pictures can be improved considerably in exchange for its field of view. Besides, an additional camera can be considered in order to obtain information on the droplet contact angle. This camera needs to be set up at the glazing surface, perpendicularly with the direction of the growth of droplets, to capture those information.

Second, we can get a higher result accuracy by improving the image post-treatment process. We remind that the process consists in finding the droplet contours in the image series. The actual process we used is the standard one. Its parameters are defined based on the trial-and-error principle. We need an automated algorithm that can determine the optimized parameters for each image. There is another method which is more sophisticated but promising. With advances in computer sciences, the image treatment process could be improved considerably by using the artificial intelligence; for instance, the artificial neural networks with deep learning-based image analysis.

Bibliography

Abramovich, G. N., 1963. The Theory of Turbulent Jets. MIT Press.

ADEME, 2015. Chiffres clés climat, air et énergie, 2015th edition.

URL <http://www.ademe.fr/sites/default/files/assets/documents/chiffres-cles-climat-air-energie-8705-bd.pdf>

AFNOR, 2017. NF EN 16798. Performance énergétique des bâtiments - Ventilation des bâtiments.

URL <https://www.boutique.afnor.org/norme/nf-en-16798-3/performance-energetique-des-batiments-ventilation-des-batiments-partie-3-pour-batiments-non-res/article/905625/fa187730>

AIVC, 1987. TN 20: Airborne Moisture Transfer: New Zealand Workshop Proceedings and Bibliographic Review. AIVC Technical Note 20.

Aksan, S., Rose, J., Feb. 1973. Dropwise condensation-The effect of thermal properties of the condenser material. International Journal of Heat and Mass Transfer 16 (2), 461–467.

URL <http://linkinghub.elsevier.com/retrieve/pii/0017931073900720>

Alfeld, P., Nov. 1984. A trivariate Clough-Tocher scheme for tetrahedral data. Computer Aided Geometric Design 1 (2), 169–181.

URL <http://www.sciencedirect.com/science/article/pii/0167839684900293>

Allard, F., 1987. Contribution a l'étude des transferts de chaleur dans les cavités thermiquement entraînées à grand nombre de Rayleigh : application aux cellules d'habitation. Ph.D. thesis, INSA de Lyon.

URL <http://www.theses.fr/1987ISAL0053>

Allard, F., Brau, J., Pallier, J., 1982. Étude de l'incidence des apports solaires sur une cellule test en ambiance climatique simulée. Technical report COMES, INSA de Lyon, Lyon.

-
- Allocca, C., Chen, Q., Glicksman, L. R., 2003. Design analysis of single-sided natural ventilation. *Energy and Buildings* 35 (8), 785–795.
URL <http://www.sciencedirect.com/science/article/pii/S0378778802002396>
- Amai, H., Liu, S., Novoselac, A., Nov. 2017. Experimental study on air change effectiveness: Improving air distribution with all-air heating systems. *Building and Environment* 125, 515–527.
URL <http://www.sciencedirect.com/science/article/pii/S0360132317304316>
- Amai, H., Novoselac, A., Nov. 2016. Experimental study on air change effectiveness in mixing ventilation. *Building and Environment* 109, 101–111.
URL <http://www.sciencedirect.com/science/article/pii/S0360132316303559>
- Antoniadou, P., Papadopoulos, A. M., Oct. 2017. Occupants' thermal comfort: State of the art and the prospects of personalized assessment in office buildings. *Energy and Buildings* 153, 136–149.
URL <http://www.sciencedirect.com/science/article/pii/S0378778817319709>
- ASHRAE, 2009. 2009 ASHRAE handbook: fundamentals. American Society of Heating, Refrigeration and Air-Conditioning Engineers, Atlanta, GA, oCLC: 525070649.
- ASHRAE, 2013. 2013 ASHRAE handbook: fundamentals. OCLC: 882088522.
URL <http://app.knovel.com/hotlink/toc/id:kpASHRAEC1/2013-ashrae-handbook>
- ASHRAE, 2016. ASHRAE 90.1-2016. Energy standard for buildings except low-rise residential buildings. ASHRAE, Atlanta, GA, oCLC: 739098624.
- ASHRAE, 2017. 2017 ASHRAE handbook: fundamentals. ASHRAE, oCLC: 988844741.
- ASHRAE, ANSI, 2016a. ASHRAE 62.1-2016. Ventilation for acceptable indoor air quality. OCLC: 1010498197.
URL <http://www.madcad.com/library/ASHRAE-Standard-62.1-2016/>
- ASHRAE, ANSI, 2016b. ASHRAE 62.2-2016. Ventilation and acceptable indoor air quality in residential buildings. OCLC: 948605440.
- ASHRAE, ANSI, 2017. ASHRAE 55-2017. Thermal environmental conditions for human occupancy. OCLC: 1006971950.
- Assaad, D. A., Ghali, K., Ghaddar, N., Habchi, C., Nov. 2017. Mixing ventilation coupled with personalized sinusoidal ventilation: Optimal frequency and flow rate for acceptable air quality. *Energy and Buildings* 154, 569–580.
URL <http://www.sciencedirect.com/science/article/pii/S037877881732039X>
- Awbi, H. B., 2003. Ventilation of buildings. Spon Press, London, oCLC: 300230189.

- Awbi, H. B., Mar. 2017. Ventilation for Good Indoor Air Quality and Energy Efficiency. *Energy Procedia* 112, 277–286.
URL <http://www.sciencedirect.com/science/article/pii/S1876610217312237>
- Baechler, M. C., Hadley, D. L., Marseille, T. J., Stenner, R. D. P. N. L., Peterson, M. R., Naugle, D. F. R. T. I. U., Berry, M. A. U. S. E. P. A. U., Jan. 1991. Sick building syndrome sources.
URL <https://www.osti.gov/biblio/5706959>
- Baker, C. B., George, Jr., W. K., Taulbee, D. B., 1982. An analysis of the axisymmetric turbulent buoyant jet. Vol. 2. pp. 383–388.
URL <http://adsabs.harvard.edu/abs/1982hetr....2..383B>
- Beysens, D., Nov. 2006. Dew nucleation and growth. *Comptes Rendus Physique* 7 (9-10), 1082–1100.
URL <http://linkinghub.elsevier.com/retrieve/pii/S1631070506002325>
- Biwole, P. H., 2009. Large scale particle tracking velocimetry for 3-dimensional indoor airflow study. Ph.D. thesis, INSA de Lyon.
URL <http://www.theses.fr/2009ISAL0070>
- Biwole, P. H., Yan, W., Zhang, Y., Roux, J.-J., 2009. A complete 3d particle tracking algorithm and its applications to the indoor airflow study. *Measurement Science and Technology* 20 (11), 115403.
URL <http://stacks.iop.org/0957-0233/20/i=11/a=115403>
- Blocken, B., Jun. 2014. 50 years of Computational Wind Engineering: Past, present and future. *Journal of Wind Engineering and Industrial Aerodynamics* 129, 69–102.
URL <http://www.sciencedirect.com/science/article/pii/S016761051400052X>
- Bosbach, J., Kühn, M., Wagner, C., Mar. 2009. Large scale particle image velocimetry with helium filled soap bubbles. *Experiments in Fluids* 46 (3), 539–547.
URL <http://link.springer.com/10.1007/s00348-008-0579-0>
- Bosbach, J., Kühn, M., Wagner, C., Raffel, M., Resagk, C., du Puits, R., Thess, A., 2006. Large scale particle image velocimetry of natural and mixed convection. In: 13th Int. Symp. on Applications of Laser Techniques to Fluid Mechanics, Lisbon, Portugal.
- Bragança, P., Oct. 2017. Ventilation par mélange utilisant des dispositifs de diffusion munis d'inserts lobés : analyse des écoulements moteurs et du confort thermique induit. Ph.D. thesis, Université de La Rochelle.
URL <https://tel.archives-ouvertes.fr/tel-01753827/document>

-
- Bragança, P., Sodjavi, K., Meslem, A., Mar. 2017. Passive Control Strategy for Mixing Ventilation in Heating and Cooling Modes Using Lobed Inserts. *Energy Procedia* 112, 232–239.
URL <http://www.sciencedirect.com/science/article/pii/S187661021731216X>
- Bragança, P., Sodjavi, K., Meslem, A., Serres, L., 2016. Experimental investigation of airflow and thermal comfort under mixing ventilation in a full scale model room – comparison of lobed and conventional diffusers. p. 8.
- Cao, G., Awbi, H., Yao, R., Fan, Y., Sirén, K., Kosonen, R., Zhang, J. J., Mar. 2014a. A review of the performance of different ventilation and airflow distribution systems in buildings. *Building and Environment* 73, 171–186.
URL <http://www.sciencedirect.com/science/article/pii/S036013231300365X>
- Cao, G., Sirén, K., Kilpeläinen, S., Jan. 2014b. Modelling and experimental study of performance of the protected occupied zone ventilation. *Energy and Buildings* 68, 515–531.
URL <http://www.sciencedirect.com/science/article/pii/S0378778813006543>
- Cao, X., Liu, J., Jiang, N., Chen, Q., 2014c. Particle image velocimetry measurement of indoor airflow field: A review of the technologies and applications. *Energy and Buildings* 69, 367–380.
URL <http://linkinghub.elsevier.com/retrieve/pii/S0378778813006944>
- Cao, Z.-J., Xia, B.-L., Zhang, Y., 2003. The possibility for realizing dropwise condensation with small contact angle. *Acta Physica Sinica* 52, 2427–2431.
- Carey, V. P., 2017. *Liquid Vapor Phase Change Phenomena: An Introduction to the Thermophysics of Vaporization and Condensation Processes in Heat Transfer Equipment*, Second Edition. CRC Press Inc.
- Castanet, S., 1998. Contribution à l'étude de la ventilation et de la qualité de l'air intérieur des locaux = Contribution to the study of ventilation and indoor air quality. Ph.D. thesis, INSA de Lyon.
- Castillo, J. E., Weibel, J. A., Garimella, S. V., Jan. 2015. The effect of relative humidity on dropwise condensation dynamics. *International Journal of Heat and Mass Transfer* 80, 759–766.
URL <http://www.sciencedirect.com/science/article/pii/S0017931014008849>
- Catalina, T., Virgone, J., Kuznik, F., Aug. 2009. Evaluation of thermal comfort using combined CFD and experimentation study in a test room equipped with a cooling ceiling. *Building and Environment* 44 (8), 1740–1750.
URL <http://linkinghub.elsevier.com/retrieve/pii/S0360132308002783>
-

- Cehlin, M., Moshfegh, B., 2002. Numerical and experimental investigations of air flow and temperature patterns of a low velocity diffuser. *Indoor Air*, 6.
- CEN, 2007. EN 15251:2007. Indoor environmental input parameters for design and assessment of energy performance of buildings addressing indoor air quality, thermal environment, lighting and acoustics.
URL <https://standards.cen.eu/>
- CEN, 2017. EN 16798:2017. Energy performance of buildings - Ventilation for buildings.
URL https://standards.cen.eu/dyn/www/f?p=204:29:0:::FSP_ORG_ID,FSP_LANG_ID:6138,25&cs=1638CC7BB2DD4EF2FDC1CF025F9CFD412#1
- Chassaing, P., 2000. Turbulence en mécanique des fluides.
URL <https://infoscience.epfl.ch/record/60955>
- Chen, C. J., Rodi, W., 1980. Vertical turbulent buoyant jets: a review of experimental data. Pergamon Press, google-Books-ID: yxhRAAAAMAAJ.
- Chen, Q., 2009. Ventilation performance prediction for buildings: A method overview and recent applications. *Building and Environment* 44 (4), 848–858.
URL <http://linkinghub.elsevier.com/retrieve/pii/S0360132308001510>
- Chen, Q., Srebric, J., Apr. 2002. A Procedure for Verification, Validation, and Reporting of Indoor Environment CFD Analyses. *HVAC&R Research* 8 (2), 201–216.
URL <https://www.tandfonline.com/doi/abs/10.1080/10789669.2002.10391437>
- Cho, Y., Awbi, H. B., Karimipannah, T., Jun. 2008. Theoretical and experimental investigation of wall confluent jets ventilation and comparison with wall displacement ventilation. *Building and Environment* 43 (6), 1091–1100.
URL <http://www.sciencedirect.com/science/article/pii/S0360132307000790>
- Corrsin, S., 1946. Investigation of Flow in an Axially Symmetrical Heated Jet of Air. Technical report Wash. Wartime Report W-94, NACA, 58.
- Courgey, S., Oliva, J.-P., 2006. La conception bioclimatique: des maisons économes et confortables en neuf et en réhabilitation. *Terre vivante*.
- Daisey J. M., Angell W. J., Apte M. G., Feb. 2003. Indoor air quality, ventilation and health symptoms in schools: an analysis of existing information. *Indoor Air* 13 (1), 53–64.
URL <https://onlinelibrary.wiley.com/doi/full/10.1034/j.1600-0668.2003.00153.x>
- Datcu, S., Ibos, L., Candau, Y., Matteï, S., Aug. 2005. Improvement of building wall surface temperature measurements by infrared thermography. *Infrared Physics & Technology* 46 (6), 451–467.
URL <http://linkinghub.elsevier.com/retrieve/pii/S1350449505000046>

-
- de Dear, R. J., Brager, G. S., Jul. 2002. Thermal comfort in naturally ventilated buildings: revisions to ASHRAE Standard 55. *Energy and Buildings* 34 (6), 549–561.
URL <http://www.sciencedirect.com/science/article/pii/S0378778802000051>
- De Dear, R. J., Brager, G. S., Reardon, J., Nicol, F., others, 1998. Developing an adaptive model of thermal comfort and preference/discussion. *ASHRAE transactions* 104, 145.
- EEA, 2015. Final energy consumption by sector and fuel.
URL <https://www.eea.europa.eu/data-and-maps/indicators/final-energy-consumption-by-sector-9>
- EIA, U., 2012. Annual Energy Review, 2011th edition.
URL <https://www.eia.gov/totalenergy/data/annual/pdf/aer.pdf>
- Einberg, G., Hagström, K., Mustakallio, P., Koskela, H., Holmberg, S., May 2005. CFD modelling of an industrial air diffuser—predicting velocity and temperature in the near zone. *Building and Environment* 40 (5), 601–615.
URL <http://linkinghub.elsevier.com/retrieve/pii/S0360132304002112>
- Etheridge, D., Sep. 2015. A perspective on fifty years of natural ventilation research. *Building and Environment* 91, 51–60.
URL <http://www.sciencedirect.com/science/article/pii/S0360132315000906>
- European-Commission, 2002. Directive 2002/91/EC. On the energy performance of buildings.
URL <http://eur-lex.europa.eu/LexUriServ/LexUriServ.do?uri=OJ:L:2003:001:0065:0071:EN:PDF>
- European-Commission, 2010. Directive 2010/31/EU. On the energy performance of buildings (recast).
URL <http://eur-lex.europa.eu/legal-content/EN/TXT/PDF/?uri=CELEX:32010L0031&from=EN>
- European-Commission, 2012. Directive 2012/27/EU. Energy Efficiency.
URL <http://eur-lex.europa.eu/legal-content/EN/TXT/?qid=1399375464230&uri=CELEX%3A32012L0027>
- European-Commission, 2014. 2020 climate and energy package.
URL https://ec.europa.eu/clima/policies/strategies/2020_en
- Faghri, A., Zhang, Y., 2006. Transport phenomena in multiphase systems. Elsevier Academic Press, Burlington, Mass, oCLC: ocm70189314.
- Fanger, P. O., al., 1970. Thermal comfort. Analysis and applications in environmental engineering. Thermal comfort. Analysis and applications in environmental engineering.

- Fanger, P. O., Melikov, A. K., Hanzawa, H., 1989. Turbulence and draft. *ASHRAE Journal* 31 (4), 18–25.
- Fanger, P. O., Melikov, A. K., Hanzawa, H., Ring, J., 1988. Air turbulence and sensation of draught. *Energy and Buildings* 12 (1), 21–39.
URL <http://www.sciencedirect.com/science/article/pii/0378778888900539>
- Fatemi, I., Wang, B.-C., Koupriyanov, M., Tully, B., Aug. 2013. Experimental study of a non-isothermal wall jet issued by a displacement ventilation system. *Building and Environment* 66, 131–140.
URL <http://www.sciencedirect.com/science/article/pii/S0360132313001303>
- Fatica, N., Katz, D. L. V., 1949. Dropwise condensation. University of Michigan.
- Feng, W., Grunewald, J., Nicolai, A., Zhang, C., Zhang, J. S., 2012. CHAMPS-Multizone—A combined heat, air, moisture and pollutant simulation environment for whole-building performance analysis. *HVAC&R Research*, 233–251.
- Foat, T. G., Parker, S. T., Castro, I. P., Xie, Z.-T., Apr. 2018. Numerical investigation into the structure of scalar plumes in a simple room. *Journal of Wind Engineering and Industrial Aerodynamics* 175, 252–263.
URL <http://www.sciencedirect.com/science/article/pii/S0167610517308899>
- Fu, S., Biwole, P. H., Mathis, C., May 2015. Particle Tracking Velocimetry for indoor air-flow field: A review. *Building and Environment* 87, 34–44.
URL <http://www.sciencedirect.com/science/article/pii/S0360132315000256>
- Gavan, V., 2009. Full-Scale experimental evaluation and modelling of a double-skin façade : optimal control of thermal and visual comfort. Ph.D. thesis, INSA de Lyon.
URL <http://www.theses.fr/2009ISAL0074>
- Gavan, V., Woloszyn, M., Kuznik, F., Roux, J.-J., Feb. 2010. Experimental study of a mechanically ventilated double-skin façade with venetian sun-shading device: A full-scale investigation in controlled environment. *Solar Energy* 84 (2), 183–195.
URL <http://linkinghub.elsevier.com/retrieve/pii/S0038092X09002588>
- Gong, G., Xu, C., Jiao, J., Liu, Y., Xie, S., Aug. 2011. Investigation of moisture condensation on papermaking plant envelopes in high humidity environment by orthogonal analysis and CFD simulation. *Building and Environment* 46 (8), 1639–1648.
URL <http://www.sciencedirect.com/science/article/pii/S0360132311000485>
- Gonzalez, R. C., Woods, R. E., 2018. Digital image processing.
- Goodfellow, H. D., 2001. *Industrial Ventilation Design Guidebook*. Academic Press, google-Books-ID: t9O8xvY_XoUC.

-
- Graham, C., Griffith, P., Feb. 1973. Drop size distributions and heat transfer in dropwise condensation. *International Journal of Heat and Mass Transfer* 16 (2), 337–346.
URL <http://www.sciencedirect.com/science/article/pii/0017931073900628>
- Griffith, P., 1983. Dropwise Condensation. In: Schlunder, E. U. (Ed.), *Heat Exchange Design Handbook*. Vol. 2. Hemisphere Publishing.
- Griffith, P., Man Suk Lee, May 1967. The effect of surface thermal properties and finish on dropwise condensation. *International Journal of Heat and Mass Transfer* 10 (5), 697–707.
URL <http://linkinghub.elsevier.com/retrieve/pii/0017931067901147>
- Grimitlyn, M., Pozin, G., 1993. Fundamentals of Optimizing Air Distribution in Ventilated Spaces. *ASHRAE Transactions* 99 (1), 1128–1138.
- Hannemann, R. J., Mikic, B. B., Nov. 1976. An analysis of the effect of surface thermal conductivity on the rate of heat transfer in dropwise condensation. *International Journal of Heat and Mass Transfer* 19 (11), 1299–1307.
URL <http://www.sciencedirect.com/science/article/pii/001793107690082X>
- Hanzawa, H., Melikov, A. K., Fanger, P. O., 1987. Airflow characteristics in the occupied zone of ventilated spaces. *ASHRAE Transactions* 93 (1), 524–539.
- Hens, H., Jan. 1992. IEA Annex 14. Condensation and Energy. *Journal of Thermal Insulation* 15 (3), 261–273.
URL <https://doi.org/10.1177/109719639201500307>
- Hinze, J. O., 1975. *Turbulence*. McGraw-Hill, New York, oCLC: 1218645.
- Hohota, R. S., 2003. Modélisation de l'humidité dans un code CFD (basses vitesses en grande cavité) : comparaison avec l'expérimental. Ph.D. thesis, INSA de Lyon.
URL <http://www.theses.fr/2003ISAL0065>
- Hosni, M. H., Jones, B. W., 2002. Development of a Particle Image Velocimetry for Measuring Air Velocity in Large-Scale Room Airflow Applications. *ASHRAE Transactions* 108, 1164–1172, oCLC: 201561651.
- Hu, H. W., Tang, G. H., Jan. 2014. Theoretical investigation of stable dropwise condensation heat transfer on a horizontal tube. *Applied Thermal Engineering* 62 (2), 671–679.
URL <http://www.sciencedirect.com/science/article/pii/S135943111300731X>
- Humphreys, M. A., Nicol, J. F., 1998. Understanding the adaptive approach to thermal comfort. *ASHRAE transactions* 104, 991.
-

Huo, Y., Haghighat, F., Zhang, J. S., Shaw, C. Y., 2000. A systematic approach to describe the air terminal device in CFD simulation for room air distribution analysis. *Building and Environment* 35 (6), 563–576.

Hurnik, M., Blaszcok, M., Popiolek, Z., Nov. 2015. Air distribution measurement in a room with a sidewall jet: A 3d benchmark test for CFD validation. *Building and Environment* 93, 319–330.

URL <http://www.sciencedirect.com/science/article/pii/S0360132315300524>

Hussein, H. J., Capp, S. P., George, W. K., Jan. 1994. Velocity measurements in a high-Reynolds-number, momentum-conserving, axisymmetric, turbulent jet. *Journal of Fluid Mechanics* 258, 31–75.

URL <https://www.cambridge.org/core/journals/journal-of-fluid-mechanics/article/velocity-measurements-in-a-highreynoldsnumber-momentumconserving-axisymmetric-turbulent-jet/9604A42E400A9F5BC0C29C7C2E1732A3>

IEA, 1996. IEA Annex 24. Heat, Air and Moisture Transport.

IEA, 2017. World Energy Balances 2017: Overview (2017th edition).

URL <https://www.iea.org/publications/freepublications/publication/WorldEnergyBalances2017Overview.pdf>

IEA, 2018. Global Energy & CO2 Status Report - 2017.

URL <http://www.iea.org/publications/freepublications/publication/GECO2017.pdf>

Ilie, V., 2017. Numerical study of heat and mass transfers in ventilated spaces (in Romanian). Ph.D. thesis, Technical University of Civil Engineering, Bucharest, Romania.

Inard, C., Bouia, H., Dalicieux, P., Jul. 1996a. Prediction of air temperature distribution in buildings with a zonal model. *Energy and Buildings* 24 (2), 125–132.

URL <http://www.sciencedirect.com/science/article/pii/0378778895009698>

Inard, C., Depecker, P., Roux, J.-J., Feb. 1997. A simplified model for the prediction of air temperature distribution in buildings. *Revue Générale de Thermique* 36 (2), 113–123.

URL <http://www.sciencedirect.com/science/article/pii/S0035315999800567>

Inard, C., Meslem, A., Depecker, P., Jul. 1996b. Use of a zonal model for the prediction of air temperature distribution in large enclosures. In: *Roomvent 96*, Yokohama, Japan. pp. Vol. 2, 177–184.

URL <https://hal.archives-ouvertes.fr/hal-00312482>

Incropera, F. P., Dewitt, D. P., 2007. Fundamentals of heat and mass transfer, 6th Edition. John Wiley, Hoboken, NJ, oCLC: ocm62532755.

-
- ISO, 2005. ISO 7730:2005. Ergonomics of the thermal environment – Analytical determination and interpretation of thermal comfort using calculation of the PMV and PPD indices and local thermal comfort criteria.
URL <https://www.iso.org/standard/39155.html>
- Jaakkola, J. J., Miettinen, P., Apr. 1995a. Type of ventilation system in office buildings and sick building syndrome. *American Journal of Epidemiology* 141 (8), 755–765.
- Jaakkola, J. J., Miettinen, P., Nov. 1995b. Ventilation rate in office buildings and sick building syndrome. *Occupational and Environmental Medicine* 52 (11), 709–714.
- Jia, W., Jones, B. W., Hosni, M. H., Meng, H., 2002. Data processing of large-scale particle image velocimetry measurements around the human body. *ASHRAE Transactions* 108, 243.
- Jiang, Y., Chen, Q., 2003. Buoyancy-driven single-sided natural ventilation in buildings with large openings. *International Journal of Heat and Mass Transfer* 46 (6), 973–988.
URL <http://www.sciencedirect.com/science/article/pii/S0017931002003733>
- Jing, L., Aizawa, Y., Yoshino, H., 2003. Experimental and CFD studies on surface condensation. relation, 1.
URL http://www.inive.org/members_area/medias/pdf/inive/ibpsa/ufsc929.pdf
- Joshi, S. M., Aug. 2008. The sick building syndrome. *Indian Journal of Occupational and Environmental Medicine* 12 (2), 61–64.
URL <https://www.ncbi.nlm.nih.gov/pmc/articles/PMC2796751/>
- Kaczmarczyk, J., Melikov, A., Fanger, P. O., 2004. Human response to personalized ventilation and mixing ventilation. *Indoor Air* 14 Suppl 8, 17–29.
- Kandzia, C., Kosonen, R., Melikov, A. K., Nielsen, P. V., 2013. Mixing Ventilation. Guide on mixing air distribution design. Vol. 19 of REHVA Guidebook.
- Kapitza, P. L., Kapitza, S. P., Dec. 1949. Wave flow of thin layers of viscous liquids. Part III. Experimental research of a wave flow regime. *Zhurnal Eksperimentalnoi i Teoreticheskoi Fiziki* 19, 105–120.
URL <http://adsabs.harvard.edu/abs/1949ZhETF.19..105K>
- Karagiozis, A., Salonvaara, M., Jul. 2001. Hygrothermal system-performance of a whole building. *Building and Environment* 36 (6), 779–787.
URL <http://linkinghub.elsevier.com/retrieve/pii/S0360132300000639>
- Karimipناه, T., Awbi, H. B., Dec. 2002. Theoretical and experimental investigation of impinging jet ventilation and comparison with wall displacement ventilation. *Building*

- and Environment 37 (12), 1329–1342.
URL <http://www.sciencedirect.com/science/article/pii/S0360132301001172>
- Kashirajima, Y., Sugiura, T., Takahashi, M., Sugihara, Y., Ooshima, N., 2002. Experimental study of indoor thermal environment for cold air distribution systems using various air outlets. ASHRAE transactions 108, 16.
- Kim, S., Kim, K. J., May 2011. Dropwise Condensation Modeling Suitable for Superhydrophobic Surfaces. Journal of Heat Transfer 133 (8), 081502–081502–8.
URL <http://dx.doi.org/10.1115/1.4003742>
- Koestel, A., 1954. Computing temperatures and velocities in vertical jets of hot or cold air. ASHRAE Transaction 60, 385–410.
- Kosutova, K., van Hooff, T., Blocken, B., Jul. 2018. CFD simulation of non-isothermal mixing ventilation in a generic enclosure: Impact of computational and physical parameters. International Journal of Thermal Sciences 129, 343–357.
URL <http://www.sciencedirect.com/science/article/pii/S1290072917311778>
- Krajčák, M., Simone, A., Olesen, B. W., Dec. 2012. Air distribution and ventilation effectiveness in an occupied room heated by warm air. Energy and Buildings 55, 94–101.
URL <http://www.sciencedirect.com/science/article/pii/S0378778812004197>
- Kuznik, F., 2005. Etude expérimentale des jets axisymétriques anisothermes horizontaux se développant près d'une paroi. Application à la modélisation numérique des cavités ventilées. Ph.D. thesis, INSA de Lyon, Lyon.
URL <http://oldgc.iut-nimes.fr/internet/auhc/Papiers/ArticlesPJC/KUZNIK-CJC06.pdf>
- Kuznik, F., Catalina, T., Gauzere, L., Woloszyn, M., Roux, J.-J., Oct. 2011. Numerical modelling of combined heat transfers in a double skin façade – Full-scale laboratory experiment validation. Applied Thermal Engineering 31 (14-15), 3043–3054.
URL <http://linkinghub.elsevier.com/retrieve/pii/S1359431111002985>
- Kuznik, F., Rusaouën, G., Brau, J., 2007. Experimental and numerical study of a full scale ventilated enclosure: Comparison of four two equations closure turbulence models. Building and Environment 42 (3), 1043–1053.
URL <http://linkinghub.elsevier.com/retrieve/pii/S0360132305004841>
- Kuznik, F., Rusaouën, G., Hohotă, R., 2006. Experimental and numerical study of a mechanically ventilated enclosure with thermal effects. Energy and Buildings 38 (8), 931–938.
URL <http://linkinghub.elsevier.com/retrieve/pii/S0378778805001945>

-
- Kwok, D., Neumann, A., 1999. Contact angle measurement and contact angle interpretation. *Advances in Colloid and Interface Science* 81 (3), 167–249.
URL <http://linkinghub.elsevier.com/retrieve/pii/S0001868698000876>
- Kyowa, 2018. Measurement of the Contact Angle: Kyowa Interface Science.
URL http://www.face-kyowa.co.jp/english/en_science/en_theory/en_what_contact_angle/
- Lafuma, A., Quéré, D., Jul. 2003. Superhydrophobic states. *Nature Materials* 2 (7), 457–460.
URL <https://www.nature.com/articles/nmat924>
- Lara, J. R., Holtzapple, M. T., Sep. 2011a. Experimental investigation of dropwise condensation on hydrophobic heat exchangers part I: Dimpled-sheets. *Desalination* 278 (1), 165–172.
URL <http://www.sciencedirect.com/science/article/pii/S0011916411004322>
- Lara, J. R., Holtzapple, M. T., Oct. 2011b. Experimental investigation of dropwise condensation on hydrophobic heat exchangers. Part II: Effect of coatings and surface geometry. *Desalination* 280 (1), 363–369.
URL <http://www.sciencedirect.com/science/article/pii/S001191641100631X>
- Le Fevre, E. J., Rose, J., 1966. A theory of heat transfer by dropwise condensation. In: *Proceedings of the 3rd International Heat Transfer Conference*. Vol. 2. Chicago, pp. 362–375.
- Le Fevre, E. J., Rose, J. W., Aug. 1965. An experimental study of heat transfer by dropwise condensation. *International Journal of Heat and Mass Transfer* 8 (8), 1117–1133.
URL <http://www.sciencedirect.com/science/article/pii/0017931065901390>
- Legifrance, 1982. Arrêté du 24 mars 1982 relatif à l'aération des logements.
URL <https://www.legifrance.gouv.fr/affichTexte.do?cidTexte=JORFTEXT000000862344>
- Lemaire, A., 1993. Room air and contaminant flow, evaluation of computational methods, Subtask-1 summary report. International Energy Agency Annex 20 "Air Flow Pattern within Buildings" 20.
- Li, Y., Sandberg, M., Fuchs, L., Jan. 1993a. Effects of thermal radiation on airflow with displacement ventilation: an experimental investigation. *Energy and Buildings* 19 (4), 263–274.
URL <http://www.sciencedirect.com/science/article/pii/037877889390011I>
-

- Li, Z., Zhang, J., Zhivov, A., Christianson, L., 1993b. Characteristics of diffuser air jets and airflow in the occupied regions of mechanically ventilated rooms - a literature review. *ASHRAE Transactions* 99, 1119–1127.
- Lipczynska, A., Kaczmarczyk, J., Melikov, A. K., Oct. 2015. Thermal environment and air quality in office with personalized ventilation combined with chilled ceiling. *Building and Environment* 92, 603–614.
URL <http://www.sciencedirect.com/science/article/pii/S0360132315300081>
- Liu, J., Aizawa, H., Yoshino, H., Aug. 2004. CFD prediction of surface condensation on walls and its experimental validation. *Building and Environment* 39 (8), 905–911.
URL <http://www.sciencedirect.com/science/article/pii/S0360132304000265>
- Lobutova, E., Resagk, C., Putze, T., Jul. 2010. Investigation of large-scale circulations in room air flows using three-dimensional particle tracking velocimetry. *Building and Environment* 45 (7), 1653–1662.
URL <http://www.sciencedirect.com/science/article/pii/S0360132310000284>
- Loomans, M. G. L. C., 1998. The measurement and simulation of indoor air flow. Ph.D. thesis, oCLC: 246635166.
- Lucon, O., Ürge Vorsatz, D., Ahmed, A. Z., Akbari, H., Bertoldi, P., Cabeza, L. F., Eyre, N., Gadgil, A., Harvey, L. D., Jiang, Y., 2014. Buildings. *Climate Change 2014: Mitigation of Climate Change. Contribution of Working Group III to the Fifth Assessment Report of the Intergovernmental Panel on Climate Change (IPCC)* (9).
- Luo, S., Heikkinen, J., Roux, B., Dec. 2004. Simulation of air flow in the IEA Annex 20 test room—validation of a simplified model for the nozzle diffuser in isothermal test cases. *Building and Environment* 39 (12), 1403–1415.
URL <http://www.sciencedirect.com/science/article/pii/S0360132304001283>
- Ma, X., Li, X., Shao, X., Jiang, X., Sep. 2013. An algorithm to predict the transient moisture distribution for wall condensation under a steady flow field. *Building and Environment* 67, 56–68.
URL <http://www.sciencedirect.com/science/article/pii/S0360132313001431>
- Ma, X., Tao, B., Chen, J., Xu, D., Lin, J., Jul. 2001. Dropwise condensation heat transfer of steam on a polytetrafluoroethylene film. *Journal of Thermal Science* 10 (3), 247.
URL <http://link.springer.com/article/10.1007/s11630-001-0027-4>
- Magnier, L., Zmeureanu, R., Derome, D., Jan. 2012. Experimental assessment of the velocity and temperature distribution in an indoor displacement ventilation jet. *Building and Environment* 47, 150–160.
URL <http://www.sciencedirect.com/science/article/pii/S0360132311002435>

-
- Malmström, T. G., Kirkpatrick, A. T., Christensen, B., Knappmiller, K. D., 1997. Centre-line velocity decay measurements in low-velocity axisymmetric jets. *Journal of Fluid Mechanics* 346, 363–377.
- Malmström, T. G., Zou, Y., 2000. Influence of output characteristics on free axial air jets. *RoomVent 2000 proceedings*.
- Mathisen, H. M., Mundt, E., Nielsen, P. V., Moser, A., 2004. Ventilation effectiveness. *REHVA Guidebook*. Rehva, Federation of European Heating and Air- conditioning Associations, Brussels, oCLC: 750506149.
- McAdams, W. H., 1954. Heat transmission. Tech. rep.
- McCormick, J. L., Westwater, J. W., Dec. 1965. Nucleation sites for dropwise condensation. *Chemical Engineering Science* 20 (12), 1021–1036.
URL <http://www.sciencedirect.com/science/article/pii/000925096580104X>
- Mei, M., Hu, F., Han, C., Cheng, Y., Sep. 2015. Time-averaged droplet size distribution in steady-state dropwise condensation. *International Journal of Heat and Mass Transfer* 88, 338–345.
URL <http://www.sciencedirect.com/science/article/pii/S0017931015004573>
- Mei, M., Yu, B., Zou, M., Luo, L., Apr. 2011. A numerical study on growth mechanism of dropwise condensation. *International Journal of Heat and Mass Transfer* 54 (9), 2004–2013.
URL <http://www.sciencedirect.com/science/article/pii/S0017931011000032>
- Melikov, A., Pitchurov, G., Naydenov, K., Langkilde, G., Jun. 2005. Field study on occupant comfort and the office thermal environment in rooms with displacement ventilation. *Indoor Air* 15 (3), 205–214.
- Melikov, A. K., Hanzawa, H., Fanger, P. O., 1988. Airflow characteristics in the occupied zone of heated spaces without mechanical ventilation. *ASHRAE Transactions* 94 (1), 52–70.
- Melikov, A. K., Langkilde, G., 1990. Displacement ventilation-air flow in the near zone. Oslo, Norway.
- Melikov, A. K., Popiolek, Z., Silva, M. C. G., Care, I., Sefker, T., Nov. 2007. Accuracy Limitations for Low-Velocity Measurements and Draft Assessment in Rooms. *HVAC&R Research* 13 (6), 971–986.
URL <http://www.tandfonline.com/doi/abs/10.1080/10789669.2007.10391465>
- Melikov A. K., Aug. 2004. Personalized ventilation. *Indoor Air* 14 (s7), 157–167.
URL <https://onlinelibrary.wiley.com/doi/abs/10.1111/j.1600-0668.2004.00284.x>
-

- Melikov A. K., Mar. 2015. Advanced air distribution: improving health and comfort while reducing energy use. *Indoor Air* 26 (1), 112–124.
URL <https://onlinelibrary.wiley.com/doi/full/10.1111/ina.12206>
- Meslem, A., Bragança, P., Sodjavi, K., 2018. Mixing ventilation efficiency using a vortex diffuser - comparison to a lobed multi-cone diffuser. In: *Proceedings of Roomvent&Ventilation 2018*.
- Meslem, A., Nastase, I., Allard, F., Dec. 2010. Passive mixing control for innovative air diffusion terminal devices for buildings. *Building and Environment* 45 (12), 2679–2688.
URL <http://www.sciencedirect.com/science/article/pii/S0360132310001770>
- Mi, J., Xu, M., Zhou, T., Jul. 2013. Reynolds number influence on statistical behaviors of turbulence in a circular free jet. *Physics of Fluids* 25 (7), 075101.
URL <https://aip.scitation.org/doi/10.1063/1.4811403>
- Mikic, B. B., Oct. 1969. On mechanism of dropwise condensation. *International Journal of Heat and Mass Transfer* 12 (10), 1311–1323.
URL <http://www.sciencedirect.com/science/article/pii/0017931069901744>
- Mitrovic, J., Ricoeur, A., May 1995. Fluid dynamics and condensation-heating of capillary liquid jets. *International Journal of Heat and Mass Transfer* 38 (8), 1483–1494.
URL <http://www.sciencedirect.com/science/article/pii/001793109400258W>
- Morison, E. E., 2008. *Men, machines, and modern times*. M.I.T. Press, Cambridge, Mass., oCLC: 917736401.
- Mortensen, L. H., Woloszyn, M., Hohota, R., Rusaouën, G., 2005. CFD modelling of moisture interactions between air and constructions. In: *Proceedings of the 9th International IBPSA Conference-Building Simulation*. Montreal, Canada, p. 8.
- Murphy, M., 2006. *Sick building syndrome and the problem of uncertainty: environmental politics, technoscience, and women workers*. Duke University Press, London, oCLC: 989593041.
- Nahavandi, M., Mehrabani-Zeinabad, A., 2012. Effect of Contact Angle on Steam Dropwise Condensation: A Simulation Approach. *ISRN Chemical Engineering* 2012, 1–7.
URL <https://www.hindawi.com/archive/2012/789489/>
- Nastase, I., Meslem, A., Apr. 2010. Vortex dynamics and mass entrainment in turbulent lobed jets with and without lobe deflection angles. *Experiments in Fluids* 48 (4), 693–714.
URL <http://link.springer.com/article/10.1007/s00348-009-0762-y>

-
- Nastase, I., Meslem, A., Vlad, I., Colda, I., Mar. 2011. Lobed grilles for high mixing ventilation – An experimental analysis in a full scale model room. *Building and Environment* 46 (3), 547–555.
URL <http://www.sciencedirect.com/science/article/pii/S0360132310002519>
- Nicol, F., Humphreys, M. A., Roaf, S., 2012. Adaptive thermal comfort: principles and practice. Routledge, London; New York, oCLC: 730403966.
- Nicol, J. F., Humphreys, M. A., Jul. 2002. Adaptive thermal comfort and sustainable thermal standards for buildings. *Energy and Buildings* 34 (6), 563–572.
URL <http://www.sciencedirect.com/science/article/pii/S0378778802000063>
- Nielsen, P. V., 1975. Prediction of air flow and comfort in air conditioned spaces. *ASHRAE Transactions* 81 (2), 247–259.
- Nielsen, P. V., 1976. Flow in air conditioned rooms. Ph.D. thesis, Denmark.
- Nielsen, P. V., 1990. Specification of a Two-Dimensional Test Case: (IEA). International Energy Agency, Energy Conservation in Buildings and Community Systems, Annex 20: Air Flow Pattern within Buildings, 23.
- Nielsen, P. V., Sep. 2015. Fifty years of CFD for room air distribution. *Building and Environment* 91, 78–90.
URL <http://www.sciencedirect.com/science/article/pii/S036013231500092X>
- Nielsen, P. V., Rong, L., Olmedo, I., 2010. The IEA Annex 20 Two-Dimensional Benchmark Test for CFD Predictions. In: *Clima 2010*.
- Niu, D., Guo, L., Hu, H. W., Tang, G. H., Sep. 2017. Dropwise condensation heat transfer model considering the liquid-solid interfacial thermal resistance. *International Journal of Heat and Mass Transfer* 112, 333–342.
URL <http://www.sciencedirect.com/science/article/pii/S0017931016343812>
- Nomura, M., Hiyama, K., Jul. 2017. A review: Natural ventilation performance of office buildings in Japan. *Renewable and Sustainable Energy Reviews* 74, 746–754.
URL <http://www.sciencedirect.com/science/article/pii/S1364032117303131>
- Nusselt, W., 1916. Die Oberflächenkondensation des Wasserdampfes. *VDI Z* 60, 541–546.
URL <https://ci.nii.ac.jp/naid/10027762174/>
- Oberkampf, W. L., Trucano, T. G., Hirsch, C., Dec. 2004. Verification, validation, and predictive capability in computational engineering and physics. *Applied Mechanics Reviews* 57 (5), 345–384.
URL <http://dx.doi.org/10.1115/1.1767847>
-

OpenCV, 2018a. OpenCV: Contours in OpenCV.

URL https://docs.opencv.org/3.4.1/d3/d05/tutorial_py_table_of_contents_contours.html

OpenCV, 2018b. OpenCV: Image Thresholding.

URL https://docs.opencv.org/3.4.1/d7/d4d/tutorial_py_thresholding.html

OpenCV, 2018c. OpenCV: Smoothing Images.

URL https://docs.opencv.org/3.4.1/d4/d13/tutorial_py_filtering.html

Otsu, N., Jan. 1979. A Threshold Selection Method from Gray-Level Histograms. *IEEE Transactions on Systems, Man, and Cybernetics* 9 (1), 62–66.

Palmowska, A., Lipska, B., Nov. 2016. Experimental study and numerical prediction of thermal and humidity conditions in the ventilated ice rink arena. *Building and Environment* 108, 171–182.

URL <http://www.sciencedirect.com/science/article/pii/S0360132316303195>

Papadopoulos, A. M., Sep. 2016. Forty years of regulations on the thermal performance of the building envelope in Europe: Achievements, perspectives and challenges. *Energy and Buildings* 127, 942–952.

URL <http://www.sciencedirect.com/science/article/pii/S0378778816305400>

Paris, S., Kornprobst, P., Tumblin, J., Durand, F., 2007. A Gentle Introduction to Bilateral Filtering and Its Applications. In: *ACM SIGGRAPH 2007 Courses*. SIGGRAPH '07. ACM, New York, NY, USA.

URL <http://doi.acm.org/10.1145/1281500.1281602>

Passarelli, G. R., Jul. 2009. Sick building syndrome: An overview to raise awareness. *Journal of Building Appraisal* 5 (1), 55–66.

URL <https://link.springer.com/article/10.1057/jba.2009.20>

Plathner, P., Woloszyn, M., Feb. 2002. Interzonal air and moisture transport in a test house: experiment and modelling. *Building and Environment* 37 (2), 189–199.

URL <http://linkinghub.elsevier.com/retrieve/pii/S0360132300000962>

Popiolek, Z., Jørgensen, F. E., Melikov, A. K., Silva, M. C. G., Kierat, W., Sep. 2007. Assessment of Uncertainty in Measurements with Low Velocity Thermal Anemometers. *International Journal of Ventilation* 6 (2), 113–128.

URL <https://doi.org/10.1080/14733315.2007.11683771>

Posner, J. D., Buchanan, C. R., Dunn-Rankin, D., Jun. 2003. Measurement and prediction of indoor air flow in a model room. *Energy and Buildings* 35 (5), 515–526.

URL <http://www.sciencedirect.com/science/article/pii/S0378778802001639>

-
- Pérez-Lombard, L., Ortiz, J., Pout, C., Jan. 2008. A review on buildings energy consumption information. *Energy and Buildings* 40 (3), 394–398.
URL <http://www.sciencedirect.com/science/article/pii/S0378778807001016>
- Qin, M., 2011. Whole-building heat, air, and moisture transfer modeling for residential buildings in different climates. *HVAC&R Research*, 860–871.
- Raffel, M. (Ed.), 2007. *Particle image velocimetry: a practical guide*, 2nd Edition. Springer, Heidelberg ; New York.
- Rajaratnam, N., 1976. *Turbulent Jets*. Elsevier, google-Books-ID: g3R4gFObzloC.
- Redlich, C. A., Sparer, J., Cullen, M. R., Apr. 1997. Sick-building syndrome. *The Lancet* 349 (9057), 1013–1016.
URL <http://www.sciencedirect.com/science/article/pii/S0140673696072200>
- Ren, H., Zhao, B., Li, X., Fan, H., Yang, X., 2003. Influence of Diffuser Jet Characteristics on Indoor Air Distribution under Actual Connecting Conditions. *Journal of Architectural Engineering* 9 (4), 141–144.
URL <http://ascelibrary.org/doi/10.1061/%28ASCE%291076-0431%282003%299%3A4%28141%29>
- Resagk, C., du Puits, R., Thess, A., Raffel, M., Bosbach, J., Aroussi, A., 2004. Large-scale flow visualization and particle image velocimetry in convective airflow. In: *Proceedings of the 11th International Symposium on*. Vol. 2. pp. 9–12.
- Rodi, W. (Ed.), 1982. *Turbulent buoyant jets and plumes*, 1st Edition. No. 6 in HMT—the science & applications of heat and mass transfer. Pergamon Press, Oxford ; New York.
- Rodler, A., Nov. 2014. *Modélisation dynamique tridimensionnelle avec tache solaire pour la simulation du comportement thermique d'un bâtiment basse consommation*. PhD Thesis, INSA de Lyon.
URL <https://tel.archives-ouvertes.fr/tel-01175518/document>
- Rose, J. W., Jun. 1967. On the mechanism of dropwise condensation. *International Journal of Heat and Mass Transfer* 10 (6), 755–762.
URL <http://www.sciencedirect.com/science/article/pii/0017931067901354>
- Rose, J. W., Dec. 1976. Further aspects of dropwise condensation theory. *International Journal of Heat and Mass Transfer* 19 (12), 1363–1370.
URL <http://www.sciencedirect.com/science/article/pii/0017931076900648>
- Rose, J. W., 1981. Dropwise condensation theory. *International Journal of Heat and Mass Transfer* 24 (2), 191–194.
URL <http://linkinghub.elsevier.com/retrieve/pii/0017931081900260>
-

- Rose, J. W., Feb. 1998. Condensation Heat Transfer Fundamentals. Chemical Engineering Research and Design 76 (2), 143–152.
URL <http://www.sciencedirect.com/science/article/pii/S0263876298716314>
- Rose, J. W., Jan. 2002. Dropwise condensation theory and experiment: A review. Proceedings of the Institution of Mechanical Engineers, Part A: Journal of Power and Energy 216 (2), 115–128.
URL <https://doi.org/10.1243/09576500260049034>
- Rose, J. W., Glicksman, L. R., Feb. 1973. Dropwise condensation-The distribution of drop sizes. International Journal of Heat and Mass Transfer 16 (2), 411–425.
URL <http://www.sciencedirect.com/science/article/pii/0017931073900689>
- Russ, J. C., Neal, F. B., 2017. The image processing handbook.
- Sakay, D., 2014. Contribution à la caractérisation expérimentale des transferts couplés en écoulement turbulent en conduite horizontale avec ou sans condensation. PhD Thesis, Poitiers, France.
URL <http://www.theses.fr/2014ESMA0024>
- Sakay, D., Couton, D., Plourde, F., Nov. 2016. Experimental dropwise condensation of unsaturated humid air – Influence of humidity level on latent and convective heat transfer for fully developed turbulent flow. International Journal of Heat and Mass Transfer 102, 846–855.
URL <http://www.sciencedirect.com/science/article/pii/S001793101531560X>
- Sandberg, M., Nov. 2007. Whole-Field Measuring Methods in Ventilated Rooms. HVAC&R Research 13 (6), 951–970.
URL <http://www.tandfonline.com/doi/abs/10.1080/10789669.2007.10391464>
- Schmidt, E., Schurig, W., Sellschopp, W., Feb. 1930. Versuche über die Kondensation von Wasserdampf in Film- und Tropfenform. Technische Mechanik und Thermodynamik 1 (2), 53–63.
URL <http://link.springer.com/article/10.1007/BF02641051>
- Sensirion, 2018. SHT7x (RH/T) - Digital Humidity Sensor | Sensirion.
URL <https://www.sensirion.com/en/environmental-sensors/humidity-sensors/pintype-digital-humidity-sensors/>
- Seppänen, O., Fisk, W. J., Jun. 2002. Association of ventilation system type with SBS symptoms in office workers. Indoor Air 12 (2), 98–112.
- Seppänen, O. A., Fisk, W. J., 2004. Summary of human responses to ventilation. Indoor Air 14 Suppl 7, 102–118.

Serra, N., Semiao, V., Oct. 2013. Characterization of non-isothermal flows typical of built environments in a laboratory scale model. Part I – Experiments with 3d PIV. *Building and Environment* 68, 225–238.

URL <http://linkinghub.elsevier.com/retrieve/pii/S0360132313001856>

Shepelev, I., 1961. Supply ventilation jets and air fountains. *Proceedings of the academy of construction and architecture of the USSR* (4).

Skistad, H., Mundt, E., Federation of European Heating and Air-conditioning Associations, 2004. Displacement ventilation in non-industrial premises. No. 1 in *REHVA Guidebook*. Brussels, oCLC: 751442191.

Smoljan, D., Balen, I., 2010. Influence of a plenum box design on uniformity of the radial air jet issuing from a vortex diffuser. *Strojarstvo* 52 (3), 379–386.

URL http://hrcak.srce.hr/index.php?show=clanak&id_clanak_jezik=96615

Sun, Y., Tan, Z., Zhang, Y., Zhao, L., 2004a. Comparison of Six CFD Models for Room Airflow Study with PIV measurement Data. ASABE Paper No. 044097. ASAE.

URL <http://elibrary.asabe.org/abstract.asp?aid=17097&t=5>

Sun, Y., Zhang, Y., 2003. Development of a Stereoscopic Particle Image Velocimetry System for Full-Scale Room Airflow Studies, Part II: Experimental Setup. *ASHRAE Transactions* 109, 540–550, oCLC: 211149353.

Sun, Y., Zhang, Y., 2007. An Overview of Room Air Motion Measurement: Technology and Application. *HVAC&R Research* 13 (6), 929–950.

URL <http://www.tandfonline.com/doi/abs/10.1080/10789669.2007.10391463>

Sun, Y., Zhang, Y., Zhang, S., Zhao, L., Wang, X., 2001. Development of a Stereoscopic Particle Image Velocimetry System for Full-Scale Room Air Flow Studies. Part I: Algorithms and Validation. *American Society of Agricultural and Biological Engineers*, pp. 301–308.

URL <http://elibrary.asabe.org/abstract.asp?JID=1&AID=7087&CID=iles2001&T=1>

Sun, Y., Zhang, Y., Zhao, L., Wang, X., 2004b. An Algorithm of Stereoscopic Particle Image Velocimetry for Full-Scale Room Airflow Studies. *ASHRAE Transactions* 110, 75–80, oCLC: 195875294.

Sundell J., Levin H., Nazaroff W. W., Cain W. S., Fisk W. J., Grimsrud D. T., Gyntelberg F., Li Y., Persily A. K., Pickering A. C., Samet J. M., Spengler J. D., Taylor S. T., Weschler C. J., May 2011. Ventilation rates and health: multidisciplinary review of the scientific literature. *Indoor Air* 21 (3), 191–204.

URL <https://onlinelibrary.wiley.com/doi/abs/10.1111/j.1600-0668.2010.00703.x>

- Swenson, S. D., 1995. HVAC: heating, ventilating, and air conditioning. American Technical Publishers, Homewood, Ill., oCLC: 31662306.
- Takaharu, T., Hiroaki, T., Shigenori, T., Nov. 1991. Experimental verification of constriction resistance theory in dropwise condensation heat transfer. *International Journal of Heat and Mass Transfer* 34 (11), 2787–2796.
URL <http://www.sciencedirect.com/science/article/pii/001793109190238A>
- Tanaka, H., Feb. 1975. A Theoretical Study of Dropwise Condensation. *Journal of Heat Transfer* 97 (1), 72–78.
URL <http://heattransfer.asmedigitalcollection.asme.org/article.aspx?articleid=1436042>
- Tariku, F., Kumaran, K., Fazio, P., Jul. 2010. Integrated analysis of whole building heat, air and moisture transfer. *International Journal of Heat and Mass Transfer* 53 (15-16), 3111–3120.
URL <http://linkinghub.elsevier.com/retrieve/pii/S0017931010001493>
- Teodosiu, C., Hohota, R., Rusaouën, G., Woloszyn, M., May 2003. Numerical prediction of indoor air humidity and its effect on indoor environment. *Building and Environment* 38 (5), 655–664.
URL <http://linkinghub.elsevier.com/retrieve/pii/S0360132302002111>
- Teodosiu, R., 2013. Integrated moisture (including condensation) – Energy–airflow model within enclosures. Experimental validation. *Building and Environment* 61, 197–209.
URL <http://linkinghub.elsevier.com/retrieve/pii/S0360132312003332>
- Tiwari, A., 2011. Characterization of mass transfer by condensation on a horizontal plate. PhD Thesis, University of Blaise Pascal, Clermont-Ferrand, France.
- Tiwari, A., Fontaine, J.-P., Dec. 2009. Towards the Prediction of Heat and Mass Transfer in an Air-Conditioned Environment for a Life Support System in Space. *Water, Air, & Soil Pollution: Focus* 9 (5-6), 539.
URL <http://link.springer.com/article/10.1007/s11267-009-9232-z>
- Tollmien, W., 1926. Sonderabdruck aus zeitschrift fur angewandte. *Mathematik und Mechank* 6, 468–478.
- Tomasi, C., Manduchi, R., 1998. Bilateral filtering for gray and color images. In: *Proceedings of the 1998 IEEE International Conference on Computer Vision*. Bombay, India, pp. 839–846.
URL <http://ieeexplore.ieee.org/document/710815/>

-
- Tomasi, R., Krajčák, M., Simone, A., Olesen, B. W., May 2013. Experimental evaluation of air distribution in mechanically ventilated residential rooms: Thermal comfort and ventilation effectiveness. *Energy and Buildings* 60, 28–37.
URL <http://www.sciencedirect.com/science/article/pii/S0378778813000200>
- Tuve, G., 1953. Air velocities in ventilating jets. *ASHVE transactions* 59, 261.
- Umur, A., Griffith, P., May 1965. Mechanism of Dropwise Condensation. *Journal of Heat Transfer* 87 (2), 275–282.
URL <http://heattransfer.asmedigitalcollection.asme.org/article.aspx?articleid=1433511>
- UN, 2017. World Population Prospects 2017.
- Van Belleghem, M., Steeman, M., Janssen, H., Janssens, A., De Paepe, M., Nov. 2014. Validation of a coupled heat, vapour and liquid moisture transport model for porous materials implemented in CFD. *Building and Environment* 81, 340–353.
URL <http://www.sciencedirect.com/science/article/pii/S0360132314002169>
- Van Belleghem, M., Steeman, M., Willockx, A., Janssens, A., De Paepe, M., Apr. 2011. Benchmark experiments for moisture transfer modelling in air and porous materials. *Building and Environment* 46 (4), 884–898.
URL <http://www.sciencedirect.com/science/article/pii/S0360132310003100>
- van Hooff, T., Blocken, B., Defraeye, T., Carmeliet, J., van Heijst, G., Oct. 2012. PIV measurements and analysis of transitional flow in a reduced-scale model: Ventilation by a free plane jet with Coanda effect. *Building and Environment* 56, 301–313.
URL <http://linkinghub.elsevier.com/retrieve/pii/S0360132312001126>
- Vemuri, S., Kim, K. J., Feb. 2006. An experimental and theoretical study on the concept of dropwise condensation. *International Journal of Heat and Mass Transfer* 49 (3), 649–657.
URL <http://www.sciencedirect.com/science/article/pii/S0017931005005399>
- Vialle, P., Leroy, E., Meslem, A., 2015. Diffusion device with lobe inserts and fan coil comprising such a device. European Patent Office.
- Wang, S., Jiang, L., Nov. 2007. Definition of Superhydrophobic States. *Advanced Materials* 19 (21), 3423–3424.
URL <http://onlinelibrary.wiley.com/doi/abs/10.1002/adma.200700934>
- Wargocki, P., Sundell, J., Bischof, W., Brundrett, G., Fanger, P. O., Gyntelberg, F., Hanssen, S. O., Harrison, P., Pickering, A., Seppänen, O., Wouters, P., Jun. 2002. Ventilation and health in non-industrial indoor environments: report from a European multidisciplinary scientific consensus meeting (EUROVEN). *Indoor Air* 12 (2), 113–128.

- Wargocki, P., Wyon, D. P., Baik, Y. K., Clausen, G., Fanger, P. O., 1999. Perceived air quality, sick building syndrome (SBS) symptoms and productivity in an office with two different pollution loads. *Indoor air* 9 (3), 165–179.
- Welch, P., 1967. The use of fast Fourier transform for the estimation of power spectra: a method based on time averaging over short, modified periodograms. *IEEE Transactions on audio and electroacoustics* 15 (2), 70–73.
- Woloszyn, M., Hohota, R., Quenard, D., 2003. Whole building heat-airflow-moisture behaviour in France : Research in Cethil and CSTB Grenoble. Contribution to Annex 41: MOIST-ENG, 9.
- Woloszyn, M., Kalamees, T., Olivier Abadie, M., Steeman, M., Sasic Kalagasidis, A., Mar. 2009. The effect of combining a relative-humidity-sensitive ventilation system with the moisture-buffering capacity of materials on indoor climate and energy efficiency of buildings. *Building and Environment* 44 (3), 515–524.
URL <http://linkinghub.elsevier.com/retrieve/pii/S0360132308000772>
- Woloszyn, M., Rode, C., 2008. IEA Annex 41. Whole building heat, air, moisture response. Modeling Principles and Common Exercises. Report, KU LEUVEN, Belgium.
- Xu, C., Nielsen, P. V., Liu, L., Jensen, R. L., Gong, G., May 2018. Impacts of airflow interactions with thermal boundary layer on performance of personalized ventilation. *Building and Environment* 135, 31–41.
URL <http://www.sciencedirect.com/science/article/pii/S0360132318301203>
- Yang, B., Sekhar, C., Melikov, A. K., Dec. 2010. Ceiling mounted personalized ventilation system in hot and humid climate—An energy analysis. *Energy and Buildings* 42 (12), 2304–2308.
URL <http://www.sciencedirect.com/science/article/pii/S0378778810002380>
- Yongji, S., Dunqi, X., Jifang, L., Siexong, T., Nov. 1991. A study on the mechanism of drop-wise condensation. *International Journal of Heat and Mass Transfer* 34 (11), 2827–2831.
URL <http://www.sciencedirect.com/science/article/pii/0017931091902438>
- You, S., Li, W., Ye, T., Hu, F., Zheng, W., Nov. 2017. Study on moisture condensation on the interior surface of buildings in high humidity climate. *Building and Environment* 125, 39–48.
URL <http://www.sciencedirect.com/science/article/pii/S0360132317303943>
- Yuan, Y., Lee, T. R., 2013. Contact Angle and Wetting Properties. In: Bracco, G., Holst, B. (Eds.), *Surface Science Techniques*. Vol. 51. Springer Berlin Heidelberg, Berlin, Heidelberg, pp. 3–34.
URL http://link.springer.com/10.1007/978-3-642-34243-1_1

-
- Zhai, Z. J., Mankibi, M. E., Zoubir, A., Nov. 2015. Review of Natural Ventilation Models. *Energy Procedia* 78, 2700–2705.
URL <http://www.sciencedirect.com/science/article/pii/S1876610215020871>
- Zhang, J., Christianson, L., Riskowski, G., 1990. Regional airflow characteristics in a mechanically ventilated room under non-isothermal conditions. In: *ASHRAE Transactions*. Vol. 96. pp. 751–759.
- Zhang, J., Christianson, L., Riskowski, G., 1992a. Detailed measurements of room air distribution for evaluating numerical simulation models. Vol. 98. pp. 58–45.
- Zhang, J., Wu, G., Christianson, L., 1992b. Full-scale experimental results on the mean and turbulent behavior of room ventilation flows. *ASHRAE Transactions* 98, 307–318.
- Zhang, J. S., 1991. A fundamental study of two-dimensional room ventilation flows under isothermal and non-isothermal conditions. Ph.D. thesis, University of Illinois, Urbana, IL., oCLC: 774712748.
URL <http://hdl.handle.net/2142/22133>
- Zhao, L., Zhang, Y., Wang, X., Riskowski, G. L., Christianson, L. L., 1999. Measurement of airflow patterns in ventilated spaces using particle image velocimetry. In: *An ASAE Meeting Presentation*, Paper.
- Zhao, L., Zhang, Y., Wang, X., Riskowski, G. L., Christianson, L. L., 2001. Measurement of Two-Dimensional Air Velocities in a Full-Scale Room Using Particle Image Velocimetry. *ASHRAE Transactions* 107, 434–444, oCLC: 193373923.
- Zhivov, A., 1993. Theory and practice of air distribution with inclined jets. *ASHRAE Transactions* 99, 1152–1159.
- Zhong, L., Xuehu, M., Sifang, W., Mingzhe, W., Xiaonan, L., Feb. 2010. Effects of surface free energy and nanostructures on dropwise condensation. *Chemical Engineering Journal* 156 (3), 546–552.
URL <http://www.sciencedirect.com/science/article/pii/S1385894709002599>
- Zhou, G., Melikov, A. K., 2002. Equivalent frequency - a new parameter for description of frequency characteristics of airflow fluctuations. *Proceedings of Roomvent*, 357–336.
- Zou, Y., 2000. Velocity Decay in Air Jets for HVAC Applications. *ASHRAE Transactions* 106, 53–59, oCLC: 203478336.
- Zou, Y., 2001. Air jets in ventilation applications. Ph.D. thesis, KTH, Building Sciences and Engineering.
- Zou, Y., 2002. An Experimental Investigation of Turbulent Wall Jets. *ASHRAE Transactions* 108, 203–209, oCLC: 195415631.
-

Appendices

Uncertainty evaluation in sensors measurements

Introduction

In an experimental investigation, all sensors measurements are subject to uncertainty. A measurement result is considered as relevant when it is associated by a measurement uncertainty. This appendix describes the principle of determination of the measurement uncertainty.

Calculation principle of measurement uncertainty

Let Y be a physical quantity. We call Y_T the true value of Y and $(Y_i)_{i=1..N_Y}$ a sample set of brut measured values (obtained independently from N_Y measurement) of Y_T . The difference between a measured value and its true value is called the measurement error (or observational error). The total measurement error is noted ξ_i^Y and is defined as follows:

$$Y_T = Y_i + \xi_i^Y \quad (\text{A.1})$$

The total measurement error whose origin can come from two types: systematic errors and random errors. In order to not overload the section, basically, a systematic error is a component of error that remains constant over measurement sets, while a random error, which caused by inherently unpredictable fluctuations, vary from measurement to another. For that reason, the total measurement error can be decomposed into N_f term of ξ_{i,f_q}^Y . Each term ξ_{i,f_q}^Y is the measurement error related to an error factor f_q , which corresponds to a physical or numerical phenomenon. Therefore, the equation A.1 become:

$$Y_T = Y_i + \sum_{q=1}^{N_f} \xi_{i,f_q}^Y \quad (\text{A.2})$$

The measurement uncertainty evaluation consists of estimate the measurement error ξ_i^Y

by a confidence interval $[-\Delta_{95\%}^{Y_i}; \Delta_{95\%}^{Y_i}]$ in which we have a chance of 95% to find the true value Y_T :

$$Y_T = Y_i \pm \Delta_{95\%}^{Y_i} \quad (\text{A.3})$$

MEASUREMENT UNCERTAINTY OF A SINGLE ERROR

Assuming that all error factors ξ_{i,f_q}^Y are taken into account through one single term ξ_i^Y . The mean value \bar{Y} from the sample of brut measured value $(Y_i)_{i=1..N_Y}$ will give a best estimated value of Y_T :

$$\bar{Y} = \frac{\sum_{i=1}^{N_Y} Y_i}{N_Y} \quad (\text{A.4})$$

It is evident that the value of Y_T remains unknown, the true value of ξ_i^Y is also undetermined. Its value can only be estimated by approximated terms $(\delta_i^Y)_{i=1..N_Y}$ of a random variable Δ^Y . Its mean value and each term are calculated as follows:

$$\delta_i^Y = Y_i - \bar{Y} \quad (\text{A.5})$$

$$\bar{\delta}^Y = \frac{\sum_{i=1}^{N_Y} \delta_i^Y}{N_Y} \quad (\text{A.6})$$

Since the uncertainty is evaluated from a finite sample of measured values, the random variable Δ^Y will follow a Student's t-distribution. The sample standard deviation s^Y of the random variable Δ^Y is calculated as follows:

$$s^Y = \sqrt{\frac{\sum_{i=1}^{N_Y} (\delta_i^Y)^2}{\nu_Y}} = \sqrt{\frac{\sum_{i=1}^{N_Y} (Y_i - \bar{Y})^2}{\nu_Y}} \quad (\text{A.7})$$

with ν_Y is the degree of freedom, which equal to N_Y minus the number of parameters needed to estimate δ_i^Y . In this case, \bar{Y} is the only one parameter needed, thus $\nu_Y = N_Y - 1$.

Since the best estimator of Y_T is the sample mean \bar{Y} , we wanted to calculate the standard deviation of the sample mean $s^{\bar{Y}}$. It is estimated as the sample standard deviation divided by the square root of the sample size N_Y :

$$s^{\bar{Y}} = \frac{s^Y}{\sqrt{N_Y}} \quad (\text{A.8})$$

Once the sample standard deviation s^Y and the standard deviation of the sample mean $s^{\bar{Y}}$ is determined, it is possible to estimate the 95% confidence interval of the brut measured

values Y_i and the sample mean \bar{Y} as follows:

$$\Delta_{95\%}^{Y_i} = t_{0.975}^{\nu_Y} \cdot s^Y \quad (\text{A.9})$$

$$\Delta_{95\%}^{\bar{Y}} = t_{0.975}^{\nu_Y} \cdot s^{\bar{Y}} = t_{0.975}^{\nu_Y} \cdot \frac{s^Y}{\sqrt{N_Y}} \quad (\text{A.10})$$

with $t_{0.975}^{\nu_Y}$ refers to the Student's t-distribution value of order 0.975 associated with ν_Y degrees of freedom. Its value can be found in a t-distribution statistical table.

In other words, at the confidence interval of 95%, the true value Y_T lies within the interval:

$$Y_i \pm t_{0.975}^{\nu_Y} \cdot s^Y$$

and we have the true sample mean \bar{Y} (best estimator of Y_T) lying within the interval:

$$\bar{Y} \pm t_{0.975}^{\nu_Y} \cdot \frac{s^Y}{\sqrt{N_Y}}$$

Besides, it is worthwhile to mention that the estimation of the measurement error can be improved by performing several sample sets of measurement. For instance, if a number of N_s samples of brut measured value $(Y_{i,s})_{i=1..N_{Y,s}}$ is performed, the total sample standard deviation $(s^Y)_{tot}$ of the random variable Δ^Y is calculated as follows:

$$(s^Y)_{tot} = \sqrt{\frac{\sum_{s=1}^{N_s} \nu_{Y,s} \cdot s_{Y,s}^2}{\nu_{Y,tot}}} \quad (\text{A.11a})$$

$$\nu_{Y,tot} = \sum_{s=1}^{N_s} \nu_{Y,s} \quad (\text{A.11b})$$

with $s_{Y,s}$, $\nu_{Y,s}$ are respectively the standard deviation and the degrees of freedom of each sample set.

MEASUREMENT UNCERTAINTY OF MULTIPLE ERROR FACTORS

Now assuming that all error factors ξ_{i,f_q}^Y are taken into account separately. In other words, the total measurement error is decomposed into N_f term of ξ_{i,f_q}^Y . Each term ξ_{i,f_q}^Y is the measurement error related to an error factor f_q and is approximated by a random variable $(\Delta^Y)_{f_q}$.

The first step consists of, for each error factor f_q , estimate the statistical parameters (i.e. the mean value and the standard deviation) associated to each random variable $(\Delta^Y)_{f_q}$.

In order to determine those statistical parameters of $(\Delta^Y)_{f_q}$, we need a sample set of

measured values $(Y_{i,f_q})_{i=1..N_{Y,f_q}}$ in which all error factors other than f_q are blocked. For example, an error factor f_2 is said to be blocked if the measurement error $(\xi_{i,f_2}^Y)_{i=1..N_{Y,f_2}}$ remains constant in the sample set of measured values $(Y_{i,f_1})_{i=1..N_{Y,f_1}}$ associated to the error factor f_1 .

The mean value \overline{Y}_{f_q} and the standard deviation $s_{f_q}^Y$ are then calculated in the same way as the previous section, i.e. (A.4) and (A.7) equations.

In addition, the estimation of those parameters can eventually be improved by performing several sample sets of measurement for each error factor f_q . The "improved" mean value and standard deviation are calculated using (A.11a) and (A.11b) equations.

Once the statistical parameters of each random variable $(\Delta^Y)_{f_q}$ related to each error factor f_q are determined, we wanted to estimate the statistical parameters of the random variable associated to the total error Δ^Y .

Assuming that all error factors f_q are independents, the standard deviation related to the total error Δ^Y is calculated as follows:

$$s^Y = \sqrt{\sum_{q=1}^{N_f} (s_{f_q}^Y)^2} \quad (\text{A.12a})$$

$$\nu_Y \simeq \left| \frac{\left(\sum_{q=1}^{N_f} \left[\frac{(s_{f_q}^Y)^2}{N_{Y,f_q}} \right] \right)^2}{\sum_{q=1}^{N_f} \left[\left(\frac{(s_{f_q}^Y)^2}{N_{Y,f_q}} \right)^2 \cdot \frac{1}{\nu_{Y,f_q}} \right]} \right| \quad (\text{A.12b})$$

with N_{Y,f_q} , ν_{Y,f_q} are respectively the sample size and the degrees of freedom associated to each error factor f_q . The equation (A.12b) is called Welch-Satterthwaite equation¹.

Afterwards, we wanted to estimate the standard deviation of the mean \overline{Y} . As mentioned in the beginning of the section, there are two types of measurement error:

- random errors $f_{q,r}$: their terms $\xi_{i,f_{q,r}}^Y$ vary from measurement to another ;
- systematic errors $f_{q,s}$: their terms $\xi_{i,f_{q,s}}^Y$ are considered to remain constant for all measurement sets.

Therefore, the standard deviation of the mean $s^{\overline{Y}}$ related to the total measurement error is expressed with the following equation:

$$s^{\overline{Y}} = \sqrt{\sum_{r=1}^{N_{q,r}} \frac{(s_{f_{q,r}}^Y)^2}{N_Y} + \sum_{s=1}^{N_{q,s}} (s_{f_{q,s}}^Y)^2} \quad (\text{A.13})$$

¹In statistics and uncertainty analysis, the Welch-Satterthwaite equation is used to calculate an approximation to the effective degrees of freedom of a linear combination of independent sample variances.

It is possible now to determine the uncertainty at 95% confidence interval of the brut measured values and the mean value as follows:

$$\Delta_{95\%}^{Y_i} = t_{0.975}^{v_Y} \cdot s^Y = t_{0.975}^{v_Y} \cdot \sqrt{\sum_{q=1}^{N_f} (s_{f_q}^Y)^2} \quad (\text{A.14})$$

$$\Delta_{95\%}^{\bar{Y}} = t_{0.975}^{v_Y} \cdot s^{\bar{Y}} = t_{0.975}^{v_Y} \cdot \sqrt{\sum_{r=1}^{N_{q,r}} \frac{(s_{f_{q,r}}^Y)^2}{N_Y} + \sum_{s=1}^{N_{q,s}} (s_{f_{q,s}}^Y)^2} \quad (\text{A.15})$$

Calibration procedure for thermocouples

Our thermocouples are calibrated in-situ at our laboratory. The calibration device consists of a reflux thermostatic bath Lauda RM6T with constant fluid temperature and a reference sensor Pt100 AOIP AN 5847, which is connected to a thermometer AOIP PHP61. A scheme of the thermostatic bath is illustrated in the Figure B.1.

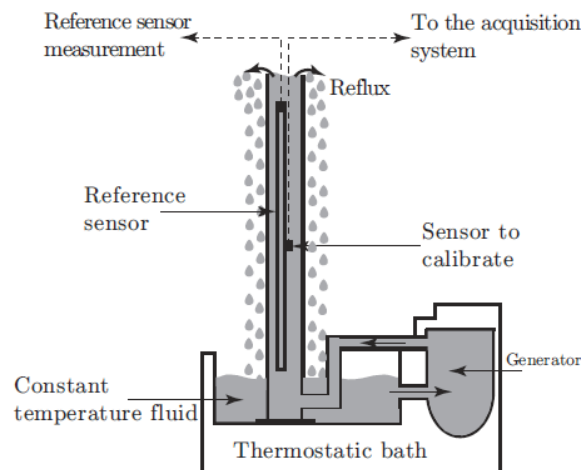


Figure B.1 – Calibration reflux thermostatic bath scheme

Calibration process steps

The steps of data acquisition, obtaining the calibration curve and the calculation of the uncertainties are explained for a single thermocouple in order to not overload the section. Data acquisition was performed at once for all the 17 thermocouples. The data processing for obtaining the calibration curves and the calculation of the uncertainties is identical for each thermocouple.

The temperature range in which the calibration is performed is situated between 1 °C and 50 °C. This range covers largely the temperature need to measure within our test configuration. A total number of $N_i = 58$ measurement sets was carried out within this

temperature range. For each measurement set, the following data have been recorded:

- one value of the reference sensor temperature $T_{ref,i}$
- one value of the acquisition card temperature $T_{ca,i}$
- one value of the cold-junction temperature $T_{sf,i}$
- $N_j = 150$ values of the thermocouple voltage $(V_{tc,ij})_{j=1..N_j}$
(data acquired simultaneously in 15 seconds at 10 Hz).

In fact, the FPGA module on the NI cRIO-9074 is capable to measure the brute thermocouple voltage, named $V_{tc,ijk}$ at very high frequency (50 Hz). These brute values are then averaged over $N_k = 650$ measurements to obtain the thermocouple voltage $V_{tc,ij}$. They are communicated at a frequency of 10 Hz, these values that will be used for the calibration. By averaging over $N_j = 150$ recordings, we obtain the mean value of the thermocouple tension measured:

$$\overline{V_{tc,i}} = \frac{\sum_{j=1}^{N_j} V_{tc,ij}}{N_j} \quad (B.1)$$

The temperature difference between the reference sensor temperature and the cold-junction temperature, as well as the reference voltage obtained with an ideal thermocouple are calculated for each measurement set:

$$\Delta T_{RS,i} = T_{sf,i} - T_{ref,i} \quad (B.2)$$

$$V_{ref,i} = f^{-1}(\Delta T_{RS,i}) \quad (B.3)$$

Then the difference between the reference thermocouple voltage and the mean thermocouple voltage measured can be deducted as follows:

$$dV_i = V_{ref,i}(\Delta T_{RS,i}) - \overline{V_{tc,i}}(\Delta T_{RS,i}, T_{ca,i}) \quad (B.4)$$

For each measurement set, a curve of dV_i is drawn as a function of the mean thermocouple voltage measured and the acquisition card temperature: $dV_i = f(\overline{V_{tc,i}}, T_{ca,i})$. A linear (or polynomial) regression is used to obtain the correction value $corrV_i(\overline{V_{tc,i}}, T_{ca,i})$.

The curve is used to determine the correlation, which can be expressed as follows:

$$corrV_i = c_0 + c_{tc} \overline{V_{tc,i}} + c_{ca} T_{ca,i} \quad (B.5)$$

Once the value of $corrV_i$ is determined along with the triple coefficient (c_0 , c_{tc} , c_{ca}), we correct the thermocouple tension value measured with the following formula:

$$V_{corr,i} = \overline{V_{tc,i}} + corrV_i \quad (B.6)$$

Measurement uncertainty determination

The principle of the uncertainty calculation is detailed in the Appendix A and is used in this case to determine the measurement uncertainty of the thermocouple.

The total error of the thermocouple tension corrected value $V_{corr,i}$ with regard to the true value of tension V_{true} can be decomposed in two terms. One term corresponds to the systematic error $\xi_{s,i}^V$ and another to the random error $\xi_{r,i}^V$. The systematic error $\xi_{s,i}^V$ is due to the calibration correction since it remains constant over measurement sets. The random error $\xi_{r,i}^V$ is due to the high-frequency noise along the measurement data acquisition center. Thus, the thermocouple tension corrected value $V_{corr,i}$ can be expressed as follows:

$$V_{corr,i} = V_{true} + \xi_{s,i}^V + \xi_{r,i}^V \quad (B.7)$$

The random error term, supposing independently from the systematic error, will statistically tend to follow a normal distribution. The sample standard deviation of the random error related to the high-frequency noise for one measurement set is calculated as follows:

$$s_{\xi_{r,i}}^V = \sqrt{\frac{\sum_{j=1}^{N_j} (V_{tc,ij} - \overline{V_{tc,i}})^2}{N_j - 1}} \quad (B.8)$$

Then, the total sample deviation related to the random error can be deducted by intrinsically averaging these $s_{\xi_{r,i}}^V$ over $N_i = 58$ measurement sets:

$$s_{\xi_r}^V = \sqrt{\frac{\sum_{i=1}^{N_i} (s_{\xi_{r,i}}^V)^2}{N_i - 1}} \quad (B.9)$$

On the other side, using the equations (B.4) and (B.5), the total sample standard deviation of the systematic error related to the calibration correction can be calculated as follows:

$$s_{\xi_s}^V = \sqrt{\frac{\sum_{i=1}^{N_i} (dV_i - corrV_i)^2}{N_i - 1}} \quad (B.10)$$

Using the equation (A.12) as mentioned in the Appendix A, it is possible to estimate the total standard deviation of the measurement error and the 95% confidence interval of the measured values as follows:

$$s^V = \sqrt{(s_{\xi_s}^V)^2 + (s_{\xi_r}^V)^2} \quad (B.11)$$

$$\Delta_{95\%}^{V_{corr}} = t_{0.975} \cdot s^V \quad (B.12)$$

with $t_{0.975}$ refers to the Student's t-distribution value of order 0.975 associated with $N_i - 1$ degrees of freedom.

In other words, at the confidence interval of 95%, the true thermocouple tension value V_{true} lies within the interval:

$$V_{true} = V_{corr} \pm \Delta_{95\%}^{V_{corr}}$$

A tension-temperature conversion gives us the measurement uncertainty of our thermocouple : $\Delta_{95\%}^{T_{corr}} \simeq 0.06^\circ\text{C}$.

Thermocouple response time

Generally, the *response time* (t_R) is the elapses time required for a sensor, after a sudden change (named a step) of a quantity from one state/condition to another, until the variation of the output of the sensor differs only by $\varepsilon\%$ of the final (asymptotic) value. One notes: t_R ($\varepsilon\%$).

If the response time was zero, the sensor would be able to instantly follow the variations of the sensed quantity. This is however impossible in reality. It follows a transitional regime that needs to be characterized.

A *time constant* (τ) is defined as the response time corresponding to an $\varepsilon \approx 63.2\%$, which means the time required by a sensor to reach approximately 63.2% of a step change of a sensed quantity. Three time constants and five time constants are required for the sensor to approach 95% and 100% of the step change value, accordingly.

Therefore, the maximum acquisition frequency allowed by the sensor is defined as:

$$f(Hz) = \frac{1}{5\tau} \quad (C.1)$$

Time constant determination

The time constant can be modeled or approximated by a first-order linear differential equation as follows:

$$T(t) = T_i + \tau \frac{\partial T}{\partial t} \quad (C.2)$$

The solution of the equation (C.2) can be expressed as follows:

$$T(t) = T_0 + (T_1 - T_0)(1 - e^{-t/\tau}) \quad (C.3)$$

$$\text{or } \frac{\Delta T(t)}{\Delta T_0} = \frac{T(t) - T_0}{T_1 - T_0} = 1 - e^{-t/\tau} \quad (C.4)$$

An illustration of the equation (C.4) is presented in the Figure C.1. The y-axis (i.e.

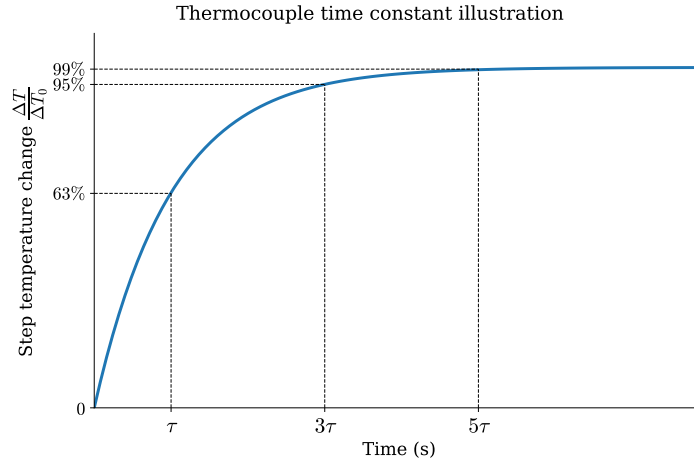


Figure C.1 – Thermocouple step change temperature as a function of time constant

the ratio $\Delta T(t)/\Delta T_0$ represents a step change of temperature in percentage. The time constant τ is defined as how long it takes the thermocouple to reach 63% of a step temperature change. It takes about five time constants to obtain steady state readings.

In the other hand, the time constant of the thermocouple sensing element can be physically determined by using the thermal energy balance established as follows:

$$\underbrace{\rho_{tc} C_{p,tc} V_{tc} \frac{\partial T_{tc}}{\partial t}}_{\text{accumulated}} = \underbrace{h_{air} S_{tc} (T_{tc} - T_{air})}_{\text{convection}} + \underbrace{\lambda_{tc} S_{tc} \frac{\partial^2 T_{tc}}{\partial x^2}}_{\text{conduction}} + \underbrace{\sigma \epsilon_{tc} S_{tc} (T_{air}^4 - T_{tc}^4)}_{\text{radiation}} \quad (C.5)$$

with:

- T_{air} : the air temperature to measure [$^{\circ}\text{C}$]
- T_{tc} : the temperature measured by the thermocouple [$^{\circ}\text{C}$]
- V_{tc} : the volume of the thermocouple sensing element [m^3]
- S_{tc} : the surface of the thermocouple sensing element [m^2]
- ρ_{tc} : the thermocouple¹ density [kg/m^3]
- $C_{p,tc}$: the thermocouple specific heat capacity [$\text{J}/\text{kg.K}$]
- h_{air} : the air convection coefficient [$\text{W}/\text{m}^2.\text{K}$]
- λ_{tc} : the thermocouple thermal conductivity [$\text{W}/\text{m.K}$]
- σ : the Stefan-Boltzmann constant [$\text{W}/\text{m}^2.\text{K}^4$]
- ϵ_{tc} : the thermocouple emissivity [-]

¹to be exactly, those are the physical properties of the thermoelement material that make the thermocouple; but for the sake of simplicity, the term "thermocouple" is used.

In our case, the two terms of conductive heat transfer and the radiative transfer can be neglected with regard to the convective heat transfer between the thermocouple and the ambient air. Thus, the equation (C.5) is reduced to:

$$\rho_{tc} C_{p,tc} V_{tc} \frac{\partial T_{tc}}{\partial t} = h_{air} S_{tc} (T_{tc} - T_{air}) \quad (C.6)$$

In order to obtain the same form as the equation (C.2), the equation (C.6) can be expressed as follows:

$$T_{air} + \frac{\rho_{tc} C_{p,tc} V_{tc}}{h_{air} S_{tc}} \frac{\partial T_{tc}}{\partial t} = T_{tc} \quad (C.7)$$

Combining both equations (C.2) and (C.7), one could deduct the expression of τ as follows:

$$\tau = \frac{\rho_{tc} C_{p,tc} V_{tc}}{h_{air} S_{tc}} \quad (C.8)$$

The evaluation of τ requires then the knowledge of the physical properties of the thermocouple, which are given by the manufacturer, and more importantly the determination of the air convection coefficient h_{air} . This coefficient, which depends on the convection type (natural or forced), vary as a function of the dimensionless Nusselt number:

$$h_{air} = \frac{\lambda_{air} Nu}{d_{tc}} \quad (C.9)$$

with:

- λ_{air} : the air thermal conductivity [$W/m.K$]
- Nu : Nusselt number, which characterizes the heat exchange between a fluid and an object [-]
- d_{tc} : the diameter of the thermocouple sensing element [m]

Generally, the Nusselt number depends on three other dimensionless number, $Nu = f(Re, Gr, Pr)$:

- Re : the Reynolds number, which is a measure of the ratio of the inertial to viscous forces acting on the fluid. It characterizes the fluid flow regime;
- Gr : the Grashof number, which is a measure of the ratio of the buoyancy forces to the viscous forces acting on the fluid. It characterizes the natural convection;
- Pr : the Prandtl number, which is the ratio of momentum diffusivity to thermal diffusivity.

These three dimensionless number are expressed as follows:

$$Re = \frac{u_{air} d_{tc}}{\nu_{air}} \quad (C.10)$$

$$Gr = \frac{g \beta_{air} (T_{tc} - T_{\infty}) d_{tc}^3}{\nu_{air}^2} \quad (C.11)$$

$$Pr = \frac{\nu_{air}}{\alpha_{air}} \quad (C.12)$$

with:

- u_{air} : the air velocity [m/s]
- ν_{air} : the air momentum diffusivity (kinematic viscosity) [m^2/s]
- g : the acceleration due to Earth's gravity [m/s^2]
- β_{air} : the air thermal expansion coefficient [$1/K$]
- T_{∞} : the quiescent temperature (fluid temperature far from the surface of the object)
- α_{air} : the air thermal diffusivity [m^2/s]

In the case of the natural convection (i.e. the ratio $Gr/Re^2 \gg 1$), the Nusselt number depends only in terms of the Grashof and the Prandtl number, $Nu = f(Gr, Pr)$ (Incropera and Dewitt, 2007):

$$Nu = \left(0.6 + \frac{0.387 Ra^{1/6}}{[1 + (0.559/Pr)^{9/16}]^{8/27}} \right)^2 \quad (C.13)$$

with: $Ra = Gr.Pr$ - the Rayleigh number, which is the product of the Grashof number and the Prandtl number.

The formula expressed above is only applicable if the following condition is satisfied: $Ra < 10^{12}$.

As for the other case (i.e. the forced convection), the ratio $Gr/Re^2 \ll 1$ and thus the Nusselt number depends only in terms of the Reynolds and the Prandtl number, $Nu = f(Re, Pr)$ (Incropera and Dewitt, 2007):

$$Nu = 2 + 0.6 Pr^{1/3} Re^{1/2} \quad (C.14)$$

The formula expressed above is only applicable if two following conditions are satisfied: $0.6 < Pr < 400$ and $Re < 7.10^4$.

The Table C.1 presents the physical properties of the ambient air, supposed at 20 °C and of the thermoelements, which are the chromel and the alumel², as for a K-type ther-

²Chromel is an alloy made of approximately 90% nickel and 10% chromium. Alumel is an alloy con-

mocouple.

Thermophysical properties		Thermoelement materials		Ambient fluid
Name	Symbol	Chromel	Alumel	Air
Density	ρ [kg/m^3]	8730	8600	1.204
Specific heat capacity	C_p [$J/kg.K$]	448	523	1012
Thermal conductivity	λ [$W/m.K$]	19.2	29.7	0.025
Thermal expansion	β [$1/K$]	-	-	3413.10^{-6}
Thermal diffusivity	α [m^2/s]	-	-	20.10^{-6}
Kinematic viscosity	ν [m^2/s]	-	-	15.10^{-6}

Table C.1 – Thermophysical properties of K-type thermocouple thermoelement materials and of ambient air at 20 °C

Junction diameter $\varnothing[\mu m]$	$u_{air} = 0.03$ m/s		$u_{air} = 1.0$ m/s		$u_{air} = 2.1$ m/s	
	τ [ms]	f [Hz]	τ [ms]	f [Hz]	τ [ms]	f [Hz]
250	783.21	0.25	443	0.45	358.5	0.56
25	8.80	22.7	6.91	28.9	6.19	32.3

Table C.2 – K-type thermocouple time constant following the junction diameter and the ambient air velocity

Thermocouple junction of diameter $\varnothing 250 \mu m$ or $\varnothing 25 \mu m$?

In our study, we are rather in the case of the forced convection since the indoor airflow is ventilated mechanically. Using the equations (C.8), (C.9) and (C.14), one could determine the time constant τ . The table C.2 presents the time constant obtained for two K-type thermocouples ($\varnothing 250 \mu m$ and $\varnothing 25 \mu m$). The calculation are based only on two extremum values and one mean value of air velocity measured, which are 0.03 m/s, 1.0 m/s and 2.1 m/s.

The results obtained from the Table C.2 for a mean air velocity measured of 1.0 m/s is illustrated in the Figure C.2. For a step temperature change, the thermocouples of $\varnothing 250 \mu m$ and of $\varnothing 25 \mu m$ takes respectively about 2 seconds and 0.03 second (quasi-instantaneous) to reach the steady state readings.

sisting of approximately 95% nickel, 2% aluminum, 2% manganese, and 1% silicon.

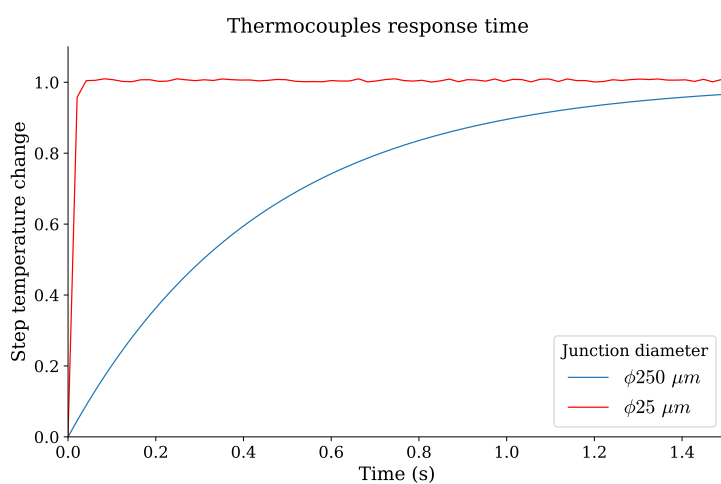
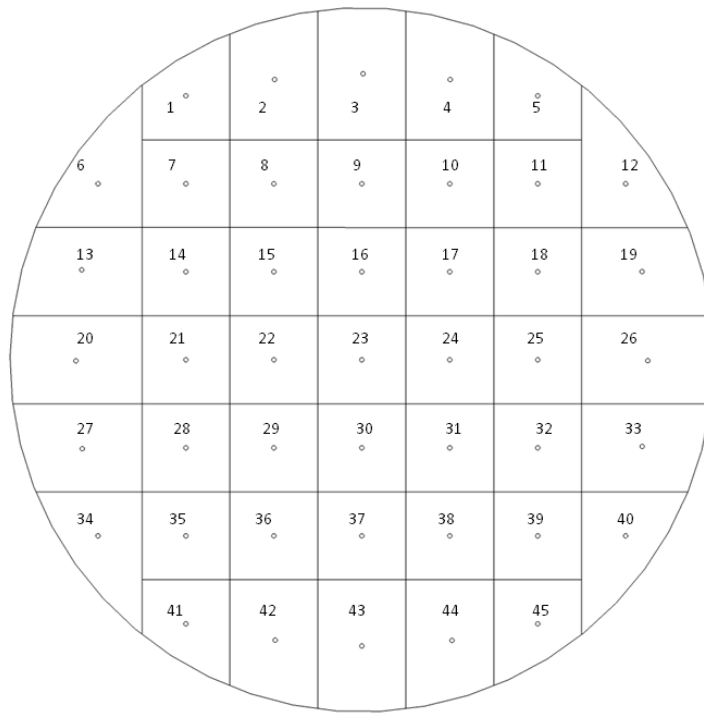


Figure C.2 – The response time of two K-type thermocouples with different junction diameter $\phi 250 \mu m$ and $\phi 25 \mu m$

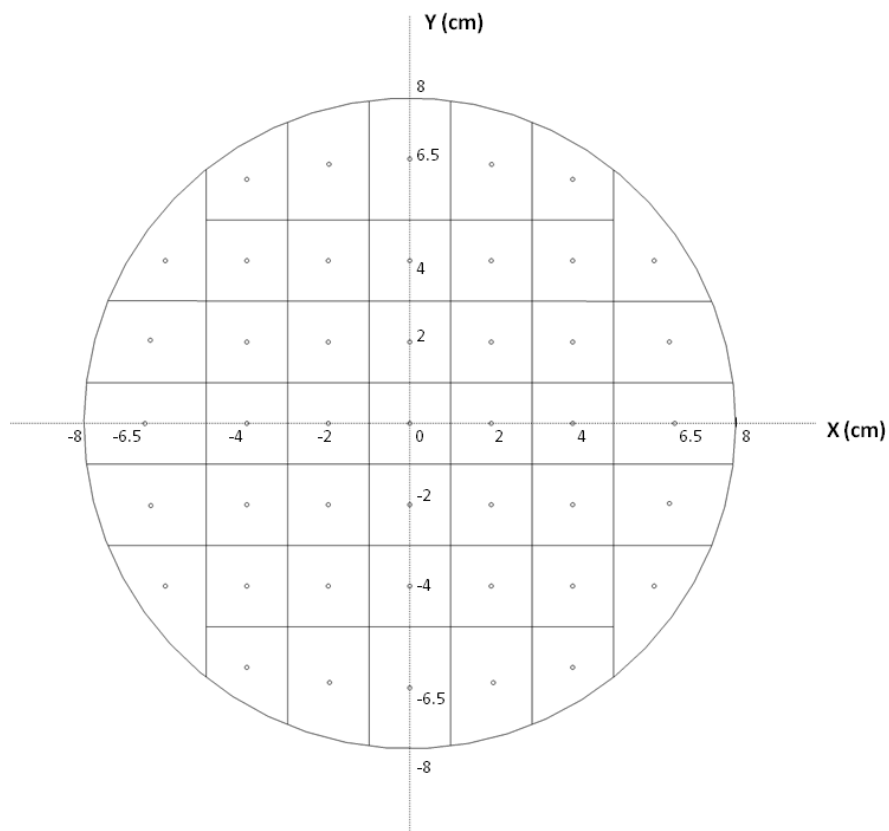
Verification of the supply air flow rate

As shown in the Figure D.1, the outlet diffuser is decomposed into multiple small zones whose area are known. We impose a flow rate in the air handling unit. We measure the air velocity in each zone and we deduct the airflow rate in each zone. The total airflow rate throughout the diffuser is the sum of all the air flow rate above-mentioned.

Two air flow rate set points are tested: $100 \text{ m}^3/\text{h}$ and $200 \text{ m}^3/\text{h}$. We found that the air flow rate difference between the air flow meter and the air supply did not excess 2%.



(a) Mesh numbering



(b) XY-coordinate definition

Figure D.1 – Decomposition of the outlet diffuser into small zones

N°	X	Y	S (cm²)	U (m/s)	Q (m³/h)
1	-4	6	3.78	1.36	1.850688
2	-2	6.35	5.44	1.44	2.820096
3	0	6.5	5.95	1.36	2.91312
4	2	6.35	5.44	1.46	2.859264
5	4	6	3.78	1.51	2.054808
6	-6	4	4.6	1.48	2.45088
7	-4	4	4	1.4	2.016
8	-2	4	4	1.24	1.7856
9	0	4	4	1.18	1.6992
10	2	4	4	1.28	1.8432
11	4	4	4	1.35	1.944
12	6	4	4.6	1.42	2.35152
13	-6.35	2	5.44	1.47	2.878848
14	-4	2	4	1.36	1.9584
15	-2	2	4	1.25	1.8
16	0	2	4	1.2	1.728
17	2	2	4	1.18	1.6992
18	4	2	4	1.34	1.9296
19	6.35	2	5.44	1.48	2.898432
20	-6.5	0	5.95	1.5	3.213
21	-4	0	4	1.41	2.0304
22	-2	0	4	1.23	1.7712
23	0	0	4	1.18	1.6992
24	2	0	4	1.19	1.7136
25	4	0	4	1.39	2.0016
26	6.5	0	5.95	1.46	3.12732
27	-6.35	-2	5.44	1.56	3.055104
28	-4	-2	4	1.39	2.0016
29	-2	-2	4	1.2	1.728
30	0	-2	4	1.17	1.6848
31	2	-2	4	1.26	1.8144
32	4	-2	4	1.4	2.016
33	6.35	-2	5.44	1.55	3.03552
34	-6	-4	4.6	1.26	2.08656
35	-4	-4	4	1.54	2.2176
36	-2	-4	4	1.44	2.0736
37	0	-4	4	1.35	1.944
38	2	-4	4	1.42	2.0448
39	4	-4	4	1.55	2.232
40	6	-4	4.6	1.44	2.38464
41	-4	-6	3.78	1.69	2.299752
42	-2	-6.35	5.44	1.64	3.211776
43	0	-6.5	5.95	1.71	3.66282
44	2	-6.35	5.44	1.65	3.23136
45	4	-6	3.78	1.7	2.31336
				Qtot	102.07487

Figure D.2 – Data table for the air flow rate of 100 m³/h

N°	X	Y	S (cm²)	U (m/s)	Q (m³/h)
1	-4	6	3.77	3.82	5.184504
2	-2	6.35	5.43	3.72	7.271856
3	0	6.5	5.94	3.55	7.59132
4	2	6.35	5.43	3.34	6.529032
5	4	6	3.77	3.66	4.967352
6	-6	4	4.58	3.6	5.93568
7	-4	4	4	3.48	5.0112
8	-2	4	4	2.87	4.1328
9	0	4	4	2.61	3.7584
10	2	4	4	2.98	4.2912
11	4	4	4	3.33	4.7952
12	6	4	4.58	3.51	5.787288
13	-6.35	2	5.43	3.18	6.216264
14	-4	2	4	2.75	3.96
15	-2	2	4	2.5	3.6
16	0	2	4	2.55	3.672
17	2	2	4	2.44	3.5136
18	4	2	4	2.63	3.7872
19	6.35	2	5.43	3.55	6.93954
20	-6.5	0	5.94	3.18	6.800112
21	-4	0	4	2.58	3.7152
22	-2	0	4	2.62	3.7728
23	0	0	4	2.7	3.888
24	2	0	4	2.55	3.672
25	4	0	4	2.83	4.0752
26	6.5	0	5.94	3.08	6.586272
27	-6.35	-2	5.43	3.05	5.96214
28	-4	-2	4	2.41	3.4704
29	-2	-2	4	2.47	3.5568
30	0	-2	4	2.17	3.1248
31	2	-2	4	2.35	3.384
32	4	-2	4	2.75	3.96
33	6.35	-2	5.43	2.88	5.629824
34	-6	-4	4.58	2.98	4.913424
35	-4	-4	4	2.69	3.8736
36	-2	-4	4	2.3	3.312
37	0	-4	4	2.24	3.2256
38	2	-4	4	2.57	3.7008
39	4	-4	4	2.93	4.2192
40	6	-4	4.58	3.01	4.962888
41	-4	-6	3.77	2.94	3.990168
42	-2	-6.35	5.43	2.86	5.590728
43	0	-6.5	5.94	2.1	4.49064
44	2	-6.35	5.43	1.46	2.854008
45	4	-6	3.77	1.45	1.96794
				Qtot	205.64298

Figure D.3 – Data table for the air flow rate of $200 \text{ m}^3/\text{h}$

Cases studied boundary conditions

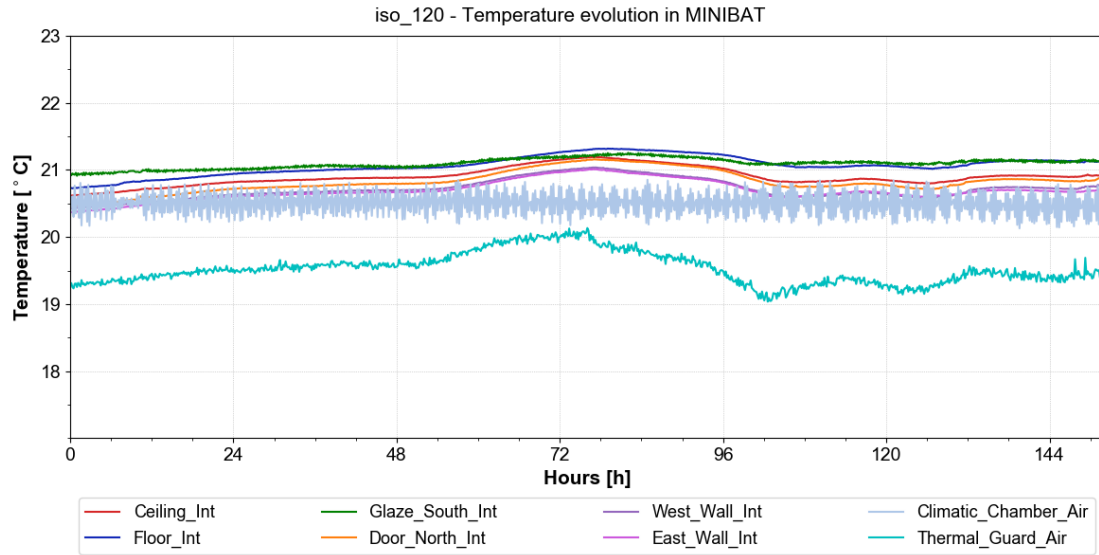
Isothermal jet (iso_120)

Category - Name		Symbol	iso_120	
			Mean	SDEV
Wall temperature [°C]	Ceiling_Int	$T_{SI,C}$	20.81	0.18
	Ceiling_Ext	$T_{SE,C}$	19.78	0.38
	Floor_Int	$T_{SI,F}$	21.02	0.15
	Floor_Ext	$T_{SE,F}$	21.07	0.24
	South_Int	$T_{SI,GL}$	20.99	0.12
	South_Ext	$T_{SE,GL}$	21.09	0.15
	North_Int	$T_{SI,NW}$	20.73	0.21
	North_Ext	$T_{SE,NW}$	20.57	0.30
	East_Int	$T_{SI,EW}$	20.59	0.20
	East_Ext	$T_{SE,EW}$	20.08	0.31
	West_Int	$T_{SI,WW}$	20.62	0.20
	West_Ext	$T_{SE,WW}$	20.09	0.34
Air temperature [°C]	Ambient air	T_{amb}	20.35	0.08
	Climatic chamber	T_{cc}	20.45	0.28
	Thermal buffer zone	T_{tbz}	19.86	0.30

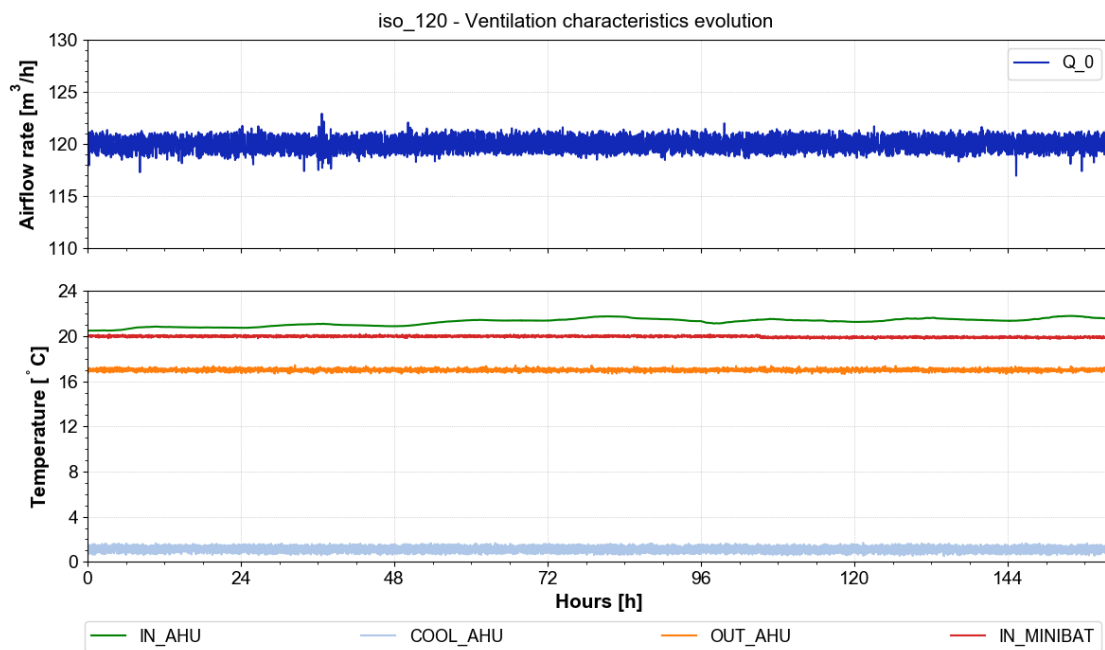
Table E.1 – iso_120 - Measured temperature boundary conditions within the MINIBAT test cell

Category - Name		Symbol	iso_120	
			Mean	SDEV
Airflow rate [m^3/h]		Q_0	119.99	0.72
Air velocity [m/s]		U_0	2.18	-
Temperature [°C]	AHU inlet	$T_{IN,AHU}$	19.97	0.07
	AHU cooling coil	$T_{COOL,AHU}$	1.12	0.27
	AHU outlet	$T_{OUT,AHU}$	17.00	0.11
	MINIBAT inlet	$T_{IN,MB}$	19.97	0.07
	MINIBAT outlet	$T_{OUT,MB}$	20.16	0.16
Specific humidity [g/kg_{as}]	AHU inlet	$r_{IN,AHU}$	4.75	0.08
	AHU cooling coil	$r_{COOL,AHU}$	3.96	0.09
	AHU outlet	$r_{OUT,AHU}$	4.55	0.09
	MINIBAT inlet	$r_{IN,MB}$	4.49	0.07
	MINIBAT outlet	$r_{OUT,MB}$	4.61	0.03
Relative humidity [%]	AHU inlet	$RH_{IN,AHU}$	30.59	0.30
	AHU cooling coil	$RH_{COOL,AHU}$	97.22	0.46
	AHU outlet	$RH_{OUT,AHU}$	38.21	0.77
	MINIBAT inlet	$RH_{IN,MB}$	31.31	0.52
	MINIBAT outlet	$RH_{OUT,MB}$	31.74	0.27

Table E.2 – iso_120 - Measured air supply characteristics



(a) Wall surface temperature



(b) Air supply characteristics

Figure E.1 – iso_120 - Evolution of the measured boundary conditions

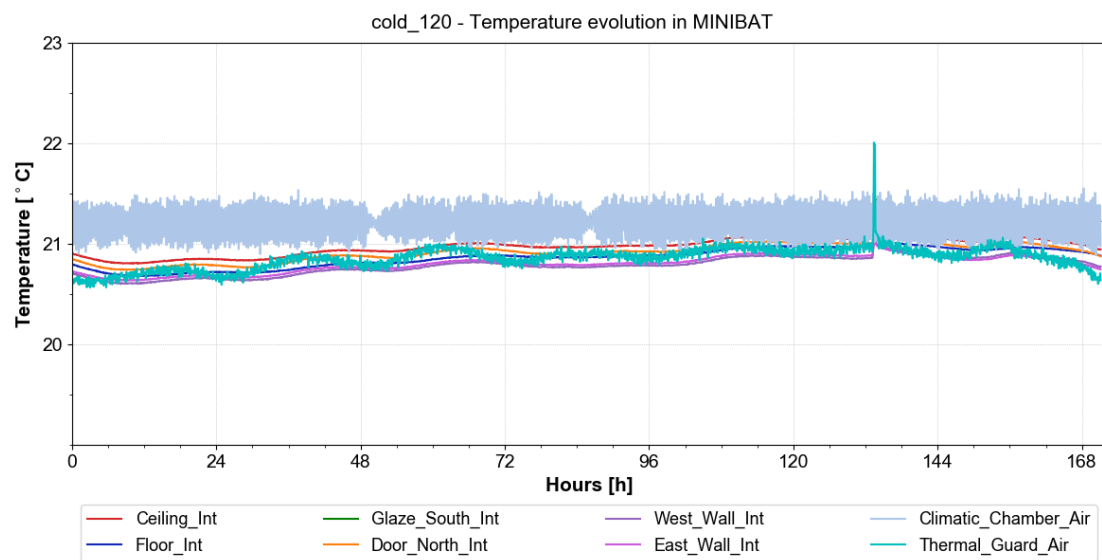
Cold jet (cold_120)

Category - Name		Symbol	cold_120	
			Mean	SDEV
Wall temperature [°C]	Ceiling_Int	$T_{SI,C}$	20.97	0.09
	Ceiling_Ext	$T_{SE,C}$	21.31	0.09
	Floor_Int	$T_{SI,F}$	20.87	0.10
	Floor_Ext	$T_{SE,F}$	21.74	0.33
	South_Int	$T_{SI,GL}$	21.25	0.06
	South_Ext	$T_{SE,GL}$	21.57	0.06
	North_Int	$T_{SI,NW}$	20.92	0.09
	North_Ext	$T_{SE,NW}$	21.56	0.12
	East_Int	$T_{SI,EW}$	20.80	0.08
	East_Ext	$T_{SE,EW}$	21.17	0.09
	West_Int	$T_{SI,WW}$	20.79	0.09
	West_Ext	$T_{SE,WW}$	21.35	0.10
Air temperature [°C]	Ambient air	T_{amb}	19.74	0.06
	Climatic chamber	T_{cc}	21.21	0.16
	Thermal buffer zone	T_{tbz}	20.86	0.11

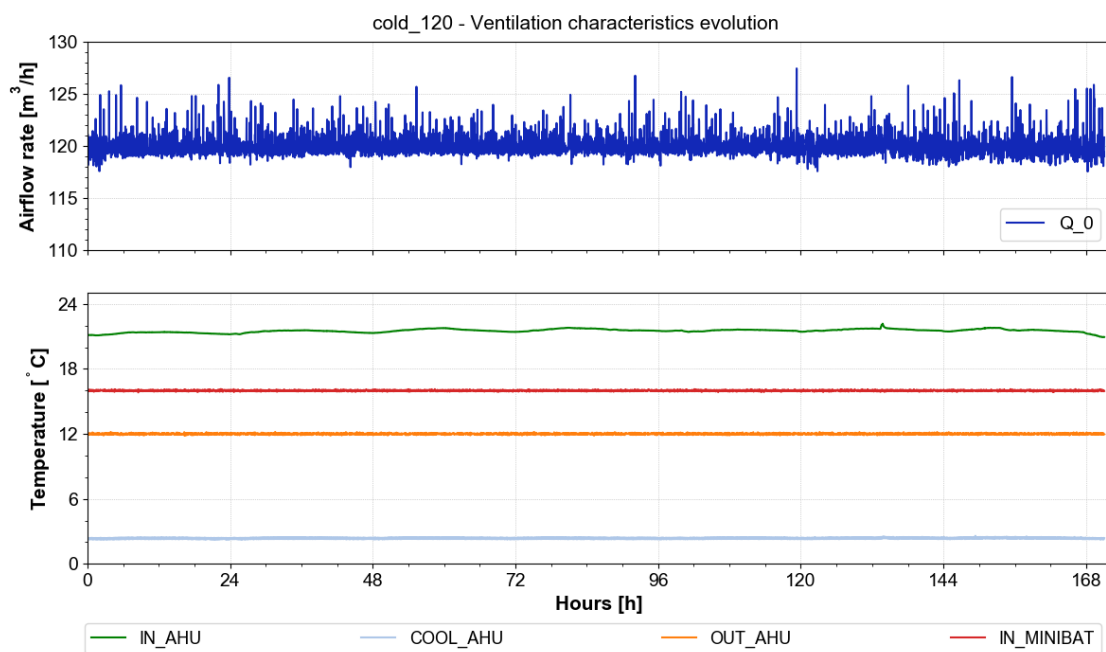
Table E.3 – cold_120 - Measured temperature boundary conditions within the MINIBAT test cell

Category - Name		Symbol	cold_120	
			Mean	SDEV
Airflow rate [m^3/h]		Q_0	119.99	0.97
Air velocity [m/s]		U_0	2.18	-
Temperature [°C]	AHU inlet	$T_{IN,AHU}$	21.52	0.16
	AHU cooling coil	$T_{COOL,AHU}$	2.37	0.06
	AHU outlet	$T_{OUT,AHU}$	12.00	0.05
	MINIBAT inlet	$T_{IN,MB}$	16.00	0.04
	MINIBAT outlet	$T_{OUT,MB}$	19.66	0.08
Specific humidity [g/kg_{as}]	AHU inlet	$r_{IN,AHU}$	5.15	0.06
	AHU cooling coil	$r_{COOL,AHU}$	4.27	0.02
	AHU outlet	$r_{OUT,AHU}$	4.83	0.03
	MINIBAT inlet	$r_{IN,MB}$	4.76	0.03
	MINIBAT outlet	$r_{OUT,MB}$	4.96	0.05
Relative humidity [%]	AHU inlet	$RH_{IN,AHU}$	32.61	0.36
	AHU cooling coil	$RH_{COOL,AHU}$	96.03	0.11
	AHU outlet	$RH_{OUT,AHU}$	55.94	0.36
	MINIBAT inlet	$RH_{IN,MB}$	42.60	0.26
	MINIBAT outlet	$RH_{OUT,MB}$	35.23	0.26

Table E.4 – cold_120 - Measured air supply characteristics



(a) Wall surface temperature



(b) Air supply characteristics

Figure E.2 – cold_120 - Evolution of the measured boundary conditions

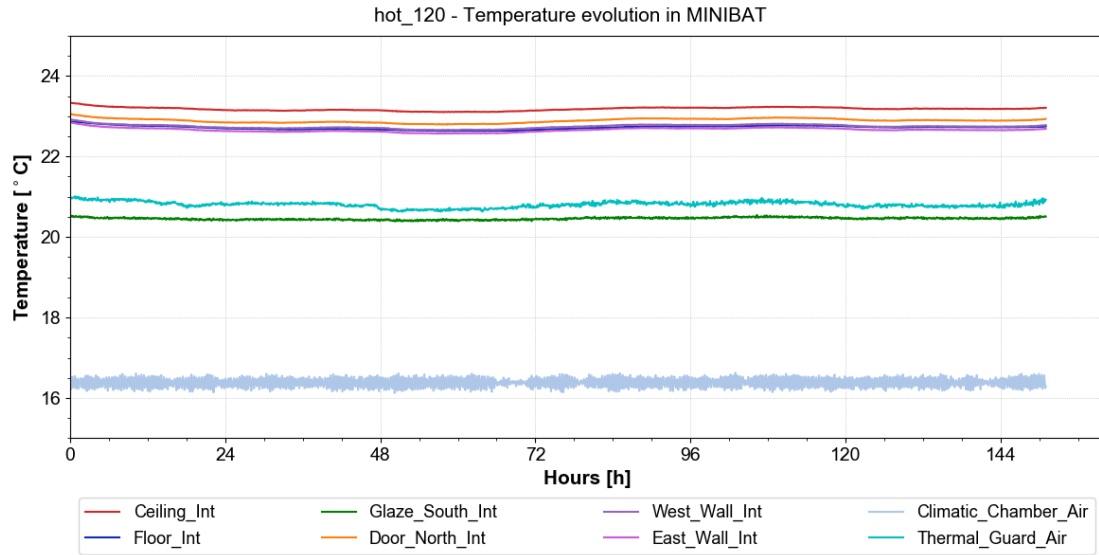
Hot jet (hot_120)

Category - Name		Symbol	hot_120	
			Mean	SDEV
Wall temperature [°C]	Ceiling_Int	$T_{SI,C}$	23.18	0.04
	Ceiling_Ext	$T_{SE,C}$	21.54	0.07
	Floor_Int	$T_{SI,F}$	22.72	0.05
	Floor_Ext	$T_{SE,F}$	20.87	0.06
	South_Int	$T_{SI,GL}$	20.46	0.03
	South_Ext	$T_{SE,GL}$	18.92	0.04
	North_Int	$T_{SI,NW}$	22.89	0.05
	North_Ext	$T_{SE,NW}$	22.01	0.07
	East_Int	$T_{SI,EW}$	22.66	0.05
	East_Ext	$T_{SE,EW}$	21.60	0.07
	West_Int	$T_{SI,WW}$	22.75	0.05
	West_Ext	$T_{SE,WW}$	21.75	0.06
Air temperature [°C]	Ambient air	T_{amb}	23.25	0.06
	Climatic chamber	T_{cc}	16.38	0.11
	Thermal buffer zone	T_{tbz}	20.81	0.07

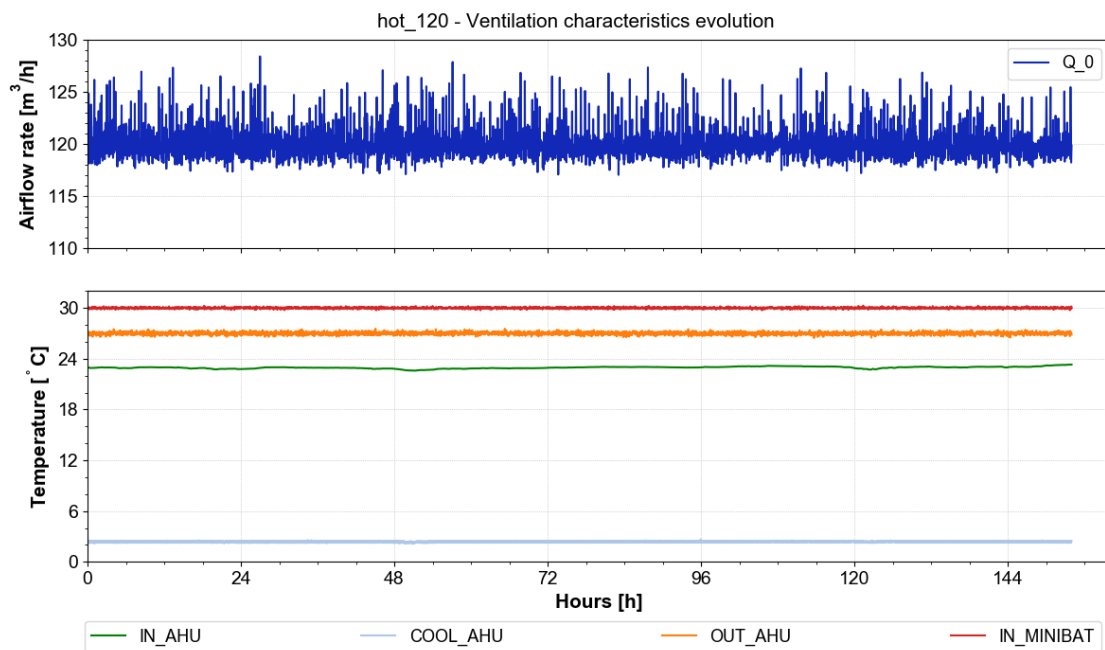
Table E.5 – hot_120 - Measured temperature boundary conditions within the MINIBAT test cell

Category - Name		Symbol	hot_120	
			Mean	SDEV
Airflow rate [m^3/h]		Q_0	119.99	1.37
Air velocity [m/s]		U_0	2.18	-
Temperature [°C]	AHU inlet	$T_{IN,AHU}$	22.96	0.12
	AHU cooling coil	$T_{COOL,AHU}$	2.39	0.08
	AHU outlet	$T_{OUT,AHU}$	27.00	0.15
	MINIBAT inlet	$T_{IN,MB}$	30.00	0.08
	MINIBAT outlet	$T_{OUT,MB}$	22.44	0.10
Specific humidity [g/kg_{as}]	AHU inlet	$r_{IN,AHU}$	5.12	0.05
	AHU cooling coil	$r_{COOL,AHU}$	4.17	0.03
	AHU outlet	$r_{OUT,AHU}$	5.27	0.06
	MINIBAT inlet	$r_{IN,MB}$	5.44	0.05
	MINIBAT outlet	$r_{OUT,MB}$	5.05	0.04
Relative humidity [%]	AHU inlet	$RH_{IN,AHU}$	29.69	0.27
	AHU cooling coil	$RH_{COOL,AHU}$	93.56	0.21
	AHU outlet	$RH_{OUT,AHU}$	24.01	0.24
	MINIBAT inlet	$RH_{IN,MB}$	20.79	0.18
	MINIBAT outlet	$RH_{OUT,MB}$	30.22	0.27

Table E.6 – hot_120 - Measured air supply characteristics



(a) Wall surface temperature



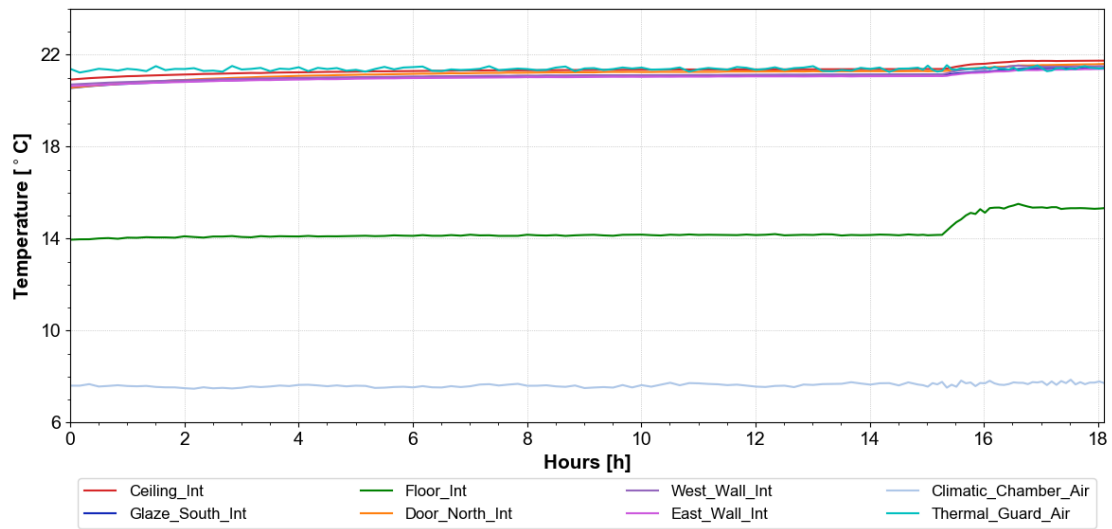
(b) Air supply characteristics

Figure E.3 – hot_120 - Evolution of the measured boundary conditions

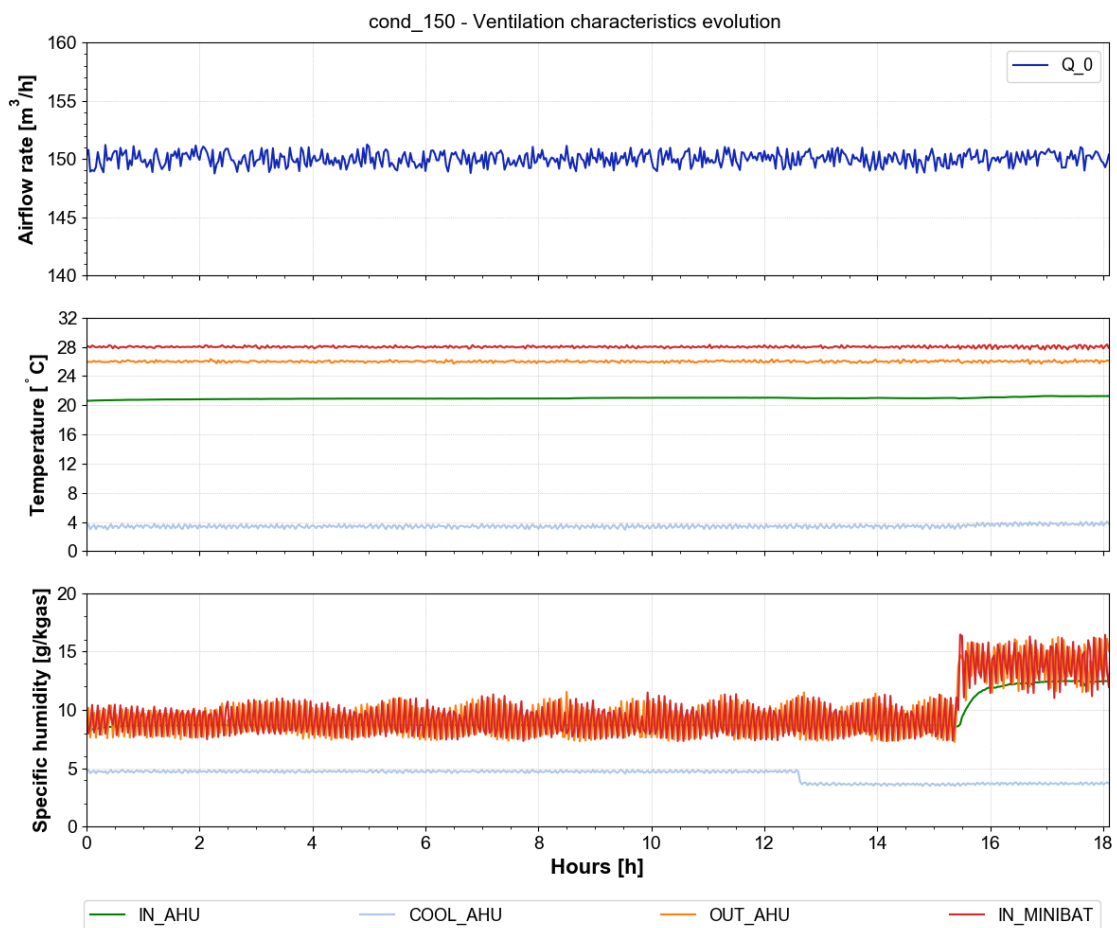
Condensation study (cond_150)

Category - Name		Symbol	cond_150	
			Mean	SDEV
Wall temperature [°C]	Ceiling_Int	$T_{SI,C}$	21.38	0.2
	Ceiling_Ext	$T_{SE,C}$	21.8	0.05
	Floor_Int	$T_{SI,F}$	21.09	0.19
	Floor_Ext	$T_{SE,F}$	20.02	0.03
	South_Int	$T_{SI,GL}$	15.29	0.46
	South_Ext	$T_{SE,GL}$	12.68	0.35
	North_Int	$T_{SI,NW}$	21.29	0.21
	North_Ext	$T_{SE,NW}$	21.22	0.12
	East_Int	$T_{SI,EW}$	21.05	0.18
	East_Ext	$T_{SE,EW}$	21.23	0.06
	West_Int	$T_{SI,WW}$	21.15	0.21
	West_Ext	$T_{SE,WW}$	21.38	0.08
Air temperature [°C]	Ambient air	T_{amb}	-	-
	Climatic chamber	T_{cc}	7.63	0.08
	Thermal buffer zone	T_{tbz}	21.38	0.07

Table E.7 – cond_150 - Measured temperature boundary conditions within the MINIBAT test cell



(a) Wall surface temperature



(b) Air supply characteristics

Figure E.4 – cond_150 - Evolution of the measured boundary conditions

Category - Name		Symbol	Initial		Test	
			Mean	SDEV	Mean	SDEV
Airflow rate [m^3/h]		Q_0	150.00	0.58	150.05	0.55
Air velocity [m/s]		U_0	2.73	-	2.73	-
Temperature [°C]	AHU inlet	$T_{IN,AHU}$	20.92	0.09	21.18	0.10
	AHU cooling coil	$T_{COOL,AHU}$	3.38	0.20	3.70	0.20
	AHU outlet	$T_{OUT,AHU}$	26.00	0.11	26.00	0.13
	MINIBAT inlet	$T_{IN,MB}$	28.01	0.10	28.01	0.19
Specific humidity [g/kg_{as}]	AHU inlet	$r_{IN,AHU}$	8.68	0.05	12.13	0.71
	AHU cooling coil	$r_{COOL,AHU}$	4.52	0.43	3.68	0.07
	AHU outlet	$r_{OUT,AHU}$	9.00	1.19	14.10	1.51
	MINIBAT inlet	$r_{IN,MB}$	9.06	1.20	14.07	1.66
Relative humidity [%]	AHU inlet	$RH_{IN,AHU}$	56.64	0.30	77.46	4.11
	AHU cooling coil	$RH_{COOL,AHU}$	94.44	8.81	75.25	0.49
	AHU outlet	$RH_{OUT,AHU}$	43.17	5.48	67.12	6.79
	MINIBAT inlet	$RH_{IN,MB}$	38.65	4.93	59.54	6.50

Table E.8 – cond_150 - Measured air supply characteristics

Scilab script for LiDAR mapping data conversion

```
// charge les données du lidar
function [PM,NP] = loadPM(filename)
    // Lecture du fichier
    f_p = mopen(filename, 'rt');
    mgetl(f_p, 3); // passer trois lignes
    mfscanf(f_p, '');
    mfscanf(f_p, '\n');
    [trash,theta_p,r_p,quali_p] = mfscanf(-1,f_p,'%f %f %d\n');
    mclose(f_p)
    // Enregistrement dans les variables globales
    NP = size(r_p,1);
    PM = zeros(NP,3);
    for(i=1:NP)
        theta_r = -theta_p(i)*%pi/180; // theta en radian
        r_m = r_p(i); // r en mm
        PM(i,1) = -r_m*sin(theta_r); // x
        PM(i,2) = r_m*cos(theta_r); // y
        PM(i,3) = quali_p(i)/10; // qualité du point entre 0 et 3
    end
endfunction

// affiche les points
function plotPM()
    plot(PM(:,1),PM(:,2),'.')
endfunction

// calcul les paramètres de MINIBAT

function MB = minibat(X0,Y0,THETA)
    MB = zeros(NS,7);
```

```

    theta_r = THETA*pi/180;
    MB(:,1) = (XP0-X0)*cos(theta_r)+(YP0-Y0)*sin(theta_r) ; // x1
    MB(:,2) = -(XP0-X0)*sin(theta_r)+(YP0-Y0)*cos(theta_r) ; // y1
    MB(:,3) = (XP0d-X0)*cos(theta_r)+(YP0d-Y0)*sin(theta_r) ; // x2
    MB(:,4) = -(XP0d-X0)*sin(theta_r)+(YP0d-Y0)*cos(theta_r) ; // y2
    MB(:,5) = MB(:,3)-MB(:,1); // x2-x1
    MB(:,6) = MB(:,4)-MB(:,2); // y2-y1
    MB(:,7) = MB(:,5).*MB(:,5)+MB(:,6).*MB(:,6); // (x2-x1)^2 + (y2-y1)^2
endfunction

// Affichage de MINIBAT

function plotMB()
    for(i=1:NS)
        plot([MB(i,1) MB(i,3)], [MB(i,2) MB(i,4)], '-')
    end
endfunction

// Distance de la série de points à Minibat
function d = d_PM_MB(MB)
    d = 0;
    XH = zeros(NS,1);
    YH = zeros(NS,1);
    for(i=1:NP)
        x = PM(i,1);
        y = PM(i,2);
        pond = PM(i,3);
        // ((x-x1)(x2-x1)+(y-y1)(y2-y1)) / ((x2-x1)^2+(y2-y1)^2)
        params = ((x-MB(:,1)).*MB(:,5)+(y-MB(:,2)).*MB(:,6))./(MB(:,7));
        for(j=1:NS)
            if(params(j)<0)
                XH(j) = MB(j,1)
                YH(j) = MB(j,2)
            elseif(params(j)>1)
                XH(j) = MB(j,3)
                YH(j) = MB(j,4)
            else
                XH(j) = MB(j,1)+params(j)*MB(j,5); // x1+params*(x2-x1)
                YH(j) = MB(j,2)+params(j)*MB(j,6); // y1+params*(y2-y1)
            end
        end
        d = d + min( sqrt( (x-XH).*(x-XH) + (y-YH).*(y-YH) ) ) * pond;
    end
endfunction

//filtre les points les plus éloignés de la première estimation

function [PM,NP] = filter(MB,PM,NP)

```

```

XH = zeros(NS,1);
YH = zeros(NS,1);
i_idx = 1;          // index du point dans le vecteur tronqué
i_counter = 1;      // compteur sur le vecteur initial
for(i_counter=1:NP)
    x = PM(i_idx,1);
    y = PM(i_idx,2);
    // ((x-x1)(x2-x1)+(y-y1)(y2-y1)) / ((x2-x1)^2+(y2-y1)^2)
    params = ((x-MB(:,1)).*MB(:,5)+(y-MB(:,2)).*MB(:,6))./(MB(:,7)));
    for(j=1:NS)
        if(params(j)<0)
            XH(j) = MB(j,1)
            YH(j) = MB(j,2)
        elseif(params(j)>1)
            XH(j) = MB(j,3)
            YH(j) = MB(j,4)
        else
            XH(j) = MB(j,1)+params(j)*MB(j,5); // x1+params*(x2-x1)
            YH(j) = MB(j,2)+params(j)*MB(j,6); // y1+params*(y2-y1)
        end
    end
    d = min( sqrt ( (x-XH).*(x-XH) + (y-YH).*(y-YH) ) );
    if(d>DISTOL)
        PM(i_idx,:) = [];
        NP = NP-1;
    else
        i_idx = i_idx+1;
    end
    i_counter = i_counter + 1;
end
endfunction

```

```

//fonction coût

```

```

function c = cost(vX)
    MB = minibat(vX(1),vX(2),vX(3));
    c = d_PM_MB(MB);
endfunction

```

```

// position mats supérieurs + bouche

```

```

function [xm,ym,xb,yb,dy] = checkbouche(posR)
    theta_r = posR(3)*%pi/360;
    xb = (1007-posR(1))*cos(theta_r)+(4204-posR(2))*sin(theta_r);
    yb = -(1007-posR(1))*sin(theta_r)+(4204-posR(2))*cos(theta_r);

```

```

        xm(1) = 242 // mat vitesses
        ym(1) = -170;
        xm(2) = -241; // mat temperatures
        ym(2) = -185;
        dy = yb+170; // distance de la bouche en face des mâts
endfunction

clear NP
clear PM
delete(gcf())
clf(figure(1))

// CONSTANTES
SHIFTHETA = - 2.7320738;
NS = 8; // nombre de segments dans minibat (contant)
DISTOL = 120; // Tolérnce sur la distance
XP0 = [ 0000 ; 3103 ; 3085 ; 3015 ; 3015 ; 0070 ; 0070 ; 0000 ];
XP0d = [ 0000 ; 0000 ; 3103 ; 3085 ; 3015 ; 3015 ; 0070 ; 0070 ];
YP0 = [ 0000 ; 0000 ; 6209 ; 6209 ; 6269 ; 6251 ; 6191 ; 6191 ];
YP0d = [ 6191 ; 0000 ; 0000 ; 6209 ; 6209 ; 6269 ; 6251 ; 6191 ];

// Chargement de la librairie
funcprot(0)
exec("lib2.sce",-1);
funcprot(1)

// Chargement du fichier de mesure des distances
[PM,NP] = loadPM('lid');

// Première estimation de la position
posR = fminsearch(cost,[1500 3000 90]);
MB = minibat(posR(1),posR(2),posR(3));

// Affichage de cette estimation
figure(1)
plotMB();
plotPM();

// Filtres des données mesurées (avec le dernier MB calculé!)
[PM,NP] = filter(MB,PM,NP)

// Seconde estimation de la position
posR2 = fminsearch(cost,posR);
MB = minibat(posR2(1),posR2(2),posR2(3));

```

```
// Affichage de cette estimation
figure(2)
plotMB();
plotPM();
isoview(-5000,3000,-5000,3000);

// Affichage des coordonnées:
disp("x (cm):");
disp(posR2(1)/10);
disp("y (cm): ");
disp(posR2(2)/10);
disp("theta (deg): ");
disp(posR2(3)+SHIFTHETA);

[xm,ym,xb,yb,dy] = checkbouche(posR2);
plot(xm,ym,'g.')
plot(xb,yb,'r.')

disp("distance de la bouche en face des mâts (cm):");
disp(dy/10);
```


Robot chassis specifications




Parts & Technical specifications			
Pictures	Parts	Parameter	Value
	Chassis	Length	400mm
		Width	307mm
		Height	123mm
		Distance between bottom and ground	21.5mm
		Material	Aluminum alloy
		Color	Blue
		Speed	0.6m/s
		Net weight	5.5kg
		Load capacity	10kg
	Motor	Type	Faulhaber 12V DC Coreless Motor
		Power	17W
		No Load Speed	8100RPM/minute
		Reduced Speed	120RPM/minute
		Diameter	30mm
		Length	42mm
		Total Length	85mm
		Diameter of Shaft	6mm
		Length of Shaft	35mm
		No Load Current	75mA
		Load Current	1400mA
		Gearbox Ratio	64:1
	Encoder	Type	Optical
		Encoder Phase	A B
		Encoder Resolution	12CPR
	Wheel	Outside wheel diameter	100mm
		Width	50mm
		Body material	Aluminium alloy
		Spacer material	Nylon
		Number of Plates	2
		Number of Rollers	9
		Length of roller	47mm
		Roller material	PA+PU
		Net weight	0.4kg
		Load capacity	15Kg

Figure G.1 – Robot chassis parts and specifications

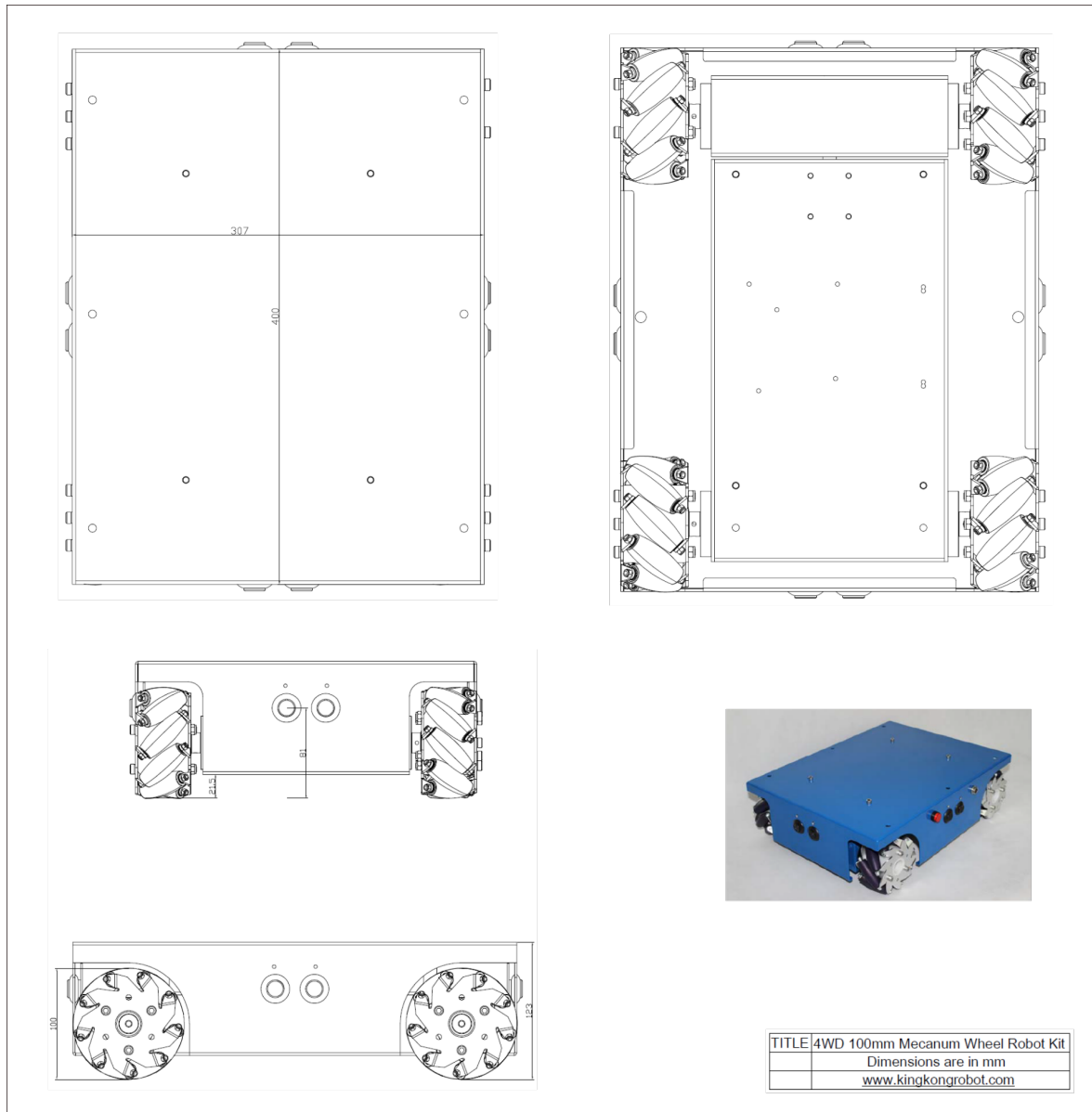


Figure G.2 – Robot chassis scheme

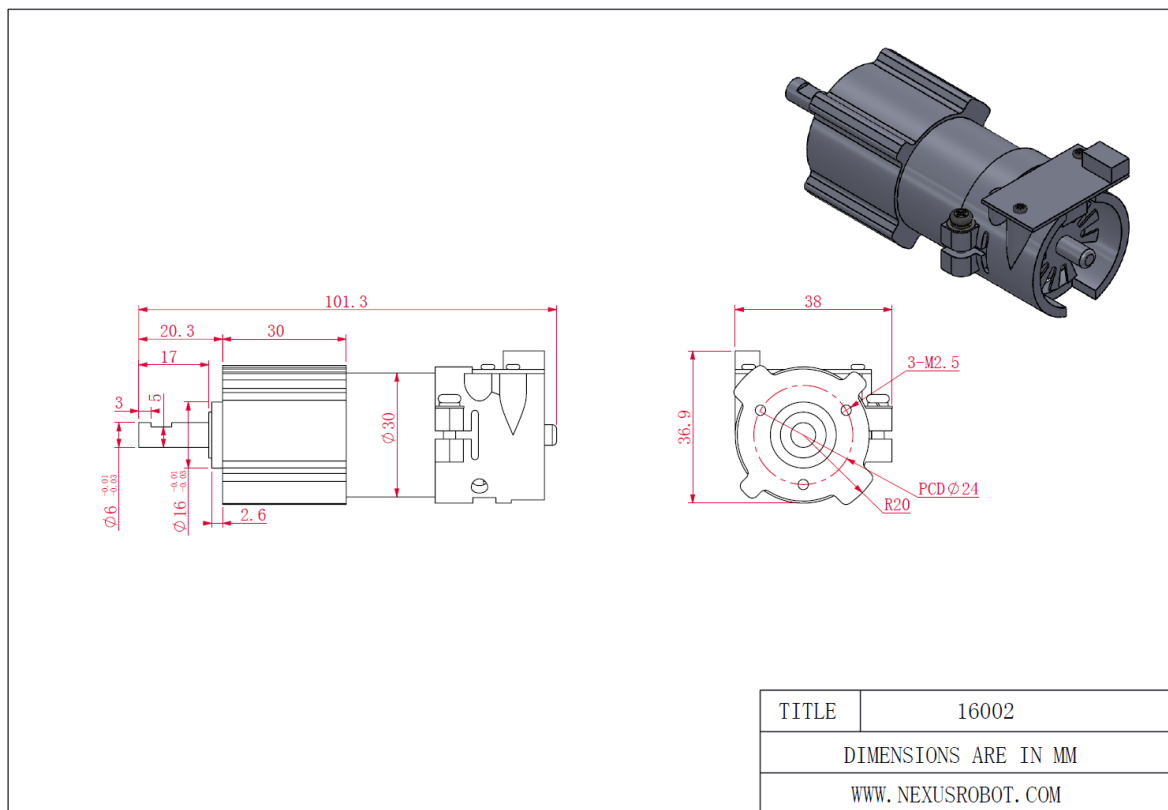


Figure G.3 – Robot chassis motors scheme

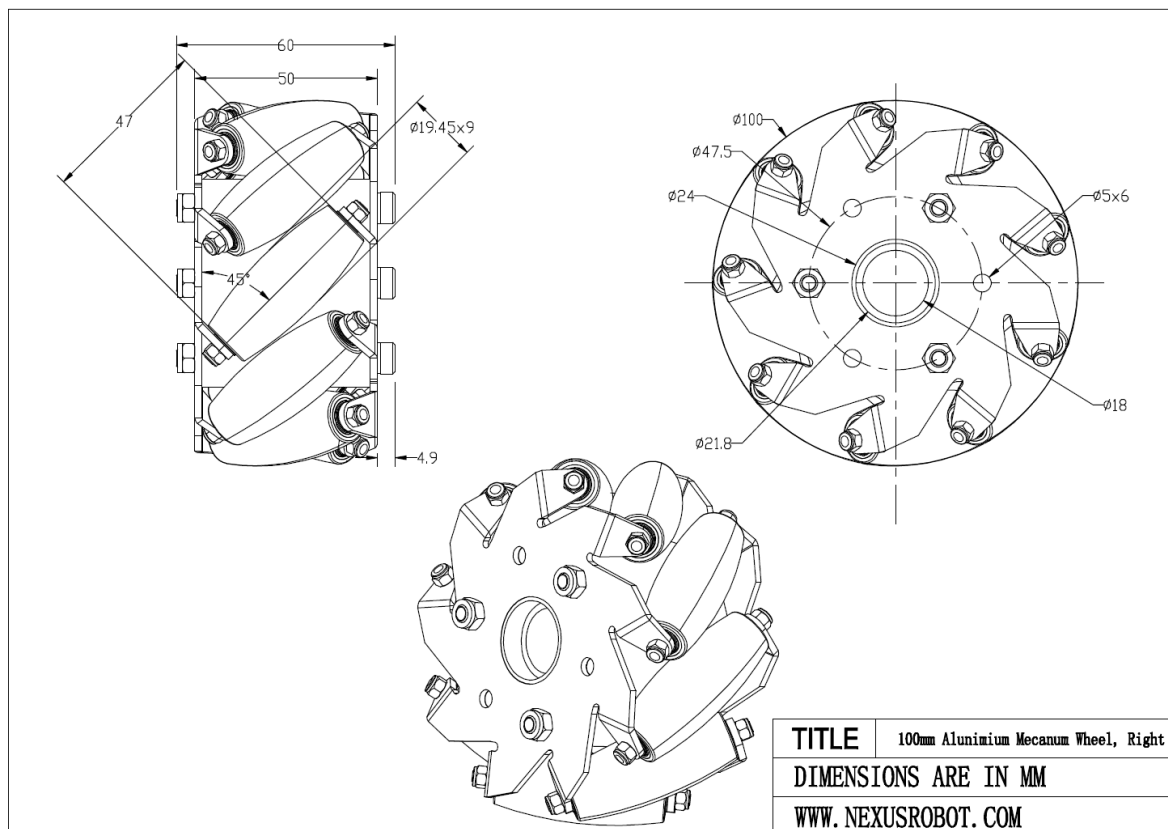


Figure G.4 – Robot chassis wheels scheme

Direction of Movement	Wheel Actuation
Forward	All wheels forward same speed
Reverse	All wheels backward same speed
Right Shift	Wheels 1, 4 forward; 2, 3 backward
Left Shift	Wheels 2, 3 forward; 1, 4 backward
CW Turn	Wheels 1, 3 forward; 2, 4 backward
CCW Turn	Wheels 2, 4 forward; 1, 3 backward

To the right: This is a top view looking down on the drive platform. Wheels in Positions 1, 4 should make X- pattern with Wheels 2, 3. If not set up like shown, wheels will not operate correctly.

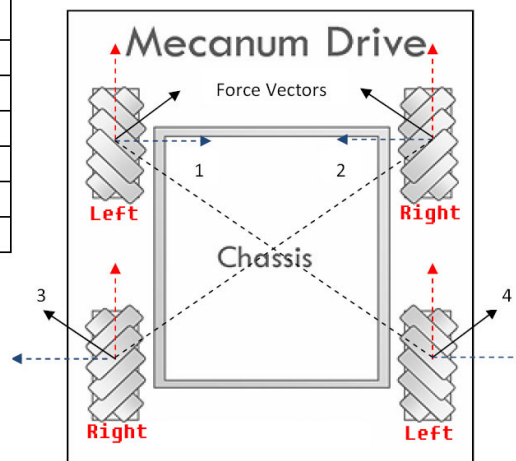


Figure G.5 – Mecanum wheel operating principle

Additional experimental results

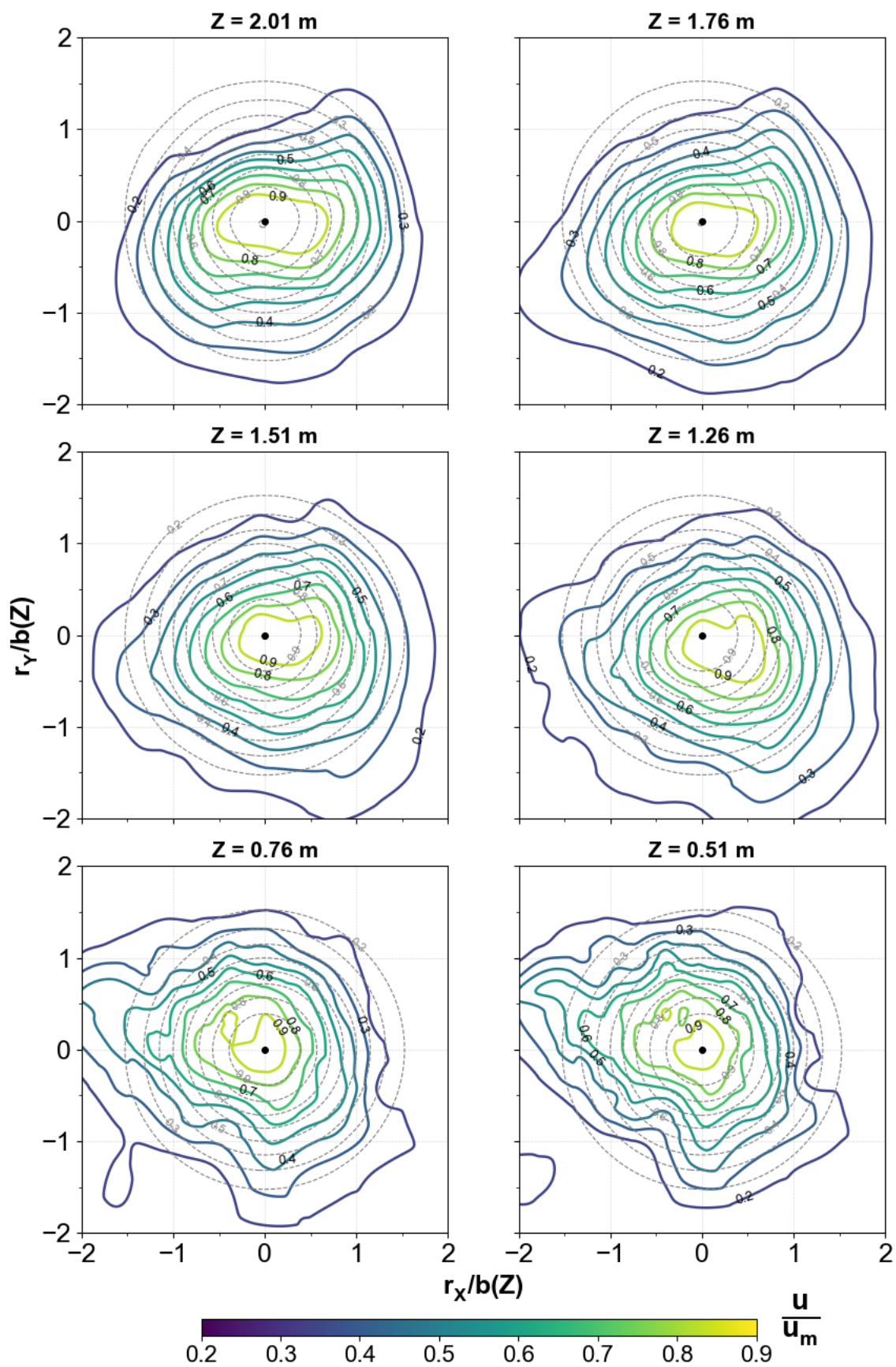


Figure H.1 – Dimensionless velocity contours map - Isothermal jet
Dashed contours: axisymmetric free jet empirical model

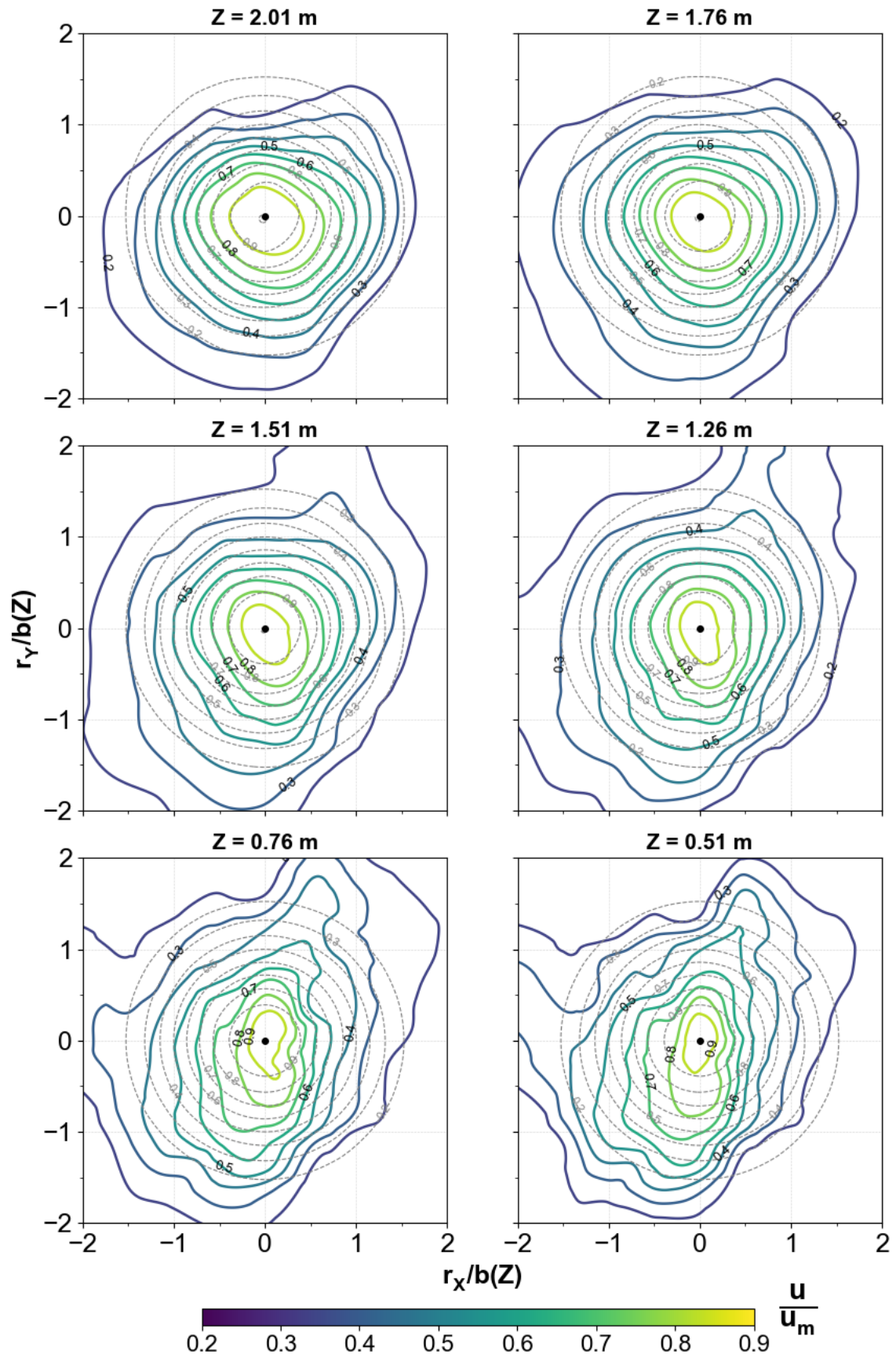


Figure H.2 – Dimensionless velocity contours map - Cold jet

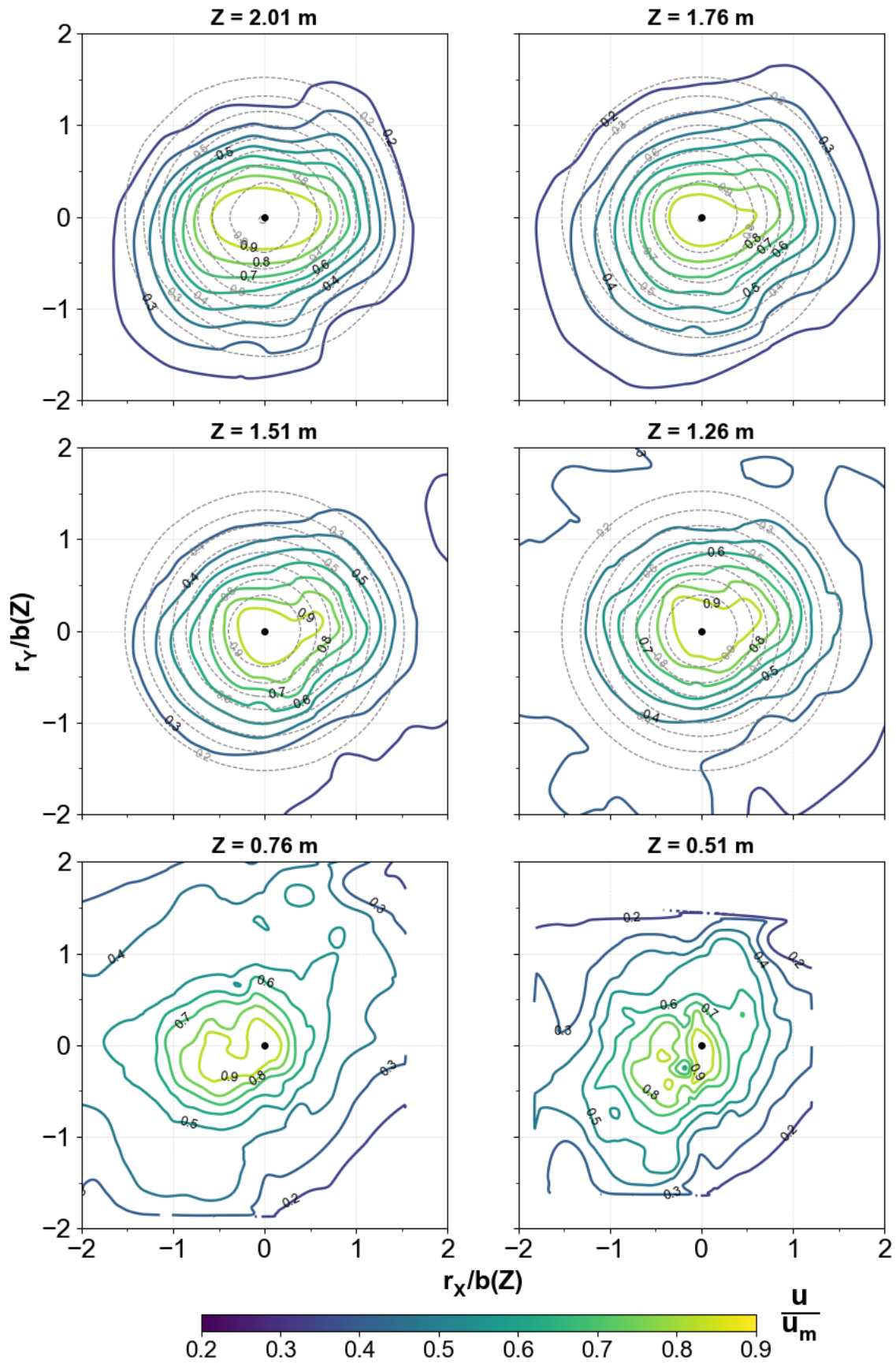


Figure H.3 – Dimensionless velocity contours map - Hot jet

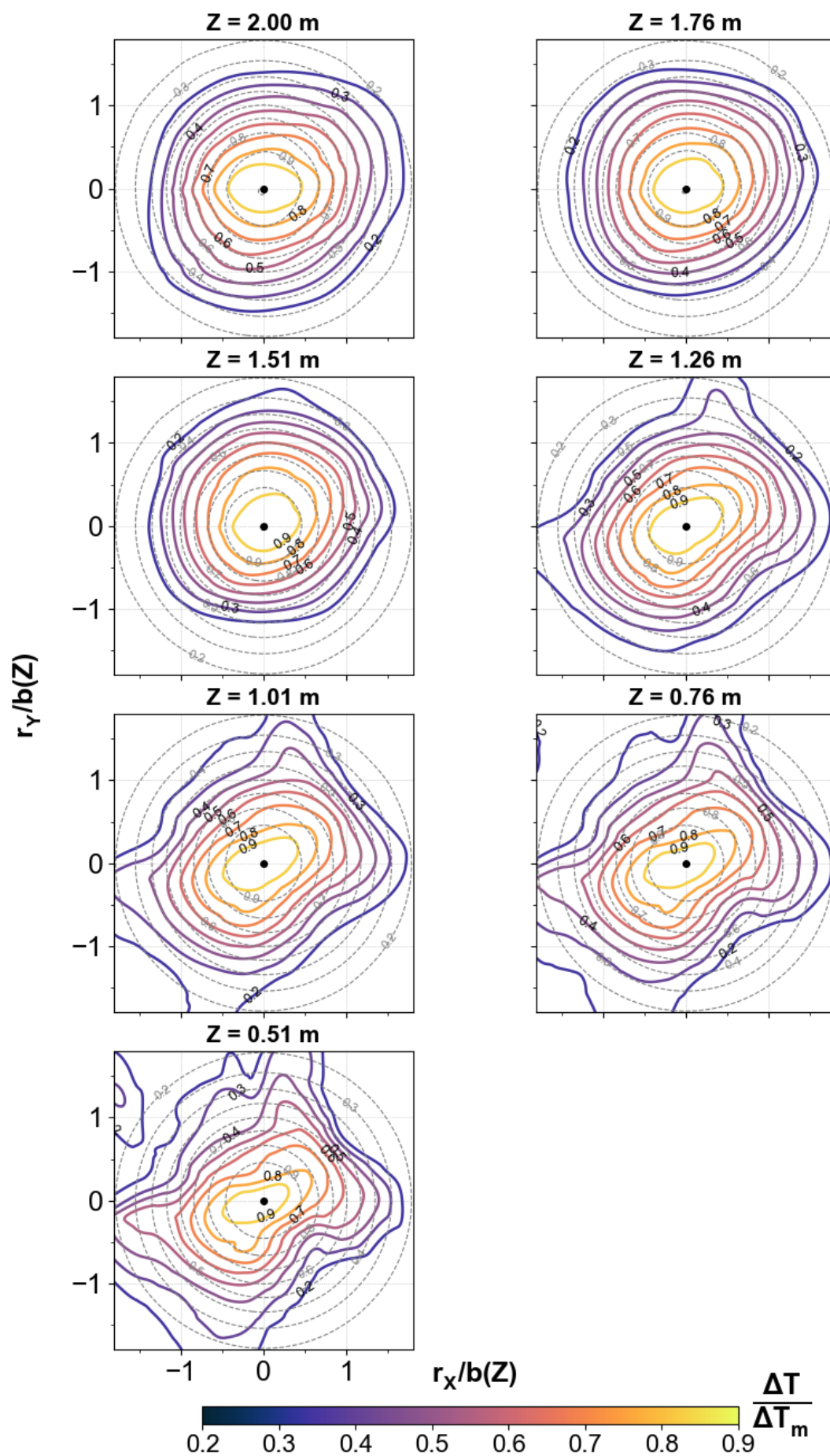
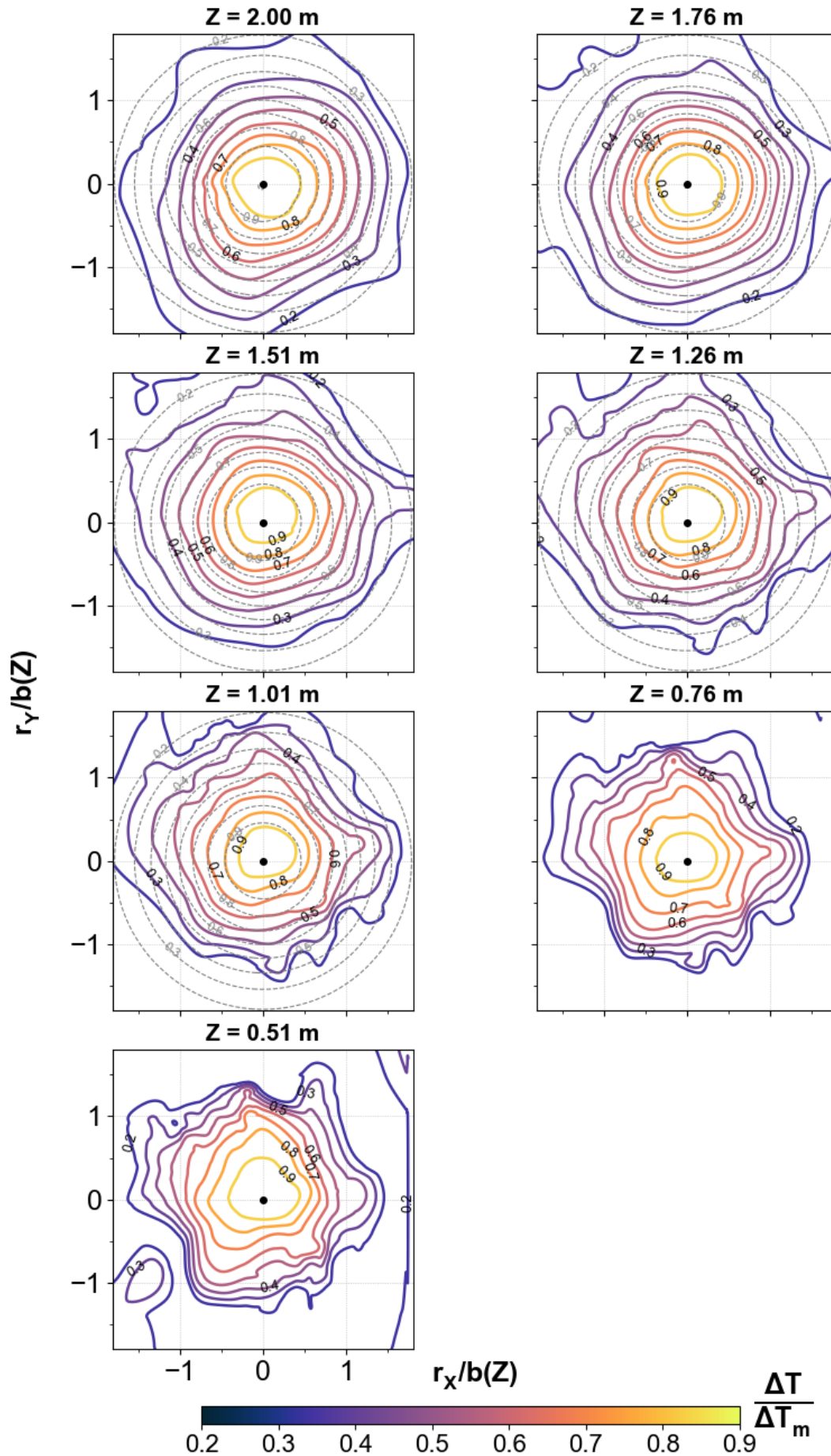


Figure H.4 – Dimensionless temprature contours map - Cold jet



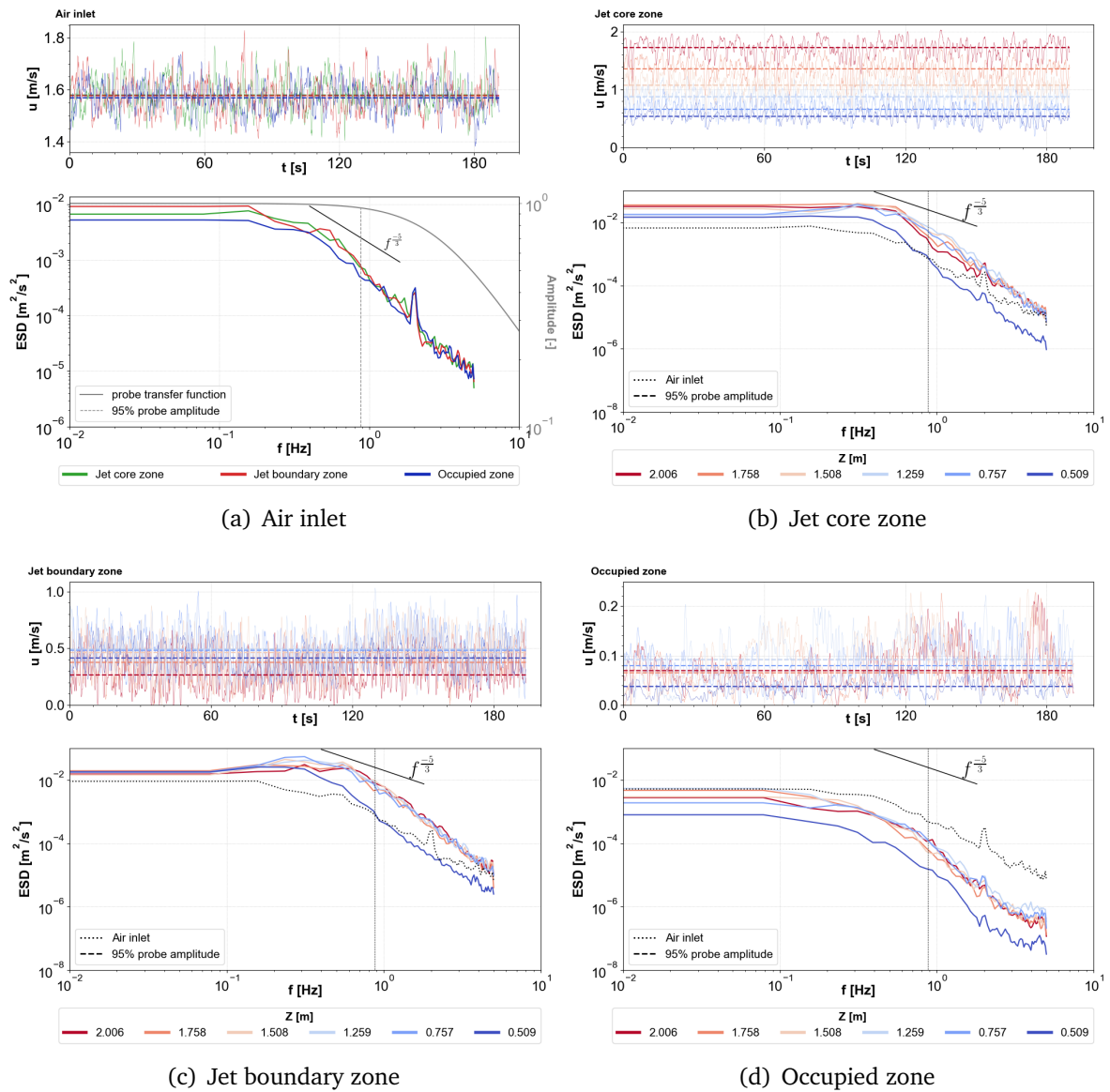


Figure H.6 – iso_120 - Energy spectral distribution

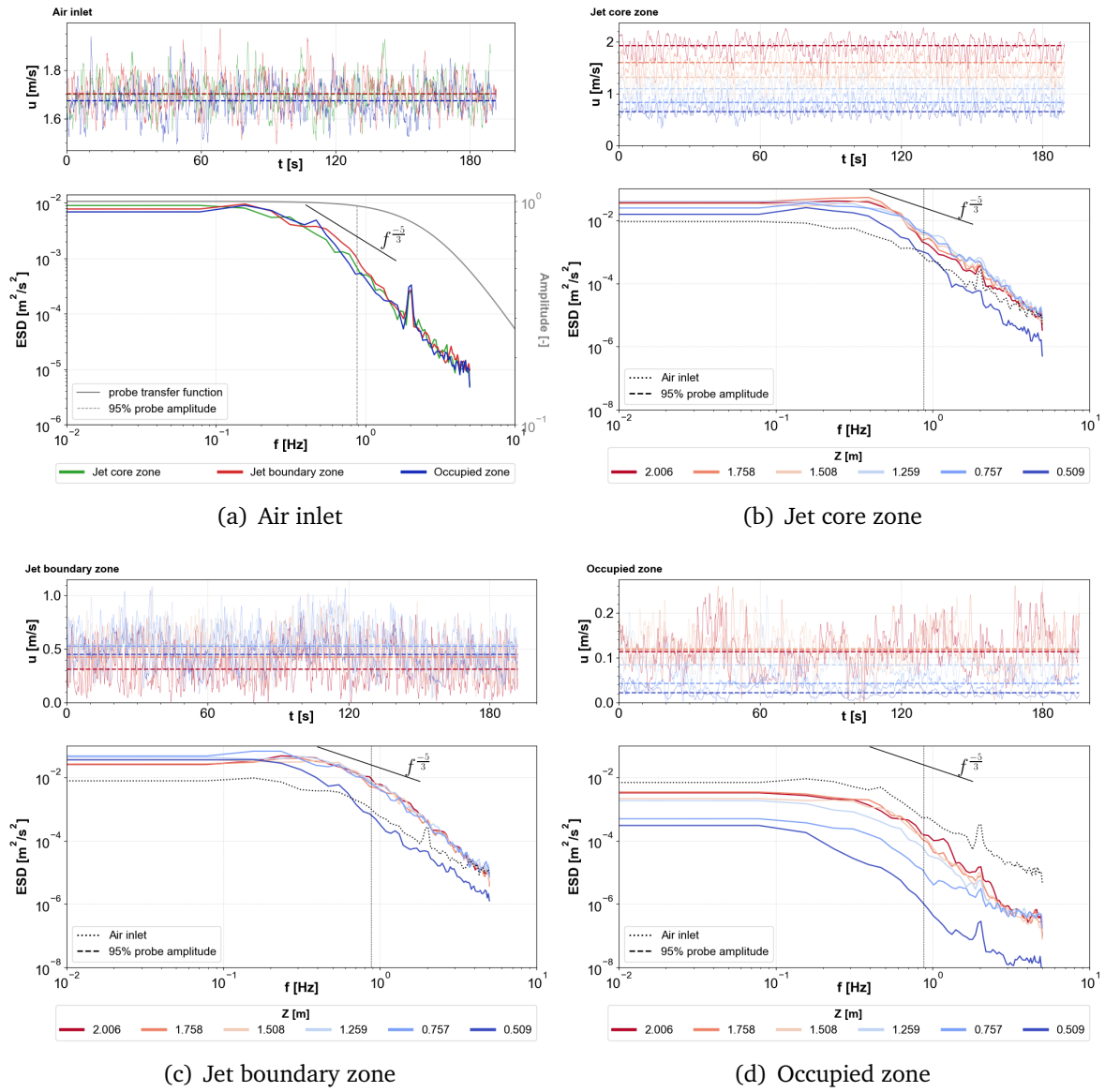


Figure H.7 – cold_120 - Energy spectral distribution



FOLIO ADMINISTRATIF

THESE DE L'UNIVERSITE DE LYON OPEREE AU SEIN DE L'INSA LYON

NOM : NGUYEN
Prénoms : Chi-Kien

DATE de SOUTENANCE : 25/10/2018

TITRE : Full-scale experimental characterization of a non-isothermal realistic air jet for building ventilation:
local interaction effects and condensation prediction

NATURE : Doctorat
Ecole doctorale : MEGA (Mécanique, Énergétique, Génie Civil, Acoustique)
Spécialité : Génie Civil

Numéro d'ordre : 2018LYSEI077

RÉSUMÉ :

La compréhension de la distribution de l'air intérieur accompagné du transfert couplé "chaleur-air-humidité" est essentielle à la conception des systèmes de ventilation des bâtiments. Une conception adéquate devrait garantir trois critères majeurs: l'efficacité énergétique, le confort thermique des occupants et la qualité de l'air intérieur, dont les exigences ne cessent d'augmenter. L'étude de la distribution de l'air intérieur implique deux méthodes courantes : la simulation numérique et les essais à l'échelle réelle. La simulation numérique utilisant des modèles CFD est la plus efficace pour prédire la distribution d'air et la performance des systèmes de ventilation dans les bâtiments. Néanmoins, leur fiabilité demeure une préoccupation majeure, compte tenu du manque d'études de validation approfondies, en particulier des essais à l'échelle réelle.

Au cours des dernières décennies, bien que de nombreuses recherches aient été menées sur les études des jets d'air, certaines questions méritent toutefois d'être examinées. En effet, la majorité de ces études se sont concentrées sur une disposition symétrique des bouches de soufflage et d'extraction par rapport à la géométrie du local. En outre, les études traitant du transfert couplé "chaleur-air-humidité", qui inclut le phénomène de condensation sur la surface interne du local, sont encore limitées dans la littérature. Par conséquent, ce travail se concentre sur les problématiques suivantes : Quel est le comportement d'un jet d'air réaliste sous des effets d'interaction et comment caractériser de tels jets d'air ? Dans des conditions d'intérieur favorisant la condensation sur une surface froide, pourrions-nous quantifier le débit massique du condensat ? Une étude expérimentale est réalisée dans la cellule d'essais MINIBAT à l'échelle réelle. Elle se compose de deux parties principales.

La première partie consiste à caractériser un jet d'air turbulent au plafond dans une configuration d'écoulement intérieur réaliste. Notre configuration introduit des éléments architecturaux qui font interagir le jet d'air avec la pièce : un plénum, une bouche de soufflage équipée de fixes ailettes et située près d'un mur latéral, une disposition asymétrique des bouches d'extraction par rapport au soufflage. La mesure de champs intérieurs est basée sur un robot mobile équipé de capteurs précis. Trois cas sont testés : un jet isotherme, un jet froid et un jet chaud. Les résultats expérimentaux montrent les effets d'interaction visibles des éléments architecturaux de la pièce sur le comportement du jet d'air : ils ont dévié la trajectoire du jet ainsi que déformé la forme du jet. Les principales caractéristiques du jet, telles que le taux d'expansion, la décroissance de vitesse et de température, sont quantifiées. Pour quantifier la déformation des profils transversaux du jet, une méthode graphique basée sur un indicateur de déformation est proposée et montre des résultats acceptables.

La deuxième partie de ce travail traite le phénomène de condensation sur une surface vitrée en reproduisant les conditions hivernales dans la cellule d'essais : un jet chaud et humide à l'intérieur et un climat extérieur froid. La prédiction qualitative de la condensation, c'est-à-dire le moment de son apparition et le mécanisme dynamique de croissance des gouttelettes, est réalisable en utilisant une technique de macrophotographie. Un post-traitement de cette série chronologique d'images rend possible l'estimation du débit massique de condensat. Les comparaisons entre les résultats expérimentaux et théoriques montrent une certaine concordance, ce qui pourrait valider la faisabilité des techniques d'imagerie dans des études de condensation à l'échelle du bâtiment.

Des données expérimentales détaillées accompagnées de conditions aux limites bien connues issues de ce travail pourraient servir de test de benchmark pour la validation des modèles CFD, en particulier pour les configurations d'écoulement avec rupture de symétrie. De plus, avec les progrès de l'informatique, le traitement d'image proposé pourrait être considérablement amélioré grâce à l'intelligence artificielle, par exemple les réseaux de neurones artificiels avec l'analyse d'images basée sur l'apprentissage profond.

MOTS-CLÉS : Jet d'air réaliste, effets d'interaction, ventilation par mélange, condensation en gouttelettes, traitement d'images.

Laboratoire de recherche : Centre d'Energétique et de Thermique de Lyon (CETHIL UMR 5008)

Directeur de thèse: Frédéric KUZNIK (CETHIL UMR 5008)

Président de jury : Pascal Henry BIWOLE

Composition du jury : Pascal Henry BIWOLE, Damien DAVID, Frédéric KUZNIK, Amina MESLEM, Catalin TEODOSIU, Monika WOLOSZYN